PHOTO- AND ELECTRON-IMPACT IONISATION OF TWO-CENTER ATOMIC SYSTEMS AND THE ROLE OF NUCLEAR MOTION THEREIN

INAUGURAL-DISSERTATION

zur Erlangung des Doktorgrades der
Mathematisch-Naturwissenschaftlichen Fakultät der
Heinrich- Heine-Universität Düsseldorf

vorgelegt von

Fiona Grüll
aus Worms

Düsseldorf, März 2021

aus dem Institut für Theoretische Physik I
der Heinrich-Heine-Universität Düsseldorf

Gedruckt mit der Genehmigung der
Mathematisch-Naturwissenschaftlichen Fakultät der
Heinrich-Heine-Universität Düsseldorf

Berichterstatter:
1. Prof. Dr. Dr. Carsten Müller
2. Prof. Dr. Reinhold Egger

Tag der mündlichen Prüfung: 27.05.2021

Abstract

Fundamental ionisation processes, induced by either an external electromagnetic field or particle impact, have long been studied in detail for one atomic center. The presence of a neighbouring atom can give rise to dynamical electron correlations leading to more complex ionisation pathways. Such processes, like Penning ionisation or electron-transfer mediated decay, rely on the radiationless energy transfer within or between atoms, and occur in a multitude of systems ranging from noble gas dimers to clusters and biological systems. One of the most prominent of those processes, Interatomic Coulombic Decay (ICD), describes the ionisation of an atom due to the radiationless energy transfer from a neighbouring atom. Here, a two-center autoionising state is created by an inner-shell vacancy in the neighbouring atom and its deexcitation via electron-electron interaction can, given a sufficient transition energy, lead to ionisation. Such correlation-driven decay pathways have been shown to be potentially more effective than direct decay processes, such as radiative decay.

The general structure of interatomic decay mechanisms of this sort is comprised in the processes investigated in this thesis, where the influence of an atom being in the vicinity of a neighbouring atom is analysed within the processes of photoionisation and electron-impact ionisation. The ionisation includes two subprocesses: the first one is the creation of the autoionising state which is followed by the interatomic decay, leading to the ionisation. Three main processes are investigated in this thesis, all of them by implementing time-dependent perturbation theory. Of particular interest in this context is the analytically manageable modelling of the effects of the nuclear motion of the system, when the two atoms involved are no longer described as two individual units, but rather as a dimer. Two-center photoionisation (2CPI), where the autoionising state is created by photoexcitation, has been originally established for fixed nuclei, treating the two atoms separately. Near resonance, this indirect process has been shown to tremendously enhance the photoionisation. Amplification, although not as drastic, has also been observed experimentally in the dimers of HeNe and NeAr. Within the experimental consideration, effects of the nuclear motion are automatically included. Therefore, the changes in the cross sections are considered when transitioning from a description of two atomic centers to a treatment of a molecular system. For this purpose, interaction potentials, vibrational wave functions and associated energy shifts, characterising the model system of LiHe, are established, expanding the original calculations for fixed nuclei accounting for the nuclear motion in a weakly bound molecule. The effects of the nuclear motion become apparent in the splitting of the resonance due to the vibrational energy shifts stemming from the potential curves of the system. Furthermore, the motion of the nuclei modifies the decay widths and can favour or hinder some vibrational transitions.

Autoionising states in a two-center system can also be formed by collisions with an incident electron. When followed by ICD, two-center electron-impact ionization, 2C(e,2e), occurs. The analysis, assuming fixed nuclei, provides rewarding insights into the possible amplification of the ionisation, the modification of the angular distribution of the ejected electron, as well as the relevance of transitions to higher lying states. The extensive impact of the different potential curves and fitting procedure on the ionisation cross sections is visualised when including molecular effects. Furthermore, the complex interconnection with respect to the energies of the involved particles can be illustrated by the analysis of the two-center ionisation cross section regarding the momenta of the two electrons in the final state. Throughout this work, the emphasis lies on analytical treatments in order to enhance the physical understanding of the processes studied.

Zusammenfassung

Grundlegende, durch ein externes elektromagnetisches Feld oder Teilchenstoß induzierte, Ionisationsprozesse sind für ein einzelnes atomares Zentrum seit langem im Detail untersucht. Allerdings kann die Anwesenheit eines benachbarten Atoms Elektronenkorrelationen erzeugen, die zu komplexeren Ionisationsvorgängen führen. Solche Prozesse, wie beispielsweise Penning-Ionisation, sind auf strahlungslosen Energietransfer in oder zwischen den beteiligten Atomen angewiesen und kommen in einer Vielzahl von Systemen vor, die von Edelgasdimeren über Cluster bis zu biologischen Systemen reichen. Einer der bekanntesten dieser Prozesse, der interatomare (oder auch intermolekulare) Coulomb-Zerfall (ICD) beschreibt die Ionisierung eines Atoms durch den strahlungsfreien Energietransfer von einem benachbarten Atom. In diesem Fall stammt der autoionisierende Zustand von einer Vakanz in einer inneren Schale und die Abregung über Elektron-Elektron-Wechselwirkung kann zur Ionisation führen, falls die Übergangsenergie ausreichend groß ist. Es wurde bereits gezeigt, dass solche korrelationsgetriebenen Zerfallsprozesse effizienter sein können als direkte Abregungsmechanismen, wie beispielsweise radiativer Zerfall.

Die allgemeine Struktur solcher interatomaren Zerfallsprozesse ist auch in den Prozessen enthalten, die in dieser Arbeit untersucht werden. Hierbei liegt der Fokus auf dem Einfluss eines Atoms auf die Ionisation eines benachbarten Atoms, welche durch die Absorption eines Photons oder durch Elektronenstoß induziert wird. Die indirekte Ionisation besteht aus zwei Unterprozessen. Der Bildung des autoionisierenden Zustands durch die Anregung eines Elektrons folgt der strahlungsfreien Zerfall, der zur Ionisation des benachbarten Atoms führt. Die Beschreibung aller Ionisationsprozesse in dieser Arbeit erfolgt mittels zeitabhängiger Störungstheorie.

Von besonderem Interesse ist in diesem Kontext vor allem die analytisch durchführbare Modellierung der durch die Kernbewegung des Systems bedingten Effekte, die dazu führen, dass die beiden Atome nicht länger als zwei einzelne Einheiten, sondern als Dimer beschrieben werden können. Zwei-Zentren Photoionisation (2CPI), bei der der autoionisierende Zustand durch Photoanregung gebildet wird, wurde ursprünglich für feste Kernabstände und zwei separate Atome untersucht. In der Nähe der Resonanz kann dieser indirekte Vorgang den Gesamtprozess der Ionisation erheblich verstärken. Eine, wenn auch nicht so drastische, Verstärkung konnte auch experimentell in den Dimeren HeNe und NeAr beobachtet werden. In der experimentellen Betrachtung werden molekulare Effekte automatisch mitberücksichtigt.

Untersucht werden deshalb vor allem die Veränderungen beim Übergang von der Beschreibung zweier atomarer Zentren hin zur Betrachtung eines molekularen Systems.

Hierzu werden die erforderlichen Wechselwirkungspotentiale, Vibrationswechselwirkungen und dazugehörige Energieverschiebungen erarbeitet, um die ursprüngliche Rechnung für feste Kernabstände um die Bewegung der Kerne in einem schwachgebundenen Molekül zu erweitern. Die Auswirkungen der Kernbewegung werden vor allem in der Aufspaltung der Resonanz ersichtlich, die durch die Verschiebung der Schwingungsenergien hervorgerufen werden, die ihrerseits wieder auf die Potentialkurven zurückgehen. Zusätzlich verändert die Schwingung der Kerne die Zerfallsbreiten und kann Übergänge zwischen Schwingungsleveln begünstigen oder erschweren.

Autoionisierende Zustände können auch durch Stöße mit einem einfallenden Elektron erzeugt werden. Zwei-Zentren Ionisation nach Elektronenstoß 2C(e,2e) findet statt, wenn der Zerfall durch ICD erfolgt. Die Untersuchung mit festen Kernabständen liefert lohnende Erkenntnisse bezüglich einer möglichen Verstärkung des Ionisationsprozesses, der Veränderung der Winkelverteilung des emittierten Elektrons im Vergleich zur Ein-Zentren-Ionisation sowie der Relevanz von Übergängen zu höheren Anregungszuständen. Der erhebliche Einfluss verschiedener Potentialkurven und Fitmethoden auf die Ionisationsquerschnitte wird durch die Einbindung der molekularen Effekte aufgezeigt. Überdies kann die komplexe Kopplung der den beteiligten Teilchen zugehörigen Energien illustriert werden, indem die Ionisationsquerschnitte bezüglich der Impulse der beiden freien Elektronen im finalen Zustand untersucht werden. Um das physikalische Verständnis der hier diskutierten Prozesse zu verstärken, liegt der Fokus im gesamten Verlauf dieser Arbeit auf der analytischen Durchführbarkeit der Rechnungen.

Contents

1 Introduction

Single ionisation of atoms by photoabsorption or electron-impact are, at first glance, simple processes, that can provide invaluable insights, not only into the structure of the atom, but particularly into the dynamics of the process itself. Accordingly, efforts are being made in order to further improve theoretical descriptions and experimental techniques.

Basic light-matter interactions, such as photoionisation and photoexcitation, have long been investigated. The photoelectric effect, observed experimentally by Hertz and Hallwachs [1, 2] and explained by Einstein [3], occurs when electrons are ejected from a solid due to the exposure to electromagnetic radiation. As a result of the technological progress, the experimental possibilities regarding such processes have improved tremendously over the last decades. Studies employing synchroton light sources and optical lasers have largely contributed to the understanding of photoionisation mechanisms. The introduction of ultrashort and ultraintense X-ray pulses, which are generated by free-electron lasers, have enabled the handling and precise manipulation of the light beams.

Collisional processes represent an integral part in atomic physics, with first experiments being performed in the late 19th century. Aside from elastic and excitation collisions, ionising collisions, where the charge of the target is changed by the ejection of an electron, have been used in order to examine the structure of atoms. However, such collisions can also provide insight into the dynamics of the particular process. Concerning electron impact, the dynamics of this ionisation pathway have first been described in detail in 1969 [4]. Electron-impact ionisation, also called (e,2e) due to the number of electrons in the continuum before and after the ionisation process, can be studied experimentally by detecting the angle and momentum of the two electrons after the collision. The theoretical description of electron-impact ionisation can be complicated due the fact that even for the simplest target of hydrogen, the final state contains three particles. Therefore, solutions can be found either numerically or by relying on approximations in order to simplify the problem to an effective two-body problem. For both photoionisation and electron-impact ionisation, the products of the events, ions and photoelectrons, are monitored in order to describe the underlying dynamics. In experiments, the products can be detected by means of spectrometers, such as time of flight spectrometers (TOF) [5].

These direct ionisation processes represent just one of many mechanisms of ionisation due to the interaction with either an external electromagnetic field or an incident electron. A vacancy, which is created via excitation or ionisation by an electromagnetic field or particle impact, leads to a unstable state in the atom, which is subject to decay. Here, electron correlation can result in more complex ionisation mechanisms, such as Auger decay.

Within this process, an autoionising state within an atom or molecule is originally created by the ionisation of an inner-valence electron and is characterised by the energy of the excited system to be sufficient for its ionisation. Its deexcitation then proceeds via the emission of another electron. These autoionising states can not only be created in an atom, but also between atoms or molecules. Especially for dimers, which are molecules built from only two atoms, decay mechanisms relying on electron correlations are relevant and can dominate over the direct decay via the emission of a photon. Some of the better known processes include Penning ionisation, electron-transfer mediated decay (ETMD) and Förster resonance energy transfer (FRET), which can be found occuring in dimers, clusters and even biological systems [6].

In 1997, one of the most prominent of these processes was proposed. Interatomic (or intermolecular) Coulombic decay (ICD) describes the ionisation of a constituent due to radiationless energy transfer from a neighbouring, participating unit. An inner-shell vacancy in the neighbouring center is filled by an outer-lying electron of the same center, where the transitional energy of the decay has to be sufficiently large for the ionisation of the second constituent to occur [7]. In the process proposed originally, the autoionising state is created via ionisation, thus the emission of an electron from an inner shell.

First experimentally observed in an electron spectroscopy experiment in neon clusters [8], a direct detection of ICD also suceeded in neon dimers [9]. Subsequent theoretical and experimental studies, including the detection of ICD in rare gas dimers [9, 10, 11] and water clusters [12], have proven this process to be an extremely efficient decay channel, which can occur over vast distances between the two participating particles. A manifold of related processes, including variously created autoionising states such as resonant ICD, has been investigated since (for a review, see [13]). Therefore, the investigation of two-center processes is of particular interest due to the effectiveness of electron-electron correlations at large distances between the partaking units.

Considering photoionisation, the effects of (intraatomic) electron correlation can be observed in single-photon double ionisation [14] as well as laser-induced autoionisation [15]. Including an ICD-like decay mechanism in the consideration of an ionisation process, two-center photoionisation (2CPI), where ionisation of one atom proceeds via photoexcitation followed by ICD in a neighbouring atom, has been theoretically established in 2010. For the system of LiHe the calculations, assuming two separate atoms and neglecting any molecular effects, predicted this indirect procress to lead to an exceptional enhancement of photoionisation [16].

LiHe is an example for van der Waals dimers including rare gas atoms. Since rare gas atoms have a closed shell, the interaction between two neighbouring atoms is limited to weak van der Waals terms. This often results in shallow interaction potential curves allowing for large bond widths, for which He_2 represents an extreme example [17]. Consequently, shifts to the ionisation energies with respect to the atomic values are limited for shallow potential curves. Due to these properties, van der Waals dimers, where ICD has been shown to be effective, are suited for the consideration of 2CPI and other processes relying on electron correlations for ionisation. Experimental studies on 2CPI have been carried out in two of those dimers, namely HeNe [18, 19] and NeAr [20], finding two-center photoionisation to be a significant ionisation pathway. Within these experimental considerations, the influence of molecular effects is included automatically. This experimental research motivates the expansion of the theoretical description of the two-center photoionisation with respect to the nuclear motion, incorporating molecular effects and, in particular, the analysis of the changes with respect to the calculation assuming fixed nuclei. Hence, comparisons between the different considerations can shed light on the extent to which calculations assuming fixed nuclei can predict the efficience of two-center ionisation processes in two-atomic molecules. Furthermore, the idea to apply the general concept of this process to a different mechanism, where the autoionising state is created by electron impact, presents itself.

For this type of two-center ionisation, comprehensive theoretical descriptions were still missing.

This thesis is organised as follows. The next section is comprised of the theoretical basics regarding the fundamental processes of photoionisation and electron-impact ionisation, interatomic processes relying on autoionisation, in particular Auger decay and ICD. Furthermore, the mathematical description of the decay channels is showcased, followed by the discussion of some of the wave functions used to describe the system. Additionally, an overview of the interaction in dimers, with particular interest on van der Waals molecules is presented, including the interaction of the electrons as well as the resulting nuclear motion. Finally, the model system for the theoretical considerations, the van der Waals dimer LiHe, is introduced. Particular emphasis lies on the properties of the ground state as well as its experimental detection.

In the third section, the process of single photoionisation is studied factoring in molecular effects. This includes both the direct pathway and the two-center channel. First, however, results are given when assuming the model system to consist of two, non-interacting atoms. The effects of the nuclear motion of the system are accounted for by establishing the interaction potential curves, from which the vibrational wave functions of the nuclei are derived. The inclusion of Franck-Condon factors and modified decay widths leads to an analytical expression for the extended transition amplitude of the two-center photoionisation. The results of this investigation consist of various cross sections, comparing the two approaches and also taking the nodal structure into account. The emergence of recent literature values for the potential curves is incorporated with special emphasis on the impact of fitting procedures and a comparison with the values obtained from the calculated potential curves.

The process of ionisation following electron-impact excitation is studied in the fourth section. Perturbative calculations for the one-center and two-center pathway yield expressions for the energy-differential and fully integrated cross sections. A simplification through one-center processes enables the estimation of the values of the two-center electron-impact ionisation using available literature values only. Numerical results are then given for the $1s$-$2p$ transition in helium with particular emphasis on the enhancement of the ionisation process as well as on the angular distribution of the ejected electrons. Furthermore, transitions to excited states requiring a higher energy are investigated, with special emphasis placed on the significance of such higher lying states with respect to the total ionisation process.

In the fifth section, the theory for the electron-impact ionisation is expanded to also include molecular effects. For this, the newly published literature values for the potential curves are employed and compared with the potential curves calculated before. Numerical results are given regarding the individual detection of the two emitted electrons, providing insight into the different energetic dependencies.

Finally, the thesis is concluded with the summary of the key results in the sixth section, where the findings are reviewed and placed within a larger context.

In the context of this thesis, three articles have been published in reviewed journals and are given in Sec. 8.

Throughout this thesis, atomic units will be used unless noted otherwise.

2 Physical Background and Theoretical Framework

In this section, theoretical foundations are provided, which are necessary for the calculations and interpretations in the following sections 3, 4 and 5, where the processes of two-center photoionisation and two-center electron-impact ionisation are investigated in a system of two atoms. First, the two atoms are considered as individual particles before incorporating the effects of a bound molecular system.

The fundamentals of the one-center processes of photoionisation and electron-impact ionisation, which will constitute the competing processes of the mechanisms derived in the following sections, are presented in Sec. 2.1.

Sections 2.2-2.5 introduce more complex processes involving the energy transfer between several electrons in an atomic center, or hereinafter, between electrons residing in two different atomic centers. Moreover, some mechanisms rely on charge transfer between two atomic or molecular centers.

In particular, the Auger decay, proceeding in a single atomic center, is introduced in Sec. 2.2.1. The consideration of processes relying on energy or charge transfer between two or more atoms and molecules leads to the introduction of Interatomic Coulombic Decay (ICD) in Sec. 2.3, where the concept of Auger decay is expanded to a system consisting of two atoms.

After establishing the interaction responsible for ICD in Sec. 2.4, the mathematical description of the decay width of an excited electronic state is provided in Sec. 2.5. It includes the spontaneous emission of a photon as well as the two-center Auger decay.

While the analytical approach of this work calls for the frequent usage of hydrogen-like wave functions, more complex wave functions for both bound electronic states as well as for electrons in the continuum, are presented in Sec. 2.6.

The processes of one- and two-center photoionisation and electron-impact ionisation are modeled in a system consisting of two atoms in vicinity of each other. Therefore, the interactions in such a setup are described in Sec. 2.7, with emphasis placed on the general form of the resulting interaction potential curve. When the interaction potential allows for a bound state, and therefore a diatomic molecule, to be formed, the relative nuclear motion of the complex has to be considered, including vibrational and rotational excitations.

The processes considered in the following sections are computed for a van der Waals dimer, where the binding energy is small. Hence, the interactions responsible for such a bond are described in Sec. 2.9.1 as well as some examples for dimers including the noble gas helium. This introduction leads to the choice of the model system used here, LiHe, which is motivated by its charateristics.

2.1 Direct electronic processes

Electrons in atomic centers can interact with external fields as well as other particles in a manifold of processes. Hereby, energy can be absorbed or released. In the following, the processes relevant for the following calculations are introduced. These include both the excitation and ionisation of an electron within an atomic center by energy transfer from either photon absorption or electron impact. More detailed descriptions are provided in the Secs. 3 and 4.

2.1.1 Absorption of photons

When a photon γ strikes an atomic center, it can be absorbed and the energy can be transferred to a bound electron. The atom can transition into an excited state

$$\gamma + A \to A^*, \tag{2.1}$$

when the photon energy matches the energy difference $\omega = \varepsilon_e - \varepsilon_g$ of a transition within the atom. Due to the resonant nature of this process, selected excited states can be reached. Furthermore, the interaction with a photon limits the quanta of angular momentum which is exchanged. Hence, not all existent states can be reached.

Given that the energy of the photon is larger than the binding energy of the electron, an electron can be emitted, resulting in the ionisation of the atomic center,

$$\gamma + A \to A^+ + e. \tag{2.2}$$

Direct photoionisation, which will be further treated in Sec. 3.1 is the fundamental process of the photoelectric effect, observed experimentally by Hertz and Hallwachs [1, 2] and described theoretically by Einstein [3]. The reverse process of direct photoionisation is called radiative recombination, where an electron from the continuum is captured by an ion

$$A^+ + e \to A + \gamma. \tag{2.3}$$

The excess energy, which is the difference between the kinetic energy of the electron and its binding energy, is emitted in the form of a photon.

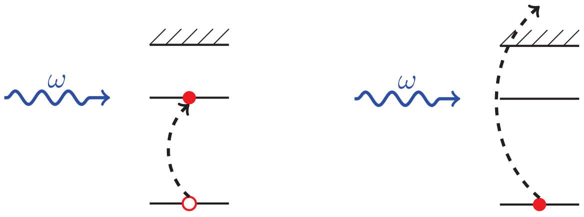

Figure 1: Scheme of two fundamental processes involving the absorption of a photon. Left: Photoexcitation of an atomic center. Right: Photoionisation of an atomic center.

It has to be noted that, in general, multi-photon ionisation is possible, and can occur when the energy of one photon does not suffice to ionise a system. Within this non-linear mechanism, at least two photons are required. Likewise, multi-photon excitation of a system is possible. However, these processes are not part of the following considerations.

In the non-relativistic regime, the description of electrons in the electromagnetic field rests upon the time-dependent Schrödinger equation. In a radiation field, it reads [21]

$$\frac{1}{2}\left(\hat{\mathbf{p}}-\frac{\mathbf{A}}{c}\right)^2\Psi-\phi\Psi+V\Psi=i\frac{\partial}{\partial t}\Psi, \tag{2.4}$$

where an electron in an one-electron atom perceives a potential $V=\frac{Z}{r}$. For the free radiation field, the Coulomb gauge is employed, leading to $\mathrm{div}\mathbf{A}=0$. Furthermore, the scalar potential $\phi(r)$ vanishes for a source-free field. When the product is expanded, the Hamiltonian reads

$$\mathcal{H}=\underbrace{\frac{\hat{\mathbf{p}}^2}{2}-\frac{Z}{r}}_{=H_0}\underbrace{-\frac{1}{2c}\mathbf{A}\hat{\mathbf{p}}-\frac{1}{2c}\hat{\mathbf{p}}\mathbf{A}+\frac{\mathbf{A}^2}{2c^2}}_{=H_{int}}, \tag{2.5}$$

To describe photoionisation, the electromagnetic field may be treated classically. For effects, such as radiative recombination or spontaneous emission (see Sec. 2.5.1), the quantisation of the vector potential is necessary. The associated mathematical description via first-order perturbation theory is presented in Sec. 3.1. One of the characteristic features of the direct single-photon ionisation is its angular distribution of the ejected electrons. It features the typical dipole pattern, see Fig. 2.

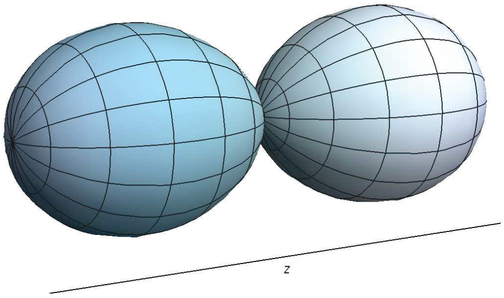

Figure 2: Spherical plot of the angular distribution of emitted electrons in the process of photoionisation. The polarisation of the external field is set along **z**.

2.1.2 Electron impact

Upon the collision of an electron, characterised by an initial momentum $\mathbf{p}_{\mathrm{in}}$, with an atomic center, energy can be transferred from the incident electron to the atom, leading to the excitation of a bound electron to a state with a higher energy:

$$e+A\rightarrow A^*+e. \tag{2.6}$$

For this to be possible, the kinetic energy of the incident electron has to be larger than the transition energy $\omega=\varepsilon_e-\varepsilon_g$ of the electronic transition in atomic center A. If the kinetic energy of the incident electron is even larger than the binding energy of an electron in A, a formerly bound electron in atom A can be emitted to the continuum, leading to the ionisation of the residual atomic center

$$e + A \rightarrow A^{+} + 2e. \tag{2.7}$$

Energy conservation results in $\frac{p_{\mathrm{in}}^2}{2} - \frac{p_{\mathrm{f}}^2}{2} + \varepsilon_g - \frac{k^2}{2} = 0$, determining the energy loss of the projectile electron, which depends on the incident electron energy and the energy of the emitted electron $k^2/2$. Any excess energy $\frac{p_{\mathrm{in}}^2}{2} + \varepsilon_g$, which can be available if the energy of the incident electron is larger than the energy required for ionisation, can be shared arbitrarily between the scattered electron and the emitted one. This will be discussed in more detail below. Furthermore, the residual ion can experience a momentum transfer. However, due to its large mass, the resulting energy transfer is negligible. Electron-impact single ionisation is also called (e,2e), since one incident electron in the inital state leads to two electrons in the continuum: the scattered as well as the emitted electron. Assuming a sufficiently large energy of the incident electron, the ejection of more than a single electron, i.e. multiple ionisations, is also possible, but will not be considered in the following of this thesis. Note, that when an electron is emitted from an inner shell, the residual ion is in an electronically excited state after the collision.

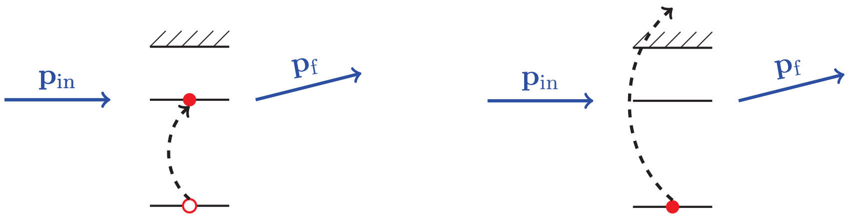

Figure 3: Scheme of two fundamental processes involving electron impact. Electron-impact excitation of an atomic center is depicted on the left, whereas single electron-impact ionisation can be seen on the right.

For the process of electron-impact ionisation, which will be discussed in greater detail in Sec. 4.1, the semi-empirical formula was developed by Lotz in 1967 [22]:

$$\sigma_{\mathrm{EI}} = \sum_{j=1}^{N} a_j q_j \frac{\ln(E/P_j)}{EP_j} \left[1 - b_j e^{-c_j(E/P_j - 1)}\right] \tag{2.8}$$

Here, a_j, b_j and c_j are parameters empirically determined, P_j denotes the binding energy of the subshell j and E is the energy of the incident electron. The formula above includes a sum over all occupied subshells of the respective atoms in order to yield a value for the ionisation from all states. The number of electrons on each subshell is denoted by q_j. For the calculation of the cross section for ionisation from a specific electronic shell, the relevant contributions have to be considered accordingly. Plots for the electron-impact ionisation cross sections calculated via the Lotz formula are depicted in Fig. 4 for lithium and helium. These elements will be part of the investigations in the Secs. 3, 4 and 5.

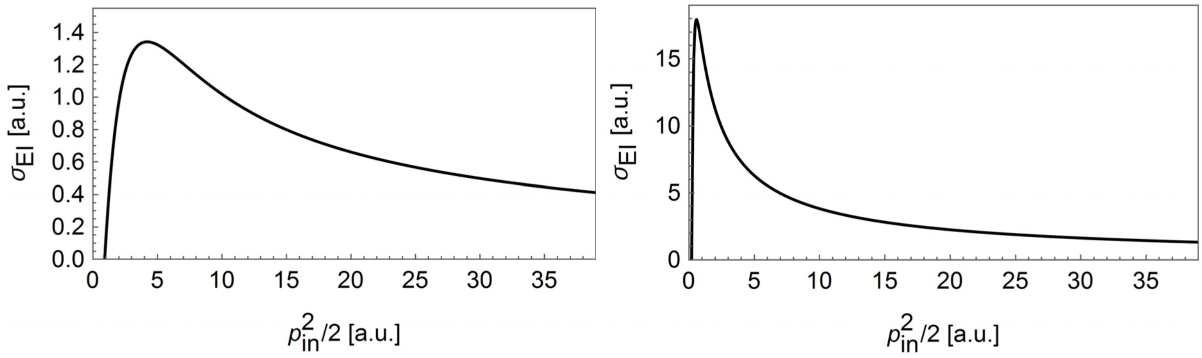

Figure 4: Plot of the electron-impact ionisation cross section calculated with the empirical Lotz formula. On the left, the ionisation from the ground state of helium is considered. Ionisation from the $2s$ orbital of lithium is depicted on the right.

The following Hamiltonian

$$\mathcal{H} = \sum_{j=1}^{n} \left(\frac{\hat{\mathbf{p}}_j^2}{2} + V_N(r_j) + \frac{1}{2} \sum_{j \neq k} \frac{1}{|\mathbf{r}_k - \mathbf{r}_j|} \right) + \frac{\hat{\mathbf{p}}_{\mathrm{in}}^2}{2} + \underbrace{V_N(\varrho) + \sum_{j=1}^{n} \frac{1}{|\boldsymbol{\varrho} - \mathbf{r}_j|}}_{H_{\mathrm{pert}}} \tag{2.9}$$

describes a system, which consists of an atom at rest with a nuclear charge number N and n bound electrons interacting with an incident electron. This expression will be used in Sec. 4.1 in order to calculate the cross sections of electron-impact ionisation applying time-dependent perturbation theory.

As mentioned above, within the process of electron-impact ionisiation, the excess energy $\frac{p_{\mathrm{in}}^2}{2} + \epsilon_g$ can in principle be shared arbitrarily between the scattered electron and the emitted one. While the residual ion can also experience a transfer of momentum, its change of energy is negligible, since its mass is large with respect to the electrons. Therefore, in the considerations in Secs. 4 and 5 the energy of the emerging ion will be assumed to remain unchanged after the ionisation process.

The observable

$$\mathbf{q} = \mathbf{p}_{\mathrm{f}} - \mathbf{p}_{\mathrm{in}} \tag{2.10}$$

characterises the momentum transfer of the incident electron and can be derived from momentum conservation. In general, the distribution of the momentum transfer, which defines a symmetry axis for the ejected electrons in the triply-differential cross sections, strongly depends on the incident electron energy. However, two lobes characterise the angular distribution. The recoil lobe and the binary lobe are directed oppositely along $\mathbf{q}$. The binary lobe is formed by the electrons emitted after the single interaction with the incident electron whereas the recoil lobe consists of ejected electrons which scatter on the potential of the remaining ion. In between these lobes, a minimum can be observed. Hence, angular distributions similar to the one in Fig. 2 can be resolved, where the two lobes are of varying size.

The extent of the incident electron energy classifies the process of electron-impact ionisation into three different regimes, classified by the energy of the incident electron, and influences the momentum transfer as well as the angular distribution, see [23].

- For high incident electron energies, which are much larger than the binding energy of the atomic center to be ionised, the interaction time is very short, restricting the intensity of the interaction. Therefore, small scattering angles of the projectile electron are dominant. This results in small values of q and, therefore, a small energy transfer to the ejected electron. In this case, the process of electron-impact ionisation resembles the process of photoionisation discussed in Sec. 2.1.1 with regard to the pattern created by the ejected electrons, see Fig. 2. In contrast, a large transfer of energy would be characterised by large scattering angles and high values of q. Since the energies of the two electrons in the continuum are greatly different, both electrons are distinguishable: The incident electron carries most of the energy, while the ejected electron is rather slow.
- When the projectile energy is lowered in a regime of about $\frac{p_{\text{in}}^2}{2} < 10|\epsilon_g|$, the scattered electron is mostly still distinguishable from the emitted one. The repulsion, which is due to the two electrons being identically charged in combination with the long-range Coulomb potential, leads to a modification of the angular distribution and is called post-collision-interaction [24]. Here, perturbative methods are not valid [25]. For the example of Ar, the complicated angular distribution is shown in [26]. Here, the two lobes are not directed along the axis defined by the momentum transfer and the symmetry is broken. Furthermore, the recoil peak is smaller the larger the absolute value of momentum transfer q is. When lowering the energy of the incident electron, more interactions and exchange effects need to be included.
- For low incident energies close to the ionisation treshold, the incident electron and the emitted one are of similar energies after the scattering process. The behaviour of the total single ionisation cross section was found to be proportional to $(\frac{p_{\text{in}}^2}{2} - \epsilon_g)^{1.127}$ [27]. The two electrons become indistinguishable due to their similar energies and the process has to be described by means of a real three-body consideration. Low energy electron-impact ionisation has been investigated for hydrogen [28, 29].

In order to allow the following investigations to be analytically feasible, the two electrons in the continuum should be distinguishable and interactions after the collision should be minimised. Therefore, all considerations in the following sections (Secs. 4, 5) are made in the regime, where the incident electron energy is high. Hence, the first Born approximation is applicable [30].

2.2 Interatomic processes

The processes described in Sec. 2.1 involve only the interaction of an external electromagnetic field or an incident electron with an electron in one atomic center. However, electron correlations, which describe the interaction between electrons within a quantum system, influence processes in atoms, small molecules as well as macromolecules in biology and also solids [16]. They create channels of deexcitation, charge and energy transfer [31, 32]. For a single atomic or molecular center, the fundamentals of an autoionising state are explained in this section, leading to the deexcitation mechanism of Auger decay. This concept is then expanded to two (or more) participating species, allowing for a multitude of processes, such as Penning ionisation and Förster resonance energy transfer, which will be briefly described. In particular, interatomic Coulombic decay is introduced and associated sub-processes are explained. A schematic overview of nonradiative decay mechanisms is given in [6].

2.2.1 Autoionisation

The content of the following sections can be found in [33], [34], and chapter 8 of [31].

A singly excited state is achieved when transferring a valence electron from the outermost occupied shell to an energetically higher state. The required energy mostly lies within the range of $1 - 10\,\mathrm{eV}$ [33]. The $1s - 2p$ transition in helium represents an exception, as it requires the transition energy of about $21\,\mathrm{eV}$. Since this excited state is unstable, the excited electron must eventually return to its ground state. An ionisation of a bound electron is only possible, when the excitation energy exceeds the first ionisation energy. However, in this case, the electron leaves the atom.

It is also possible to doubly excite an atom, meaning that two or more electrons are excited simultaneously. Doubly excited states consist of two electrons residing in energetically excited states. They can either be excited to the same orbital or to different ones and excitation of the atom is also possible via the ionisation of an electron. In principle, these two excited electrons can return to their ground state by the emission of a photon for each excitation. Another possible decay mechanism is due to radiationless energy transfer, when one of the excited electrons returns to its ground state and tranfers energy to the other excited one. When the excited electron absorbs the energy, it can be excited even further. This process, however, occurs with a low probability, since it relies on the transferred energy to match the transition energy to a higher excitation.

Most doubly excited states feature energies above the single ionisation threshold. Hence, doubly excited states can be described as 'discrete states embedded in the continuum' [35] in contrast to the 'genuinely discrete states' of single excitations. A different formulation can be found in [31], where this state is described as 'a bound state of an atom whose discrete level lies above the boundary of continuous spectrum'. Consequently, the energy transfer due to the deexcitation of one of the electrons can lead to the ionisation of the energy accepting electron. This process is named autoionisation and an electronic configuration in an atom, in which autoionisation is possible, is called autoionising state.

For autoionisation to occur after the excitation through ionisation, two criteria have to be met.

To begin with, the conservation of energy requires the energy of the final state, which is doubly ionised, to be lower than that of the singly ionised initial state. Furthermore, for the decay channel to be open the efficiency of this process in comparision with other decay mechanisms has to be ensured.

2.2.2 Auger process

The Auger process, first described by Lise Meitner in 1922 [36], but named after Pierre Auger for the discovery of this mechanism in 1925 using X-ray ionisation experiments [37], is a radiationless transition within an atom with a vacancy in an inner shell. Alongside the direct emission of an electron due to the absorption of a photon, a second electron can be emitted via the following process: Absorbing the X-ray photon, an electron from an inner shell can be pulled out, leaving a vacancy. This vacancy can then be filled by an electron from an upper energy level, whose excess energy can lead to the ionisation of an outer shell electron (see Fig. 5).

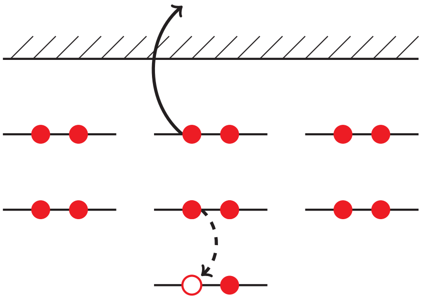

Figure 5: Scheme of the Auger process. The inner vacancy created by the ionisation of an inner electron is filled by an electron from an energetically higher lying state. The transition energy is transferred to an electron on a outer shell leading to its ionisation.

This process, where two electrons are in the continuum for the final state, also represents autoionisation. For the energy criterion to be satisfied, a high ionisation energy is required in order for the initial state energy to exceed the final state energy.

2.2.3 Resonant Auger process

An autoionising state can not only be prepared by the excitation of two valence electrons or the ionisation of an inner electron, but also by the excitation of an inner electron. Due to the instability of this doubly excited state, a channel of radiationless transition from the excited state to an ionised state is created. If the transition is allowed, the interaction between the electrons leads to the radiationless decay of an electron in order to fill the vacancy. The energy transfer then leads to the ionisation of another electron within the atomic center releasing the second electron. This process is called resonant Auger decay, and differs from the original Auger decay by the fact that, at the end of the process, only one electron is in the continuum, not two. The process of resonant Auger decay can further be classified [38]:

- **Participator resonant Auger decay**
  The process is called participator resonant Auger decay when the excited electron is the

same electron filling the vacancy its excitation caused, and transfers its energy to another electron within the atom. Therefore, the electron, whose transition created the vacancy, is directly partaking in the following ionisation process.

- **Spectator resonant Auger decay**
  The process of spectator resonant Auger decay is characterised by the fact that the excited electron is not the one to fill the vacancy created by its excitation. Instead, an energetically lower lying electron fills the vacancy, leading to the ionisation of a different electron in the atom. Since the electron excited in order to create the vacancy was not the one to fill it, the atom remains in an excited state even after the Auger decay has taken place. However, a new vacancy is created due to the ionisation, which can then be filled.

Figure 6: Scheme of the two variations of resonant Auger decay. Participator resonant Auger decay, where the electron, which was excited in the first step (dotted line), decays (dashed line) and leads to the ionisation is depicted on the left (solid line). Spectator resonant Auger decay, where a different electron than the excited one leads to the autoionisation process is depicted on the right.

The electron emitted in both Auger processes exhibits a kinetic energy which is determined by the difference in binding energies of the autoionising state and the final state of the residual ion. Consequently, autoionisation appears in the form of sharp peaks in the absorption spectrum [35] and Auger electrons are used to investigate atomic structures. The lifetime of an autoionising state is finite and its decay width, which will be calculated in Sec. 2.5, is small compared to the excitation energy of this level [31]. The radiationless decay as a result of the autoionisation process competes with radiative decay, which also allows for the stabilisation of the state, and is described in Sec. 2.5.

Autoionising states can be created via multiple mechanisms such as photoionisation, photoexcitation and electron impact, which will be further discussed in Secs. 3, 4 and Sec. 5, and lead to various resulting systems. Furthermore, the filling of an inner vacancy can be a stepwise process, in which several shells can be involved. Hence, more electrons can be emitted.

For example, the process of Dielectronic Recombination forms a multicharged ion with a charge that is lower than in the initial state [31]:

$$e + A^{+Z} \longleftrightarrow [A^{+(Z-1)}]^{**};\ [A^{+(Z-1)}]^{**} \longrightarrow A^{+(Z-1)} + \hbar\omega. \tag{2.11}$$

Here, $[A^{+(Z-1)}]^{**}$ is an autoionising state of the multicharged ion. In particular, this process is of interest in a plasma, including electrons and multicharged ions, as the resulting spectral lines provide information on plasma parameters [31].

The process of photoionisation of an atom can include the direct ionisation process as well as the decay of an autoionising state. For dipole-allowed transitions, the photoionisation exhibits a resonant structure, caused by the decay of a photoexcited state

$$\hbar\omega + A \rightarrow \left\{ \begin{array}{c} A^{+} + e \\ A^{**} \rightarrow A^{+} + e \end{array} \right. . \tag{2.12}$$

Since both the direct photoionisation and the autoionisation channel create equal final states, thw two processes can interfere with each other.

2.2.4 Autoionisation in multi-atom systems

Autoionising states can also be formed between electrons situated at two different atomic centers. This configuration, in which the available excitation energy of an electron in one atom is sufficient to ionise an electron in the neighbouring atom, can lead to more complex processes.

Penning ionisation, which was discovered in 1927, is a process which belongs to a branch called ”non-local electronic effects” [13, 39]. Here, the autoionising state is formed between an electronically excited atom or molecule and a second atom or molecule, which are not chemically bound, and therefore usually treated individually. Upon collision, the excitation energy is transferred radiationlessly, leading to the ionisation of the second atom or molecule,

$$A + B^{*} \leftrightarrows [AB]^{**} \rightarrow (AB)^{+} + e \rightarrow A^{+} + B + e. \tag{2.13}$$

Other products of this process, especially in the case of molecular constituents, are possible [40]. The excited state often involves a metastable state, when the excitation originates from a dipole-forbidden transition. This metastability results in lifetimes much larger than the collisional times [13]. Penning ionisation mostly occurs for small distances between the two constituents, leading to an overlap of the molecular wave functions. Consequently, charge transfer dominates the process. As a result, the process exhibits an exponential dependency on the internuclear distance [13]. With decreasing distance between the two constituents, the individual description breaks down and the process of Penning ionisation can be modeled as an Auger decay of an intermediate molecular state [13].

An inner vacancy, caused by the ionisation of an electron in B, can not only be filled by an electron from the same atom or molecule, as in Auger decay, but also by an electron from a neighbouring atom or molecule A. For a sufficiently large transition energy, electron-transfer mediated decay (ETMD) [41, 42] can occur, which was initially described for dimers of NeAr [43]. First, the excess energy causes the autoionisation of an electron in A

$$\left[AB^{+}\right]^{*} \rightarrow \left[A^{2+}B\right] + e. \tag{2.14}$$

The second process describes the autoionisation of an system consisting of three units [44].

$$\left[AB^{+}C\right]^{*} \rightarrow \left[A^{+}BC^{+}\right] + e. \tag{2.15}$$

The initally ionised atom is neutralised in the final state. The two neighbouring units, hwoever, are ionised. Consequently, they repell each other, causing the breakdown of the system. Due to the charge transfer, ETMD was predicted to rely on the overlap of the molecular wave functions [43]. Consequently, it is more efficient for small internuclear distances.
In biological systems, 'Förster resonance energy transfer' (FRET) can occur. Within this process, energy is transferred between systems which do not share a covalent bond [13]. The molecular wave functions do not overlap, and therefore, the individual electrons do not wander between the two molecules involved [45]. Within the process of FRET, the energy transfer of the formerly excited complex B leads to an excited state within the consitutent A, as described in

$$B^{*} + A \rightarrow B + A^{*}. \tag{2.16}$$

The radiationless energy transfer relies on the electron interaction of a dipole-dipole coupling, see Sec. 2.4. Consequently, the process heavily depends on the intermolecular distance R by R^{-6}. These characteristics are shared with the process of ICD, which will be discussed in the next section.

2.3 Interatomic Coulombic Decay (ICD)

This section is mainly based on the review paper by Jahnke [13]. For a more recent review, published in late 2020, see [6].

Interatomic (or intermolecular) Coulombic Decay (ICD) fits into the phenomena of non-local electron correlation processes previously described. The original form of this decay mechanism proceeds the following way: Upon the ionisation of an atom, an inner vacancy is created. Then, an electron of an energetically higher lying shell fills this vacancy. The resulting deexcitation energy is transferred radiationlessly to a neighbouring atom. Such radiationless energy transfers are based on the Coulomb interaction between the electrons. If the transferred energy is sufficiently large, the neighbouring atom can be ionised. Therefore, radiationless decay can occur in the system even when a single-center Auger decay is energetically forbidden. Since the autoionising state is created via the ionisation of one constituent, and the neighbouring atom is ionised within the process of ICD, the final state is comprised of two atoms which are charged positively. Therefore, the two atomic sites repell each other, leading to Coulomb explosion [46].

The mechanism was first proposed by Cederbaum, et al. in 1997 for small compounds of HF and water molecules [7]. The experimental observation of the predicted process of ICD was realised in an electron spectroscopy experiment in neon clusters [8]. A direct detection of ICD also suceeded in neon dimers [9]. Here, the ionisation of a $2s$-electron leads to an inner vacancy. The decay of a $2p$-electron in the same atom cannot lead to a double ionisation of the same atom, since the transition energy $\epsilon_{2p} - \epsilon_{2s} \approx 27\,\text{eV}$ is not large enough to remove a second $2p$ valence electron, requiring around $41\,\text{eV}$ [47] for its ionisation. Therefore, a single-center Auger decay, as described in Sec. 2.2.1 is energetically impossible. However, the transition energy resulting from the decay of the $2p$-electron to the $2s$-vacancy can be transferred to the neighbouring atom. The transition energy is sufficiently large to lead to the ionisation of a $2p$-electron of the neighbouring neutral atom [48, 49], for which $21.5\,\text{eV}$ are necessary [47]. Treating the two constituents individually, the final state consists of two electrons in the continuum, leaving both atoms in ionised states. With the help of this exemplary process, the mechanism of ICD can be visualised, as in Fig. 7.

Denoting the atom, which contains the vacancy, by B and the atom to be ionised by A, the transition matrix element of the direct contribution reads [13]

$$\left\langle \varphi_{\mathbf{k}}(\mathbf{r}_A)\chi_{2s}(\mathbf{r}_B) \left| \frac{1}{|\mathbf{r}_B - \mathbf{r}_A|} \right| \varphi_{2p}(\mathbf{r}_A)\chi_{2p}(\mathbf{r}_B) \right\rangle . \tag{2.17}$$

The transition is a result of the dipole-dipole interaction, which is described in Sec. 2.4. Consequently, the decay width scales accordingly with R^{-6} and therefore depends strongly on the internuclear distance of the two constituents A and B. In general, a matrix element for the exchange contribution has to be taken into account, see [13]. However, for ICD, the direct term dominates, which is why ICD is efficient for a large internuclear distance R, where the wave functions of the two constituents do not overlap. For small distances, however, which allow for the overlap of the wave functions, the probability for ICD shows an exponential dependency [50, 51] due to exchange terms.

Although ICD and FRET, described in the section above, seem to be of similar nature, the

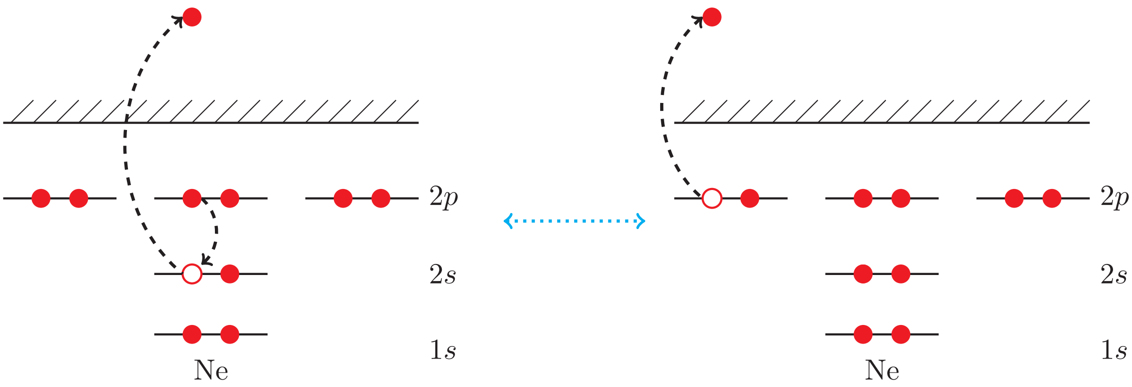

Figure 7: Scheme of the original process of ICD in Ne_2. The autoionising state is created between the two atoms by the ionisation of a $2s$-electron. The arising vacancy is filled by a $2p$-electron in the same atom. The energy that is now available is transferred to a $2p$- electron in the neighbouring electron. The transition energy is sufficiently large in order to ionise an electron. This process leaves two ions, since both atoms have lost one bound electron.

’resonance’ conditions are not always fulfilled for Förster resonance energy transfer, in contrast to ICD. Since FRET leads to an excited state, a bound state with matching energy is required. In the case of ICD, however, the final state lies in the continuum, where the ’right’ energy is always possible [13]. Note that Penning ionisation and ETMD rely on charge exchange and can therefore be well distinguished from ICD.

The original process of Interatomic Coulombic Decay consists of two subunits, A and B, where an inner valence vacancy is created in B. Here, the vacancy is formed by the ionisation of an inner valence electron in B, leading to an ionised atom in which an addtional excitation is present, B^{+^*}. This excited state does not, contrary to the state created by the ionisation of a core electron, exhibit an energy sufficient to enable double-ionisation of B via an Auger decay [52]. However, as mentioned before, the vacancy in an inner-valence orbital allows the double ionisation of the system consisting of both A and B. Radiationless energy transfer then leads to the doubly ionised system A^+B^+ [7], which is predominantly unstable. Therefore, the process of ICD is of the form

$$AB^{+^*} \to A^+B^+ + e. \tag{2.18}$$

The mechanism of ICD is characterised by consisting of a ’non-local electron effect’ [13] and was first observed experimentally in the neon dimer Ne_2. ICD has been studied theoretically in this van der Waals dimer [48], where the time evolution as well as the dependence on the internuclear distance R, including the nuclear motion, was investigated. The nodal structure of the vibrational levels is reflected in the energy of the ejected electron as well as the remaining fragments [54]. ICD has also been studied in the homonuclear dimer He^+He, showing that this indirect process can dominate over the radiative decay mechanism [55] for large range of interatomic distances. For this system, experiments provided a direct measurement of the time evolution concerning the vibrational wave packet of the dimer [56]. Experiments on argon dimers have been performed examining the effects of the nuclear dynamics and the strong dependence on R [57]. Furthermore, associated experiments have been carried out comprising noble gas dimers [9, 10, 11], clusters [8] and water molecules [12].

Core-level ICD, where the vacancy is created by the ionisation of a core electron, has been recently observed in argon clusters [58] and its efficiency with regard to local Auger decay has been studied theoretically [59]. For calcium, the ratio between Core-level ICD and Auger decay has been shown to be up to 10, illustrating the relevance of this process [60].

2.3.1 Resonant ICD

Interatomic Coulombic decay can not only occur from an autoionising state created by the ionisation of an atom from an inner-valence orbital but also from an autoionising state, where an inner-valence electron is excited but still bound [61]. Resonant ICD (RICD), where the autoionising state is not created by ionisation, but excitation of an inner valence, has also been studied in clusters of MgNe [52] as well as in HeNe [62].

The relation between ICD and resonant ICD equals the relation between the process of Auger decay and resonant Auger decay, described in Sec. 2.2.1. The excitation, instead of ionisation, leads to more possible decay mechanisms, where, for example, the electron whose excitation created the vacancy, can participate in. This results in the resonant ICD process and the intra-atomic autoionisation competing with each other.

In the following, the different decay processes of an inner-valence excitation are described and schematically visualised in Fig. 8, as done in [52].

- **Spectator resonant interatomic Coulombic decay (sRICD)**
  When the vacancy in the inner valance shell is not filled by the excited electron, but by a different electron with a lower energy than the excited one, the excited electron does not partake in the process. Consequently, the process is called spectator resonant ICD. The process leads to a system where the atomic center B is excited after the interatomic decay.

$$AB^* \to A^+B^* + e. \tag{2.19}$$

- **Participator resonant interatomic Coulombic decay (pRICD)**
  Here, the excited electron is the one filling the vacancy in the inner valance. Therefore, the atomic center B is in its electronic ground state after the energy transfer.

$$AB^* \to A^+B + e. \tag{2.20}$$

When the excitation affects an outer valence electron, spectator ICD is not possible. Hence, only pRICD is possible. In this case, the process is also called excitation transfer ionisation [63].

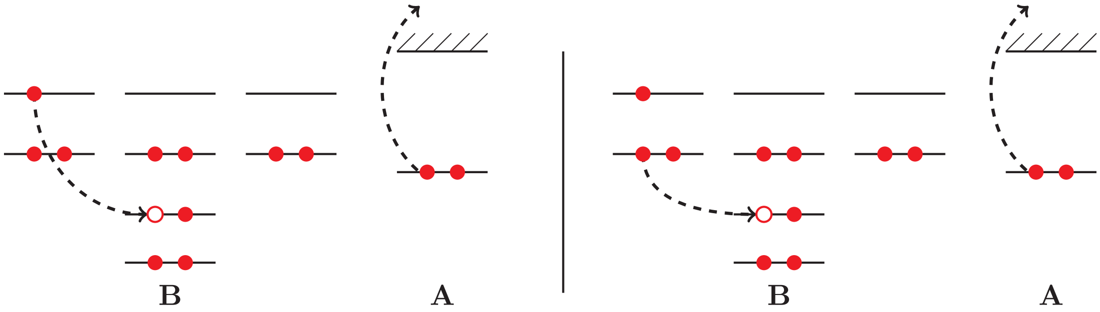

Figure 8: Scheme of the two channels of RICD. Participator resonant Interatomic Coulombic decay (pRICD) is depicted on the left side, whereas the spectator resonant Interatomic Coulombic decay (sRICD) is visualised on the right.

Furthermore, double ionisation as a consequence of interatomic Coulombic decay is possible, see [52, 53]. However, it will not be considered in the following sections.

2.3.2 Characteristics of ICD processes

Recent experiments on helium nanodroplets found that the emitted electrons are merely perturbed by the droplet and therefore, the ICD process strongly resembles ICD in a dimer of the same species [64]. Vibrationally resolved widths of ICD in the photoexcited heteroatomic dimer of HeNe have been studied in [18] and [62], where the results were directly compared to experimental data. In the same system, the angular spectrum of the electrons emitted via RICD have been investigated experimentally and theoretically [19], including the underlying vibrational structure.

The process of ICD depends, as already mentioned, heavily on the internuclear distance. The characteristic proportionality R^{-6} leads to a distinction from other processes, such as the charge exchange contribution to the process, which leads to the same electronic configuration but scales exponentially with R [65]. Furthermore, the decay width is also associated with the characteristics of the system in which the transition occurs. The interaction potential curve of a particular system, which will be discussed in Sec. 3.2.1, influences the magnitude of the decay width, since it determines the internuclear distances over which bound states exist. Furthermore, the nuclear motion, described in Sec. 2.8, of a dimer controls the time-resolved behaviour of ICD [66]. For dimers including rare gases, theoretical and experimental investigations have been performed, see [62, 65, 66].

Corresponding calculations require an elaborate mathematical description. Hence, numerical ab initio methods are frequently employed. While this technique can yield precise results, the development of a qualitative physical understanding is hindered.

The process of ICD occurs not only in rare gas dimers, which will be studied further in the next sections, but also in other systems such as large biological molecules to name an example. Here, the process of ICD has to be considered with regard to a large amount of competing processes as well as to various partaking particles. For a review on the range of systems, in which ICD has been studied, see [6].

2.4 Dipole-dipole interaction

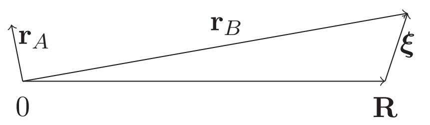

Figure 9: Scheme of the spatial dependencies considered in the calculation of the Coulomb interaction.

During the radiationless energy transfer, which was described in Sec. 2.3, the two participating atoms A and B can be treated as two quantum mechanical dipoles. The perturbation operator, describing the Coulomb interaction, is of the form

$$V_{AB} = \frac{1}{|\mathbf{r}_B - \mathbf{r}_A|} = \frac{1}{|\mathbf{R} + (\boldsymbol{\xi} - \mathbf{r})|}, \tag{2.21}$$

where $\mathbf{r}_B = \mathbf{R} + \boldsymbol{\xi}$, as illustrated in Fig. 9.
Expanding the expression in Eq. (2.21) for $R \gg r\,, \xi$, the interaction reads

$$\begin{aligned} V_{AB} = \frac{1}{R} - \frac{\boldsymbol{\xi}\mathbf{R} - \mathbf{r}\mathbf{R}}{R^3} + \left(\frac{3\left((\boldsymbol{\xi}\mathbf{R})^2 + (\mathbf{r}\mathbf{R})^2 - 2(\boldsymbol{\xi}\mathbf{R})(\mathbf{r}\mathbf{R})\right)}{2R^5} - \frac{r^2 + \xi^2 - 2\boldsymbol{\xi}\mathbf{r}}{2R^3} \right) \\ - \left(\frac{3(\boldsymbol{\xi} - \mathbf{r})^2(\boldsymbol{\xi}\mathbf{R} - \mathbf{r}\mathbf{R})}{2R^5} - \frac{15(\boldsymbol{\xi}\mathbf{R} - \mathbf{r}\mathbf{R})^3}{R^7} \right) \end{aligned} \tag{2.22}$$

Only terms including both $\boldsymbol{\xi}$ and $\mathbf{r}$ contribute to the matrix elements which involve dipole transitions on both centers A and B. Such transitions are considered in Secs. 3, 4 and 5 and calculated in the Appendices, see Sec. 7. Therefore, the expression can be simplified, yielding

$$\begin{aligned} V_{AB} = \left(\frac{-3\left((\boldsymbol{\xi}\mathbf{R})(\mathbf{r}\mathbf{R})\right)}{R^5} + \frac{\boldsymbol{\xi}\mathbf{r}}{R^3} \right) \\ - \left(\frac{3(r^2(\boldsymbol{\xi}\mathbf{R}) - \xi^2(\mathbf{r}\mathbf{R}) - 2(\boldsymbol{\xi}\mathbf{r})(\boldsymbol{\xi}\mathbf{R} - \mathbf{r}\mathbf{R}))}{2R^5} - \frac{15((\boldsymbol{\xi}\mathbf{R})^2(\mathbf{r}\mathbf{R}) + (\mathbf{r}\mathbf{R})^2(\boldsymbol{\xi}\mathbf{R}))}{2R^7} \right) \end{aligned} \tag{2.23}$$

Here, all terms within the second parantheses vanish in the matrix elements. Therefore, only the second order term is included in the calculations here and the interaction reads

$$V_{AB} = \frac{\boldsymbol{\xi}\mathbf{r}}{R^3} - \frac{3(\boldsymbol{\xi}\mathbf{R})(\mathbf{r}\mathbf{R})}{R^5}. \tag{2.24}$$

Note, that the expression above is symmetric in $\mathbf{r}$ and $\boldsymbol{\xi}$. Since the dipole-dipole interaction is proportional to R^{-3}, it is relevant for long distances. Furthermore, the interaction described by V_{AB} is anisotropic as it depends on the two orientations of the involved dipoles.

2.5 Decay of unstable excited states

The lifetime of an excited state of a system is finite, when a transition to an energetically lower lying state is possible. The deexcitation of this state can occur via multiple processes, as described above. The width Γ is linked to the lifetime of the unstable state in an atom B. In the following sections, it includes the radiative width Γ_{rad} and the two-center Auger width Γ_{aug}, yielding

$$\Gamma = \Gamma_{\text{rad}} + \Gamma_{\text{aug}}. \tag{2.25}$$

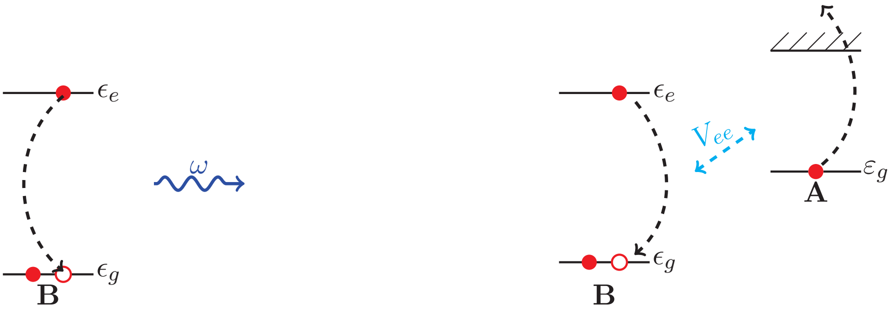

Figure 10: Left: Scheme of the spontaneous emission of a photon due to the deexcitation of an excited state in atom B. Right: Scheme of the two-center Auger decay of atom B: The excitation energy of atom B is transferred radiationlessly to atom A, leading to its ionisation.

2.5.1 Radiative decay

An excited state can transition to an energetically lower state via emission of a photon

$$B^* \to B + \gamma. \tag{2.26}$$

Due to the conservation of energy, the photon energy is defined by the excitation energy $\omega_e = |\epsilon_e - \epsilon_g|$.

Spontaneous emission, whose process is depicted in Fig. 10, was first accurately described by Dirac in 1929 [67]. As the interaction (see Eq. (2.39)) represents a weak perturbation, its rate can therefore be derived by Fermi's golden rule [21, 68]:

$$\Gamma_{m,n} = 2\pi \left[\delta(\epsilon_m - \epsilon_n - \omega) \left|\langle n \left| O_{\text{pert}} \right| m \rangle\right|^2 + \delta(\epsilon_m - \epsilon_n + \omega) \left| \left\langle n \left| O^{\dagger}_{\text{pert}} \right| m \right\rangle \right|^2 \right]. \tag{2.27}$$

Initially, the radiation field is in its ground state and the electron is in an excited state m. Whereas the initial state is described by $|0\rangle|m\rangle$, spontaneous decay results in the final state to read $a^{\dagger}_{\mathbf{k},\lambda}|0\rangle|n\rangle$. The contributing perturbation is given by

$$O_{\text{pert}} = \int d^3x \left[-\frac{1}{c} \mathbf{j}(\mathbf{x}) \cdot \mathbf{A}(\mathbf{x}) \right] \tag{2.28}$$

with

$$\mathbf{j}(\mathbf{x}) = \frac{1}{2} \sum_i \left(\hat{\mathbf{p}}_i \delta(\mathbf{x} - \mathbf{x}_i) + \delta(\mathbf{x} - \mathbf{x}_i) \hat{\mathbf{p}}_i \right) \tag{2.29}$$

$$\mathbf{A}(\mathbf{x}) = \sum_{\mathbf{k},\lambda} \sqrt{\frac{2\pi c}{kV}} \left(a_{\mathbf{k},\lambda} \boldsymbol{\varepsilon}_{\mathbf{k},\lambda} e^{i\mathbf{kx}} + a^{\dagger}_{\mathbf{k},\lambda} \boldsymbol{\varepsilon}^{*}_{\mathbf{k},\lambda} e^{-i\mathbf{kx}} \right) \tag{2.30}$$

Consequently, only the second term in Eq. (2.27) contributes. The decay width then reads

$$\Gamma_{m\to n,\mathbf{k},\lambda} = \frac{(2\pi)^2}{kc} \delta(\varepsilon_m - \varepsilon_n - ck) \left| \left\langle n \left| \int d^3x \mathbf{j}(\mathbf{x}) \cdot \boldsymbol{\varepsilon}^{*}_{\mathbf{k},\lambda} \frac{e^{-\mathbf{kx}}}{\sqrt{V}} \right| m \right\rangle \right|^2 . \tag{2.31}$$

Inserting the Fourier transformation of the current density

$$\mathbf{j}(\mathbf{k}) = \int d^3x \, \mathbf{j}(\mathbf{x}) e^{-i\mathbf{k}(\mathbf{x})} \tag{2.32}$$

yields

$$\Gamma_{m\to n,\mathbf{k},\lambda} = \frac{(2\pi)^2}{kc} \delta(\epsilon_m - \epsilon_n - ck) \left| \left\langle n \left| \mathbf{j}(\mathbf{k}) \cdot \boldsymbol{\varepsilon}^{*}_{\mathbf{k},\lambda} \frac{1}{\sqrt{V}} \right| m \right\rangle \right|^2 . \tag{2.33}$$

Integration over all states in the k-space leads to

$$\Gamma_{m\to n} = \int \frac{d^3k}{(2\pi)^3} \frac{(2\pi)^2}{kc} V \delta(\epsilon_m - \epsilon_n - ck) \left| \left\langle n \left| \mathbf{j}(\mathbf{k}) \cdot \boldsymbol{\varepsilon}^{*}_{\mathbf{k},\lambda} \frac{1}{\sqrt{V}} \right| m \right\rangle \right|^2 \tag{2.34}$$

For atoms, $\mathbf{k} \cdot \mathbf{x} \ll 1$ and therefore $\mathbf{j}(\mathbf{k}) = \int d^3x (1 - i\mathbf{k} \cdot \mathbf{x} + \frac{1}{2}(i\mathbf{k} \cdot \mathbf{x})^2 + ...)\mathbf{j}(\mathbf{x})$. Due to selection rules, only dipole transitions contribute with

$$\mathbf{j}_0 = \mathbf{j}(\mathbf{x}). \tag{2.35}$$

Applying

$$\mathbf{j}_0 = \mathbf{P} = i[H_0, \mathbf{X}], \tag{2.36}$$

where H_0 defines the unperturbed Hamiltonian, results in

$$\langle n|\mathbf{P}|m\rangle = i\langle n|[H_0, \mathbf{X}]|m\rangle = i(\epsilon_n - \epsilon_m)\langle n|\mathbf{X}|m\rangle. \tag{2.37}$$

This leads to

$$\Gamma_{m\to n} = \frac{4\pi}{3} \frac{1}{2\pi} \frac{\omega^3}{c^3} \left| \langle n \left| \mathbf{X} \right| m\rangle \right|^2 . \tag{2.38}$$

The radiative width, characterising the transition of one electron from an excited state e in an atom to its ground state g reads

$$\Gamma_{\mathrm{rad},g,e} = \frac{4\omega_B^3}{3c^3} \left| \langle \chi_g \left| \boldsymbol{\xi} \right| \chi_e\rangle \right|^2 . \tag{2.39}$$

Note that in general, the radiative width Γ_{rad}, which is incorporated in the total decay width Γ, includes the sum over transitions from an excited state e to various lower lying states. Within the following sections, and in particular for the systems considered therein, $\Gamma_{\mathrm{rad}} = \Gamma_{\mathrm{rad},g,e}$ holds, where $\Gamma_{\mathrm{rad},g,e}$ denotes the decay width of a particular transition from a selected electronically excited state to its ground state. Therefore, no distinction is made in the following.

2.5.2 Two-center Auger decay

The two-center Auger decay (which is synonymous with the process of RICD) width describes the radiationless energy transfer from atom B to atom A. Therefore, the electron in atom B transitions from an excited state e to its ground states g, while the electron positioned in atom A is ionised to the continuum with momentum k from its respective ground state g

$$B^* + A \to (BA)^{**} \to B + A^+ + e. \tag{2.40}$$

The transition is induced by V_{AB} as described in Sec. 2.4, Eq. (2.24), where $\mathbf{R}$ denotes the internuclear distance between the two atomic centers. Since this decay mechanism includes processes in two atomic centers, the interaction involves a two-center matrix element

$$\mathcal{V}^{AB}(\mathbf{k}', \mathbf{R}) = \langle \varphi_{\mathbf{k}'}(\mathbf{r})\chi_g(\boldsymbol{\xi}) \left| V_{AB} \right| \varphi_g(\mathbf{r})\chi_e(\boldsymbol{\xi}) \rangle \,, \tag{2.41}$$

where V_{AB} is defined in Eq. (2.24). Via Fermi's golden rule [68] the width of the two-center decay, assuming two individual atoms, reads

$$\Gamma_{\text{aug}}(\mathbf{R}) = \int \frac{d^3k'}{(2\pi)^2} |\mathcal{V}^{AB}(\mathbf{k}', \mathbf{R})|^2 \delta(\varepsilon'_k + \epsilon_g - \varepsilon_g - \epsilon_e). \tag{2.42}$$

The δ-distribution incorporates the energy conservation. The energy of the emitted electron is determined by the difference between the transition energy $\omega_B = \epsilon_e - \epsilon_g$ in atom B and the binding energy of the electron in atom A. Consequently, the integration over $k^{'}$ is performed by fixing the momentum of the ejected electron. In contrast to the radiative width, which is a constant for a particular transition, the two-center Auger decay strongly depends on the internuclear distance, since the dipole-dipole interaction is proportional to R^{-3}.

Note, that the expression derived here does not include any other interaction between the two constituents. As mentioned above, the ICD width depends on the characteristics of the molecule. Numerical calculations show, that it can feature a behaviour which does not only include the characterstic proportionality R^{-6}, especially for small internuclear distances, see [117]. As explained in Sec. 2.3, exchange effects are relevant for internuclear distances, where the wave functions of the partaking atoms overlap, leading to the contribution of an exponential dependency. Furthermore, the decay width can feature a plateau, as can be seen in [50, 51]. This plateau is located at internuclear distances around the minimum of the potential energy curve of the dimer, explained in Sec. 2.7. Hence, the contribution of this behaviour is negligible with regard to the widespread states of the model system used in the following.

2.6 Wave functions

In this work hydrogen like wave functions are often employed for the description of the active electrons in order for the analytical approach to be feasible. Aside from the mathematical description of the bound electrons, there is the need to describe electrons in the continuum. Within the process of electron-impact ionisation, the incident, and eventually scattered electron is assumed to be undisturbed and is therefore described by the Hamiltonian

$$H_0 = -\frac{1}{2}\Delta_r^2. \tag{2.43}$$

The incident electron strikes a neutral atom. After the electron impact, the fast, scattered electron experiences a virtually neutral system since the residual ion is shielded by the slow emitted electron. Consequently, they can be described using a plane wave [69]

$$\varphi_{\mathbf{k}}(\mathbf{r}) = \frac{1}{\sqrt{V}} e^{i(\mathbf{kr})}. \tag{2.44}$$

In the following sections, however, the calculations require the use of more complex, but still analytically manageable wave functions, which will be explained in the following sections.

2.6.1 Motion in a Coulomb field

This section is based on [70], [71] and [72]. When neglecting any interaction with the remaining core or an external field, an ejected electron can be assumed to be undisturbed. Such an undisturbed electron can be easily described by a plane wave, see Eq. (2.44). After the ionisation of a former neutral atomic center, however, the residual ion is positively charged and creates a long-ranging Coulombic potential. This can lead to a perturbation of the electron's motion. Taking the influence of a centrally symmetric field like the Coulomb field, where a potential of the form $U = \pm\frac{\alpha}{r}$ is included, the Schrödinger equation, reads

$$\left(-\frac{\nabla^2}{2} \pm \frac{\alpha}{r}\right)\Psi_{\mathbf{k}}(\mathbf{r}) = \frac{k^2}{2}\Psi_{\mathbf{k}}(\mathbf{r}). \tag{2.45}$$

The positive charge of the residual ion is described as a point-like charge, generating a spherically symmetric potential. Due to the symmetry, only the radial part of the wave functions describing the emitted electron is modified, leaving the angular part unaffected [69]. Here, only attractive Coulomb fields are considered, leading to the radial functions to be of the form

$$\frac{d^2R}{dr^2} + \frac{2}{r}\frac{dR}{dr} - \frac{l(l+1)}{r^2}R + 2\mu\left(E + \frac{\alpha}{r}\right)R = 0, \tag{2.46}$$

where, in this case, the reduced mass μ can be assumed to be the mass of the electron.
In general, the system requires a summation over all angular quantum numbers l

$$\varphi_{\mathbf{k}}(\mathbf{r}) = \frac{1}{k}\sqrt{\frac{\pi}{2}}\sum_{l=0} i^l(2l+1)R_{pl}(r)P_l(\mathbf{e}_k\mathbf{e}_r). \tag{2.47}$$

The P_l denote the Legendre polynomials. Here, phase factors are omitted since they are unimportant for all following calculations. Considering a residual ion with effective an charge Z, the radial wave function reads

$$R_{pl} = \frac{2ke^{\frac{Z\pi}{2k}}\left|\Gamma\left(l+1-\frac{Zi}{k}\right)\right|}{(2l+1)!}(2kr)^l e^{-ikr}F(l+1+i\left(\frac{Z}{k}\right), 2l+2, 2ikr). \tag{2.48}$$

Here, F is the hypergeometric function, and $\mathbf{k}$ is the wave vector of the particle at infinity. In the limiting case of a vanishing nuclear charge $Z=0$, the Coulomb wave becomes a plane wave [69]. When comparing the plane wave to the Coulomb wave, the radial part of the Coulomb wave exhibits more oscillations of the same kinetic energy $k^2/2$.

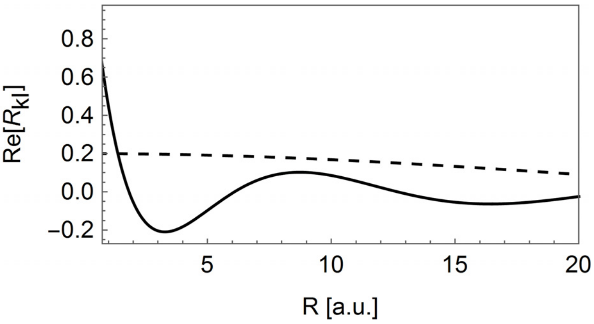

Figure 11: Comparison of the real part of the radial function $Re[R_{kl}(r)]$ for $k=0.1$ and $l=0$. $Z=1$ is depicted by the solid curve while $Z=0$ is denoted by the dashed line.

As can be seen in Fig. 11, the Coulomb wave exhibits a larger value than the plane wave at the origin. However, for an increasing distance R, this value becomes smaller, showing an oscillating behaviour. This reflects the fact that the low energy electrons are more probable to be near the positive charge [69].

When inserted in a matrix element describing a dipole transition, the selection rule for l can simplify the expression in Eq. (2.47). Consequently, ionisation from an s-state only allows p-states, which is why $l=1$ is the only contributing term. Therefore, the simplified expression

$$\varphi_{\mathbf{k}}(r) = \frac{3}{k}\sqrt{\frac{\pi}{2}}e^{-i\delta_1}R_{p1}(r)P_1(\mathbf{e}_k\mathbf{e}_r) \tag{2.49}$$

can be used in the calculation of the transition matrix elements, which is done in the Appendix, see Sec. 7.1.1.

In the case of scattering, the emitted particle does not have a definitive value of orbital angular momentum l and m. Here, another representation of the Coulomb wave functions is suitable, where the particular asymptotic behaviour of the continuous spectrum is implemented in the wave functions. An emitted electron under the influence of an attracting Coulomb potential is then described via a wave function consisting of a plane wave as well as an ingoing spherical wave (denoted by $\varphi_{\mathbf{k}}^-$). In the special case of a Coulomb field a closed form can be found

$$\varphi_{\mathbf{k}}(r) = \frac{1}{(2\pi)^{3/2}}e^{\frac{Z\pi}{2k}}\Gamma(1-\frac{Zi}{k})e^{i\mathbf{kr}}F(\frac{Zi}{k}, 1, -ikr-i\mathbf{kr}). \tag{2.50}$$

It has been shown that the mathematical description of photoionisation of formerly neutral atoms requires the use of the Coulomb wave to take the interaction of the emitted electron with the residual ion into account. Note, however, that more complex wave functions, taylored to the process studied, can account for more effects and interactions, see [69] for a short summary.

2.6.2 Bates-Damgaard function

The content presented in this section can be found in [73], [74] and [75].

Considering an alkali metal rare gas van der Waals dimer, the mathematical description of the alkali metal can be improved when comparing to the description by using hydrogen-like wave functions. However, the form has to be sufficiently simple in order to allow for an analytical calculation of transition matrix elements, as done in Secs. 3, 4 and 5. Alkali atoms are of intermediate complexity with regard to other many-electron atoms since they contain only one electron in an open shell. Regarding the binding energies, the energy of the external electron is about one order of magnitude smaller than the electrons on the closed shells [75]. As a consequence, it is reasonable to describe alkali atoms within a one-electron approximation. Due to the electrons on the closed shells, however, the electron on the outer shells is under the influence of a potential which differs from a Coulomb potential at small distances. In order to account for these characteristics, approximative wave functions have been developed for decades.

In 1949 [73], Bates and Damgaard developed an asymptotic series using Coulomb wave functions. The method used for this simplification is called quantum defect method (QDM) [75]. Here, a central atomic potential is assumed, as well as a single-particle approximation. For the Coulomb interaction between the valence electron and the atomic core, an approximation is developed, using a hydrogen-like wave function with an effective principal quantum number

$$n^* = n - \delta_l, \tag{2.51}$$

where δ_l denotes the quantum defect of the state defined by l, and n^* is linked to the experimental values for binding energies with the formula $E_n = \frac{-Z^2}{2n^{*2}}$. Due to the approximative interaction, the resulting wave functions do not properly describe the close-up range around the core. Since the contribution from these small distances is, in general, negligible, the method leads to improved results for atoms with only one electron on a closed shell [73].

The radial solutions for a central field model have to satisfy

$$\frac{d^2R}{dr^2} + (2V(r) - \frac{l(l+1)}{r^2} - E)R = 0, \tag{2.52}$$

where $V(r)$ is the potential. When allowing the wave functions to be accurate only for moderate and large distances, the potential $V(r)$ is replaced by the asymptotic value $\frac{C}{r}$, where C depicts the excess charge of the nucleus when removing the active electron [73]. Therefore, Eq. (2.52) becomes

$$\frac{d^2R}{dr^2} + \left(2\frac{C}{r} - \frac{l(l+1)}{r^2} - E\right) R = 0. \tag{2.53}$$

An appropriate solution was given by Eddington [76] and Sugiura [77]

$$R = W_{n^*,l+\frac{1}{2}}\left(2\frac{Cr}{n^*}\right), \tag{2.54}$$

where W is the confluent hypergeometric function, which can be expanded as

$$W_{n^*,l+\frac{1}{2}}\left(2\frac{Cr}{n^*}\right) = e^{-\frac{rC}{n^*}}\left(\frac{2rC}{n^*}\right)^{n^*}\left(1+\sum_{t=1}^{\infty}\frac{a_t}{r^t}\right) \tag{2.55}$$

with

$$a_1 = \frac{n^*}{2C}\left[l(l+1) - n^*(n^*-1)\right] \tag{2.56}$$

$$a_t = a_{t-1}\frac{n^*}{2tC}\left[l(l+1) - (n^*-t)(n^*-t+1)\right]. \tag{2.57}$$

With respect to normalisation, the proposal by Hartree [78] was adapted in the original version of the method [73] by multiplying confluent hypergeometric function by

$$\frac{1}{\sqrt{(n^*)^2\Gamma(n^*+l-1)\Gamma(n^*-l)/C}}. \tag{2.58}$$

Note, that the method by Bates and Damgaard leads to an issue regarding the normalisation of the wave function for small n^*. In 1968, a new normalisation factor was suggested for $n^* < l+1$. More detailed information on this problem and references to further studies can be found in [74]. The asymptotic behaviour of the wave function for the valence electron of an alkali atom as $r \to \infty$ reads

$$\Phi_{\text{Bates-Damgaard}}(r) = \frac{1}{\sqrt{8\pi}}\frac{1}{\Gamma(a+1)}\left(\frac{2}{a}\right)^{a+1/2} r^u \left(1+\frac{v}{r}+\mathcal{O}(\frac{1}{r^2})\right) e^{-r/a}. \tag{2.59}$$

Here, all parameters $a = \frac{1}{\sqrt{2|E|}}$, $u = a-1$ and $v = -\frac{a^2}{2}(a-1)$ depend on the first ionisation energy E [79].

In order to visualise the differences between the hydrogen-like function and the function calculated with the method by Bates and Damgaard, the wave functions are plotted for lithium, which will be of interest in the later sections. Note that the Bates Damgaard wave function is not normalised to 1.

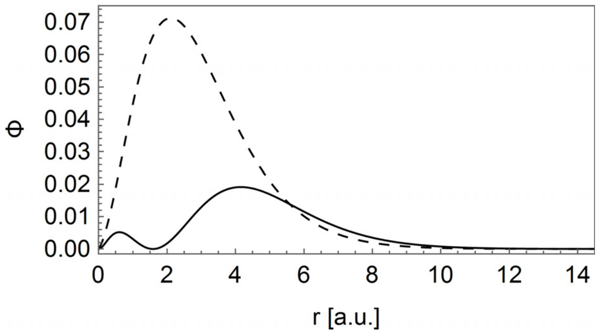

Figure 12: Comparison between the wave functions for the ground state of lithium. Solid: Hydrogen-like wave functions with effective charge $Z = 1.259$. Dashed: Bates-Damgaard function with parameters from [79]. Note, that the Bates-Damgaard function is not normalised to 1.

Whereas the hydrogen-like wave functions features two maxima, the Bates-Damgaard function is characterised by only one maximum which is positioned between the two maxima of the hydrogen-like wave function. This represents the fact, that while the hydrogen-like wave function only describes the electron in the $2s$ state, the Bates-Damgaard wave function also includes effect of the two electrons in the shell below. Therefore, the Bates-Damgaard wave functions describes the total ground state of the lithium atom.

2.7 Interaction in two-atomic molecules

The better part of this section can be looked up in [21], [35] and [80].

A dimer is a molecule or a molecular compound consisting of two monomers. Consequently, it represents the simplest form of a polymer. In contrast to an isolated atom, the electrons and nuclei can interact with each other across the two atoms, leading to a complicated description of the system. Ignoring the translative motion of the two-atomic molecule, the Hamiltonian of the system reads [80]

$$\mathcal{H} = -\frac{1}{2\mu}\nabla_R^2 + \sum_{i=1}^{\mathcal{N}} \left(-\frac{1}{2}\nabla_{r_i}^2\right) + V(\mathbf{r}, \mathbf{R}), \tag{2.60}$$

where $V(\mathbf{r}, \mathbf{R})$ includes all interactions between electrons and nuclei. Considering a dimer consisting of two atoms, A and B, the complicated mathematical description of a many-body system can be simplified, since the mass of the electrons is negligible with respect to the mass of the nuclei. Applying the Born-Oppenheimer approximation, the fast movement of the light electrons is separated from the motion of the heavy nuclei. On the short time scale of the fast electronic motion, the nuclei can be considered to be 'at rest'.

2.7.1 Potential curves

For a fixed internuclear distance R, the interaction of the involved particles leads to a shift compared to the sum of energies corresponding to the two individual atoms. The adiabatic potential curve of a distinct electronic state of the system depicts the energy of the system when varying the internuclear distance R infinitely slowly. Here, the potential energy denotes the energy relative to the sum of energies of the individual constituents. In general, those potential curves are comprised of two parts: One part accounts for the repulsion of the two atoms, whereas the second one is responsible for the potential molecular binding [80]. The form of a typical potential curve is depicted in Fig. 13.

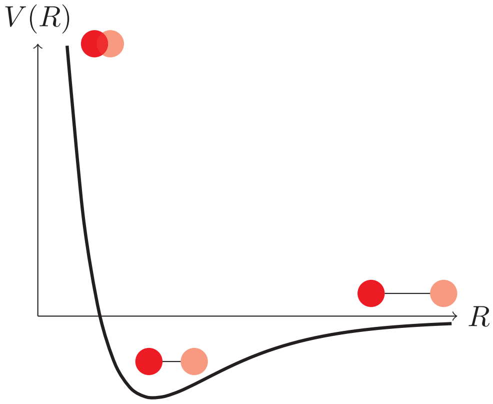

Figure 13: Scheme of an interaction potential curve. Furthermore, the internuclear distance between the two constituent atoms is visualised.

Some general characteristics can be given for the behaviour of such a potential curve:

- For small internuclear distances R, the Coulomb interaction of the two nuclei results in a strongly repulsive potential.
- For a lot of molecules, one of the following three types of chemical bonds results in the forming of a molecular complex [81] for intermediate internuclear distances.
  - **Ionic bond**
    The ionic bond stems from the transfer of electrons from one atomic species to another one. This results in positively charged ions for the electron donors and in negatively charged ions for the electron acceptors. Consequently, the attraction of the opposite charges creates the binding.
  - **Covalent bond**
    In a covalent bond, atoms are tied together by sharing their electrons. In a simple covalent bond, two atoms share a pair of electrons. The formation of covalent bonds leads to a lowering of the energy of the system, since the many no-metal atoms can hereby attain the equivalent of the configuration of a noble gas, which is a fully occupied valence shell.
  - **Metallic bond**
    Electrons can also be shared by more than two atoms. If the number of involved atoms is sufficiently high, every atom contributes with one or more valence electrons to an electron gas, in which a large amount of electrons are delocalised and belong to all atoms at the same time. These electrons can move freely and create the binding.

  Note, that in most bonds, the type of binding is not pure [81], but rather comprised of a combination of contributions.
- For large internuclear distances R, the form of the potential curve depends on the atoms involved. Coulombic interaction can dominate for systems involving ions, whereas dipole interactions, see Sec. 2.9.1, dominate for neutral atoms. However, all potential curves converge to the energy comprised of the energies of the individual constituents as R increases.

A universal approach to mathematically describe an interaction potential was proposed in 1903 by Gustav Mie [82] and is of the form

$$V(R) = -\frac{C}{R^n} + \frac{D}{R^m}, \tag{2.61}$$

where C and D are positive coefficients. A special case of this formula is the Lennard-Jones potential in Sec. 2.9.1. The calculation of potential curves for van der Waals dimers will be studied in more detail in Sec. 3.2.

2.8 Vibrational and rotational motion in a dimer

The simple setup of a dimer requires not only the consideration of the electronic motion around the nuclei at rest, but also the inclusion of the nuclear motion with regard to vibration and rotation.

Consequently, molecules show a spectrum that is more complex than that of atoms. Since rovibrational transitions require a lower energy than electronic transitions, the possibility to excite a molecule on an energy scale that is much smaller compared to electronic transitions gives rise to a multitude of phenomena. Although abundant homonuclear dimers, such as N_2 or O_2, are not able to absorb infrared radiation emitted from their environment, other molecules can. CO_2 [83] or H_2O feature a dipole moment, which allows for rovibrational transitions and therefore, the absorption of heat radiation, influencing the temperature on earth's surface [33].

As a consequence of the Born-Oppenheimer approximation, an effective Schrödinger equation is obtained for electrons and nuclei, respectively. When using relative coordinates as well as coordinates of the center of mass, the Schrödinger equation for the nuclei reads [21]

$$\left(-\frac{1}{2\mu}\nabla^2 + V(R)\right)\Psi(\mathbf{R}) = E\Psi(\mathbf{R}), \tag{2.62}$$

where μ depicts the reduced mass of the system and $V(R)$ is the potential curve. Note, that the potential curve for the nuclear motion solely depends on the value of the interatomic distance R and is, therefore, spherically symmetric. A discrete spectrum exists for a binding potential, in which the nuclei move. For a distinguishable potential curve, that is for energetically separated potential curves for different states n, the system can be described by a Schrödinger equation including the potential $V(R)$.

In the following, the excitations of the nuclear motion are explained in more detail. Here, rotation and vibration of the dimer are treated individually. Note that a more accurate description calls for consideration of the complete rovibrational motion.

2.8.1 Vibrational motion

Figure 14: Schematic visualisation of the vibrational motion of a dimer, which is characterised by a periodic change of the internuclear distance R along a fixed axis.

A dimer, consisting of two atoms, A and B, can perform a vibrational motion, meaning a periodic variation of the internuclear distance R, where the center of mass of the molecule as well as the orientation of $\mathbf{R}$ remain unaltered. For a diatomic molecule, the vibrational motion is limited to the one depicted in Fig. 14. For a molecule consisting of more atoms, the arising degrees of freedom lead to more complex vibrational motion [33]. Since this problem features a rotational symmetry, the ansatz $\Psi(\mathbf{R}) = \psi_{\text{vib}}(R)Y_{lm}(\vartheta, \varphi)$ leads to the radial equation

$$\left[-\frac{1}{2\mu}\left(\frac{d^2}{dR^2} + \frac{2}{R}\frac{d}{dR}\right) + V(R) + \frac{J(J+1)}{2\mu R^2}\right]\psi_{\text{vib}}(R) = E\psi_{\text{vib}}(R). \tag{2.63}$$

Here, $V_{\text{eff}} = V(R) + \frac{J(J+1)}{2\mu r^2}$ is the effective potential and J is the angular momentum with respect to the nuclear motion. For small J, the effective potential features a minimum at R_J, which depends on J. In the vicinity around R_J, V_{eff} can be approximated by a Taylor expansion. Small displacements allow for omitting terms of higher order than the second degree. The resulting Schrödinger equation of a harmonic oscillator leads to approximative results for the vibrational wave functions and energies, see [21] and [35].

For a non-rotating dimer ($J = 0$), the assumption of a harmonic potential leads to a vibrational energy shift of

$$E_{\text{vib}}(\nu) = \left(\nu + \frac{1}{2}\right)\sqrt{\frac{k}{\mu}}, \tag{2.64}$$

where k is the parameter of the harmonic potential [33]. As seen in Fig. 13 as well as Sec. 3.3.2, the potential curve of a molecule differs from the curve of an harmonic oscillator. Due to the behaviour for large internuclear distances, this mathematically simple description does not provide satisfactory results, especially for higher excitations of the nuclei, reaching into the anharmonic part of the potential ($R \gg R_{\text{eq}}$).

In order to account for this, better fitting potentials are required for the calculation of the vibrational energies. A general power series approach

$$V(R) = \sum_n \frac{1}{n!}\left(\left.\frac{\partial V}{\partial R^n}\right|_{R_{\text{eq}}} (R - R_{\text{eq}})^n\right) \tag{2.65}$$

leads to a Schrödinger equation which can only be solved by numerical methods [33].

A reasonable approximative potential is given by the Morse potential

$$V_{\text{Morse}}(R) = D\left[\left(1 - e^{-\alpha(R - R_{\text{eq}})}\right)^2 - 1\right], \tag{2.66}$$

which is characterised by the potential minimum D, the position of this minimum R_{eq}, and potential width α, which will be further explained in Sec. 3.2. An advantage of the Morse potential is that it allows for an exact solution of the Schrödinger equation. However, the Morse potential converges for $R \to 0$, whereas the real potential curve should diverge [33]. The energy shift induced by the vibrational motion in a Morse potential (see also Eq. (3.25)) reads

$$E_{\text{vib}}(\nu) = \sqrt{\frac{2D\alpha^2}{\mu}}\left[\left(\nu + \frac{1}{2}\right) - \frac{1}{k}\left(\nu + \frac{1}{2}\right)^2\right], \tag{2.67}$$

with the reduced mass μ and the vibrational level $\nu = 0, 1, 2, ...$ The characteristics of the energy shifts are described in more detail in Sec. 3.2. In contrast to the description using a harmonic potential, the spacing been adjacent energy levels is no longer constant, but decreases for increasing vibrational levels ν. Therefore, the energy levels emerging from the Morse potential can reproduce the general behaviour of the vibrational energy shift, which can be observed in [18]. Note that, even though the distance between adjacent vibrational levels decreases when the excitation level increases, it remains finite. Consequently, only a finite number of bound vibrational levels exist for a diatomic molecule [33].

2.8.2 Rotational motion

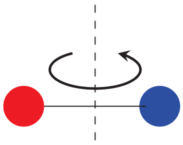

Figure 15: Schematic visualisation of the rotational motion of a dimer, treated as a rigid rotator. Note, that the position of the rotational axis depends on the mass distribution in the dimer and that the dimer can be positioned arbitrarily in space.

At the equilibrium distance R_{eq}, where the minimum of the potential curve is located, the Schrödinger equation for the angular motion reads [33]

$$\frac{1}{\sin\vartheta}\frac{\partial}{\partial\vartheta}\left(\sin\vartheta\frac{\partial Y_{lm}(\vartheta,\varphi)}{\partial\vartheta}\right)+\frac{1}{\sin^2\vartheta}\frac{\partial^2 Y_{lm}(\vartheta,\varphi)}{\partial^2\varphi}Y_{lm}(\vartheta,\varphi)+(J(J+1))Y_{lm}(\vartheta,\varphi)=0. \tag{2.68}$$

Here, the rotational excitation level J is identified with the angular momentum l. For the description of the rotational motion of a dimer, the system is considered as a rigid rotator. This assumption is reasonable, since the vibrational motion is much faster than the rotational motion [80]. A rigid rotator is characterised by a fixed internuclear distance R. Therefore, the two atoms are linked by the vector $\mathbf{R}$ like a barbell with a massless bar, see Fig. 15. Note, that, in general, the dimer can be positioned arbitrarily in space. The dimer then can rotate around an axis through its center of mass. The rotational motion leads to an energy shift depending on the level of the rotational excitation $J = 0, 1, 2, ...$. At the equilibrium distance, it reads

$$E_{\mathrm{rot}} = \frac{1}{2\mu R_{\mathrm{eq}}^2}J(J+1) = 2\pi c B J(J+1). \tag{2.69}$$

Here, the moment of inertia is $I_0 = \mu R_{\mathrm{eq}}^2$ and the rotational constant reads $B = \dfrac{1}{4\pi I_0 c}$ [80]. Note that, in contrast to the vibrational energy shift, the rotational ground state does not contribute to an energy shift. Furthermore, the spacing between rotational energy levels increases with its excitation level J.

A rough estimate can be made regarding the comparison of the electronic, vibrational and rotational energies [35]. As a result, it can be found that the magnitude of the rotational excitations is, in general, much smaller than the vibrational levels [35]. Furthermore, both energy shifts due to the nuclear motion are smaller than the typical energy scale of the electronic energy. Consequently, the rotational motion can be seen as a 'second-order' splitting of the line spectrum [35], which is visualised in Fig. 16.

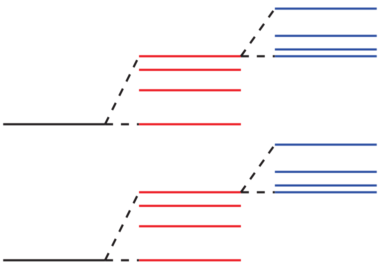

Figure 16: Schematic visualisation of the energy splitting due to vibrational (red) and rotational (blue) motion.

Approximative calculations of the nuclear motion can also be used in order to compare the time scales of the nuclear motion to the electronic one. Typically, the rotational frequency is about two orders of magnitude smaller than the one of the vibrational motion [33]. When considering the rovibrational motion of the dimer, the internuclear distance continously varies within the time it takes for one rotation. Therefore, the rotational energy denotes the mean value over many vibrational cycles and has to be calculated by averaging over the vibrational wave function [33]. Since the total energy $E = E_{\text{vib}} + E_{\text{rot}} + V_{\text{pot}}$ remains constant, there is a constant exchange of energy between rotational and vibrational motion as well as the interaction between the electrons [33]. Due to the long periods of the vibrational motion, the Born-Oppenheimer approximation is reasonable for further calculation [35].

2.9 Van der Waals dimers

In this section, the formation and characteristics of van der Waals molecules are described and van der Waals dimers, linear molecules including only two atoms, are introduced before presenting the practical example of the LiHe dimer, which is selected for the numerical calculations in this work.

2.9.1 Van der Waals force

Molecular bonds are formed mostly by covalent interactions, which were described in Sec. 2.7.1. In a covalent bond, two constituents share their valence electrons, leading to the lowering of the total energy of the system. Noble gases, however, are characterised by a fully populated valence shell. Therefore, the sharing of valence electrons does not lead to a lowered energy and consequently to no covalent bond either.

Van der Waals molecules, named after Dutch physicist Johannes Diderik van der Waals, are systems of atoms or molecules which are not subject to chemical bonding [84], as introduced in Sec. 2.7.1. Instead, they are weakly bound by the interplay between dipoles.

Three kinds of interactions between dipoles can arise:

- The strongest force originates from two permanent dipoles which can, for instance, be found in LiF or HCl [85, 86]. Another example is the hydrogen bond between two water molecules. Since H_2O features a permanent dipole moment, a water molecule can attract a neighbouring molecule due to the interaction of two dipoles.
- A permanent dipole can induce a dipole in an atom due to its polarisability by repelling its electrons. Therefore, the interaction describes the attractive interplay between one permanent and one induced dipole. The force resulting from this interaction is called Debye-force and is much weaker than the force between two permanent dipoles.
- The weakest force arises from the interaction between two induced dipoles and is also called London dispersion force [86, 87]. Dispersion forces arise from fluctuations in electronic clouds around atoms or molecules. Due to this behaviour, these forces can arise in neutrally charged systems, where no permanent dipole or multipole moment exists [88]. Due to the induced dipole moment and its influence on the first fluctuating dipole, the mutual interaction leads to a non-vanishing mean time value of the dipole moments.

While van der Waals interactions are often restricted to the inclusion of the leading R^{-6} terms, the name here is used including all attractive and repulsive interactions in chemically non-bound systems [84]. The latter allows for the creation of noble gas systems [17, 89] and explains the chemical behaviour: The fact that the boiling point of the noble gas elements increases with their period in the periodic system can be explained by the increase of the attractive force with the number of electrons.

A qualitative picture, taken from [21], can be achieved by considering an atom with a fluctuating dipole moment $\mathbf{p}_1$ with the electric field

$$\mathbf{E} = -\frac{\mathbf{p}_1}{R^3} + 3\frac{(\mathbf{p}_1\mathbf{R})\mathbf{R}}{R^5}, \tag{2.70}$$

inducing a dipole moment

$$\mathbf{p}_2 = \alpha_2 \mathbf{E} \tag{2.71}$$

in the second atom, which features a polarisability of α_2. The interaction energy then reads

$$E_{\text{pot}} = \frac{\mathbf{p}_1\mathbf{p}_2}{R^3} - 3\frac{(\mathbf{p}_1\mathbf{R})(\mathbf{p}_2\mathbf{R})}{R^5} = -\frac{\alpha_2}{R^6} p_{1j}\left(\delta_{ij} + 3\delta_{i1}\delta_{j1}\right) p_{1i} < 0, \tag{2.72}$$

which is attractive.

On the basis of two hydrogen atoms in their respective ground states, separated by the internuclear distance $\mathbf{R}$, the energy shift due to the dipole-dipole interaction can be calculated as a perturbation [90]: Fixing the orientation of the internuclear linking vector along the z-axis $\mathbf{R} \parallel \mathbf{e}_z$, the interaction between two dipoles, see Eq. (2.24), simplifies to $V = \frac{1}{R^3}(x_1x_2 + y_1y_2 - 2z_1z_2)$. The first order correction to the ground state energy of this system

$$E_n^{(1)} = \left\langle n^0 \left| V \right| n^0 \right\rangle = \left\langle \Phi_{100}^{(1)}\Phi_{100}^{(2)} \left| \frac{1}{R^3}(x_1x_2 + y_1y_2 - 2z_1z_2) \right| \Phi_{100}^{(1)}\Phi_{100}^{(2)} \right\rangle \tag{2.73}$$

vanishes since the atomic ground states feature a spherical symmetry. The second-order energy correction reads

$$E_n^{(2)} = \sum_{n \neq m} \frac{\left|\left\langle m^0 \left| V \right| n^0 \right\rangle\right|^2}{E_n^0 - E_m^0}, \tag{2.74}$$

where E_n^0, E_m^0 are the energies of the unperturbed states n and m, respectively. In the case of hydrogen, this expression becomes

$$E^{(2)} = \sum_{n,l,m,n',l',m'} \frac{\left|\left\langle \Phi_{nlm}^{(1)}\Phi_{n'l'm'}^{(2)} \left| V \right| \Phi_{100}^{(1)}\Phi_{100}^{(2)} \right\rangle\right|^2}{2E_{100} - E_n - E_{n'}}. \tag{2.75}$$

Due to the selection rules, only $l = 1$ and $l' = 1$ contribute. Approximating the denominator by $2E_{100}$ simplifes the expression further and a rough but good estimate can be given as [90]

$$E^{(2)} \approx -\frac{6}{R^6}. \tag{2.76}$$

However, this method becomes laborious for more complex atoms and electron configurations. Furthermore, mutually induced charge fluctuations can also lead to the induction of dipole-quadrupole, quadrupole-quadrupole, dipole-octopole, as well as higher order interactions. Consequently, the energy shift due to van der Waals interactions for large distances is of the general form

$$E_{\text{vdW}}(R) = \sum_{n=6}^{\infty} \frac{C_n}{R^n}, \tag{2.77}$$

where the coefficients C_n depend on the maximum depth of the potential curve and the equilibrium distance between the nuclei.

When considering homonuclear molecules, only even powers of R contribute to the interaction potential [33]. The inclusion of van der Waals terms will be further described in Sec. 3.2.

For small internuclear distances, the overlap of the wave functions has to be accounted for.

Damping functions, which will be described in Sec. 3.2, modify the form of the energy shift given in Eq. (2.77). The overlap of the wave functions eventually leads to a repulsive potential when the nuclei get too close to each other.

To incorporate this aspect, an empirical approach leads to the Lennard-Jones potential

$$E_{\text{pot}} = \frac{C_{12}}{R^{12}} - \frac{C_6}{R^6}, \tag{2.78}$$

where the coefficients depend on the binding partners and the position of the potential minimum. Note, however, that this formula is not suitable for chemically bound molecules [80].

Long-range dispersion forces are symptomatic for van der Waals molecules and give rise to binding energies which are diminutive compared to ionic bonds leading to largely separated nuclei [91]. Moreover, the electronic ground state of the molecule can often be described by wave functions, which do not differ by much from the wave functions describing the individual atoms composing the system [91].

The van der Waals interaction is smaller than typical binding energies by a factor of $10^2 - 10^3$ [80]. In the case of the noble gas dimer $\mathrm{Ar_2}$, the potential shows a minimum of $\approx 0.08\,\mathrm{eV}$. Being positioned directly next to argon in the periodic table, the energy of the potential minimum of $\mathrm{Cl_2}$ at $2.48\,\mathrm{eV}$ is much larger, even though this chemical bound is rather weak [80]. Experimental work on van der Waals molecules requires extensive cooling, since the binding energies can be of the order of about $1\,\mathrm{K}$ [91]. For low temperatures, all noble gases form atomic clusters, leading to weakly-bound dimers of all sorts of atoms. Due to the particular properties of the systems, described above, van der Waals molecules have been experimentally studied, with special emphasis placed on their role in the dynamics of chemical and surface interactions [91, 92].

The creation of van der Waals molecules is, in general, based on the sufficient cooling of a vapor consisting of atoms or molecules [93]. Wihin such an environment, supersonic jet expansions [94] lead to the formation of van der Waals molecules. They can be trapped when their kinetic energy is low. More detailed information on the experimental setup is presented in Sec. 2.9.3.

2.9.2 Van der Waals dimers including He

Helium (He) is the first element in the noble gas group. With only two protons and two neutrons in its nucleus, it is the second lightest element. The isotopic composition shows that the isotope featuring only one neutron has an abundance of only $1.38 \times 10^{-4}\%$ [47].

Holding two electrons, which fully occupy the $1s$ orbital, helium represents the simplest neutral few-electron system. This electron configuration is energetically beneficial and leads to the highest ionisation potential of about $24.6\,\mathrm{eV}$ [47] of all neutral atoms. Because of its charge distribution being perfectly symmetric, London dispersion forces are especially weak for helium [86]. Due to the low polarisablity, bonding with neighbouring atoms is avoided [17, 95]. As described above, noble gases do not experience a lowering of energy when sharing valence electrons. However, the fact that the electrons are tightly bound allows for the distance between He and other atoms to be determined by the other constituent. This could enable a fragile bound state for $^4\mathrm{He}_2$ to form at an internuclear distance, where the van der Waals force is not yet outperformed by repulsive forces [17].

Therefore, the question regarding the existence of a helium dimer He_2 was of particular interest to researchers. The first calculation by Slater [96] in 1928 proposed a potential minimum for an internuclear distance of about 5.6 a.u.. Subsequent calculations came to varying results [97]. Due to the extremely shallow potential curve, the existence of a bound vibrational level (see Sec. 2.8.1) relies on exact calculations. Ab initio calculations, which do not rely on experimentally determined parameters, improved the predictions leading to accuracy of neV [98]. Here, the recommended values include a potential minimum of 138.9(5) neV and a mean internuclear distance of 47.13(8) Å [98]. Due to the shallow binding potential of the helium dimer, whose sole supported vibrational level is bound by only about 1 mK, its size becomes remarkably large. The mean separation between the two atoms is about 50 Å. Although the potential features a classical turning point at around 14 Å, the dimer is able to escape the restriction by the binding energy and exhibits bond lengths which are classically forbidden [17].

Experimental work with the aim to prove the existence of the homonuclear dimer began in 1961 with the observation of helium clusters in an expansion of cooled helium [99]. After decades of experimental work, He_2 was the first noble gas dimer to be directly detected in experiment [100]. For the purpose of detection, a pre-cooled gas jet of helium was diffracted on microstructured transmission gratings [101]. However, the experiment could not yield the wave functions of He_2, but only a mean value. The direct observation of the square of the vibrational wave functon was first accomplished by Havermeier, et al. [11], ionising isolated dimers using synchrotron radiation. Due to its minuscule potential depth, the dimer can only be produced when using a cold supersonic jet, which is formed during the expansion of the gas in vacuum. Within such a gas jet, temperatures below 1 mK can be realised [11].

Since dimers including helium are one of the most weakly bound forms of molecular matter [102], the investigation of such systems is of particular interest. For HeNe, which is a heteronuclear dimer consisting of the two lightest noble gases, experiments and theoretical calculations have been executed, particularly with respect to ICD [18, 19, 56, 62, 65, 103]. The ground state of the dimer features a potential minimum at $R = 3\,\text{Å}$ with a binding energy of 2 meV [18]. Potential curves have been calculated for several excited states [18] as well as for the ionic systems [104]. Calculations for numerous dimers consisting of two noble gas atoms have been performed with regard to their potential surfaces, including HeAr and HeKr [105, 106].

Aside from noble gas dimers, van der Waals complexes can form between alkali metals and noble gases. Since alkali metals possess only a single valence electron, their theoretical consideration is advantageous over more complex atoms. While it was first assumed that the ground states are repulsive [107], later calculations proposed attractive ground states [79, 108].

2.9.3 LiHe

Lithium (Li) is the lightest alkali metal with the nucleus consisting of three protons. The isotopic composition of lithium shows an abundance ($\approx 92.4\%$) of atoms featuring four neutrons and a small percentage with three neutrons ($\approx 7.6\%$), [47]. While two electrons fill the $1s$ orbital in the electronic ground state of lithium, the third electron resides in the $2s$ orbital. Alkali metals are characterised by having an ns^1 valence electron configuration, leading to rather large atomic radii and a simplified excitation of this electron [109].

The system, consisting of helium and lithium, has long been studied theoretically [79, 108, 110]. Alkali-rare-gas interactions are of particular interest in spectroscopic experiments, since they exhibit generally large transition dipole moments [111]. In 1996, theoretical calculations of the potential energy curves for the ground state of LiHe as well as excitations of Li were proposed, using basis sets, as well as excitation spectra, which are comparable with experimental data [111].

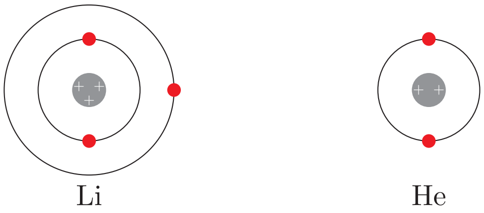

Figure 17: Scheme of the model system consisting of lithium and helium.

Early studies suggested a repulsive ground state [107, 112], contradicting the studies of Patil [79] and in particular Kleinekathöfer [108], who proposed theoretically calculated potential energy curves for various alkali-helium dimers. Following theoretical studies have focussed on the ground state and excited states in lithium [113], also including the attachment of lithium to helium nanodroplets [114].

More than twenty years after the experimental detection of He_2, the existence of a bound ground state in LiHe was proven experimentally by Naima Tariq, et al. [17, 115, 116]. Recent theoretical studies on LiHe obtained values comparable to the experimental measurements [102, 117]. The interaction potential features a minimum that is even more shallow than the one corresponding to He_2 [79]. This shallowness gives rise to a large extension of the dimer. Its mean distance $R \approx 55\,\mathrm{a.u.}$ exceeds not only the equilibrium distance $R_{\mathrm{eq}} \approx 11.3\,\mathrm{a.u.}$, where the potential has a minimum, but also the outer turning point at about $32\,\mathrm{a.u.}$ [17]. The only supported bound vibrational state exhibits a binding energy of only $6\,\mathrm{mK}$ [17]. Due to the fragile binding, the process of forming the molecule has to include extensive cooling of the atoms [115] and its formation is disadvantageous in comparison to other van der Waals molecules involving helium. For the experimental detection, helium buffer-gas cooling is applied [115] for lithium, which is produced by laser ablation of a solid target [115, 118]. Within the general mechanism, the species to be cooled is inserted as a hot vapor into a different vapor, usually He, which is moderately dense and cryogenically cooled. The temperature of the buffer gas is achieved after about 100 collisions [91]. The van der Waals molecules produced by three-body combination of the form

$$\mathrm{Li} + \mathrm{He} + \mathrm{He} \rightarrow \mathrm{LiHe} + \mathrm{He} \tag{2.79}$$

are then detected by laser induced flourescence with a power of a few mW, while lithium is measured simultaneously as well [115].

The isotopic composition of the molecule plays an important role concerning the binding energy and the nuclear dynamics thereinafter. Many van der Waals dimers involving helium and alkali metals are presumed to form bound states [86, 108]. However, all considerations here are restricted to ^{7}Li^{4}He, which was experimentally created by three body recombination and spectroscopically detected in 2013 [115]. This is based on the abundance of ^{7}Li with respect to ^{6}Li [86]. ^{6}Li^{4}He is expected to exhibit an even longer bond length of 91.6 a.u. and an even more shallow binding energy of 1.4mK [86, 108]. Note that Li^{3}He is not expected to feature a bound state [108].

The dimer of LiHe is chosen for the considerations in Secs. 3, 4, and 5, because of the manageable amount of electrons in the system. A popular van der Waals dimer, studied theoretically and experimentally, is HeNe, which is much more complex in its electronic configuration. This impedes the effort of a mostly analytical approach.

Current theoretical studies on the potential curves of the $(1s2p)$-state in helium and the ionised state HeLi$^+$ [102], as well as on ICD in this system [117], have been conducted throughout the process of this thesis and will be discussed within Sec. 3.4. Furthermore, theoretical work on collisions including lithium and helium, resulting in bound systems, has been published recently [119].

3 Influence of the nuclear motion on two-center photoionisation

In this section, the process of two-center photoionisation of an atom A in the presence of a neighbouring atom B is considered.

Within the process of photoionisation, an electromagnetic field interacts with an electron in an atomic or molecular center A. The energy transfer from the radiation field can, if ω is sufficiently large, lead to the emission of an electron. The kinetic energy of the emitted electron is given by

$$E_{\text{kin}} = \frac{k^2}{2} = \omega - I_A, \tag{3.1}$$

where $I_A > 0$ is the binding energy of an atom A, see Sec. 2.1.1.

Photoionisation (PI) processes in atoms and molecules present long-standing mechanisms to improve the understanding of the underlying electron structure and dynamics. While synchrotron light sources and optical lasers represented the standard experimental methods for decades, the introduction of ultrashort and ultraintensive X-ray pulses generated by free-electron lasers provides new and more complete studies on photoionisation [16, 120].

In 2010, B. Najjari, A. B. Voitkiv, and C. Müller predicted the enhancement of the photoionisation of an atom A in proximity to an atom B, given that the field frequency is close to one transition frequency in atom B [16]. This process relies on the possibility for the transition energy of the deexcitation process to be transferred radiationlessly from the atom to one in its vicinity [7, 8, 9], similar to ICD, discussed in Sec. 2.3. Note, that ICD solely describes the decay mechanism, whereas the proposed process includes both the creation of the autoionising state as well as the decay and the resulting ionisation.

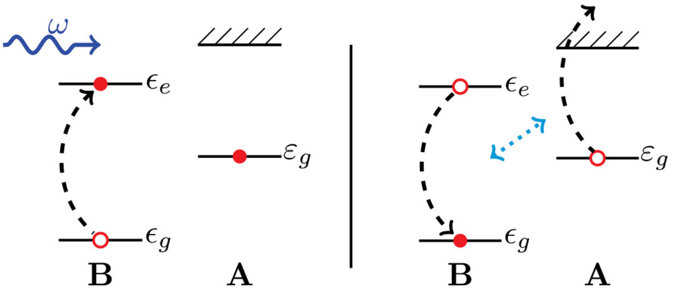

Figure 18: Scheme of two-center photoionisation (2CPI). Initially, the photoexcitation in atom B creates autoionising state over two atomic systems A and B, which is illustrated on the left. When the decay of the excited electron occurs via radiationless energy transfer to atom A, depicted on the right, this atomic center is ionised.

In the process of 2CPI, it is possible for atom A to be ionised via radiationless transfer of excitation energy from atom B, which has previously been excited by an external electromagnetic field, creating a two-center autionising state, as depicted in Fig. 18. Therefore, resonant 2CPI represented a new interatomic process, see Sec. 2.2. The two-center photoionisation was predicted to dominate the cross section of the direct ionisation process for the model system LiHe by up to 6 orders of magnitude, when the internuclear distance is set to $R = 10\AA$ [16]. Here, the autoionising state is created by the excitation of helium to the $1s2p$-state. The theoretical prediction of the enhancement of photoionisation due to the indirect mechanism, calculated for the model system of LiHe, was supported experimentally for HeNe dimers by Trinter, et al. in 2013 [18]. Besides, the angular distribution of the emitted electrons resulting from resonant ICD has been studied experimentally for HeNe dimers, focussing on the decay process (RICD) [19]. Furthermore, theoretical studies on the angular distribution of the elctrons emitted via 2CPI have been conducted for HeNe, also including their vibrational level structure [19]. For He_2, angular distributions of the electron emitted by ICD have been investigated in [121]. Furthermore, the efficiency of this process has been shown experimentally for a system consisting of Ne and Ar [20]. Recently, 2CPI has been studied theoretically in slow atomic collisions, in which the internuclear distance is subject to the relative atomic motion, assuming a straight-line trajectory [122].

All experiments found a significant enhancement of the photoelectron yield as compared with the direct ionisation channels of Ne or Ar, respectively. However, the immense effects calculated for LiHe were not reproduced. Within these experiments, the internuclear distance R between the two atoms is not fixed as in the original theoretical investigation, but rather varies as a result of the vibrational motion of the HeNe or NeAr molecule.

In order to improve the theoretical description of the process, the original theory of 2CPI [16] is further developed here to account for the nuclear motion of the system. Of particular interest is the impact of the molecular treatment of the two atomic centers, A and B, on the total cross section of 2CPI and the ratio of the indirect and direct ionisation processes.

In the following, the nuclear motion is incorporated in the theoretical descripton of 2CPI in the system of a weakly bound hetereoatomic dimer. While the process of 2CPI in a van der Waals dimer becomes more complex when including molecular effects, the analytical approach pursued here has the intention to analyse the changes with respect to the predictions on 2CPI for fixed internuclear separations [16, 123].

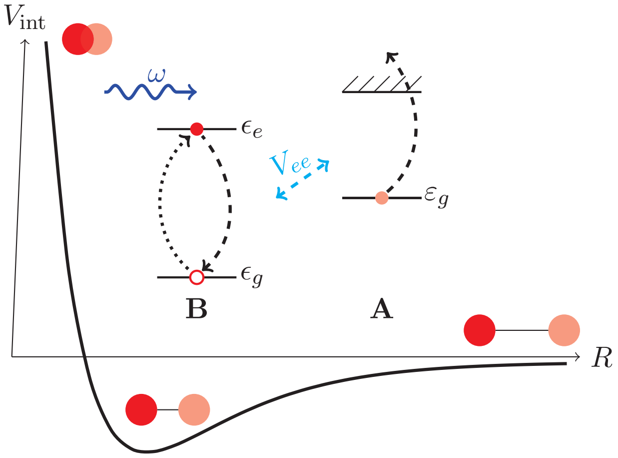

Figure 19: Scheme of the process of 2CPI, also accounting for the interaction between the two atomic centers, A and B, and the resulting nuclear motion. Besides the visualisation of the 2CPI process, a schematic interaction potential shows the influence of the internuclear distance R. A rough sketch, depicting the form of the dimer, is provided for different internuclear distances.

To begin with, the mathematical description of both direct and two-center photoionisation, applying the Born-Oppenheimer approximation, is presented in Sec. 3.1. In Sec. 3.2, the effects of the nuclear motion, caused by the interaction potential of the partaking electrons on this description, are considered. For this purpose, vibrational wave functions and Franck-Condon factors are introduced in Sec. 3.2.2 and Sec. 3.2.3. In Sec. 3.3.1, the results for fixed internuclear distances are given for the system formed by lithium and helium. Including molecular effects, an expression for the 2CPI cross section in a weakly bound dimer is derived in Sec. 3.3, which contains the transition matrix elements not only between the electronic, but also between the relevant molecular vibrational states. This expression is then used to present numerical results for the heteroatomic dimer LiHe, which was described in Sec. 2.9.3. An approximated expression enables a more general examination of the process, which also allows for a comparison with other systems. Furthermore, literature data for the potential curves is employed, showing the changes based on the parameters of the vibrational motion.
The results of this section were included in [124] and [125].

3.1 Theoretical description of one- and two-center photoionisation

Before including molecular effects, the process of resonant two-center photoionisation, first proposed in 2010 [16], is described mathematically by applying second order time-dependent perturbation theory. In [16], as well as in the calculations conducted in Sec. 4, the nuclei of A and B are assumed to be at rest with respect to the electronic motion and the atoms can be treated neglecting all interactions between them. This simple system is characterised by the vector $\mathbf{R}$, linking the two atomic centers. The Born-Oppenheimer approximation is utilised, which implies that the movement of the light and fast electrons can be separated from the movement of the slow and heavy nuclei. This approximation will be used again in Sec. 3.2, when molecular effects are considered. As before, the internuclear distance R has to be sufficiently large in order for the following approximations to be applicable. Throughout this thesis, the internuclear distance is sufficiently large when R is at least a few bohr radii. However, this classification can strongly depend on the investigated system. Setting the position of the nuclei with corresponding charge Z_A as the origin, Z_B is situated at $\mathbf{R}$. Restricting the consideration to one active electron in every atomic center, the positions of the two electrons involved in the process are denoted with $\mathbf{r}$ and $\mathbf{r}' = \mathbf{R} + \boldsymbol{\xi}$, respectively, see Fig. 20.

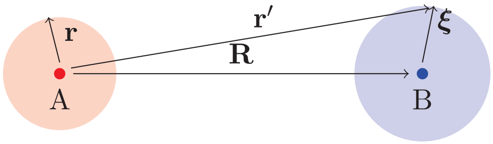

Figure 20: Scheme of the spatial dependencies considered in the calculation of the molecular effects in a two atomic system.

The interaction of an electron with an external electromagnetic field is described by the Hamiltonian

$$\mathcal{H} = \frac{\left(\hat{\mathbf{p}} - \frac{1}{c}\mathbf{A}\right)^2}{2} - V(\mathbf{r}) = \underbrace{\frac{p^2}{2} - V(\mathbf{r})}_{=H_0} \underbrace{- \frac{1}{2c}\left(\mathbf{A}\hat{\mathbf{p}} + \hat{\mathbf{p}}\mathbf{A} - \frac{1}{c}A^2\right)}_{=H_{\text{photo}}}. \tag{3.2}$$

For the process of photoionisation, the term $\sim A^2$ is neglected, since it describes a nonlinear interaction with the electromagnetic field. The direct photoionisation pathway is then described employing the coupling of the electromagnetic field to the electron in atom A, where the external field is described classically with linear polarisation along the z-axis. The application of the dipole approximation yields

$$\mathbf{A}(t) = \mathbf{A}_0 \cos(\omega t) = \mathbf{A}_0 \frac{e^{i\omega t} + e^{-i\omega t}}{2} \text{ and } W_A = \frac{\mathbf{A}_0 \cdot \hat{\mathbf{p}}}{2c}. \tag{3.3}$$

In Eq. (3.3), the two exponential functions describe the absorption and emission of a photon, respectively. Here, energy conservation only allows the absorption and therefore leads to the perturbation

$$W_A e^{-i\omega t}, \tag{3.4}$$

which is included in the expression for the first-order transition amplitude

$$S^{(1)} = -i \int\limits_{-\infty}^{\infty} dt\, \langle \varphi_{\mathbf{k}}(\mathbf{r}) | W_A(\omega) | \varphi_g(\mathbf{r}) \rangle e^{-i(\varepsilon_g + \omega - \varepsilon_k)t} \tag{3.5}$$

$$= -i2\pi\delta(\varepsilon_g + \omega - \varepsilon_k) \langle \varphi_{\mathbf{k}}(\mathbf{r}) | W_A(\omega) | \varphi_g(\mathbf{r}) \rangle \tag{3.6}$$

The two-center photoionisation of atomic center A can be described in two subprocesses, the photoexcitation of atom B and the subsequent decay of the autoionising state, leading to the ionisation of atom A. Thus, the three electronic states have to be established, which are illustrated in Fig. 18.

(I) The initial state $\Phi_{g,g} = \varphi_g(\mathbf{r})\chi_g(\boldsymbol{\xi})$ with total energy $E_{g,g} = \varepsilon_g + \epsilon_g$ features both electrons in A and B in their respective ground states.

(II) The photoexcited electron of B characterises the intermediate state $\Phi_{g,e} = \varphi_g(\mathbf{r})\chi_e(\boldsymbol{\xi})$ with the electron in A remaining in its ground state. Its total energy reads $E_{g,e} = \varepsilon_g + \epsilon_e$.

(III) In the final state $\Phi_{\mathbf{k},g} = \varphi_{\mathbf{k}}(\mathbf{r})\chi_g(\boldsymbol{\xi})$ with the energy $E_{\mathbf{k},g} = \varepsilon_k + \epsilon_g$, atom B has returned to its ground state while atom A is ionised. The electron emitted from A into the continuum, is characterised by an asymptotic momentum $\mathbf{k}$ and energy $\varepsilon_k = \frac{k^2}{2}$.

For an atom A to be ionised in a two-center process including a neighbouring atom B, the energy difference $\omega_B = \epsilon_e - \epsilon_g$ of the incorporated transition in atom B has to surpass the ionisation energy $I_A = |\varepsilon_g|$ of atom A. The application of second-order time-dependent perturbation theory yields the transition amplitude

$$\begin{aligned} S^{(2)} &= -\int\limits_{-\infty}^{\infty} dt\, \mathcal{V}^{AB}(\mathbf{k},\mathbf{R}) e^{-i(E_{g,e} - E_{k,g})t} \\ &\quad \times \int\limits_{-\infty}^{t} dt'\, \mathcal{W}^{B}(\omega) e^{-i(E_{g,g} + \omega - E_{g,e})t'} \end{aligned} \tag{3.7}$$

with the two matrix elements

$$\mathcal{V}^{AB}(\mathbf{k},\mathbf{R}) = \langle \Phi_{\mathbf{k},g} | V_{AB}(\mathbf{R}) | \Phi_{g,e} \rangle\,,\ \mathcal{W}^{B}(\omega) = \langle \Phi_{g,e} | W_B(\omega) | \Phi_{g,g} \rangle. \tag{3.8}$$

In general, the complete transition amplitude requires the summation over all intermediate states, even those forbidden by the conservation of energy. However, the photon energy is chosen such that the selected intermediate state is strongly favoured and transitions to other states can be neglected. The photoexcitation of atom B is induced by $W_B e^{-i\omega t}$ with

$$W_B = \frac{\mathbf{A}_0 \cdot \hat{\mathbf{p}}_\xi}{2c}. \tag{3.9}$$

The radiationless energy transfer is caused by V_{AB} in a dipole-allowed transition. Neglecting retardation effects, which is justified for $R \ll c/\omega_B$, the interaction reads

$$V_{AB}(\mathbf{R}) = \frac{\mathbf{r} \cdot \boldsymbol{\xi}}{R^3} - \frac{3(\mathbf{r} \cdot \mathbf{R})(\boldsymbol{\xi} \cdot \mathbf{R})}{R^5}, \tag{3.10}$$

as described in Sec. 2.4. Integration of Eq. (3.7) over time leads to

$$S^{(2)} = -2\pi i \delta(E_{\mathbf{k},g} - E_{g,g} - \omega) \frac{\mathcal{V}^{AB}(\mathbf{k}, \mathbf{R}) \mathcal{W}^B(\omega)}{\Delta + \frac{i}{2}\Gamma}, \tag{3.11}$$

where the energy detuning reads $\Delta = \epsilon_g + \omega - \epsilon_e$ and the total decay width $\Gamma = \Gamma_{\text{rad}} + \Gamma_{\text{aug}}$ accounts for the instability of the excited state of atom B, as described in Sec. 2.5. Note, that the Dirac function in Eq. (3.11) equals the one from Eq. (3.5), as the energy ϵ_g of the ground state in atom B cancels out. The indirect ionisation process competes with the direct channel of photoionisation, described in Eq. (3.5) by $S^{(1)}$. Leading to the same final state as the two-center photoionisation, the direct ionisation channel can interfere with the indirect process. This total transition amplitude reads

$$S^{(12)} = S^{(1)} + S^{(2)}. \tag{3.12}$$

For all transitions, cross sections are computed from the corresponding transition amplitude according to

$$\sigma^{(M)} = \frac{1}{\tau j} \int \frac{d^3k}{(2\pi)^3} |S^{(M)}|^2. \tag{3.13}$$

Note, that the integral is divided by the incident photon flux $j = \frac{\omega A_0^2}{8\pi c}$. Due to the square of the Dirac function, the interaction time τ cancels out. The ratio between the indirect and direct photoionisation process

$$\eta^{(2)} = \frac{\sigma^{(2)}}{\sigma^{(1)}}, \tag{3.14}$$

as well as the ratio between the total cross section and the one-center process

$$\eta^{(12)} = \frac{\sigma^{(12)}}{\sigma^{(1)}} \tag{3.15}$$

will be of special interest, since they show the importance of the indirect ionisation mechanism with respect to the well-known direct one.

Considering $\mathbf{R}$ along the z-axis, the cross section for direct and indirect photoionisation can be related to each other:

$$\begin{aligned} \sigma^{(2)} &= \frac{1}{j} \frac{4}{R^6} \int \frac{d^3k}{(2\pi)^3} \left| \langle \varphi_{\mathbf{k}} \chi_g \left| z \xi_z \right| \varphi_g \chi_e \rangle \right|^2 \times \\ &\quad 2\pi \delta(E_{\mathbf{k},g} - E_{g,g} - \omega) \frac{\left| \langle \chi_e \left| \frac{1}{2c} \mathbf{A} \cdot \hat{\mathbf{p}}_\xi \right| \chi_g \rangle \right|^2}{\Delta^2 + \frac{1}{4}\Gamma^2} \\ &= \sigma^{(1)} \frac{\Gamma_{\text{rad}}^2}{\Delta^2 + \frac{1}{4}\Gamma^2} \left(\frac{3c^3}{2R^3\omega^3} \right)^2, \end{aligned} \tag{3.16}$$

where the identity

$$\langle \Phi_2 \left| \hat{\mathbf{p}} \right| \Phi_1 \rangle = i \left\langle \Phi_2 \left| H\mathbf{r} - \mathbf{r}H \right| \Phi_1 \right\rangle = i \left(\varepsilon_2 - \varepsilon_1 \right) \langle \Phi_2 \left| \mathbf{r} \right| \Phi_1 \rangle \tag{3.17}$$

is applicable for eigenstates of H. On resonance, the energy detuning vanishes ($\Delta = 0$) and the ratio $\frac{\sigma^{(2)}}{\sigma^{(1)}}$ can therefore be calculated by inserting the decay widths, for which literature values and Eq. (4.19) can be used.

3.2 Theoretical description of molecular effects

In this section, the theoretical framework regarding the molecular effects in a heteroatomic dimer is presented. An analytical approach for the calculation of the potential energy surface is shown [79], from which vibrational wave functions and associated energy levels can be derived [126].

3.2.1 Potential energy surface

The potential energy of a system consisting of two neighbouring atoms, A and B, becomes a potential curve due to their interaction. Therefore, the potential energy depends on the vector $\mathbf{R}$ linking the two atoms. First-order perturbations are included, namely the Coulombic terms as well as terms accounting for the exchange energy. Besides, higher order perturbations in the form of van der Waals terms are incorporated as well. These more complex contributions become more relevant for larger internuclear distances R [79]. The energy shift induced by Coulombic interaction has the following form:

$$\begin{aligned} V_{\text{coul}}(\mathbf{R}) &= \int d^3r d^3\xi \Big(\frac{\beta_1}{R} - \frac{\beta_2}{|\mathbf{R}-\mathbf{r}|} - \frac{\beta_3}{|\mathbf{R}+\boldsymbol{\xi}|} \\ &\quad + \frac{\beta_4}{|\mathbf{R}-\mathbf{r}+\boldsymbol{\xi}|}\Big)|\Phi(\mathbf{r},\boldsymbol{\xi})|^2. \end{aligned} \tag{3.18}$$

Since $\Phi(\mathbf{r},\boldsymbol{\xi})$ is a product of two one-electron wave functions for the electrons of A and B, the coefficients β_m take into account the number of particles involved in the considered interaction. The indistinguishability of electrons leads to the exchange term, where the positions of the electrons are swapped in the arguments of the electronic wave functions

$$\begin{aligned} V_{\text{ex}}(\mathbf{R}) &= -\frac{1}{2}\int d^3r d^3\xi \Big(\frac{\beta_1}{R} - \frac{\beta_2}{|\mathbf{R}-\mathbf{r}|} - \frac{\beta_3}{|\mathbf{R}+\boldsymbol{\xi}|} \\ &\quad + \frac{\beta_4}{|\mathbf{R}-\mathbf{r}+\boldsymbol{\xi}|}\Big)\Phi(\mathbf{r},\mathbf{R}+\boldsymbol{\xi})\Phi^*(\mathbf{R}+\boldsymbol{\xi},\mathbf{r}). \end{aligned} \tag{3.19}$$

Here, the factor of $\frac{1}{2}$ is due to the spin. The energy shift caused by the van der Waals interaction, which was introduced in Sec. 2.9.1, can be calculated as a second order perturbation

$$V_{\text{vdW}}(R) = \sum_{n\neq m} \frac{|\langle\Phi_m|V_{AB}|\Phi_n\rangle|^2}{E_n^{(0)} - E_m^{(0)}}, \tag{3.20}$$

where V_{AB} denotes the same interaction as in Eq. (3.10). However, better accuracy can be obtained by including higher order terms $(\frac{C_8}{R^8}, \frac{C_{10}}{R^{10}})$. To employ literature values, the direction of the molecular linking vector $\mathbf{R}$ has to be fixed with respect to the orientation of the atomic orbitals for the purpose of defining the relative orbital configuration of the two constituents to each other. The resulting terms are individually multiplied by a corresponding damping factor [79]

$$f_{2L+4}(R) = 1 - e^{-R/\overline{a}} \sum_{n=0}^{2L+7} \frac{1}{n} \left(\frac{R}{\overline{a}} \right)^{n}, \tag{3.21}$$

where $\overline{a} = \frac{1}{4}\left(\frac{1}{\sqrt{2|\varepsilon_g|}} + \frac{1}{\sqrt{2|\epsilon_g|}}\right)$ is defined by the first ionisation energy of both constituents A and B. The damping functions are introduced in order to include the effects of charge overlap for small values of R [127].

Consequently, the van der Waals interaction can be described by

$$V_{\mathrm{vdW}}(R) = -f_6(R)\frac{C_6}{R^6} - f_8(R)\frac{C_8}{R^8} - f_{10}(R)\frac{C_{10}}{R^{10}}. \tag{3.22}$$

Hence, the total interaction energy is given by the sum of these three interactions

$$V_{\mathrm{int}}(\mathbf{R}) = V_{\mathrm{coul}} + V_{\mathrm{exc}} + V_{\mathrm{vdW}}. \tag{3.23}$$

3.2.2 Vibrational wave functions

The interaction of neighbouring atoms, A and B, can lead to a complex of these two constituents which cannot be treated individually anymore. Furthermore, the system is no longer characterised only by its motion as a whole along a trajectory, with the distance between the atoms R being fixed, but also by the vibrational and rotational motion, as described in Sec. 2.8. Here, only diatomic molecules are investigated, since they allow for extensive studies regarding the numerical results and facilitate the investigation with respect to the influence of the nuclear motion.

- **Rotational excitations**
  A system of two atoms forms a linear complex, which can rotate around the axis linking its two constituents. The energy scale of the levels created by rotational excitations is much smaller than the levels created by vibration of the complex [35]. Furthermore, the system considered here, LiHe, does not support any rotational excitation in its electronic ground state [17]. For the final state, the spacing between rotational levels is about one order of magnitude smaller than the spacing of vibrational levels [128]. Therefore, rotational effects are neglected in the following.

- **Vibrational excitations**
  The two constituents can also move relative to each other. Hence, the internuclear distance R varies within a vibrational cycle. Within a bound potential well, a discrete spectrum of vibrations exists. In general, the vibrational motion is calculated by solving the radial Schrödinger equation while considering the potential curve $V(R)$ [129]. Note, that there is a contribution to the energy shift even for the vibrational ground state with $\nu = 0$, as can be seen in Sec. 2.8.1.

  As explained in Sec. 2.8, the periods of the nuclear oscillations are considerably longer than those of the electronic motion. Consequently, a separate treatment of these two motions, where the electronic movement is described assuming fixed nuclei, is a valid approximation [35]. The Born-Oppenheimer approximation, which is used for diatomic molecules in the following sections, rests upon the different timescales on which light and heavy particles change their motion. Therefore, the included vibrational motion of the nuclei hardly influences the fast movement of the electrons.

In order to include vibrational effects into the mathematical description, the vibrational wave functions and the corresponding energy levels are defined for the three electronic states described in Sec. 3.1.

(I) The vibrational wave function for the initial system, where both atoms A and B are in their respective electronic ground state, reads $\Psi_{g,g} = \psi_{\mathrm{i}}(R, \nu_{\mathrm{i}})$. Thus, the corresponding energy shift from vibrations is given by $E_{\mathrm{i}}(\nu_{\mathrm{i}}) = -D_{\mathrm{i}} + E_{\mathrm{vib}}(\nu_{\mathrm{i}})$, where D_{i} is the minimum value of the interaction potential curve calculated for the initial state (see Fig. 25).

(II) The intermediate state, where atom B is electronically excited and atom A remains in its ground state, features the vibrational wave function $\Psi_{g,e} = \psi_{\mathrm{a}}(R, \nu_{\mathrm{a}})$. The vibrational motion leads to the energy shift $E_{\mathrm{a}}(\nu_{\mathrm{a}}) = -D_a + E_{\mathrm{vib}}(\nu_{\mathrm{a}})$.

(III) In the final configuration, atom A is ionised and B has returned to its ground state. This leads to the vibrational wave function $\Psi_{k,g} = \psi_{\mathrm{f}}(R, \nu_{\mathrm{f}})$ and the energy shift $E_{\mathrm{f}}(\nu_{\mathrm{f}}) = -D_{\mathrm{f}} + E_{\mathrm{vib}}(\nu_{\mathrm{f}})$.

The vibrational wave functions as well as the associated energy levels are calculated from the potential curves described in Sec. 2.7 and depicted in Fig. 25. In Sec. 2.8.1, the energy shift due to the vibrational motion was first introduced when assuming a harmonic interaction potential. However, an analytically manageable, but better approximation is given by a Morse potential, also mentioned in Sec. 2.8.1, of the form

$$V_{\mathrm{Morse}}(R) = D\left[\left(1 - e^{-\alpha(R-R_{\mathrm{eq}})}\right)^2 - 1\right], \tag{3.24}$$

which is fitted to the calculated interaction potential curves. From these parameters, where D is the depth of the potential, R_{eq} is the equilibrium distance and α describes the width of the potential, the energy levels read

$$E_{\mathrm{vib}}(\nu) = \sqrt{\frac{2D\alpha^2}{\mu}}\left[\left(\nu + \frac{1}{2}\right) - \frac{1}{k}\left(\nu + \frac{1}{2}\right)^2\right]. \tag{3.25}$$

Here, μ denotes the reduced mass of the system. In contrast to rotational excitations, the vibrational ground state $\nu = 0$ already exhibits an energy shift with respect to the potential minumum D. From the Morse potential, the vibrational wave functions can be deduced the following way [126]:

$$\psi(R, \nu) = \sqrt{\frac{\alpha b(\nu!)}{\Gamma(\kappa - \nu)}} e^{-z/2} z^{(\kappa-2\nu-1)/2} \mathcal{L}_{\nu}^{(\kappa-2\nu-1)}(z). \tag{3.26}$$

Here, $\mathcal{L}_{\nu}^{(\kappa-2\nu-1)}(z)$ denotes the associated Laguerre polynomial. The remaining parameters are given by $\kappa = \frac{4D}{\sqrt{\frac{2D\alpha^2}{\mu}}}$, $b = \kappa - 2\nu - 1$ and $z = \kappa e^{-\alpha(R-R_{\mathrm{eq}})}$.

3.2.3 Franck-Condon factors

The vibrational wave functions discussed above have to be included in the calculation of the transition amplitude. In the processes considered here, each transfer of energy due to an electronic transition can also give rise to a vibrational one. Note, that in general, vibrational transitions are not bound to electronic transitions.

Franck-Condon factors (FC) describe the overlap between two vibrational wave functions associated with the electronic states involved in a transition. The absolute square of the factor determines the probability of such a process [130] and benefits from transitions with similar positioning regarding their potential surface, see Fig. 21. Therefore, the most probable transition exhibits no change in position or nuclear kinetic energy [131].

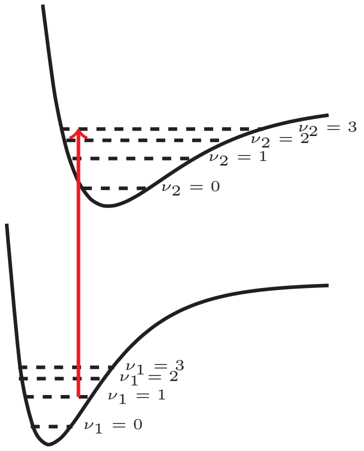

Figure 21: Scheme of a vertical vibrational transition within an electronic transition. The latter is described by the change of the electronic interaction curve.

The vibrational wave functions and their transitions are included in the perturbative calculations of the ionisation process. Hence, every matrix element describing an electronic transition is consequently extended to:

$$\mathcal{M}_{\mathrm{i,f}} = \langle \Phi_{\mathrm{f}}^{el}(\mathbf{r},\boldsymbol{\xi})\Psi_{\mathrm{f}}(R,\nu_{\mathrm{f}})|V(\mathbf{R},\mathbf{r},\boldsymbol{\xi})|\Phi_{\mathrm{i}}^{el}(\mathbf{r},\boldsymbol{\xi})\Psi_{\mathrm{i}}(R,\nu_{\mathrm{i}})\rangle, \tag{3.27}$$

where V is an arbitrary operator, i and f depict the initial and final states of the transition described in $\mathcal{M}_{\mathrm{i,f}}$, which depends on the vibrational levels of the initial and final state ν_{i} and ν_{f}. While the matrix element for the electronic transition can include selection rules regarding the parity as well as the angular momentum, this is not the case with the Franck-Condon factor. However, the overlap favours transitions with particular combinations of vibrational levels [80].

Within the widely applied Condon approximation [132], any dependence on the internuclear distance R resulting from the electronic transition is ignored. Therefore, the approximated probability of a vibrational transition reads

$$P_{\mathrm{i}\to\mathrm{f}} = \left| \int dR\, \Psi_{\mathrm{f}}^*(R,\nu_{\mathrm{f}})\Psi_{\mathrm{i}}(R,\nu_{\mathrm{i}}) \right|^2 . \tag{3.28}$$

The electron-electron interaction of the Auger decay strongly depends on the internuclear distance. In the following calculations, the squares of the Franck-Condon factors thus are not entirely of the form of Eq. (3.28).

For the process of photoionisation, three different Franck Condon overlaps have to be calculated. The direct photoionisation yields

$$FC_{\mathrm{i,f}}(\nu_{\mathrm{i}},\nu_{\mathrm{f}}) = \int dR\, \psi_{\mathrm{i}}(R,\nu_{\mathrm{i}})\psi_{\mathrm{f}}^*(R,\nu_{\mathrm{f}}). \tag{3.29}$$

Here, the transition from the electronic ground state to the final state, where lithium is ionised, is considered.

The two-center photoionisation is described via two subprocesses and therefore contains two overlaps. The creation of the autoionising state by excitation from the initial state includes the overlap

$$FC_{\mathrm{i,a}}(\nu_{\mathrm{i}},\nu_{\mathrm{a}}) = \int dR\, \psi_{\mathrm{i}}(R,\nu_{\mathrm{i}})\psi_{\mathrm{a}}^*(R,\nu_{\mathrm{a}}). \tag{3.30}$$

Both overlaps in Eqs. (3.30) and (3.29) can be separated from the matrix elements describing the associated electronic transitions, since W_A and W_B do not depend on R, see Eqs. (3.3),(3.9). For the nonradiative energy transfer however, the R-dependency of V_{AB} has to be incorporated. The factor in question can be simplified to $1/R^3$, which yields

$$FC_{\mathrm{a,f}}(\nu_{\mathrm{a}},\nu_{\mathrm{f}}) = \int dR\, \frac{\psi_{\mathrm{a}}(R,\nu_{\mathrm{a}})\psi_{\mathrm{f}}^*(R,\nu_{\mathrm{f}})}{R^3}. \tag{3.31}$$

Due to the possible multitude of vibrational transitions, the two-center photoionisation transition amplitude $S^{(2)}$ has to be summed coherently over all intermediate vibrational states. Moreover, all possible final vibrational levels are taken into account in the incoherent sum over the individual two-center cross sections.

Additionally, also the Auger decay rate $\Gamma_{\mathrm{aug}}(R)$ is a characteristic feature of the dimer and therefore depends on the vibrational levels of the transition. Here, the vibrationally resolved two-center Auger decay rate is calculated by integrating the R-depending decay rate for fixed nuclei given in Eq. (2.42) multiplied by the probability density $|\Psi_{\mathrm{a}}(\nu_{\mathrm{a}},R)|^2$, yielding

$$\bar{\Gamma}_{\mathrm{aug}}(\nu_{\mathrm{a}},\nu_{\mathrm{f}}) = \int_{x_0}^{\infty} dR\, \Gamma_{\mathrm{aug}}(\nu_{\mathrm{a}},\nu_{\mathrm{f}},R)|\Psi_{\mathrm{a}}(\nu_{\mathrm{a}},R)|^2. \tag{3.32}$$

The lower limit x_0 of the integral comes into play when the potential energy curves of the intermediate and final state intersect [48]. As a consequence of the averaging, $\Gamma_{\mathrm{aug}}(R)$ becomes $\bar{\Gamma}_{\mathrm{aug}}(\nu_{\mathrm{a}},\nu_{\mathrm{f}})$ and therefore no longer depends on R but on ν_{a} and ν_{f}. Note, that this calculation of $\bar{\Gamma}_{\mathrm{aug}}$ represents an approximation. A higher precision for the quantity can be obtained in a more rigorous approach by the numerical solution of the time-independent Schrödinger equation with a complex potential. Here, the imaginary part of the potential contains $\Gamma_{\text{aug}}(\mathbf{R})$. This method is, for example, depicted in [62]. For the radiative width, the atomic value from Eq. (2.25) is inserted because Γ_{rad} remains practically unaltered in the presence of the neighbouring atom. These modifications lead to the expressions for the transition amplitudes

$$\begin{aligned} S^{(2)}_{\text{mol}} =& -2\pi i \sum_{\nu_{\text{a}}} \delta(E_{\mathbf{k},g} + E_{\text{f}}(\nu_{\text{f}}) - E_{g,g} - E_{\text{i}}(\nu_{\text{i}}) - \omega) \times \\ & \frac{\langle \Phi_{\mathbf{k},g}\Psi_{\mathbf{k},g} | V_{AB}(\mathbf{R}) | \Phi_{g,e}\Psi_{g,e}\rangle \langle \Phi_{g,e}\Psi_{g,e} | W_B(\omega) | \Phi_{g,g}\Psi_{g,g}\rangle}{\epsilon_g + E_{\text{i}}(\nu_{\text{i}}) + \omega - \epsilon_e - E_{\text{a}}(\nu_{\text{a}}) + \frac{i}{2}(\Gamma^B_{\text{rad}} + \bar{\Gamma}^B_{\text{aug}})} \end{aligned} \tag{3.33}$$

$$S^{(1)}_{\text{mol}} = -2\pi i \delta(E_{\mathbf{k},g} + E_{\text{f}}(\nu_{\text{f}}) - E_{g,g} - E_{\text{i}}(\nu_{\text{i}}) - \omega) \langle \Phi_{\mathbf{k},g}\Psi_{\mathbf{k},g} | W_A(\omega) | \Phi_{g,g}\Psi_{g,g}\rangle . \tag{3.34}$$

The vibrational levels ν_{a} and ν_{f} for the intermediate and final state give rise to a multitude of transitions. Each of these now requires a specific energy ω of the photon in order to minimise the denominator. In the case of LiHe, the resonant photon energy only depends on the vibrational level of the intermediate state since $\nu_{\text{i}} = 0$ is the only bound vibrational state of the electronic ground state. The cross sections are obtained similarly to Eq. (3.13), but require the incoherent sum over all final vibrational state.

$$\sigma^{(2)}_{\text{mol}} = \sum_{\nu_{\text{f}}=0}^{\nu_{\text{f},max}} \frac{1}{\tau j} \int \frac{d^3k}{(2\pi)^3} |S^{(2)}_{\text{mol}}|^2 \tag{3.35}$$

$$\sigma^{(1)}_{\text{mol}} = \sum_{\nu_{\text{f}}=0}^{\nu_{\text{f},max}} \frac{1}{\tau j} \int \frac{d^3k}{(2\pi)^3} |S^{(1)}_{\text{mol}}|^2 \tag{3.36}$$

The implications of these changes with respect to the consideration with fixed internuclear distance R will be discussed in the next section.

3.3 Results

Now, the theory established in Secs. 3.1 and 3.2 is applied to a weakly bound van der Waals dimer. As pointed out previously, ^{7}Li^{4}He is chosen for the numerical calculations, for which theoretical investigations had been carried out [108, 133] long before an experimental detection was possible [17, 115]. Its shallow potential curve of the electronic ground state lends itself to large internuclear distances, as already described in Sec. 2.9.3. Further information on this system will be given when discussing the interaction potential curve (see Fig. 25).

Within the general theory of the process given in Sec. 3.1, lithium assumes the role of atom A, whereas the transition in helium from $1s^2$ to $1s2p$ is associated with the excitation of atom B. For the analysis given here, the internuclear axis of the dimer is set along the z-axis, also serving as the quantisation axis. As a consequence of the dipole selection rules, the photoexcitation in helium to $n = 2$ is restricted to the $1s2p_0$ state. The dipole characteristic of direct photoionisation has already been pointed out in Sec. 2.1.1. When considering a multitude of dimers, the orientations of the molecules with respect to an axis of coordinates are mixed and arbitrary. The alignment of a molecule is possible, however, in practice it requires additional experimental manipulation [134]. Although the orientation of the dimer does not change the fundamental physics involved, the alignment facilitates the numerical calculation and visual display of the results. Within this approach of utilising mostly analytical methods, effective electronic states χ (for helium) and φ (for lithium) are chosen to describe the atomic states considered in the process in order to facilitate the calculations. For helium, hydrogen-like wave functions with an effective charge Z_{He} are employed. However, neither lithium nor helium are single-electron atoms. In order to describe helium as a system consisting of two electrons, symmetrised superpositions of product states are introduced. Correspondingly, the ground state of helium reads

$$\chi_{1s}(\boldsymbol{\xi}_1)\chi_{1s}(\boldsymbol{\xi}_2), \tag{3.37}$$

whereas the excited state is of the form

$$\frac{1}{\sqrt{2}}[\chi_{1s}(\boldsymbol{\xi}_1)\chi_{2p_0}(\boldsymbol{\xi}_2) + \chi_{2p_0}(\boldsymbol{\xi}_1)\chi_{1s}(\boldsymbol{\xi}_2)]. \tag{3.38}$$

Then, the interaction Hamiltonians in Eqs. (3.9) and (2.24) have to be extended accordingly

$$W_B \rightarrow \sum_{\ell=1,2} W_{B_{\boldsymbol{\xi}_l}} \tag{3.39}$$

$$V_{AB} \rightarrow V_{AB}(\mathbf{r}, \boldsymbol{\xi}_1 + \boldsymbol{\xi}_2). \tag{3.40}$$

These alterations result simply in the additional factor of 2 in the transition amplitude in contrast to the description with one electron.

Note, that this modification also impacts the expression of the two-center Auger decay width Γ_{aug} given in Eq. (2.42). This way, the two electrons are taken into account despite using only a one-particle wave function. The excitation energy $\omega_B = 21.218$ eV for the transition to the $1s2p_0$-state determines the effective nuclear charge of both states considered here to be $Z_{\mathrm{He}} = 1.435$.

For the description of the valence electron of the alkali atom lithium in its ground state, the Bates-Damgaard wave function

$$\varphi_g(\mathbf{r}) = \frac{1}{\sqrt{8\pi}} \frac{1}{\Gamma(a+1)} \left(\frac{2}{a}\right)^{a+\frac{1}{2}} r^{a-1} \left(1 + \frac{v}{r}\right) e^{-r/a} \tag{3.41}$$

is employed, where $v = -\frac{1}{2}a^2(a-1)$ is defined as described in Sec. 2.6.2 and [79]. Here, the parameter $a = \frac{1}{\sqrt{2|\varepsilon_g|}}$ depends of the binding energy and can therefore also be associated with an effective nuclear charge $Z_{\text{Li}} \approx 1.259$ for its binding energy of $|\varepsilon_g| = 5.39\,\text{eV}$ [47]. The electron emitted from lithium in the final state of the two-center photoionisation is influenced by the remaining, positively charged lithium ion. This is accounted for by the use of a Coulomb wave $\varphi_{\mathbf{k}}$ [70] with the same effective nuclear charge $Z = Z_{\text{Li}}$ of the wave function corresponding to the ground state, as described in Sec. 2.6. This continuum state is normalised to a quantisation volume of unity in accordance with Eq. (3.13).

3.3.1 Cross sections for fixed nuclei

Next, numerical results for the system of LiHe are provided. Before calculating these results including the molecular effects, the one- and two-center photoionisation cross sections are calculated for a fixed internuclear distance. Therefore, any molecular effects are neglected in this consideration. The direct photoionisation, described in Sec. 3.1, is a process, whose fully integrated cross sections shows a smooth dependence on the incidenct photon energy ω. This is in sharp contrast to the two-center process, which exhibits a resonance [16, 18, 123] for a suitable incident energy, leading to a vanishing energy detuning $\Delta = 0$.

For the indirect ionisation process, the decay width has to be calculated for the system of LiHe. Employing the wave functions mentioned in Sec. 3.3, the radiative decay width reads

$$\begin{aligned}
\Gamma_{\text{rad}}^{\text{He}} &= \frac{4\omega_{\text{He}}^3}{3c^3} \left| \int_0^{2\pi} d\varphi \int_{-1}^{1} d\cos\vartheta \int_0^{\infty} d\xi \xi^2 \sqrt{\frac{Z_{\text{He}}^8}{32\pi^2}} \cos\vartheta \boldsymbol{\xi} e^{-\xi\frac{3}{2}Z_{\text{He}}} \right|^2 \\
&= \frac{4\omega_{\text{He}}^3}{3c^3} \left| \sqrt{\frac{Z_{\text{He}}^8}{32\pi^2}} \frac{4\pi}{3} \mathbf{e}_z \int_0^{\infty} d\xi \xi^4 e^{-\xi\frac{3}{2}Z_{\text{He}}} \right|^2 \\
&= \frac{4\omega_{\text{He}}^3}{3c^3} \left| \sqrt{\frac{Z_{\text{He}}^8}{32}} \frac{4}{3} \frac{768}{\left(\frac{3}{2}Z_{\text{He}}\right)^5} \right|^2 \\
&= 6.62 \times 10^{-8}\,\text{a.u.},
\end{aligned} \tag{3.42}$$

which differs from the literature value $\Gamma_{\text{rad}}^{\text{He}} = 4.35 \times 10^{-8}\,\text{a.u.}$ [47] by a factor of about 1.5. The influence of Γ_{rad} on the ratio of the photoionisation cross sections is investigated below and shown in Fig. 23.

Without the inclusion of molecular effects, the two-center Auger decay rate Γ_{aug} in Eq. (2.42) strongly depends on the internuclear distance R, which is depicted on the left side of Fig. 22 on resonance. Both Γ_{aug} and the square of the matrix element of the radiationless energy transfer comprise the dependency on $\frac{1}{R^6}$. Inserting the wave functions into Eq. (2.42) in Sec. 2.5.2, where the relevant matrix elements are calculated in the Appendix, see Sec. 7, the two-center Auger decay reads

$$\Gamma_{\mathrm{aug}}(R) = \frac{0.624732}{R^6} \tag{3.43}$$

when considering the two electrons in helium.

The two-center cross section $\sigma^{(2)}$ strongly depends on the internuclear distance R, whereas the direct process of photoionisation does not contain any dependence on R, since the second atom is not involved. The ratio $\eta^{(2)}(\omega, R) = \sigma^{(2)}/\sigma^{(1)}$ is depicted for the resonant photon energy $\omega_0 = \epsilon_{\mathrm{e}} - \epsilon_{\mathrm{g}}$ and varying distance R in Fig. 22. Furthermore, the ratio $\eta^{(2)}$ is plotted against the incident photon energy ω for two values of fixed internuclear distances $R = 10\,\mathrm{a.u.}$ and $R = 20\,\mathrm{a.u.}$.

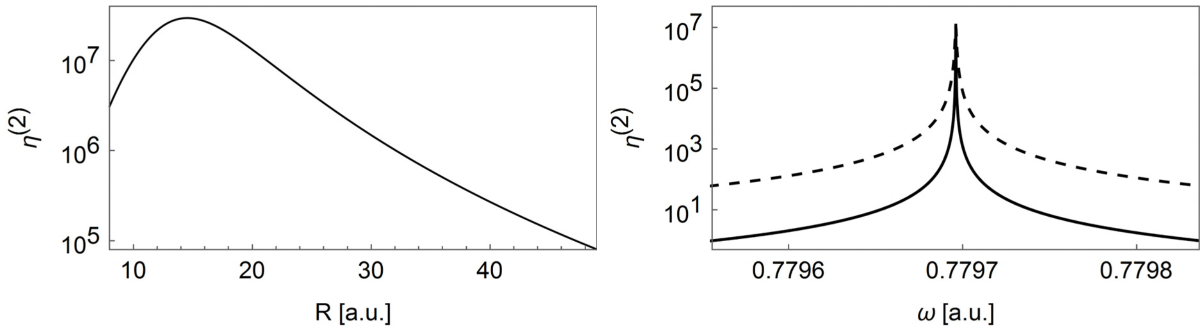

Figure 22: Ratios $\eta^{(2)}(\omega, R) = \frac{\sigma^{(2)}}{\sigma^{(1)}}$ in a LiHe system for fixed nuclei. The dependence of $\eta^{(2)}(\omega, R)$ on the internuclear distance R is depicted on the left. Here, the photon energy meets the resonant condition $\omega = \omega_0$, where the energy detuning Δ vanishes. On the right, the ratio $\eta^{(2)}(\omega, R)$ is plotted against the incident photon energy ω for fixed internuclear distance $R = 10\,\mathrm{a.u.}$ (dashed) and $R = 20\,\mathrm{a.u.}$ (solid).

For rather small spacings between lithium and helium, the ratio of cross sections increases with R. Here, the two-center Auger decay plays a significant role for the total decay width Γ. The two-center decay width decreases with larger R, resulting in increasing values for the two-center photoionisation cross section. For sufficiently large separations, Γ_{aug} becomes negligible with respect to Γ_{rad}. Consequently, the total decay width remains comparatively constant and the behaviour of the ratio is dominated by the factor $\frac{1}{R^6}$ in the numerator of $\sigma^{(2)}$, which stems from the matrix element describing the dipole-dipole interaction in the numerator of the transition amplitude.

The single peak of the ratio between the cross sections illustrates the resonant characteristic of the indirect photoionisation process. The immense height of the peak shows the possibility of 2CPI to dominate over the direct photionisation channel. Slightly larger peak heights are obtained in comparison to [16]. This effect stems from the fact that both electrons in helium are taken into consideration. Moreover, a different wave function for lithium was employed.

The cross sections for the two varied separations show differences in the peak height as well as the peak width. The peak height is larger for the greater internuclear distance R. This is because for $R = 20\,\mathrm{a.u.}$, the total decay width is dominated by the radiative decay width, which implies a small value. On resonance, the denominator in Eq. (3.33) approximately comprises only the radiative width, leading to large amplifications. Due to the larger decay width for $R = 10\,\mathrm{a.u.}$, the ratio decreases more slowly. This explains the differences off resonance. The effectiveness of the two-center pathway can be appraised by considering the integral resonance strength, whose value can be roughly estimated by calculating the product of peak height and its width. Here, the integral resonance strength for the smaller internuclear distance $R = 10\,\mathrm{a.u.}$ surpasses the value for $R = 20\,\mathrm{a.u.}$ by the factor of about 7. Consequently, the maximum peak height does not solely dictate the effectiveness of the process.

Note, that when inserting the symmetrised wave function for helium, the value for Γ_{aug} is multiplied by the factor of 2. For the sake of consistency, this should be also applied for the radiative decay width Γ_{rad}, since the same wave function should be included in the calculation of the corresponding matrix element. However, as discussed before, the calculated value for the decay width is already bigger than the reference value. Therefore, a multiplication by the factor of 2 would further increase this discrepency. In order to investigate the influence of this value, the ratio $\eta^{(2)}$ is plotted for two interatomic distances R and three different values for Γ_{rad}: The value calculated in Eq. (3.42) $\Gamma_{\mathrm{rad},1} = 6.6 \times 10^{-8}\,\mathrm{a.u.}$, the literature value from [47] $\Gamma_{\mathrm{rad},2} = 4.4 \times 10^{-8}\,\mathrm{a.u.}$ as well as the value from Eq. (3.42) multiplied by 2, $\Gamma_{\mathrm{rad},3} = 1.3 \times 10^{-7}\,\mathrm{a.u.}$.

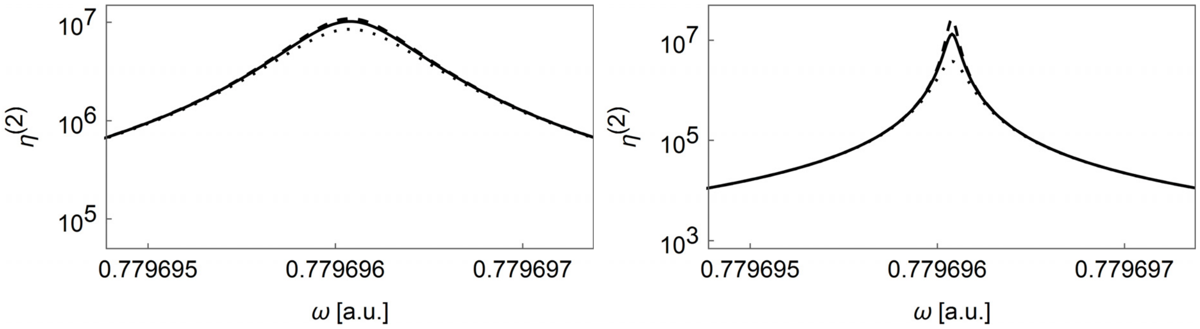

Figure 23: Ratios $\eta^{(2)}$ in a LiHe system, for fixed nuclei and different values of the radiative decay widths $\Gamma_{\mathrm{rad},1}$ (solid), $\Gamma_{\mathrm{rad},2}$ (dashed) and $\Gamma_{\mathrm{rad},3}$ (dotted). On the left, the internuclear distance is set to $R = 10\,\mathrm{a.u.}$, whereas on the right, it is set to $R = 20\,\mathrm{a.u.}$.

In Fig. 23 the ratio $\eta^{(2)}$ is plotted around the resonant photon energy for the three different values of Γ_{rad}. Since the value from [47] is the smallest, the peak height on resonance is the largest for $\Gamma_{\mathrm{rad},2}$, because the value is inserted in the denominator. Consequently, the peak height decreases, when inserting the larger values from Eq. (3.42), and even more so for double this value. The peak heights are denoted in Table 1.

R	$\eta^{(2)}(\Gamma_{\mathrm{rad},1})$	$\eta^{(2)}(\Gamma_{\mathrm{rad},2})$	$\eta^{(2)}(\Gamma_{\mathrm{rad},3})$
10	1.02×10^7	2.09×10^7	3.78×10^6
20	1.32×10^7	2.69×10^7	8.53×10^6

Table 1: Peak heights of the ratio $\eta^{(2)}(\omega_0, R)$ on resonance for different internuclear distances and three different values for the radiative width Γ_{rad}.

The influence of different radiative widths on the peak value of the ratio is more intense for the internuclear distance of $R = 20\,\mathrm{a.u.}$, since here, the total decay width is dominated by

the radiative width. For $R = 10\,\text{a.u.}$, however, the two-center Auger decay width contributes significantly and therefore, the difference between the radiative widths does not change the total decay width as much. Hence, unless stated otherwise, the value $\Gamma_{\text{rad},1}$, calculated in Eq. (3.42) is inserted in the following calculations. Here, the same wave functions are included as in the transition matrix elements, however, the similarity to the literature value is preserved.
Allowing for interference between the two ionisation channels, the ratio between the total cross section and the one describing the direct photoionisation pathway,

$$\eta^{(12)}(\omega, R) = \frac{\sigma^{(12)}}{\sigma^{(1)}}, \tag{3.44}$$

is plotted in Fig. 24 for the same internuclear separations as depicted in Fig. 22.

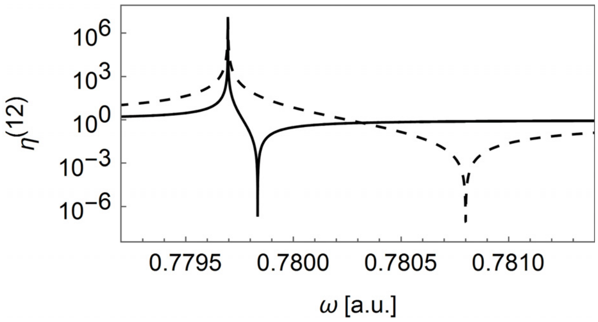

Figure 24: Ratios $\eta^{(12)}(\omega, R) = \frac{\sigma^{(12)}}{\sigma^{(1)}}$ in a LiHe system for fixed nuclei. The ratios of the cross sections are plotted against the incident photon energy ω for fixed internuclear distance $R = 10\,\text{a.u.}$ (dashed) and $R = 20\,\text{a.u.}$ (solid).

The interference of the photoionisation processes leads to a Fano profile, for which the form of cross section reads

$$\frac{\left(q^2 + \frac{\omega-\omega_0}{2\Gamma}\right)^2}{1 + \left(\frac{\omega-\omega_0}{2\Gamma}\right)^2}. \tag{3.45}$$

The characteristic parameter q describing the asymmetry of the profile is fitted to the curves enabling the comparison to those calculated including molecular effects in later sections.

	$R = 10\,\text{a.u.}$	$R = 20\,\text{a.u.}$
q	3.2×10^3	3.6×10^3

Table 2: Numerically fitted Fano parameter q for the ratios $\eta^{(12)}$ of total cross sections for fixed nuclei.

3.3.2 Effects of nuclear motion

In this section, results for the photoionisation cross sections will be given including the molecular effects described in Sec. 3.1. The influence of two neighbouring atoms leads to a potential surface depending on their separation R. These potential energy curves are considered for the three electronic states included in the direct and indirect photoionisation process. In general, the direction of the linking vector **R** with respect to the atomic orbitals can change the form of the potential energy curve. Therefore, the direction is set to $\mathbf{R} \parallel \mathbf{e}_z$, as mentioned earlier. However, for the initial and final state, the direction of R is irrelevant since both orbitals are symmetric. In order for the influence of the two atoms to be calculated as a perturbation, the assumption of a weak interaction between the two atoms has to hold true. This is the reason why a van der Waals dimer was chosen. Due to the shallow interaction potential curve, the resulting molecular binding energy is small in comparison to the indiviual atomic ionisation energies. For this setup, literature values for the van der Waals coefficients can be found for all three states of ^{7}Li^{4}He.

(I) For the initial state, $C_6 = 22.5\,\text{a.u.}$ and $C_8 = 1.06 \times 10^3\,\text{a.u.}$ are used [79].

(II) The intermediate state is described using $C_6 = 6123\,\text{a.u.}$, $C_8 = 7.85 \times 10^5\,\text{a.u.}$ and $C_{10} = 1.02 \times 10^8\,\text{a.u.}$ [135].

(III) For the ionic system of the final state, $C_6 = 0.298\,\text{a.u.}$ and $C_8 = 1.98\,\text{a.u.}$ are employed. This way, the relevant terms are obtained as in [128].

With these values, the potential energy curves are calculated as described in Sec. 3.1 and depicted in Fig. 25.

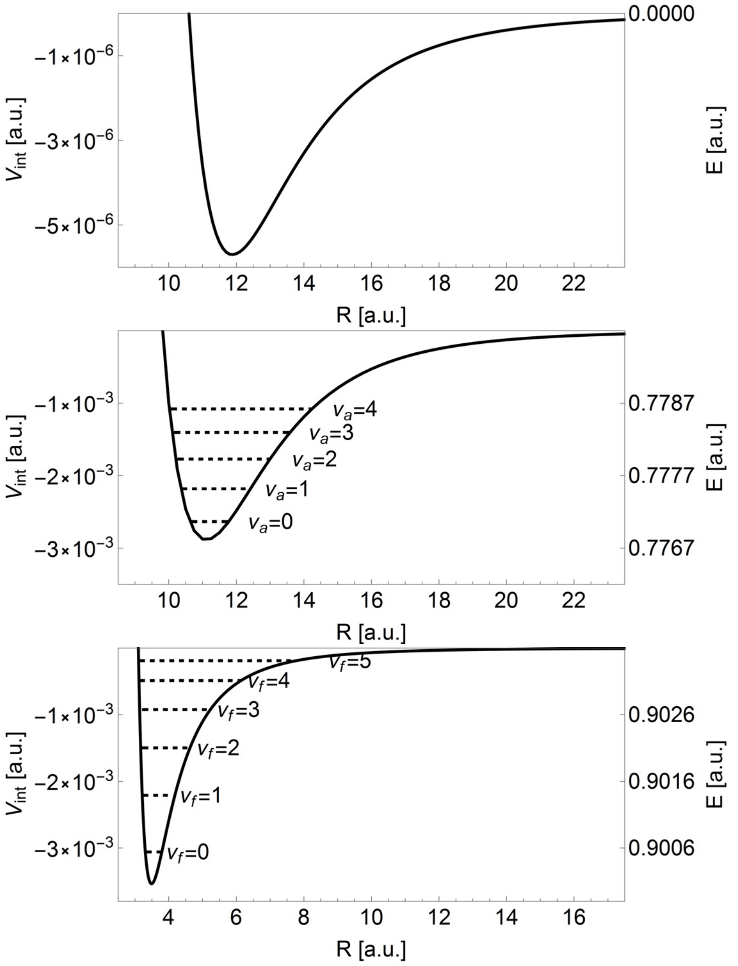

Figure 25: Calculated interaction potential curves (solid) for the electronic states considered in the two-center photoionisation process in LiHe. Several corresponding vibrational levels (dashed) are depicted. Upper panel: The initial state exhibits only one bound vibrational state with $\nu_{\mathrm{i}} = 0$. The associated binding energy is too small to be visually resolved in this plot. Middle panel: The intermediate state is depicted with the lowest lying vibrational levels. Overall, 11 vibrational levels ($0 \leq \nu_a \leq 10$) were computed to form bound molecular states, which all are included in the results of this section. Lower panel: The potential curve of the final state yields 6 bound vibrational states ($0 \leq \nu_{\mathrm{f}} \leq 5$), which are all depicted here. On the right side, the potential energy E relative to the ground state energy of the two atoms at an infinitively large internuclear distance is illustrated.

As a result of the calculations, the positions of the potential minima are similar for the initial and intermediate state ($\Phi_{g,g}$, $\Phi_{g,e}$). However, the minimum of the final state $\Phi_{\mathbf{k},g}$ is shifted to a much smaller internuclear distance R. Whereas the depths of the minimum of the intermediate and final state are comparable, the initial state exhibits a much more shallow minimum. Literature values for the potential curves can be found for the initial and final electronic state [79, 107, 128]. The data calculated here shows a good agreement (within about 10%) with the literature data. However, no literature values could be found at the time of publication [124] for the intermediate state beyond the van der Waals coefficients. The implications of the newfound literature data are shown in Sec. 3.4.

The form of the potential energy curve determines the vibrational wave functions. Due to the analytical approach to the calculation of the cross sections, the approximated vibrational wave functions can be deduced from a Morse potential, as described in Secs. 2.8.1 and 3.2, which is fitted to the potential curves. Focussing on the area on the right side of each minimum, the following parameters are obtained:

These parameters are inserted in Eq. (3.25) to yield the vibrational energy levels as well as the vibrational wave functions. Some of these vibrational levels are shown in Fig. 25. For the initial state, only one vibrational level is supported [17], with a literature binding energy of 6mK $\approx 1.9 \times 10^{-8}$ a.u.. The shallow depth of the potential leads to a vibrational wave function in Fig. 26, which is spread out to large internuclear distances. This aspect matches

	ground state	intermediate state	final state
R_{eq}	11.9	11.0	3.5
D	5.7×10^{-6}	2.9×10^{-3}	3.5×10^{-3}
α	0.43	0.44	0.80

Table 3: Fitted Morse parameters (in a.u.) for the three calculated interaction potential curves.

the characteristics of LiHe described in Sec. 2.9.3. The weak bond further justifies the choice of ^{7}Li^{4}He to be the system considered here, since the energy of the system does not differ much from the sum of the atomic energies. The dimer including the isotope ^{7}Li is chosen because the experimental detection succeeded by identifying ^{7}Li^{4}He [115]. The fact that only one vibrational state can be populated in the electronic ground state results in the advantage for the initial state to be fixed. Therefore, the vibrational level ν_{i} is always 0.

The vibrational levels of the intermediate and final state can assume a variety of values. Therefore, their corresponding vibrational wave functions are modified with respect to the vibrational level ν. With increasing vibrational excitation, the oscillations of the wave functions increase and the wave functions spreads out to larger internuclear distances.

The vibrational levels result in a shift concerning the energy of the system, and therefore the energies required for the resonance are blueshifted in comparison to the binding energies of the two individual atoms [20]. Despite the R-dependence of the interaction potential, the energy of the system no longer depends directly on the internuclear distance, but rather on the vibrational level ν. However, the vibrational levels provide information on probable positions due to the arising vibrational wave functions. For the initial state, the vibrational ground state spans over a large range of interatomic distances R, allowing for a bond length much larger than the equilibrium distance [17], where the potential curve has its minimum.

The vibrational wave functions are calculated as described in Eq. (3.26), Sec. 3.1. For all electronic states, some vibrational wave functions are illustrated in Fig. 26.

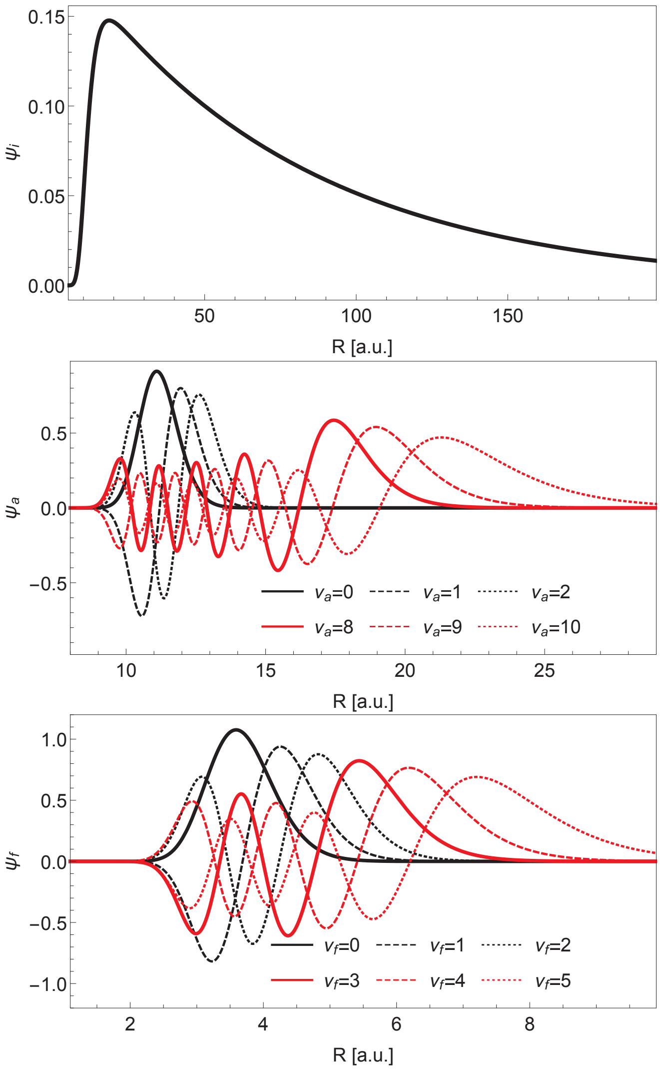

Figure 26: Plot of the vibrational wave functions for the three electronic states involved in 2CPI. Upper panel: The vibrational wave function of the ground state, $\nu_\mathrm{i} = 0$ is the only supported vibrational state. Middle panel: The wave functions for some selected vibrational levels of the intermediate state are depicted. Lower panel: The vibrational wave functions for the final state of LiHe are visualised for all bound vibrational levels.

Due to the similar positions of their respective potential minima, the vibrational wave functions for the initial and intermediate state are located at internuclear distances $R \gtrsim 8\,\mathrm{a.u.}$. Therefore, they are expected to show a significant overlap for all vibrational levels ν_a of the intermediate state. Note, however, that the vibrational wave function of the ground state is greatly spread out.

Since the minimum of the potential curve of the final state is shifted to smaller internuclear distances R, a significant overlap exists only for high vibrational levels ν_f. This observation can be supported quantitatively by calculating the Franck-Condon factors, previously described in Sec. 3.1, and defined in Eqs. (3.29), (3.30), and (3.31).

ν_f	FC_if	ν_f	FC_if	ν_f	FC_if
0	4.416×10^{-7}	2	4.596×10^{-5}	4	02.414×10^{-3}
1	5.231×10^{-6}	3	3.472×10^{-4}	5	1.637×10^{-2}

Table 4: Franck-Condon factor FC_if denoting the overlap of the vibrational wave functions for the only vibrational level $\nu_\mathrm{i} = 0$ of the initial state.

The Franck-Condon factor FC_if describes the overlap of the vibrational wave functions corresponding to the electronic initial and final state. Therefore, it is included in the calculation of the direct photoionisation cross section. The overlap increases with higher vibrational excitations since the wave functions spread out to larger internuclear distances when ν_f is augmented.

ν_a	FC_ia	ν_a	FC_ia	ν_a	FC_ia
0	1.258×10^{-1}	4	1.267×10^{-1}	8	1.852×10^{-1}
1	6.532×10^{-2}	5	1.153×10^{-1}	9	2.095×10^{-1}
2	1.151×10^{-1}	6	1.479×10^{-1}	10	2.891×10^{-1}
3	9.00×10^{-2}	7	1.485×10^{-1}		

Table 5: Franck-Condon factor FC_ia denoting the overlap of the vibrational wave functions of the initial and intermediate state. Note, that the only bound vibrational level of the initial state is $\nu_\mathrm{i} = 0$.

The Franck-Condon factor FC_ia is included in the transition from the initial to the autoionising state within the indirect photoionisation process. Since the calculation of the potential curves resulted in the two minima of the initial and autoionising state to be positioned close to each other, the overlap is quite large.

For the process of radiationless energy transfer, a multitude of vibrational combinations have to be considered, since every transition from each vibrational level of the intermediate state to each vibrational level of the final state is possible. For the sake of clarity, only two vibrational levels $\nu_\mathrm{f} = 0$ and $\nu_\mathrm{f} = 5$ are considered in order to limit the amount of values to be depicted in Table 6.

ν_a	FC_af	ν_a	FC_af	ν_a	FC_af
0	5.716×10^{-16}	4	4.976×10^{-15}	8	7.566×10^{-16}
1	-1.368×10^{-15}	5	-6.168×10^{-15}	9	-6.849×10^{-15}
2	2.434×10^{-15}	6	7.095×10^{-15}	10	5.266×10^{-15}
3	-3.680×10^{-15}	7	-7.605×10^{-15}		
ν_a	FC_af	ν_a	FC_af	ν_a	FC_af
0	2.443×10^{-5}	4	2.785×10^{-5}	8	2.166×10^{-5}
1	-2.400×10^{-5}	5	-2.729×10^{-5}	9	-1.818×10^{-5}
2	2.693×10^{-5}	6	2.612×10^{-5}	10	1.335×10^{-5}
3	-2.751×10^{-5}	7	-2.426×10^{-5}		

Table 6: Franck-Condon factors ν_af denoting the overlap of vibrational wave functions for the process of radiationless energy transfer in LiHe. Two vibrational levels of the final state $\nu_\mathrm{f} = 0$ (upper table) and $\nu_\mathrm{f} = 5$ (lower table) are considered for the sake of clarity.

The overlap of the wave functions strongly depends on the vibrational level of the final state ν_f. The potential minima of the relevant potential curves are distanced by about 7 Bohr radii. Therefore, the overlap can only be enhanced by high vibrational excitations of the final state, where the wave functions reach larger internuclear distances.

Not only the matrix elements included in the transition amplitude (see Eq. (3.8)) are modified by the vibrational wave functions in accordance with the Franck-Condon factors. The R-dependant two-center decay width has to be treated including molecular effects as well (see Eq. (3.32)). The value for fixed nuclei of the radiative width $\Gamma_\mathrm{rad}^\mathrm{He} = 6.62 \times 10^{-8}$ a.u. , calculated in Sec. 3.3.1, is adopted into this calculation, since it remains practically unaltered in the presence of the neighbouring atom. The total decay width depends on the vibrational levels of the intermediate and the final state ν_{a}, ν_{f}. Since the cross section contains the coherent sum over ν_{a} in the amplitude as well as an incoherent sum over the final states ν_{f} after integration, values for the resulting total decay widths will be presented in Table 7, where the widths are extracted from the data displayed in Fig. 27. In fact, the two-center Auger decay width depends not only on ν_{a}. Due to the inclusion of the vibrational energy shift of the final state in the energy conservation, the decay width also depends on ν_{f}, although the influence of ν_{f} is small. The extracted values depict an effective decay width for every resonant energy, which only depends on ν_{a}.

With this preparatory work, numerical results of the ratios $\eta^{(2)}(\omega) = \frac{\sigma^{(2)}(\omega)}{\sigma^{(1)}(\omega)}$ and $\eta^{(12)}(\omega) = \frac{\sigma^{(12)}(\omega)}{\sigma^{(1)}(\omega)}$ are given in Fig. 27. Here, vibrational levels $\nu_{\mathrm{a}} = 0, 1, ..., 10$ and $\nu_{\mathrm{f}} = 0, 1, .., 5$ are included. Note, that the direct ionisation cross section reads $\sigma^{(1)}(\omega_B) = 0.000037$ and is reduced in comparison to the calculation for fixed nuclei $\sigma^{(1)}(\omega_B) = 0.0024$.

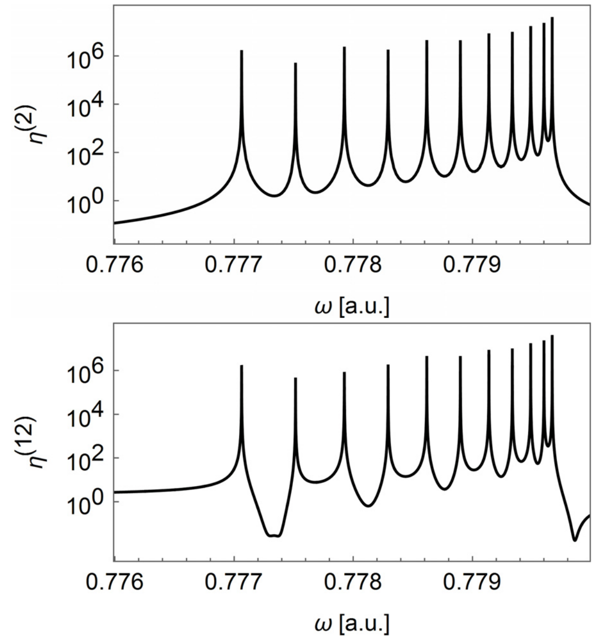

Figure 27: Ratios of cross sections in LiHe including the vibrational levels $\nu_{\mathrm{a}} \in \{0, 1, 2, .., 10\}$ and $\nu_{\mathrm{f}} \in \{0, 1, 2, 3, 4, 5\}$.
Upper panel: $\eta^{(2)}(\omega)$ depicts the ratio between the two-center and the direct ionisation processes.
Lower panel: $\eta^{(12)}(\omega)$ describes the ratio between the total two-center process, where the interference of direct and two-center photoionisation is included, and the direct ionisation mechanism.

Both ratios depicted in Fig. 27 feature a multiplet of peaks in contrast to the single peak of the two-center process depicted in Fig. 22. This fanning-out of the peaks is caused by the dependence of the resonance condition $\Delta = 0$ (see Sec. 3.1) on the vibrational level ν_{a} of the intermediate state. The energy shift caused by ν_{a} changes the particular resonant energy. The final state, however, is not included in the resonance condition and does not lead to an additional splitting. The shifts of the resonant energy increase with increasing vibrational level ν_{a}. Therefore, the peak far to the left side is associated with $\nu_{\mathrm{a}} = 0$ and ν_{a} ascending from left to right.

From the data depicted in Fig. 27, the total decay widths for every vibrational level ν_{a} is calculated and shown in Table 7.

The total decay widths are descending with increasing vibrational levels ν_{a}. Hence, the radiative decay width becomes more and more relevant for higher vibrational excitations. This can be understood when referring to the vibrational wave functions in Fig. 26. Highly excited vibrational states are spread out widely, allowing for a large internuclear distance between the two

ν_a	Γ(a.u.)	ν_a	Γ(a.u.)	ν_a	Γ(a.u.)
0	5.3×10^{-7}	4	3.8×10^{-7}	8	2.2×10^{-7}
1	5.0×10^{-7}	5	3.4×10^{-7}	9	1.8×10^{-7}
2	4.6×10^{-7}	6	3.0×10^{-7}	10	1.4×10^{-7}
3	4.2×10^{-7}	7	2.6×10^{-7}		

Table 7: Total decay widths Γ from the intermediate state in LiHe, depending on the vibrational level ν_a. The values are extracted from data depicted in Fig. 27. For fixed nuclei the decay width amounts to $\Gamma = 6.91 \times 10^{-7}$ a.u. ($\Gamma = 7.59 \times 10^{-8}$ a.u.) at $R = 10$ a.u. ($R = 20$ a.u.).

constituents. The higher the vibrational level of the intermediate state ν_a, the more outspread is the vibrational wave function, which is used for averaging over the two-center Auger decay. For highly excited vibrational states, the smaller internuclear distances do not contribute as much to the decay width as for smaller vibrational excitations. This trend of decreasing ICD widths has also been observed in HeNe dimers [18, 19].

The ratio $\eta^{(12)}$ in Fig. 27 shows the interference effects of the total cross section which includes both the one-center and the two-center photoionisation processes. Here, a sequence of Fano profiles, alternating in phase between adjacent vibrational levels ν_a and $\nu_a + 1$ is expected, in accordance to the profile depicted in Fig. 24. However, the Fano profile of each resonance is strongly modified, and therefore is weakend compared to the strongly pronounced Fano profile depicted in Fig. 24 and [16]. This modification stems from the summation over the vibrational levels ν_f of the final state. For each level ν_f, the position of the maximum peak remains the same, while the characteristics of the minimum differ. This can be supported visually by plotting the ratio $\eta^{(12)}$ for a fixed ν_a and for every ν_f individually, see Fig. 28.

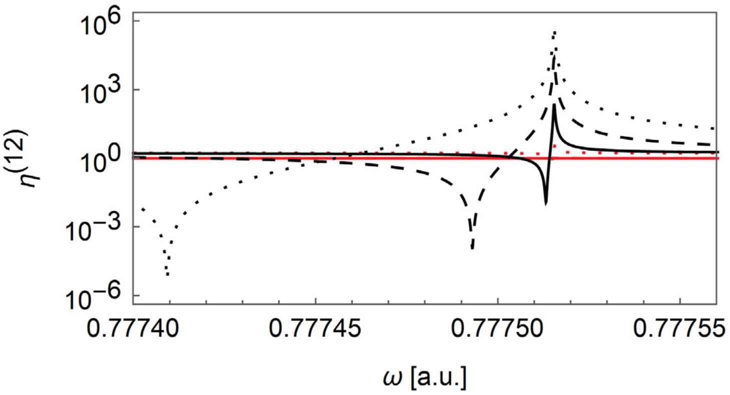

Figure 28: Ratio of cross sections in LiHe describing the interference of direct and two-center photoionisation. The vibrational level of the intermediate state is set to $\nu_a = 1$ while the vibrational level of the final state varies with $\nu_f \in \{0, 1, 2, 3, 4, 5\}$ as following: $\nu_f = 0$ (black, solid), $\nu_f = 1$ (black, dashed), $\nu_f = 2$ (black, dotted), $\nu_f = 3$ (red, solid), $\nu_f = 4$ (red, dashed), $\nu_f = 5$ (red, dotted).

It can be observed in Fig. 28 that, while the peak of the maximum remains unaltered for all vibrational levels ν_f of the final state, the position of the minimum varies significantly. Since the values are summed over all ν_f in order to calculate the complete cross section, the minima do not stay as pronounced, if visible at all. Note, that the shape of the Fano profile is inverted due to the vibrational level $\nu_\mathrm{a} = 1$.

As a result of these differences in depth and position of the minima, some Fano minima are cancelled. A pronounced minimum can be observed between the peaks of $\nu_\mathrm{a} = 0$ and $\nu_\mathrm{a} = 1$ and on the left side of the peak corresponding to $\nu_\mathrm{a} = 10$. Off resonance, the ratio drops to 1 as already seen in Fig. 24.

In Table 8, the Fano parameters q are given for the vibrational level of the intermediate $\nu_\mathrm{a} = 0$ and varying ν_f in order to further illustrate the characteristics depicted in Fig. 27. Here, increasing ν_f lead to larger values of q, enlarging the asymmetry of the Fano-profile. In Table 9, Fano parameters q are shown for varying ν_a and $\nu_\mathrm{f} = 5$, since the transition to $\nu_\mathrm{f} = 5$ yields the biggest contribution to the peak of an intermediate vibrational level, see also Fig. 28. Comparing these values to those of the calculation ignoring molecular effects in Table 2, one finds that the Fano parameters for fixed nuclei are larger, whereas the order of magnitude is comparable. Note again, that the cross sections in Fig. 27 include a coherent sum over ν_a in the transition amplitude, allowing for mixed terms, and an incoherent sum over ν_f in the cross section. Therefore, this individual consideration does not reflect the behaviour of the cross section including the summations.

ν_f	q	ν_f	q	ν_f	q
0	$\ll 1$	2	1.5×10^0	4	1.5×10^2
1	$\ll 1$	3	1.2×10^1	5	1.0×10^3

Table 8: Approximated Fano parameters q for each vibrational state ν_f for $\nu_\mathrm{a} = 0$.

ν_a	q	ν_a	q	ν_a	q
0	1.0×10^3	4	1.7×10^3	8	3.3×10^3
1	-5.6×10^2	5	-1.7×10^3	9	-3.8×10^3
2	1.2×10^3	6	2.3×10^3	10	5.0×10^3
3	1.1×10^3	7	-2.5×10^3		

Table 9: Approximated Fano parameters q for each vibrational state ν_a for $\nu_\mathrm{f} = 5$. For fixed nuclei and internuclear separations $R = 10\,\mathrm{a.u.}$ ($R = 20\,\mathrm{a.u.}$) one finds $q \approx 3.2 \times 10^3$ ($q \approx 3.6 \times 10^3$) as presented in Table 2.

Comparing the peak height in Fig. 27 to the peak heights of the calculation with fixed nuclei in Figs. 22 and 24, the orders of magnitude are similar. Since the peak heights of the ratio ranges between $\eta^{(2)} = (0.31 - 24.5) \times 10^6$ for the differential vibrational levels, they correspond to the atomic ratio for internuclear distances between $R = 5.5\,\mathrm{a.u.}$ and $R = 38.5\,\mathrm{a.u.}$. Therefore, the inclusion of molecular effects does not appear to change the magnitude of the resonant enhancement significantly. As seen in Table 7, the total widths of the peaks descrease from left to right, leading to a tendency of reaching larger maximum values.

Another relevant quantity to be studied is the approximated integral resonance strength, calculated for the atomic consideration in Sec. 3.3.1. The data concerning $\sigma^{(2)}$ for the vibrational level $\nu_\mathrm{a} = 0$ yields $\sigma^{(2)}\Gamma\big|_{\nu_a=0} \approx 1.34 \times 10^{-7}\,\mathrm{a.u.}$, whereas the relative integral resonance strength

amounts to $\eta^{(2)}\Gamma|_{\nu_\mathrm{a}=0} \approx 0.927\,\mathrm{a.u.}$, see Table 10.
The values $\eta^{(2)}\Gamma|_{\nu_\mathrm{a}}$ are calculated for every vibrational level ν_a with the widths from Table 7 and presented in Table 10.

ν_a	$\eta^{(2)}\Gamma\|_{\nu_\mathrm{a}}$	ν_a	$\eta^{(2)}\Gamma\|_{\nu_\mathrm{a}}$	ν_a	$\eta^{(2)}\Gamma\|_{\nu_\mathrm{a}}$
0	0.543	4	1.027	8	2.282
1	0.155	5	0.910	9	2.535
2	0.657	6	1.551	10	3.438
3	0.487	7	1.556		

Table 10: Approximated relative integral resonance strength $\eta^{(2)}\Gamma|_{\nu_\mathrm{a}}$ with numerically calculated peak heights and fitted peak widths from Table 7.

Summing over all these values, a total value of about $\sum \eta^{(2)}\Gamma|_{\nu_\mathrm{a}} \approx 15\,\mathrm{a.u.}$ is obtained. Note, that when multiplying the peak values with the calculated decay widths, a total value of about 11 is obtained. The values are comparable to values resulting from the atomic calculations $\sum \eta^{(2)}(\omega_B, R)\Gamma(R) \approx 7\,\mathrm{a.u.}$, when setting the internuclear distance to the equilibrium distance of the initial state $R_\mathrm{eq} = 11.9\,\mathrm{a.u.}$. Roughly speaking, the resonance height obtained when ignoring molecular effects is redistributed over the vibrational multiplet of resonance lines including the effects of nuclear motion.

In an experimental setup, the frequency of the external field is not exactly defined as is the case for the calculations performed above, but rather exhibits a width $\Delta\omega$. This can be incorporated into the calculation by employing a Gaussian distribution with $\varsigma = \frac{\Delta\omega}{2\sqrt{2\ln 2}}$. Averaging over all frequencies leads to

$$\bar{\sigma}^{(M)}(\omega) = \int d\omega' \sigma^{(M)}(\omega') \frac{1}{\sqrt{2\pi\varsigma^2}} e^{-\frac{(\omega'-\omega)^2}{2\varsigma^2}}. \tag{3.46}$$

In Fig. 29, the ratio $\bar{\eta}^{(2)}$ is depicted for a FWHM (full width at half maximum) energy width $\Delta\omega = 1.7\,\mathrm{meV}$ of the incident photon beam, which is used in [18].

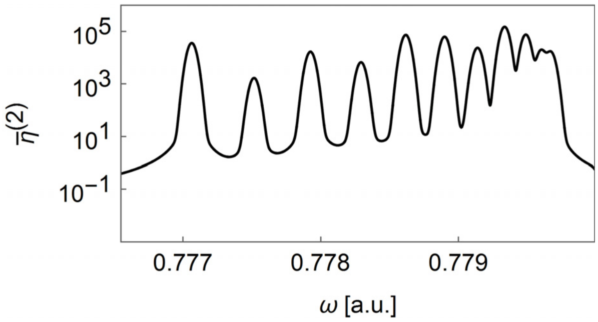

Figure 29: The ratio of the averaged cross sections $\bar{\eta}^{(2)} = \frac{\bar{\sigma}^{(2)}}{\bar{\sigma}^{(1)}}$ for the LiHe dimer.

The peaks in Fig. 29 are reduced in height due to the finite width of the field frequency. However, they are also broadened. Consequently, the integral resonance strength remains comparable to the value computed from the data shown in Fig. 27. Approximating the relative integral resonance strength again for $\nu_\mathrm{a} = 0$, the obtained value is of the same order of magnitude as above.

Before proceeding, it has to be noted that the inclusion of molecular rotations, which have been disregarded in this treatment, are expected to form an additional fine structure of the resonance lines depicted in Fig. 27. Each peak would be split into a multiplet of lines associated with the rovibrational transition from the ground to the intermediate state. Recall, that for LiHe, the ground state does not support any rotational excitations [17]. Within such a multiplet, the resulting line splitting is expected to be extremely narrow, the reason for this being that the rotational energy shifts for a fixed vibrational level are very small (see Sec. 3.2). Therefore, the experimental resolution of the substructure is expected to be challenging.

3.3.3 Analytical study of the molecular effects

The results of this section can be found in [125].

One advantage of the analytical approach lies in the capability to further analyse the expressions with respect to the direct and indirect photoionisation of atom A, developed in Sec. 3.3.2. As mentioned in Sec. 3, experimental observations of 2CPI have been made for HeNe and ArNe [18, 20]. While both investigations found a substantial amplification of photoionisation, the relative enhancement up to about 60 for HeNe [18] is much smaller than the predicted value of about 10^6 in the original proposal [16]. The decay in HeNe, which has been calculated in [18] proceeds much faster than what has been calculated for LiHe (on a timescale of hundreds of femtoseconds), which is due to the fact that the interaction potential curves for the relevant electronic states in HeNe are located at much smaller internuclear distances of around $(2-6)$ a.u. [19]. The efficiency of the decay mechanism makes the discrepency regarding the enhancement seem astonishing.

A reasonable assumption is that effects of the nuclear motion, which were not accounted for in the original prediction [16], are responsible for the differences observed, especially since ICD in HeNe and other noble-gas dimers is highly sensitive to the vibrational nuclear motion [11, 103, 136]. However, the results for LiHe in Sec. 3.3 suggest that the effects of nuclear motion do not alter the overall order of magnitude of the enhancement, see Sec. 3.3.2.

In this section, a simplified expression for the ratio of the direct and indirect photoionisation processes, including nuclear motion, will be developed and used in order to explain the differences between LiHe and HeNe, and to present the general dependance on the internuclear separation R.

In Sec. 3.1, a general expression for $\eta^{(2)}$ is presented for fixed internuclear distances R, see Eq. (3.16). On resonance, this yields:

$$\sigma_{\text{atom}}^{(2)} = \sigma_{\text{atom}}^{(1)} \frac{\Gamma_{\text{rad}}^2}{\Gamma^2} \left(\frac{3\alpha c^3}{2R^3\omega^3} \right)^2 . \tag{3.47}$$

Here, the factor α accounts for the orientation of $\mathbf{R}$ with respect to the field polarisation. By rewriting the Auger width according to

$$\Gamma_{\text{aug}}(R) = \frac{3\alpha^2}{8\pi} \frac{c^4}{\omega R^6} \Gamma_{\text{rad}} \sigma_{\text{atom}}^{(1)}, \tag{3.48}$$

the expression for the two-center ionisation cross section depicted in Eq. (3.47) can be put in the form

$$\sigma^{(2)}_{\text{atom}} = 2\sigma^{(\text{exc})}_{B} \frac{\Gamma_{\text{rad}}\Gamma_{\text{aug}}}{\Gamma^2}, \tag{3.49}$$

where $\sigma^{(\text{exc})}_{B} = 3\pi c^2/\omega^2$ is the cross section for resonant photoexcitation of atom B [35].

This way, the two-center ionisation cross section can, apart from a numerical factor, be represented as a product of two terms, namely $\sigma^{(\text{exc})}_{B}\frac{\Gamma_{\text{rad}}}{\Gamma}$ and $\frac{\Gamma_{\text{aug}}}{\Gamma}$. Here, the first term denotes the step of photoexcitation, which creates the autoionising intermediate state. Since the factor $\frac{\Gamma_{\text{rad}}}{\Gamma}$ is smaller than one, the resonant excitation of atom B is less probable in the system consisting of A and B compared to the process in an isolated atom B. This is due to a broadening of the resonance which is a consequence of the presence of an additional pathway of deexcitation. The second term depicts a branching ratio determining the probability for the intermediate state to decay via ICD and, therefore, not via radiative decay. Hence, the branching ratio increases with Γ_{aug} and approaches 1 for large values of Γ_{aug}. Consequently, the process of 2CPI is optimised when $\Gamma_{\text{aug}} \approx \Gamma_{\text{rad}}$ and decreases, when of the decay widths dominates, namely $\Gamma_{\text{aug}} \ll \Gamma_{\text{rad}}$ as well as $\Gamma_{\text{aug}} \gg \Gamma_{\text{rad}}$. The dependence of Γ_{aug} on the internuclear distance R therefore suggests a non-monotonous behaviour of 2CPI on the size of the dimer. Considering the transition amplitudes including the nuclear motion in Eqs. (3.33) and (3.34), the cross sections of both channels can be linked in the following way:

$$\left.\frac{\sigma^{(2)}_{\text{mol}}}{\sigma^{(1)}_{\text{mol}}}\right|_{\omega=\omega_{\text{res}}} \approx \left.\frac{\sigma^{(2)}_{\text{atom}}}{\sigma^{(1)}_{\text{atom}}}\right|_{R=R_{\text{eq}}} \underbrace{\left(R^3_{\text{eq}}\frac{FC_{\text{i,a}}FC_{\text{a,f}}}{FC_{\text{i,f}}}\right)^2}_{=F_{\text{nuc}}}. \tag{3.50}$$

This expression is obtained by multiplying the ratio of the atomic cross sections by the parentheses, which include the Franck-Condon overlaps. The equilibrium distance R_{eq} is inserted in the parentheses of Eq. (3.50) to make the ratio of Franck-Condon factors dimensionless, since $F_{\text{a,f}}$ includes the R-dependence of the electron-electron interaction. Note, that the ratios for LiHe calculated from an atomic point of view (see Eq. (3.47)) still depend on R. Recall, that the two-center cross section $\sigma^{(2)}_{\text{atom}}$ includes the term R^{-6}. The expression above is only valid for a given set of vibrational quantum numbers ν_{i}, ν_{a} and ν_{f}. It has to be stressed that the full calculation of the 2CPI cross sections including molecular effects requires a coherent sum over the intermediate state, including ν_{a} in the transition amplitude as well as an incoherent sum over the final states including ν_{f} of the cross sections. As already described in the previous sections, the direct and indirect pathways of photoionisation can, in general, be subject to quantum interference, since both processes lead to the same final state. For parameters, for which 2CPI dominates, the modifications of the cross section due to interference can be neglected. Note, that α accounts for the different relative orientations of the dimer with respect to the field direction. For $\mathbf{R} \parallel \mathbf{A}_0$, the value reads $\alpha = 2$, whereas in the case of $\mathbf{R} \perp \mathbf{A}_0$, $\alpha = 1$ is inserted. For definitiveness, $\alpha = 1$ is chosen.

Based on these equations, comparisons between the systems of LiHe and HeNe can be drawn. This can be realised using literature values for the quantities in Eq. (3.47). For the system of LiHe, the dipole allowed transition $1s \to 2p$ with a transition energy of $\omega = 21.2\,\text{eV}$ is considered.

As described in Sec. 3.3.1, an enhancement of about 10^6 is obtained on resonance for $R = 20\,\mathrm{a.u.}$, where the literature value for the radiative width $\Gamma_{\mathrm{rad}} = 4.35 \times 10^{-8}\,\mathrm{a.u.}$ [47] is much bigger than the two-center Auger width Γ_{aug}. Although the two-center Auger decay width is larger for $R = 5\,\mathrm{Å}$, the resulting enhancement is of the same order of magnitude for $\alpha = 1$.

As can be seen in Sec. 3.3.2, the inclusion of the nuclear motion leads to a splitting of the single resonance peak into a multiplet correlating with the various vibrational transitions [18, 124]. On each peak, the enhancement is slightly descreased by the nuclear motion. Values for the factor F_{nuc} are given in Table 11.

ν_a	F_{nuc}	ν_a	F_{nuc}	ν_a	F_{nuc}
0	0.062	4	0.082	8	0.106
1	0.016	5	0.065	9	0.096
2	0.063	6	0.099	10	0.098
3	0.041	7	0.086		

Table 11: Factors F_{nuc} for the system of LiHe for final vibrational level $\nu_{\mathrm{f}} = 5$, which provides the biggest value, and varying vibrational levels ν_{a}. The equilibrium distance of the intermediate state is $R_{\mathrm{eq}} = 11\,\mathrm{a.u.}$.

Overall, the reduction of the enhancement is of the order 0.1 for favoured vibrational transitions. Furthermore, a random distribution of dimers with respect to the electromagnetic field has to be accounted for. An averaging over all molecular orientations leads to a slight reduction in the cross section of the order of unity [137]. Note, that the resulting enhancement around 10^5 refers to the peak height of 2CPI.

For the system of HeNe, the transition to $1s2p$ is not suited, since the transition energy lies below the ionisation potential of Ne. Therefore, the transition to $1s3p$ with a corresponding energy of $\omega = 23.1\,\mathrm{eV}$ is selected, as used in [18]. Here, the radiative decay width reads $\Gamma_{\mathrm{rad}}^{(3p1s)} = 1.37 \times 10^{-8}\,\mathrm{a.u.}$ [47] and is therefore smaller than the width for the transition from $2p$. The largest enhancement in experiment was found to result from the population of the $1s \to 3p\pi$ state with the intermediate vibrational level $\nu_{\mathrm{a}} = 2$, leading to a factor of about 60-100 [18, 62]. The equilibrium distance of the intermediate state $1s \to 3p\pi$ is around $R = 5\,\mathrm{a.u.}$.

For the π-state to be populated, the molecular axis has to be perpendicular to the field orientation, making it appropriate to consider $\alpha = 1$. The Auger width Γ_{aug} can be approximated by calculating the local Auger width from Eq. (3.48) and averaging over the probability density $|\psi_{\mathrm{a}}(R, \nu_a)|^2$ of the vibrational state. This value is extracted from the data in [18, 19] by fitting a Morse potential as described in Sec. 3.1. In doing so, a value of $\Gamma_{\mathrm{aug}} \approx 1\,\mathrm{meV}$ is employed, which agrees reasonably well with the results of advanced quantum chemical calculations in [18]. Furthermore, the vibrational wave functions $\psi_{\mathrm{a}(R,\nu_{\mathrm{a}})}$ are also employed in the calculations of F_{nuc}, leading to values $F_{\mathrm{nuc}} \approx 1$ for favoured transitions. This seems reasonable, since the proximity of the minima of the interactions curves allow for transitions within a small range of internuclear distances. When setting $\alpha = 1$, the field component is orientated perpendicular to the molecular axis in order to achieve the excitation of the π-state. Since the distribution of molecular orientations is arbitrary, an averaging over all orientations leads to a factor of 2/3 at $\vartheta_R = \pi/2$, As a result, the ratio reads $\bar{\sigma}^{(2)})_{\mathrm{mol}}/\sigma_{\mathrm{mol}}^{(1)} \approx 80$, which is 3-4 orders of magnitude smaller than theoretically predicted in LiHe. This first result already shows that in this calculation, the enhancement in HeNe is significantly smaller than in LiHe since in this system, the Auger decay width is much larger when comparing it to the radiative decay width. The interplay between photoexcitation and the decay steps of 2CPI appears to be of great importance when trying to understand the counterintuitive result that the enhancement of photoionisation due to 2CPI can be weaker in more compact dimers.

As already mentioned in Sec. 3.3.2, the synchrotron beam which was applied in the experiment on HeNe [18] was not monochromatic, but rather included an incoherent superposition of frequency components with a spectral width of $\Delta\omega = 1.7\,\mathrm{meV}$. This width effectively broadens the resonance. In the case of HeNe, where both the Auger decay width and $\Delta\omega$ are much larger than the radiative decay width, the replacement $\Gamma^2 \to \Gamma_{\mathrm{aug}}(\Gamma_{\mathrm{aug}} + \Delta\omega)$ in the denominator of Eq. (3.48) can be performed. This leads to a damping of the indirect photoionisation cross section in HeNe by a factor of about $\Gamma_{\mathrm{aug}}/(\Gamma_{\mathrm{aug}} + \Delta\omega) \approx 0.37$. As a result, the ratio is reduced to $\bar{\sigma}^{(2)}_{\mathrm{mol}}/\sigma^{(1)}_{\mathrm{mol}} \approx 30$ which is to be compared with an enhancement of about 60 which was observed in experiment [18].

Note, that the decay width presented in [18] is deduced to be $2 - 2.5\,\mathrm{meV}$, and therefore larger than $1\,\mathrm{meV}$ as used in this thesis. As a consequence, the ratio is further reduced to $\bar{\sigma}^{(2)}_{\mathrm{mol}}/\sigma^{(1)}_{\mathrm{mol}} \approx 20$.

In addition to the work on 2CPI in HeNe [18], which served as a comparison, further results have been published regarding the angular distribution of emitted electrons [19]. Here, ab initio calculations including the electronic structure and nuclear dynamics were performed, also incorporating the interference with the direct ionisation channel. The approximative calculations performed in this context indicate that the spectral width may have a disadvantageous impact on the enhancement effect. This factor, however, can be avoided by the use of a coherent light source with a high degree of monochromaticity.

Note, that the information on the properties of the excited state in LiHe was extracted from the potential curve for the $2p_0$ state, which was available at that time. However, employing the calculated potential curve and equilibrium distance $R_{\mathrm{eq}} = 8.3\,\mathrm{a.u.}$ for the excitation to $2p \pm 1$ leads to estimated values of the same order of magnitude, although the contribution of individual components may vary.

3.4 Improved calculations

As mentioned previously, the results concerning the effects of the molecular characteristics on the two-center photoionisation process have been based on mostly analytical, and therefore approximative calculations of the potential curves. As discussed in Sec. 3.3.2, the interaction potential curves obtained for the electronic ground and final state agree with literature values that were available. However, no comparison was possible for the intermediate state. The publication of numerical research on ICD in the dimer LiHe within the process of the present thesis work has provided reference values in terms of this interaction potential [102, 117].

3.4.1 Potential curves

Potential surfaces for the two configurations $2p\Sigma$ and $2p\Pi$ as well as for the final electronic state, comprising the ionised lithium atom and the helium atom in its electronic ground state, were calculated numerically by employing finite basis functions. For the process of photoionisation considered here, where $\mathbf{R}$ is set along the quantisation axis of the electromagnetic field, the excitation to $2p\Sigma$ corresponds to the excitation to $2p_0$. The data from [102] is plotted in Fig. 30.

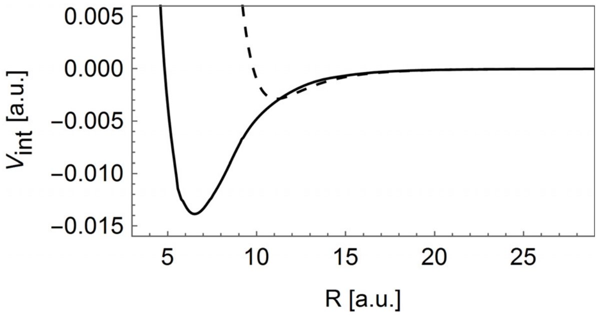

Figure 30: The interaction potential of the $2p_0$ state of helium in the LiHe dimer, when the interatomic linking vector $\mathbf{R}$ is set along $\mathbf{z}$. Literature values from [102] (black, solid) are compared with the values calculated in Sec. 3.3 (black, dashed).

In Fig. 31, potential curves of the final state are plotted, including literature values from [128] and [117] as well as the results of the calculations from Sec. 3.3.

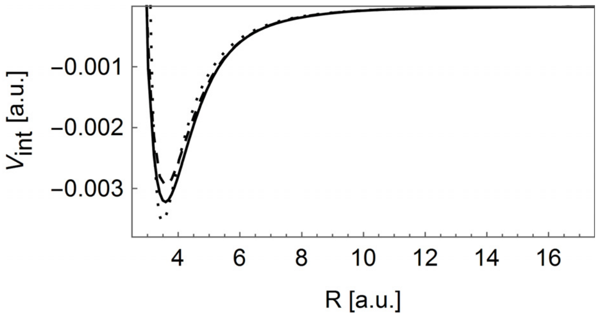

Figure 31: Potential surfaces for the final electronic state of LiHe dimer, where the $2s$ electron in lithium is ejected to the continuum. Literature values from [117] (black, solid) and [128] (black, dashed), as well as the calculated values from Sec. 3.3.2 (black, dotted) are depicted.

The comparison of the two potential curves for the excited state in Fig. 30 shows a drastic difference both in the position of the minimum as well as the potential depth. The results of the sophisticated numerical approach concerning the calculation of the potential surface illustrates the limits of the analytical calculation employing one-electron wave functions with respect to the electronically excited state. The consequences of a modified potential curve therefore have to be analysed in order to obtain an improved insight into the effects of the molecular characteristics of the system as well as the photoionisation process.

The comparison of the potential curves for the final electronic state, however, confirms the fundamental characteristics, which have been calculated in Sec. 3.3. Therefore, the analytical calculations regarding the initial and final states can provide adequate values for the interaction in the dimer. This has also been observed for the initial state, which is not included in [102, 117], but showed a good agreement with literature values, see Sec. 3.3.2.

The new data on the excited state also include predictions concerning the amount of vibrational levels ν_a. For the configuration depicted in Fig. 31, 20 bound vibrational levels are found [117]. This represents an enormous extension in comparison to the 11 levels employed in Sec. 3.3.2. As in the calculations in Sec. 3.3, the vibrational energy shifts and wave functions will be computed from a Morse potential, which is fitted to the data of the interaction curve. While the calculation of the interaction curve presented in Sec. 3.3.2 for the ionic state of LiHe yields results comparable to the curves from literature, only 6 vibrational levels ν_f were included, as proposed in [107]. However, 8 bound vibrational levels are predicted in both [128] and [117].

In [128], also the vibrational energy shifts are provided for the respective potential curve. In the following, this reference is used in order to improve the fit for the vibrational levels and wave functions. Therefore, the literature values for the potential curve from [128] are employed. The fitting of the Morse potential to the potential curve cannot give satisfying energy shifts for all vibrational levels when using one parameter α in Eq. (2.66). As a consequence, the vibrational levels and wave functions are described by an individual fit parameter $\alpha(\nu_\mathrm{f})$ for each level. The Morse potential with fixed minimum depth D and equilibrium distance R_eq is fitted for each vibrational level ν_f in order to provide energy shifts matching the ones given in [128].

No values for the vibrational energy shifts are provided for the electronically excited state. It is possible to achieve a Morse potential curve with a good fit to the potential curve. However, the resulting parameter gives rise to more than 20 bound vibrational levels. When enforcing the amount of bound vibrational levels to the literature value of 20, a small range of parameters $0.555 < \alpha < 0.58$ is possible.

When analysing the fit parameter for the last vibrational level of the final state, the vibrational energy shift of the literature values [128] is best achieved for the largest parameter α possible. Therefore, and due to the lack of literature values for the intermediate state, the largest possible fit parameter is chosen.

The fitting parameters are presented in Table 12.

Configuration	D	R	α			
Li$(1s^2 2s)$He$(1s2p_0)$	0.01386	6.52	0.464 0.58			
Li$^+(1s^2)$He$(1s^2)$	0.00296	3.59	$\alpha(0) = 1.13$	$\alpha(1) = 1.08$	$\alpha(2) = 1.02$	$\alpha(3) = 0.98$
			$\alpha(4) = 0.92$	$\alpha(5) = 0.85$	$\alpha(6) = 0.76$	$\alpha(7) = 0.69$

Table 12: Parameters for the Morse potential fitted to the interaction potential curves for the intermediate [102, 117] and final state [128]. For the intermediate state, the upper value for the fitting parameter α corresponds to the Morse curve which overlaps the potential curve from [102] and the lower value yields the right amount of bound vibrational levels. All values are in atomic units.

As can be seen in Table 12, the Morse parameter α, which determines the width of the Morse potential, decreases significantly for the final state with increasing vibrational level ν_f. This explains why the Morse fit in Table 3 cannot provide 8 vibrational levels. Furthermore, the equilibrium distance of the intermediate state is shifted to a much smaller internuclear distance R. This shift has implications on the vibrationally resolved decay rate, since the vibrational wave function for the intermediate state now favours smaller separations R.

3.4.2 Decay widths and overlaps

In order to assess the changes with respect to the values obtained in Sec. 3.3.2, the total decay widths $\Gamma = \Gamma_\mathrm{rad} + 2\Gamma_\mathrm{aug}$ are presented in Tables 13 and 14. In contrast to the data depicted in Table 7, the widths here are calculated directly and not read out from the cross section data. The vibrational level of the final state is fixed. However, the influence of ν_f on the two-center Auger width is marginal ($< 1\%$) and limited to the momentum of the ejected electron, defined by the energy conservation. As explained in Sec. 3.2.3, the calculation of the two-center Auger width via Eq. 3.32, which no longer depends on R, is an approximation. Particularly, it does not include the wave functions of the final state. The inclusion would lead to the following dependencies in the absolute square of the transition amplitude

$$\int dt \int dt' \, \langle \psi_\mathrm{a} \left| \mathcal{V}_{AB}(\mathbf{k}, \mathbf{R})^* \right| \psi_\mathrm{f} \rangle \, \langle \psi_\mathrm{f} \left| \mathcal{V}_{AB}(\mathbf{k}, \mathbf{R}) \right| \psi_\mathrm{a} \rangle \, e^{-iEt} e^{iEt'}, \tag{3.51}$$

which has to be summed over all final states of the nuclear motion. When ignoring the dependency of the energy E on the final state, a completeness relation regarding the wave functions ψ_f becomes apparent, which reduces the expression to the approximated calculation in Eq. 3.32. The numerical evaluation of the more complex calculation, summing over all bound final states for a fixed vibrational level ν_a, yields similar values as obtained when calculating the Auger width according to Eq. 3.32 for small vibrational levels of the intermediate states. Consequently, the approximation by averaging over the vibrational wave function of the intermediate state represents a reasonable simplification. Above all, the approximation should, in general, include all possible final states, and therefore mark a form of an upper barrier, disregarding the error made by neglecting the dependency of the energies in the exponent.

Note, that the radiative decay width $\Gamma_\mathrm{rad} = 6.62 \times 10^{-8}$ a.u. remains unaltered.

While the parameter $\alpha = 0.464$ for the intermediate state yields too many bound vibrational levels, a comparison between the two parameters for the intermediate state is presented in order to illustrate the strong dependence of the results on the fitting procedure.

Note, that the decay widths are calculated for $\nu_\mathrm{f} = 7$, for which the decay width is maximised. The two-center decay width depends only marginally on the vibrational level of the final state and only on the induced energy shift.

ν_a	Γ	ν_a	Γ	ν_a	Γ	ν_a	Γ
0	8.48×10^{-6}	5	6.98×10^{-6}	10	5.29×10^{-6}	15	3.49×10^{-6}
1	8.19×10^{-6}	6	6.66×10^{-6}	11	4.94×10^{-6}	16	3.11×10^{-6}
2	7.91×10^{-6}	7	6.33×10^{-6}	12	4.59×10^{-6}	17	2.74×10^{-6}
3	7.61×10^{-6}	8	5.99×10^{-6}	13	4.22×10^{-6}	18	2.36×10^{-6}
4	7.29×10^{-6}	9	5.65×10^{-6}	14	3.86×10^{-6}	19	1.98×10^{-6}

Table 13: Total decay widths Γ for every bound vibrational level ν_a of the intermediate state and $\nu_\mathrm{f} = 7$. Values are in atomic units and $\alpha = 0.464$ (for the intermediate state).

ν_a	Γ	ν_a	Γ	ν_a	Γ	ν_a	Γ
0	8.40×10^{-6}	5	6.20×10^{-6}	10	4.02×10^{-6}	15	1.86×10^{-6}
1	7.96×10^{-6}	6	5.76×10^{-6}	11	3.59×10^{-6}	16	1.42×10^{-6}
2	7.52×10^{-6}	7	5.33×10^{-6}	12	3.16×10^{-6}	17	9.86×10^{-7}
3	7.08×10^{-6}	8	4.89×10^{-6}	13	2.72×10^{-6}	18	5.45×10^{-7}
4	6.64×10^{-6}	9	4.46×10^{-6}	14	2.29×10^{-6}	19	9.38×10^{-8}

Table 14: Total decay widths Γ for every bound vibrational level ν_a of the intermediate state and $\nu_\mathrm{f} = 7$. Values are in atomic units and the parameter for the intermediate state is $\alpha = 0.58$.

Comparing these values to those in Table 7, the ones obtained in this section are considerably larger. As in Table 7, the decay width decreases for increasing vibrational levels ν_a. While the decay widths are smaller than those for HeNe in [18], they are increased by more than one order of magnitude. Note, that the widths in Table 7 are larger than the calculated value for the biggest contribution coming from $\nu_\mathrm{f} = 5$. This is because the peak in the cross section corresponding to a vibrational level of the intermediate state ν_a comprises the sum over the all vibrational levels ν_f of the final state and the values for Γ in Table 7 are extracted from the numerical data for the cross section.

When comparing the values in Tables 13 and 14 to each other, the values are similar for mostly all vibrational levels. For the highest three levels however, the decay width is decreased significantly for the parameter $\alpha = 0.58$.

In Sec. 3.3.2, the influence of the value for the radiative width on the ratio of the photoionisation cross sections, and therefore on the two-center cross section, was discussed. Regarding the total decay widths depicted in the tables above, for most of the transitions considered, the radiative decay width does not contribute significantly, in contrast to the two-center Auger decay width. Therefore, the choice of the value for Γ_rad has even less relevant implications than before.

The shift of the minimum of the potential curve of the intermediate state in the process of two-center photoionisation also impacts the overlaps of the vibrational wave functions within a vibrational transition. As a consequence, the Franck-Condon factors are modified, leading to the values presented in the Tables below. The overlap corresponding to the direct photoionisation is given in Table 15. Here, the intermediate state is not involved and therefore, there is no change due to the two different fitting parameters α.

ν_f	FC_if	ν_f	FC_if	ν_f	FC_if	ν_f	FC_if
0	5.36×10^{-7}	2	1.47×10^{-4}	4	1.64×10^{-2}	6	3.59×10^{-1}
1	1.04×10^{-5}	3	1.77×10^{-3}	5	9.58×10^{-2}	7	9.92×10^{-1}

Table 15: Franck-Condon factors FC_if denoting the overlap of vibrational wave functions for the direct process of photoionisation. The only bound vibrational level of the ground state is $\nu_\mathrm{i} = 0$.

While the values for the first 6 vibrational levels are comparable to those in Table 4, the additional two bound vibrational levels lead to large overlaps. This data shows the importance of including all possible bound vibrational levels for a transition, since this overlap strongly influences the value of the one-center process.

Considering the indirect process, two overlaps have to be considered. First, the values for the process of photoexcitation are given in Tables 16 and 17.

ν_a	FC_ia	ν_a	FC_ia	ν_a	FC_ia	ν_a	FC_ia
0	1.67×10^{-3}	5	1.10×10^{-2}	10	3.33×10^{-2}	15	7.44×10^{-2}
1	2.69×10^{-3}	6	1.42×10^{-2}	11	3.98×10^{-2}	16	8.56×10^{-2}
2	4.21×10^{-3}	7	1.80×10^{-2}	12	4.71×10^{-2}	17	9.83×10^{-2}
3	6.00×10^{-3}	8	2.25×10^{-2}	13	5.53×10^{-2}	18	1.13×10^{-1}
4	6.28×10^{-3}	9	2.75×10^{-2}	14	6.43×10^{-2}	19	1.30×10^{-1}

Table 16: Franck-Condon factors FC_ia denoting the overlap of vibrational wave functions for the process of photoexcitation in LiHe. The only bound vibrational level of the ground state is $\nu_\mathrm{i} = 0$, and $\alpha = 0.464$ is the fitting parameter for the intermediate state.

ν_a	FC_ia	ν_a	FC_ia	ν_a	FC_ia	ν_a	FC_ia
0	1.49×10^{-3}	5	1.01×10^{-2}	10	3.68×10^{-2}	15	1.11×10^{-1}
1	2.29×10^{-3}	6	1.34×10^{-2}	11	4.62×10^{-2}	16	1.40×10^{-1}
2	3.64×10^{-3}	7	1.76×10^{-2}	12	5.76×10^{-2}	17	1.83×10^{-1}
3	5.24×10^{-3}	8	2.28×10^{-2}	13	7.16×10^{-2}	18	2.65×10^{-1}
4	7.39×10^{-3}	9	2.91×10^{-2}	14	8.88×10^{-2}	19	8.28×10^{-1}

Table 17: Franck-Condon factors FC_ia denoting the overlap of vibrational wave functions for the process of photoexcitation in LiHe. The only bound vibrational level of the ground state is $\nu_\mathrm{i} = 0$ and $\alpha = 0.58$ is the fitting parameter for the intermediate state.

When comparing these values in Table 16 with those in Table 5, the overlaps are reduced by about one to two orders of magnitude. This modification is reasonable, since the potential minimum of the intermediate state is shifted to smaller internuclear distances, and therefore further away from the potential minimum of the ground state. Consequently, the overlap of the vibrational wave functions is reduced for lower vibrational levels ν_a. The Franck-Condon factors in Table 16, however, are more similar to those in Table 5 for higher vibrational levels. The larger fitting parameter α leads to the higher vibrational levels to feature smaller binding energies and therefore a larger spreading of the wave functions. Thus, a larger overlap can be achieved.

The displayal of the Franck-Condon factors associated to the radiationless energy transfer would require more than 100 entries. Therefore, exemplary values are presented in Table 18 for $\nu_\mathrm{f} = 0$ and $\nu_\mathrm{f} = 7$.

ν_a	FC_af	ν_a	FC_af	ν_a	FC_{af}	ν_a	FC_af
0	2.42×10^{-6}	5	-1.81×10^{-5}	10	3.58×10^{-5}	15	-4.44×10^{-5}
1	-4.82×10^{-6}	6	2.19×10^{-5}	11	-3.85×10^{-5}	16	4.44×10^{-5}
2	7.67×10^{-6}	7	-2.56×10^{-5}	12	4.08×10^{-5}	17	-4.36×10^{-5}
3	-1.09×10^{-5}	8	2.93×10^{-5}	13	-4.26×10^{-5}	18	4.21×10^{-5}
4	1.44×10^{-5}	9	3.27×10^{-5}	14	4.38×10^{-5}	19	-3.97×10^{-5}
ν_a	FC_af	ν_a	FC_af	ν_a	FC_af	ν_a	FC_af
0	9.96×10^{-5}	5	5.11×10^{-6}	10	4.31×10^{-6}	15	3.62×10^{-5}
1	4.89×10^{-5}	6	-8.52×10^{-5}	11	3.22×10^{-5}	16	5.62×10^{-5}
2	-1.10×10^{-5}	7	1.27×10^{-5}	12	3.31×10^{-5}	17	3.33×10^{-5}
3	1.24×10^{-5}	8	-2.68×10^{-5}	13	3.63×10^{-5}	18	5.55×10^{-5}
4	-1.24×10^{-5}	9	2.37×10^{-5}	14	4.96×10^{-5}	19	2.90×10^{-5}

Table 18: Franck-Condon factors F_af denoting the overlap of vibrational wave functions for the process of radiationless energy transfer in LiHe. Two vibrational levels of the final state $\nu_\mathrm{f} = 0$ (upper table) and $\nu_\mathrm{f} = 7$ (lower table) are considered for the sake of clarity. The fitting parameter for the intermediate state is set to $\alpha = 0.464$.

ν_a	FC_af	ν_a	FC_af	ν_a	FC_af	ν_a	FC_af
0	1.57×10^{-6}	5	-8.02×10^{-6}	10	1.23×10^{-5}	15	-1.10×10^{-5}
1	-2.80×10^{-6}	6	9.19×10^{-6}	11	-1.26×10^{-5}	16	9.86×10^{-6}
2	4.10×10^{-6}	7	-1.02×10^{-5}	12	1.26×10^{-5}	17	-8.26×10^{-6}
3	-5.43×10^{-6}	8	1.11×10^{-5}	13	-1.24×10^{-5}	18	5.99×10^{-6}
4	6.76×10^{-6}	9	-1.18×10^{-5}	14	1.19×10^{-5}	19	-1.41×10^{-6}
ν_a	FC_af	ν_a	FC_af	ν_a	FC_af	ν_a	FC_af
0	1.08×10^{-4}	5	-2.02×10^{-6}	10	-1.20×10^{-5}	15	6.91×10^{-5}
1	4.24×10^{-5}	6	-9.28×10^{-5}	11	5.87×10^{-5}	16	4.14×10^{-5}
2	-8.01×10^{-5}	7	-5.21×10^{-5}	12	1.82×10^{-5}	17	6.03×10^{-5}
3	2.55×10^{-6}	8	3.91×10^{-5}	13	6.89×10^{-5}	18	3.93×10^{-5}
4	-1.14×10^{-4}	9	3.91×10^{-5}	14	3.55×10^{-5}	19	3.04×10^{-5}

Table 19: Franck-Condon factors F_af denoting the overlap of vibrational wave functions for the process of radiationless energy transfer in LiHe. As before, two vibrational levels of the final state $\nu_\mathrm{f} = 0$ (upper table) and $\nu_\mathrm{f} = 7$ (lower table) are considered. The fitting parameter for the intermediate state is set to $\alpha = 0.58$.

When comparing these overlaps to the ones in Table 6, the values depicted in Table 18 are larger for small vibrational levels ν_f.

While for the considerations in Sec. 3.3.2, the Franck-Condon factors increase for increasing ν_{f}, this is not the case here. Since the distance between the two potential minima is not as large as in Sec. 3.3.2, a significant overlap is not restricted to the highest vibrational level.
As consequence, the maximum value is not obtained for $\nu_{\mathrm{f}} = 7$ but for $\nu_{\mathrm{f}} = 2$, $\nu_{\mathrm{f}} = 3$ and $\nu_{\mathrm{f}} = 4$. Both sets of Franck-Condon factors for $\nu_{\mathrm{f}} = 0$ are similar for the two fit parameters α. However, the overlaps for $\nu_{\mathrm{f}} = 7$ oscillate for the fit with $\alpha = 0.58$. While the two parameters for the Morse fit of the intermediate potential curve do not yield decay widths and Franck-Condon factors, which differ by several orders of magnitude, differences are observable. The consequences are now considered with respect to the photoionisation cross sections.

3.4.3 Cross sections

The new characteristics of the vibrational motion also lead to modified cross sections of the one- and two-center photoionisation. As before, the cross section of the direct ionisation process depends smoothly on the photon energy and comprises the incoherent sum over ν_{f}. Note, that the inclusion of the two highest vibrational states due to the modified fitting parameters lead to an enlargement of the direct ionisation cross section. Especially, the Franck Condon factor for $\nu_{\mathrm{f}} = 7$ provides a strong contribution to the cross section. As a consequence, the single-center cross section $\sigma^{(1)}(\omega_B) = 0.0027$ is large compared to the result from the calculations executed in Sec. 3.3.2 and comparable to the value for fixed nuclei. However, the value for the single-center cross section is comparable to the one obtained from the calculation assuming fixed nuclei. This amplification will also influence the ratio of photoionisation cross sections, depicted in Fig. 27.
For the indirect ionisation process, the multiplet of peaks, seen in Sec. 3.3.2, is expected to fan out even more, since 20 vibrational levels are now considered for the intermediate state. Due to the modified potential curve and associated vibrational energy shifts, the resonant energies are also changed slightly. This is also true for the two fit parameters $\alpha = 0.464$ and $\alpha = 0.58$.

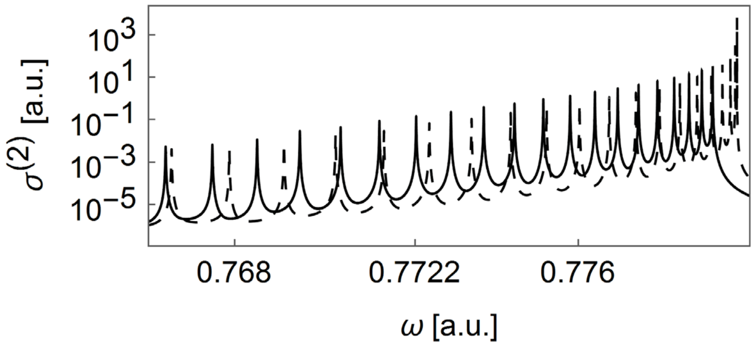

Figure 32: Cross section for the indirect photoionisation of lithium in the LiHe dimer with respect to the photon energy ω. The two different fit parameters α are accounted for by the solid curve ($\alpha = 0.464$) and the dashed curve ($\alpha = 0.58$), respectively.

In Fig. 32, the two-center photoionisation cross sections feature 20 peaks for the resonant energies of the photon ω. Particularly noticeable is the fact that the distance between the peaks reduces for the increasement of the vibrational excitation. This is in accordance with the characteristics of the vibrational energy shift, as explained in Sec. 3.1. Furthermore, the decay widths decrease from left to right, whereas the peak heights increase. Consequently, the contribution to the total photoionisation is enlarged for higher vibrational excitations of the intermediate electronic state in LiHe. When comparing the curves for the two fit parameters of the intermediate state, the peaks are shifted to lower resonant energies ω for $\alpha = 0.464$ in contrast to the peak of the same vibrational level for $\alpha = 0.58$. This can be explained by the fact that for $\alpha = 0.464$, more than 20 bound vibrational levels could fit in the potential curve and therefore, $\nu_{\mathrm{a}} = 19$ does not denote the last bound vibrational state. Consequently, all levels are shifted down with respect to the 'steeper' Morse fit. A tremendous difference between the two curves can be observed for the peak corresponding to the last bound vibrational level of the intermediate state. Here, the last peak for $\alpha = 0.58$ is strongly enhanced compared to the neighbouring peaks as well as to the last peak for $\alpha = 0.464$. Since the last bound vibrational state is bound much more shallow for $\alpha = 0.58$ than $\alpha = 0.464$, the significance of transitions including this vibrational level is enlarged. Note, that the calculation of the cross section for $\alpha = 0.464$ does not include all possible vibrational levels, which were calculated for the intermediate state. Therefore, the peak for ν_{a} does not represent the transition to the largest vibrational excitation.

The consideration of the ratio between the indirect and direct photoionisation cross section leads to the plot in Fig. 33.

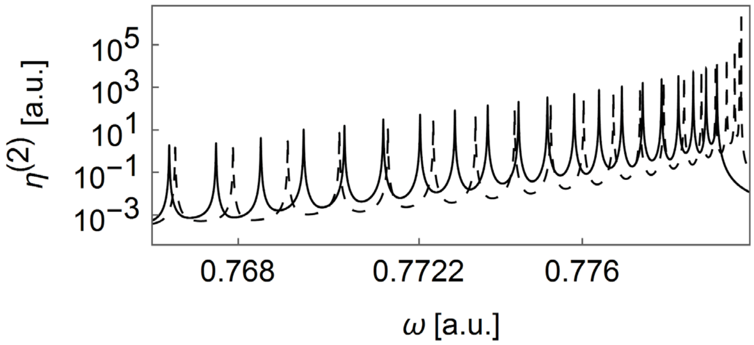

Figure 33: Ratio of the cross sections for the indirect and direct photoionisation of lithium in the LiHe dimer with respect to the photon energy ω. The two different fit parameters α are accounted for by the solid curve ($\alpha = 0.464$) and the dashed curve ($\alpha = 0.58$), respectively.

The ratios depicted in Fig. 33 feature peak values, which are strongly reduced compared to those obtained in Sec. 3.3.2. This is mainly due to the increased direct photoionisation cross section, which reduces the significance of the indirect process. In particular, for low vibrational excitations of the intermediate state, the two-center photoionisation cross section is small or similar compared to the direct mechanism for this photon energy. The ratio generally increases for a larger photon energy. As already observed in Fig. 32, the behaviour for the highly excited vibrational states strongly differs for the two diverse fit parameters. Again, the resonant energies are shifted as described for Fig. 32. Furthermore, the last vibrational level is enhanced tremendously due to the shallow bound. Whereas in Sec. 3.3.2, amplifications of $10^6 - 10^7$ were obtained for each individual peak, the highest amplification here is reached with a ratio $\eta^{(2)} \approx 1.19 \times 10^5$ for $\nu_{\mathrm{a}} = 19$ and $\alpha = 0.464$, as well as $\eta^{(2)} \approx 2.38 \times 10^6$ for $\nu_{\mathrm{a}} = 19$ and $\alpha = 0.58$. For the vibrational ground state with $\nu_{\mathrm{a}} = 0$ however, values of only $\eta^{(2)} \approx 1.89$

for $\alpha = 0.464$ and $\eta^{(2)} \approx 1.43$ for $\alpha = 0.58$ are obtained. Although the corresponding decay widths are substantially larger, the approximation for the relative integral resonance strength is still reduced. Summing over all 20 ν_{a} and multiplying the ratio by the calculated decay rate $\Gamma = \Gamma_{\mathrm{rad}} + 2\bar{\Gamma}_{\mathrm{aug}}$ yields $\eta^{(2)}\Gamma = 0.069$ a.u. for $\alpha = 0.464$ and $\eta^{(2)}\Gamma = 0.378$ a.u. for $\alpha = 0.58$. This consideration leads to the conclusion that the molecular motion does reduce the strength of the efficience of the two-center photoionisation pathway. To further analyse the differences between the previous calculations from Sec. 3.3.2 and the ones presented here, the integral resonance strength is calculated for individual peaks, see Table 20.

potential curve	ν_{a}	$\eta^{(2)}\Gamma$	ν_{a}	$\eta^{(2)}\Gamma$	ν_{a}	$\eta^{(2)}\Gamma$
from Sec. 3.3.2	0	5.43×10^{-1}	5	9.10×10^{-1}	10	3.44×10^{0}
from [102], $\alpha = 0.464$	0	1.61×10^{-5}	10	1.77×10^{-3}	19	2.37×10^{-2}
from [102], $\alpha = 0.58$	0	1.20×10^{-5}	10	1.64×10^{-3}	19	2.22×10^{-1}

Table 20: Approximated relative integral resonance strengths for individual peaks. Values are presented for the potential curves calculated in Sec. 3.3.2, see also Table 10 as well as the literature values, including the two fitting parameters of the intermediate state, $\alpha = 0.464$ and $\alpha = 0.58$.

For the calculated potential curve, the values are generally larger, leading to a summed relative integral resonance strength similar to the one for the consideration assuming fixed nuclei. All values increase for larger vibrational levels of the intermediate state. The two different fitting parameters α yield similar results for small vibrational levels. However, the last bound vibrational level leads to significantly different values. This goes along with the different behaviour of the two-center cross sections and rations, depicted in Figs. 32 and 33, where the peak heights strongly diverge for large vibrational excitations.

In general, the inclusion of the new literature data into the numerical calculations does not change the qualitative behaviour of the photoionisation cross sections, but strongly modifies the quantitative results. The decay width of the metastable intermediate state is strongly enlarged, leading to values which are more comparable to those referenced for the system of HeNe. The increased decay width as well as the enhancement of the direct photoionisation result in the reduction of the effectiveness of the indirect ionisation mechanism regarding the total photoionisation.

The comparison with respect to the fit parameter α shows the strong influence of the Morse parameters with respect to both ionisation processes, including the two-center Auger decay width as well as the resonance energies. Both are highly sensible to the fitting mechanism and therefore, a slight change can lead to drastically different results.

The calculations employing the literature values for the potential curves lead to a reduction of the ratio of the indirect and direct photoionisation cross section, particularly with respect to the integral resonance strength. While the equilibrium distance of the electronic ground state is at 11.9 a.u. and leads to large amplifications in the ratio of the cross sections as well as the integral resonance strength, this value for R cannot account for the widespread wave functions of the heteroatomic dimer. However, an amplification of $\eta^{(2)} = 2 \times 10^{6}$ can be obtained when inserting $R = 28$ a.u., which is similar to the value obtained for $\nu_{\mathrm{a}} = 19$ and $\alpha = 0.58$. For other vibrational levels, the internuclear distance would have to increase even further. Regarding the integral resonance strength, the consideration assuming fixed nuclei can yield a value of $\eta^{(2)}\Gamma \approx 0.38$ for $R = 24\,\text{a.u.}$ which is similar to the value obtained for $\alpha = 0.58$ within the calculation including molecular effects. Note that the bond length of the ground state in LiHe is predicted to be 55 a.u.. Consequently, the calculation assuming fixed nuclei overestimates the efficiency of the two-center ionisation pathway for internuclear distances around the equilibirum distances with respect to the inclusion of molecular effects. However, similar values can be obtained when incorporating larger internuclear distances.

In all previous investigations presented here, transitions to bound states are considered. However, ionisation can also lead to the dissociation of the dimer. The break-up of the molecular bound allows for an additional spectrum of energies of the final state. Therefore, the process is no longer restricted to the summation over the vibrational levels, but requires the inclusion of the dissociative energies. In [117], the dissociative states are included in the description of ICD in LiHe. Here, the dissociative states are found to be dominating with respect to the efficience of the decay process. The inclusion of dissociative states can influence the two-center Auger width, when calculating the value by including both wave functions of the intermediate and the final state, as explained in Sec. 3.4.2. Within this description, the argument of the completeness relation requries the inclusion of all final states, which also means dissociative states. When averaging over the vibrational wave function of the intermediate state, the contributions should already be included since the completeness relation is used, implying the summation over all possible final states.

A preliminary investigation of the dissociative states regarding the decay width as well as the ionisation cross section provides interesting estimates, suggesting an important contribution. The direct ionisation cross section including the effects of nuclear motion is enlarged by one order of magnitude when considering dissociative final states. Their effect on the two-center photoionisation cross section strongly increases for larger vibrational levels of the intermediate state, leading to contributions of the same order of magnitude as for the transition to bound final states. The same behaviour is true regarding the two-center Auger decay width, where the inclusion of the dissociative states results in values approaching the ones calculated by averaging over the vibrational wave functions of the intermediate state.

However, the inclusion of the dissociative states does not show a modification of the qualitative physical effects presented in this section. A complete consideration of the dissociative states would have been beyond the scope of this thesis, though. This motivates a more detailed study regarding the relevance to both the internuclear decay as well as to the two-center ionisation cross section in comparison to the bound final states.

3.5 Summary

In this section, resonant two-center photoionisation has been studied in a weakly bound system consisting of two atoms A and B. Initially, the theory assuming spatially fixed nuclei, originally proposed in 2010 [16], was recapitulated, yielding a 'local' cross section of 2CPI. Applying the theory to a system consisting of lithium (A) and helium (B), where the autoionising state is produced via photoexctation in helium, the two-center cross section strongly depends on the internuclear distance $\mathbf{R}$ and exhibits a single peak for a resonant incident photon energy matching the transition energy in helium. For photon energies near resonance, the indirect ionisation channel strongly dominates the photoionisation of lithium. The total cross section, comprising both pathways of direct and indirect photoionisation, yields a pronounced Fano profile, which visualises the interference between the two ionisation channels.

Next, the interaction between the two atoms is considered. This consideration includes the interaction potential surface, the resulting vibrational wave functions with the respective vibrational energy levels, as well as the Franck-Condon factors, which are employed in the transition matrix elements. Treating the system as a molecule instead of two individual atoms, the dependency on the internuclear distance is incorporated 'globally' by the vibrational states of the nuclear motion. The inclusion of vibrational transitions requires a summation over the vibrational states both coherently in the transition amplitude as well as incoherently in the cross section. As a result, the 2CPI cross section fans out to create a multiplet of peaks for resonance energies, which depend not only on the electron energy, but also on the vibrational level of the intermediate state ν_{a}. For the $^7\mathrm{Li}^4\mathrm{He}$ dimer, the peak height associated with an individual vibrational level ν_{a} is slightly reduced compared to the value obtained for a fixed (equilibrium) internuclear distance. However, the approximative computation of the relative integral resonance strength yields a value similar to the one of the 'local' resonant cross section for a separation R close to the equilibrium distance.

Within the analytical discussion of the procress in Sec. 3.3.3, the approximative expression (see Eq. (3.50)) shows that the modification of the calculation for fixed R can mostly be attributed to Franck-Condon overlaps and vibrational levels. The analytical examination shows that for the resonant two-center coupling to be effective, the coupling itself can be too strong when occuring at internuclear ditances which are too small. As a result, intermediate distances, where a balance between the radiative decay and the two-center Auger decay is established, optimise the efficiency of 2CPI. Given the abundance of interatomic and intermolecular processes in nature, the approximated expression can indicate, in which physical, chemical or biological systems these energy-transfer phenomena may be most efficient. This analysis can also provide an indication for the theoretical treatment of other two-center processes. Mechanisms such as electron-impact ionisation, investigated in Sec. 4 and [138], and photo double ionisation [139], resonant electron scattering and recombination [140], and electron capture [141], assuming fixed internuclear distances, can be expected to provide meaningful predictions for weakly bound molecular systems.

The introduction of numerical data regarding the intermediate and final state of helium in the dimer of LiHe illustrated the limitations of the calculations presented. While the approximative calculations provide satisfactory results for the potential surface in case of the initial and final state, the characteristics of the intermediate state show significant changes. Therefore, the calculation is repeated with particular focus on the numerical dependencies. The investigation shows the sensitivity of the Franck-Condon factors, decay widths and cross sections on the choice of the fitting parameters of the Morse potential. Moreover, the shifted position of the minimum of the intermediate state towards smaller internuclear distances increases the two-center Auger decay width significantly, leading to values which are now comparable to those calculated for HeNe in [18]. Furthermore, the ratios of the cross sections are reduced in comparison with the prior results. Hence, the new calculations lead to the conclusion that the inclusion of the nuclear motion does indeed reduce the importance of the indirect photoionisation mechanism. This conclusion is also influenced by the amplification of the direct process with respect to the former calculation. Comparisons with the calculation assuming fixed nuclei show that while the simple consideration of two separate atomic centers overestimates the efficiency of the two-center ionisation process for internuclear distances around the equilibrium distance of the ground state, larger distances can produce values similar to those obtained by the molecular calculation. Therefore, the approach assuming two individual atoms can provide a preliminary evaluation of the relevance regarding the ionisation process.

Aside from HeNe, where experiments on 2CPI have been performed, the theoretical predictions presented here may be tested experimentally in other heteroatomic van der Waals dimers such as ArHe or LiHe. Furthermore, theoretical investigations may increase the understanding of the role of dissociative final states in the photoionisation processes.

4 Two-center electron-impact ionisation

Ionisation via electron impact is a fundamental collision process occuring, for example, in laboratory or astrophysical plasmas [142, 143]. In addition to the well-known direct electron-impact ionisation, briefly explained in Sec. 2.1.2, more complex processes involving autoionising resonances are possible. An autoionising state, as described in Sec. 2.2.1, can not only be created by photon absorption, but also after a collision of an incident electron with an atomic center. The deexcitation can then proceed via Auger decay [144, 145], as shown in Sec. 2.5. Moreover, dielectronic capture of the incident electron followed by double Auger ionisation has been observed [144, 146].

Aside from these one-center processes, autoionising states via electron impact can also be created between two centers. In order to study interatomic coulombic decay, however, autoionisation is mostly induced by the absorption of a photon, as done in Sec. 3, where two-center photoionisation was studied. However, the use of electron impact has already been employed in some studies. For argon dimers, experiments have been carried out for an incident energy of 3 keV [147, 148], the same element was used in the form of dimers and trimers, a molecule constisting of three subunits, in experiments at projectile energies of 129 eV. Additionally, the processes of ICD and radiative charge-transfer were studied in Ne_2 for 380 eV projectiles [149]. In these experiments, the final state features three electrons in the continuum state, since the autoionising state is created via electron-impact ionisation of one center. Therefore, the incident electron leads to the emission of the secondary ejected electron as well as the ICD electron.

Only a few interatomic processes induced by electron impact have so far been studied theoretically. One of them is the two-center dielectronic recombination (2CDR), in which an ion captures the incident electron and a neighbouring atom is consequently excited. Subsequently, this excited state decays spontaneously through radiative decay [150]. However, instead of radiative decay, the deexcitation of the unstable state can also take place via the re-emission of the captured electron. As a result, two-center resonance scattering (2CRS) occurs [140].

Another process following electron impact is called interatomic Coulombic electron capture (ICEC), which can occur for large energies of the incident electron [151, 152, 153, 154]. The capture of a high-energy electron, leading to the release of most of this energy, can result in the ionisation of a neighbouring atom. Hence, ICEC illustrates an interatomic exchange of charge.

Thus, the process of electron-impact ionisation involving excitation-autoionisation, considered in a system of two atomic centers A and B, had yet to be studied in a comprehensive theoretical way, which takes all steps of the process into account.

In this section, electron-impact ionisation via excitation-autoionisation is studied in a system consisting of two atomic centers A and B. This indirect process, which will be called resonant two-center electron-impact ionisation 2C(e,2e), can be described via two sub-processes. First, the autoionising state is established by excitation of atom B through a collision with an incident electron. When the stabilisation proceeds via two-center Auger decay (see Eq. (2.42)), the radiationless energy transfer can result in the ionisation of atom A, which is depicted in Fig. 34.

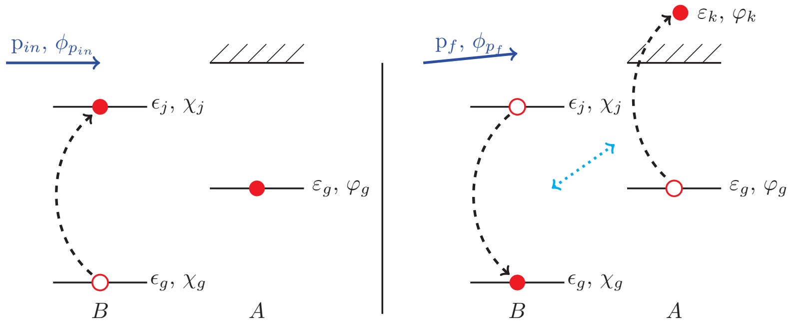

Figure 34: Scheme of two-center electron-impact ionisation 2C(e,2e). The projectile electron creates a two-center autoionising state via collisional excititation of atom B (left). The latter eventually transfers the excess energy radiationlessly to atom A, leading to its ionisation via two-center Auger decay (right).

Contrary to the studies mentioned previously [147, 148, 149, 155, 156], here, the final state of the considered process only includes two electrons in the continuum. Given that the electron impact leads to excitation instead of ionisation, only the scattered projectile as well as the electron, produced by the Auger process, are in the continuum. Since both the direct and indirect ionisation process result in the identical final state, the indirect ionisation pathway interferes and competes with the direct ionisation of atom A by electron impact, which has been studied extensively in [22]. For the direct ionisation process, results from perturbative calculations will be presented in Sec. 4.3.

As before, all transition amplitudes $S^{(1)}$, $S^{(2)}$ and $S^{(1+2)}$ of the electron-impact ionisation of LiHe are derived via time-dependent perturbation theory, using one-electron wave functions for each constituent. Ratios of these two processes are calculated, presenting the singly differential cross sections as well as the partially integrated values. The resonant two-center electron-impact ionisation 2C(e,2e) is also investigated regarding the angular distribution of ejected electron momentum as well as excitations to energetically higher lying states.

The results of this section can be found in [138].

4.1 Theoretical description

In order to calculate the energy-differential cross sections for the direct and indirect electron-impact ionisation, the spatial coordinates of all particles involved need to be established. Although the process of the direct electron-impact ionisation of atomic center A does not include the involvement of the neighbouring atom B, the following setup is applicable to both ionisation pathways. This is because when including atom B in the calculation of the direct ionisation of atom A, all terms describing the electronic configurations of B contribute a factor of one.

The spatial coordinates of the considered system are shown in Fig. 35. The nucleus of atomic center A, carrying an effective charge Z_A, is situated at the origin, the coordinates of the nucleus corresponding to atomic center B are denoted by its effective charge Z_B. The internuclear distance between both centers is denoted by the vector $\mathbf{R}$. Here, the orientation as well as the absolute value R is assumed to be fixed, meaning both nuclei are at rest. Since these calculations serve the purpose of presenting the fundamental physics of the described process, the two constituents shall be treated individually. In order for any molecular effects to be negligible, R has to be sufficiently large (at least a few Bohr radii). This also limits the extent of the interaction between A and B. Having taken this into consideration, the process of 2C(e,2e) is described as two consecutive sub-processes (see Fig. 34), as mentioned above. As already shown for the process of photoionisation in Sec. 3, the influence of molecular effects on the process of two-center ionisation following electron impact will be studied in Sec. 5.

Considering one 'active' electron for each atomic center, the one associated with atom A is described by $\mathbf{r}$, whereas $\mathbf{r}' = \mathbf{R} + \boldsymbol{\xi}$ denotes the position of the electron belonging to atomic center B. The momentum of the incident electron $\mathbf{p}_{\text{in}}$ is placed along the z-axis, which also serves as the quantisation axis, and its position is denoted by $\boldsymbol{\varrho}$.

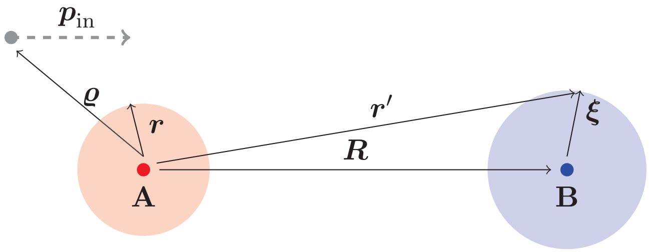

Figure 35: Spatial dependencies of the two-center system consisting of atomic centers A and B.

Regardless of the considered ionisation pathway, initial (I) and final state (III) are identical.

(I) The initial state $\Phi_{\mathbf{p}_{\text{in}},g,g} = \phi_{\mathbf{p}_{\text{in}}}(\boldsymbol{\varrho})\varphi_g(\mathbf{r})\chi_g(\boldsymbol{\xi})$ features the incident electron, which has not yet scattered, and the electrons corresponding to atoms A and B, in their ground states. Therefore, the energy reads $E_{\mathbf{p}_{\text{in}},g,g} = \frac{p_{\text{in}}^2}{2} + \varepsilon_g + \epsilon_g$. Here, ε and ϵ depict the energy of the electron associated with atomic centers A and B, respectively.

(III) In the final state the incident electron has scattered and atom A is ionised, therefore its 'active' electron is transferred to the continuum. The electron of atom B, however, is in its ground state, leading to $\Phi_{\mathbf{p}_{\text{f}},\mathbf{k},g} = \phi_{\mathbf{p}_{\text{f}}}(\boldsymbol{\varrho})\varphi_{\mathbf{k}}(\mathbf{r})\chi_g(\boldsymbol{\xi})$.

The energy of the considered system reads $E_{\mathbf{p}_\mathrm{f},\mathbf{k},g} = \frac{p_\mathrm{f}^2}{2} + \varepsilon_k + \epsilon_g$, where $\varepsilon_k = \frac{k^2}{2}$ is the energy of the emitted electron with momentum $\mathbf{k}$.

The interaction between the incident electron and the electrons bound to the atomic center is described using time-dependent perturbation theory. The initial and final states of the atomic electrons are denoted by φ_i and φ_f, respectively and the incident electron is described by ϕ_i and ϕ_f. Employing the perturbation W from Eq. (2.9), the transition amplitude reads

$$a_{\mathrm{i}(t)\to\mathrm{f}} = -i \int\limits_{-\infty}^{t} dt' \, \langle \varphi_\mathrm{f}\phi_\mathrm{f} \left| W \right| \varphi_\mathrm{i}\phi_\mathrm{in} \rangle \, e^{-i(\varepsilon_\mathrm{i} + p_\mathrm{in}^2/2 - \varepsilon_\mathrm{f} - p_\mathrm{f}^2/2)t'} . \tag{4.1}$$

In the following, one electron per collision and one 'active' electron per atomic center are considered, as well as a nucleus of atomic number Z_N. When the incident electron is described by a plane wave, the transition matrix element is given by (omitting the factor $1/V$)

$$\begin{aligned}
\langle \phi_\mathrm{f}\varphi_\mathrm{f} \left| W \right| \phi_\mathrm{i}\varphi_\mathrm{i} \rangle &= \int d^3\mathbf{r} \int d^3\boldsymbol{\varrho}\, \varphi_\mathrm{f}^*(\mathbf{r}) e^{-i\mathbf{p}_\mathrm{f}\boldsymbol{\varrho}} \left(\frac{-Z_N}{\varrho} + \frac{1}{|\boldsymbol{\varrho} - \mathbf{r}|} \right) \varphi_\mathrm{i}(\mathbf{r}) e^{i\mathbf{p}_\mathrm{in}\boldsymbol{\varrho}} \\
&= \frac{1}{2\pi^2} \int d^3\mathbf{r} \int d^3\boldsymbol{\varrho}\, \varphi_\mathrm{f}^*(\mathbf{r}) \varphi_\mathrm{i}(\mathbf{r}) e^{i(\mathbf{p}_\mathrm{in} - \mathbf{p}_\mathrm{f})\boldsymbol{\varrho}} \int d^3\mathbf{b} \left(-Z_N \frac{e^{i\mathbf{b}\boldsymbol{\varrho}}}{b^2} + \sum_{j=1}^{n} \frac{e^{i\mathbf{b}(\boldsymbol{\varrho} - \mathbf{r})}}{b^2} \right) \\
&= \frac{(2\pi)^3}{2\pi^2} \frac{1}{(\mathbf{p}_\mathrm{in} - \mathbf{p}_\mathrm{f})^2} \left\langle \varphi_\mathrm{f} \left| Z_N - \sum_{j=1}^{N} e^{i(\mathbf{p}_\mathrm{in} - \mathbf{p}_\mathrm{f})\mathbf{r}} \right| \varphi_\mathrm{i} \right\rangle ,
\end{aligned} \tag{4.2}$$

using the Fourier transform

$$\frac{1}{|\mathbf{x}|} = \frac{4\pi}{(2\pi)^3} \int d^3\mathbf{b} \frac{e^{i\mathbf{b}\mathbf{x}}}{b^2} . \tag{4.3}$$

In the following, one-particle wave functions are employed in order to describe the active electrons. Hence, effective charges Z_A and Z_B are calculated. They replace the atomic number of the nucleus Z_N in Eq. (4.2) with the effective charge of the ionic core, including screening effects.

The incident and then scattered electron is described by a plane wave. This approximation is reasonable, since the velocity of the incoming electron is assumed to be large. Consequently, the influence of the atomic centers on the incident electron during the scattering process, and therefore the change of momentum, is limited. Due to the small transfer of energy, the emitted electron is low in energy and therefore distinguishable from the incident electron. Consequently, the emitted electron is sensitive to the residual ion A after the ionisation process. This influence is accounted for by employing a Coulomb wave function with an effective charge Z_A, as described in Sec. 2.6.1.

4.1.1 Direct electron-impact ionisation

The one-center process describes the direct electron-impact ionisation of atom A and has been studied theoretically and experimentally, see also the references in Sec. 2.1.2. The well-known empirical formula by W. Lotz [22] (see Eq. (2.8)), for which results are plotted in Fig. 4, has

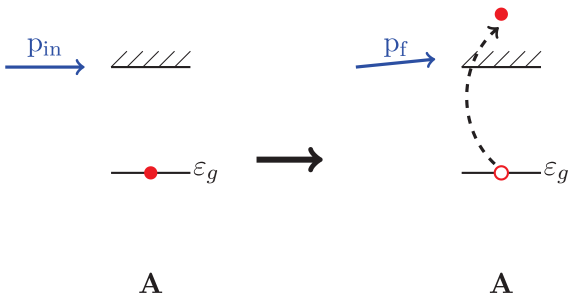

Figure 36: Scheme of the direct electron-impact ionisation process. An incident electron scatters and the energy transfer to a bound electron can lead to its ionisation. The momentum of the incident electron is altered after the collision.

been used to calculate electron-impact ionisation cross sections for more than 50 years. More profound theoretical descriptions have been developed over the years [157, 158]. The direct ionisation process is characterised by the incident electron being scattered by atom A, where the energy transfer induced by this interaction leads to the ionisation of the atomic center A. To remain consistent within the calculation, the cross section for the direct electron-impact ionisation is calculated employing the same wave-functions used in the upcoming calculation of the indirect process.

Applying first-order time-dependent perturbation theory, the transition amplitude reads

$$S^{(1)} = -i \int\limits_{-\infty}^{\infty} dt \langle \phi_{\boldsymbol{p}_{\mathrm{f}}}(\boldsymbol{\varrho})\varphi_{\mathbf{k}}(\mathbf{r})|W_A|\phi_{\boldsymbol{p}_{\mathrm{in}}}(\boldsymbol{\varrho})\varphi_g(\mathbf{r})\rangle e^{-i((\varepsilon_g+\frac{p_{\mathrm{in}}^2}{2})-(\varepsilon_k+\frac{p_{\mathrm{f}}^2}{2}))t}.$$

The perturbation describing the interaction between an incident electron and an electron is given by

$$W_A = -\frac{Z_A}{|\boldsymbol{\varrho}|} + \frac{1}{|\boldsymbol{\varrho}-\boldsymbol{r}|}. \tag{4.4}$$

Here, the first term constitutes the interaction with the ionic core, whereas the second terms denotes the electron-electron interaction.

As outlined in Sec. 3.1, the singly differential direct ionisation cross section is obtained by omitting the integration over ε_k

$$\frac{d\sigma^{(1)}}{d\varepsilon_k} = \frac{1}{p_{\mathrm{in}}} \int \frac{k d\Omega_k}{(2\pi)^3} \frac{1}{\tau} \left|S^{(1)}\right|^2, \tag{4.5}$$

where p_{in} is the momentum of the incident electron. $\frac{d\sigma^{(1)}}{d\varepsilon_k}$ depends not only on $\mathbf{p}_{\mathrm{in}}$, but also on the energy of the ejected electron $\varepsilon_k = \frac{k^2}{2}$.

4.1.2 Indirect electron-impact ionisation

The indirect process of electron-impact ionisation can be described by two subprocesses, as depicted in Fig. 34. The electron-impact excitation of atom B is followed by the deexcitation and the energy transfer to atom A via dipole-dipole interaction. This energy transfer leads to the ionisation of atom A, as described in Sec. 4.

This process is linked to the direct electron-impact ionisation similarly to the way that the two-center photoionisation process was linked to the direct process. Note, that for the process of photoionisation, the polarisation of the electromagnetic field can be used to select the electronic quantum number m for the excitation transition. The excitation by electron impact, however, is not selective with respect to a transition, especially with regard to m. As a consequence, all intermediate states m associated with a transition to the state characterised by (n, l) have to be considered. In general, all possible transitions to excited states have to be included. Here, however, a specific excitation level (n, l) is examined. In Sec. 4.3.4, transitions to other excited states are considered.

For the description of the process via two subprocesses, initial, intermediate and final electronic states have to be defined. The initial (I) and final (III) state are the same as for the direct process and therefore have already been described in Sec. 4.1. Consequently, only the intermediate state remains to be defined.

(II) The intermediate state consists of the scattered incident electron with changed momentum $\mathbf{p}'_\mathrm{f}$, the active electron of atom A remaining in its ground state and the electron from B transfered to an excited state: $\Phi_{\mathbf{p}'_\mathrm{f},g,j} = \phi_{\mathbf{p}'_\mathrm{f}}(\boldsymbol{\varrho})\varphi_g(\mathbf{r})\chi_j(\boldsymbol{\xi})$.
The energy reads $E_{\mathbf{p}'_\mathrm{f},g,j} = \frac{p'^2_\mathrm{f}}{2} + \varepsilon_g + \epsilon_j$. Here, j stands for the specific excited state of the electron associated with atom B.

In order for the radiationless energy transfer between atoms A and B to result in the ionisation of atom A, the energy difference $\omega_B = \epsilon_j - \epsilon_g$ of the transition in atom B within the process has to surpass the binding energy $I_A = |\varepsilon_g|$.

Then, the transition amplitude reads

$$\begin{aligned} S^{(2)} = & -\int\limits_{-\infty}^{\infty} dt \sum\!\!\!\!\!\!\!\int \mathcal{V}^{AB}(\mathbf{p}'_\mathrm{f}, \mathbf{p}_\mathrm{f}, \mathbf{k}) e^{-i(E_{\mathbf{p}'_\mathrm{f},g,j} - E_{\mathbf{p}_\mathrm{f},\mathbf{k},g})t} \\ & \times \int\limits_{-\infty}^{t} dt' \mathcal{W}^B_{\mathrm{e},j}(\mathbf{q}) e^{-i(E_{\mathbf{p}_\mathrm{in},g,g} - E_{\mathbf{p}'_\mathrm{f},g,j})t'}, \end{aligned} \tag{4.6}$$

where $\sum\!\!\!\!\!\!\!\int = \int \frac{d^3p'_\mathrm{f}}{(2\pi)^3} \sum\limits_j$ implies the inclusion of all intermediate states. It consists of the summation over electronic states of atom B and the integration over all continuum states of the scattered electron characterised by p'_f. However, $\mathbf{p}'_\mathrm{f} = \mathbf{p}_\mathrm{f}$ is valid since V_{AB} has no influence on $\boldsymbol{\varrho}$ and $\{\phi_{\mathbf{p}'_\mathrm{f}}(\boldsymbol{\varrho}), \phi_{\mathbf{p}_\mathrm{f}}(\boldsymbol{\varrho})\}$ is an orthogonal set. Thus, the momentum of the scattered electron does not change during the second step of the 2C(e,2e) process.

In order to describe the process of indirect electron-impact ionisation, the following matrix elements have to be inserted

$$\mathcal{V}^{AB}(\mathbf{p}'_\mathrm{f}, \mathbf{p}_\mathrm{f}, \mathbf{k}) = \langle \Phi_{\mathbf{p}_\mathrm{f},\mathbf{k},g} | V_{AB} | \Phi_{\mathbf{p}'_\mathrm{f},g,j}, \rangle \tag{4.7}$$

$$\mathcal{W}^B_\mathrm{e}(\mathbf{q}) = \langle \Phi_{\mathbf{p}'_\mathrm{f},g,j} | W^\mathrm{e}_B | \Phi_{\mathbf{p}_\mathrm{in},g,g} \rangle. \tag{4.8}$$

Here, $\mathbf{q} = \mathbf{p}_\mathrm{f} - \mathbf{p}_\mathrm{in}$ denotes the momentum transfer of the incident electron.

The interaction W_B^{e} describes the excitation of atom B by electron-impact and is given by

$$W_B^{\mathrm{e}} = -\frac{Z_B}{|\boldsymbol{\varrho} - \mathbf{R}|} + \frac{1}{|\boldsymbol{\varrho} - \mathbf{R} - \boldsymbol{\xi}|}. \tag{4.9}$$

As mentioned before, the interaction of the incident electron with atom B does not restrict the angular momentum projection m for the configuration (n, l) considered. Therefore, it is required to sum over all possible intermediate states in $S^{(2)}$.

The two-center interaction between the electrons of A and B is given by the dipole-dipole interaction V_{AB}, see Eq. (2.24)

$$V_{AB} = \frac{\mathbf{r} \cdot \boldsymbol{\xi}}{R^3} - \frac{3(\mathbf{r} \cdot \mathbf{R})(\boldsymbol{\xi} \cdot \mathbf{R})}{R^5}.$$

Retardation effects are neglected, which is reasonable for $R \ll c/\omega_B$, where ω_B is the transition energy in atom B. Executing the integrations over time leads to

$$S^{(2)} = -2\pi i \delta(E_{\mathbf{p}_{\mathrm{f}},\mathbf{k},g} - E_{\mathbf{p}_{\mathrm{in}},g,g}) \frac{\mathcal{V}^{AB}(\mathbf{p}_{\mathrm{f}}, \mathbf{k}) \mathcal{W}_{\mathrm{e}}^{B}(\mathbf{q})}{\Delta + \frac{i}{2}\Gamma}. \tag{4.10}$$

The denominator consists of the detuning $\Delta = \frac{p_{\mathrm{in}}^2}{2} + \epsilon_g - \epsilon_j - \frac{p_{\mathrm{f}}^2}{2}$, whereas the decay rate Γ accounts for the instability of the excited state $\chi_e(\boldsymbol{\xi})$ in atom B (see Eqs. (2.39),(2.42)). The conservation of energy gives

$$\left(\frac{p_{\mathrm{f}}^2}{2} + \frac{k^2}{2} + \epsilon_g\right) - \left(\frac{p_{\mathrm{in}}^2}{2} + \varepsilon_g + \epsilon_g\right) = 0, \tag{4.11}$$

where the energy ϵ_g of the ground state of atom B cancels out, since atom B acts as a catalyser. From the transition amplitude $S^{(2)}$, the energy-differential cross section is obtained as described in Eq. (4.5) for the direct ionisation process. Hence, the cross section

$$\frac{d\sigma^{(2)}}{d\varepsilon_k} = \frac{1}{p_{\mathrm{in}}} \int \frac{d^3 p_{\mathrm{f}}}{(2\pi)^3} \int \frac{k d\Omega_k}{(2\pi)^3} \frac{1}{\tau} \left| S^{(2)} \right|^2 \tag{4.12}$$

depends on the energies of the incident electron $\frac{p_{\mathrm{in}}^2}{2}$ and the ejected electron ε_k.

4.1.3 Interference of the processes

The two processes, considering atom A in the vicinity of atom B, yield the same final state, where atom B is in its electronic ground state and atom A is ionised with two electrons in the continuum, the incident electron and the one emitted from atomic center A. Therefore, the direct and indirect channels of electron-impact ionisation can interfere with each other. The transition amplitude of the total process of electron-impact ionisation reads

$$S^{(12)} = S^{(1)} + S^{(2)}. \tag{4.13}$$

From this, the total, energy-differential cross sections can be calculated as described in Eq. (4.12).

4.2 Simplification through one-center processes

The approach taken in this section allows for studying the analytical form of the two-center electron-impact ionisation cross section. One way to further comprehend the process is to compare the numerical calculations with literature values. For this purpose, the energy-differential cross section $\frac{d\sigma^{(2)}}{d\varepsilon_k}$ is expressed as a combination of single-center processes. In order for the calculation to remain manageable, the transition $1s \to 2p$ in atom B is considered, where only $m = 0$ will be included as intermediate electron state of atom B. Furthermore, the orientation of the molecule is set to $\mathbf{R} = R\mathbf{e}_z$, along the incident electron momentum $\mathbf{p}_{\text{in}}$. Without any alignment of the molecule, averaging over all spatial orientations would be required. This, however, does not change the qualitative features of the 2C(e,2e) process, so that $\mathbf{R} \parallel \mathbf{e}_z$ is assumed as before. Analysing the expression

$$\begin{aligned}\frac{d\sigma^{(2)}}{d\varepsilon_k} &= \frac{1}{p_{\text{in}}} \int \frac{d^3p_{\text{f}}}{(2\pi)^3} \int \frac{k d\Omega_k}{(2\pi)^3} 2\pi\delta\left(\varepsilon_k - \varepsilon_0 + \frac{p_{\text{f}}^2}{2} - \frac{p_{\text{in}}^2}{2}\right) \frac{1}{\Delta^2 + \frac{1}{4}\Gamma^2} \\ &\times \left| \left\langle \varphi_k(\mathbf{r})\chi_0(\boldsymbol{\xi}) \left| \frac{-2z_A z_B}{R^3} \right| \varphi_0(\mathbf{r})\chi_j(\boldsymbol{\xi}) \right\rangle \left\langle \phi_{\mathbf{p}_{\text{f}}}(\boldsymbol{\varrho})\chi_j(\boldsymbol{\xi}) \left| \frac{1}{|\boldsymbol{\varrho} - \mathbf{R} - \boldsymbol{\xi}|} \right| \phi_{\mathbf{p}_{\text{in}}}(\boldsymbol{\varrho})\chi_j(\boldsymbol{\xi}) \right\rangle \right|^2,\end{aligned} \tag{4.14}$$

three one-center processes can be identified. The first step of the two-center ionisation – the electron-impact excitation of atom B – can be directly rewritten as the cross section

$$\begin{aligned}\sigma_{\text{exc}}^B &= \frac{1}{p_{\text{in}}} \int \frac{d^3p_{\text{f}}}{(2\pi)^3} 2\pi\delta\left(\epsilon_j - \epsilon_0 + \frac{p_{\text{f}}^2}{2} - \frac{p_{\text{in}}^2}{2}\right) \\ &\times \left| \left\langle \phi_{\mathbf{p}_{\text{f}}}(\boldsymbol{\varrho})\chi_j(\boldsymbol{\xi}) \left| \frac{1}{|\boldsymbol{\varrho} - \mathbf{R} - \boldsymbol{\xi}|} \right| \phi_{\mathbf{p}_{\text{in}}}(\boldsymbol{\varrho})\chi_j(\boldsymbol{\xi}) \right\rangle \right|^2\end{aligned} \tag{4.15}$$

of the one-center excitation. The matrix element describing the two-center Auger decay can be splitted into two individual processes for atoms A and B, respectively. The matrix element, which applies to atom B, can be related to the radiative decay rate Γ_{rad} described in Eq. (2.39). For atom A, the one-center photoionisation cross section σ_{PI}^A (see also Eq. (4.4)) can be identified. Again, the identity in Eq. 3.17 is applied here. When inserting these terms, however, the conditions of energy conservation do not add up. Looking at the two one-center processes σ_{exc}^B and σ_{PI}^A, both include different criteria for energy conservation. σ_{exc}^B determines p_{f}, whereas σ_{PI}^A regulates the energy of the ejected electron $k^2/2$. However, the expression in Eq. (4.14) includes only one specification which connects p_{f} and k. This combined law can be disentangled by calculating the energy-differential cross section at resonance $\left.\frac{d\sigma^{(2)}}{d\varepsilon_k}\right|_{k=k_0}$. In doing so, one can assume that

$$\frac{1}{2}\left(p_{\text{f}}^2 - p_{\text{in}}^2\right) = \epsilon_g - \epsilon_j \tag{4.16}$$

holds for the electron-impact excitation and $\frac{1}{2}k_A^2 := \varepsilon_g + \omega$ is valid for the electron emitted from A by non-radiative energy transfer. Resonance occurs, where the denominator $\frac{1}{\Delta^2 + \frac{1}{4}\Gamma^2}$ is minimised. Therefore, k_0 is defined by

$$\frac{1}{2}k_0^2 := \varepsilon_g + \epsilon_j - \epsilon_g. \tag{4.17}$$

This leads to the compact formula of the two-center process 2C(e,2e)

$$\left.\frac{d\sigma^{(2)}}{d\varepsilon_k}\right|_{k=k_0} = \frac{2}{\pi}\frac{\Gamma_{\text{aug}}}{\Gamma^2}\sigma^B_{\text{exc}}(p_{\text{in}}) \tag{4.18}$$

with the two-center Auger rate

$$\Gamma_{\text{aug}} = \frac{3}{2\pi}\frac{c^4}{\omega^4 R^6}\Gamma^{(B)}_{\text{rad}}\sigma^A_{\text{PI}}(\omega). \tag{4.19}$$

Here, $\omega = \omega_B$ describes the energy difference of the transition of B and is used in all quantities when inserting $k = k_0$. From Eq. (4.19), fundamental characteristics of the two-center electron-impact ionisation can be derived. At sufficiently large internuclear distances R, where $\Gamma_{\text{rad}} \gg \Gamma_{\text{aug}}$, and the momentum of the incident electron $\mathbf{p}_{\text{in}}$ is fixed, the cross section decreases with R^{-6}. For small R, the rapid change of Γ_{aug} and R^{-6} creates a more complex behaviour. For fixed values of R, the cross section only depends on the one-center cross sections of the electron-impact excitation of atom B as well as the photoionisation of atom A. Consequently, combinations of atoms with large associated cross sections benefit the 2C(e,2e) cross section.

Inserting literature values in Eq. (4.19), the two-center cross section can easily be estimated. In order to rate the results, the ratio between the energy-differential cross sections for the direct and indirect processes at the two-center resonance is calculated

$$\eta_{k_0} = \left.\frac{d\sigma^{(2)}/d\varepsilon_k}{d\sigma^{(1)}/d\varepsilon_k}\right|_{k=k_0}. \tag{4.20}$$

Considering the cross section integrated over all ejected electron momenta k, the total cross sections can be approximated via

$$\sigma^{(2)} \approx \left.\frac{d\sigma^{(2)}}{d\varepsilon_k}\right|_{k=k_0}\delta_{\text{res}} \tag{4.21}$$

$$\sigma^{(1)} \approx \left.\frac{d\sigma^{(1)}}{d\varepsilon_k}\right|_{k=k_0}\delta_{\varepsilon_k}. \tag{4.22}$$

As in [22] and Sec. 4.3, the direct electron-impact ionisation proceeds smoothly, and therefore exhibits a rather broad width δ_{ε_k}. The two-center process, however, features a resonant behaviour. The effective resonance width $\delta_{\text{res}} = \frac{\pi}{2}\Gamma$ holds for a Lorentzian curve of the form $d\sigma^{(2)}/d\varepsilon_k \sim 1/\left(\Delta^2 + \frac{1}{4}\Gamma^2\right)$. The resulting formula

$$\sigma^{(2)} \approx \frac{\Gamma_{\text{aug}}}{\Gamma}\sigma^B_{\text{exc}}(p_{\text{in}}) \tag{4.23}$$

provides a physically intuitive explanation of the process. The excitation of atom B by electron impact is described by its one-center cross section $\sigma^B_{\text{exc}}(p_{\text{in}})$. For resonant 2C($e$,2$e$) to proceed, the Auger-state has to decay radiationlessly in order to transfer its transition energy to the electron of atom A. However, there are two decay mechanisms, radiative decay and two-center Auger decay, as discussed in Sec. 2.5. The branching ratio $\Gamma_{\text{aug}}/\Gamma$, which depicts the relevance of the two-center Auger decay with respect to the total decay, is represented in Eq. (4.23).

Results for HHe

Before studying the van der Waals molecule LiHe, already employed in the study on photoionisation in Sec. 3, results are presented for the simplest heteroatomic dimer, with respect to the amount of bound electrons, HHe. Considering the $1s$-$2p_0$ transition in helium, hydrogen takes on the role of atomic center A. The advantage of this system is the simplicity of the hydrogen atom in contrast to lithium, which holds three electrons. An internuclear separation of $R = 20\,\text{a.u.}$ is chosen, where the radiative decay rate $\Gamma_{\text{rad}} = 4.35 \times 10^{-8}\,\text{a.u.}$ [47] is of the same order as the two-center Auger decay rate Γ_{aug} calculated from $\sigma_{\text{PI}}^{\text{H}} = 0.064\,\text{a.u.}$ for $\omega = \omega_B$ [159]. Note, that the two-center Auger decay width Γ_{aug} in Eq. (4.19) is mutliplied by a factor of two in order to account for the two valence electrons in helium (see Eqs. (3.37), (3.38)). Results are presented for energies $\frac{p_{\text{in}}^2}{2} = 250\,\text{eV}$ and $\frac{p_{\text{in}}^2}{2} = 1\,\text{keV}$ of the incident electron due to the availability of literature values.

On resonance, the literature values $\sigma_{\text{exc}}^{\text{He}}(250\text{eV}) = 0.25\,\text{a.u.}$ [47] and $\frac{d\sigma_{\text{H}}^{(1)}}{d\varepsilon_k}|_{k=k_0} = 1.94\,\text{a.u.}$ [160] lead to an energy-differential ratio

$$\eta_{k_0} \approx 4.7 \times 10^5. \tag{4.24}$$

This value illustrates the tremendous influence of the neighbouring atom B on the electron-impact ionisation of hydrogen for ejected electron energies close to resonance. Calculating the width of the distribution δ_{ε_k} from literature values [22, 160] yields $\delta_{\varepsilon_k} \approx 17$ eV. This value is 7 orders of magnitude larger than the width for the indirect process, δ_{res}. These dramatic differences in the widths of the cross sections lead to drastically different total cross sections for the direct and indirect process, respectively.

Employing these values, the total resonant two-center cross section becomes

$$\sigma_{\text{HHe}}^{(2)}\Big|_{\frac{p_{\text{in}}^2}{2}=250\text{eV}} \approx 0.12\,\text{a.u.}, \tag{4.25}$$

whereas the literature value for the one-center cross sections reads [22]

$$\sigma^{(1)}\Big|_{\frac{p_{\text{in}}^2}{2}=250\text{eV}} = 1.22\,\text{a.u.}. \tag{4.26}$$

Applying the formula from Eq. (4.23), the ratios of the fully integrated cross section can be calculated at, for example, $R = 20\,\text{a.u.}$ and yield

$$\frac{\sigma_{\text{HHe}}^{(2)}}{\sigma_{\text{H}}^{(1)}}\Bigg|_{\frac{p_{\text{in}}^2}{2}=250\text{eV}} \approx 0.097, \tag{4.27}$$

$$\frac{\sigma_{\text{HHe}}^{(2)}}{\sigma_{\text{H}}^{(1)}}\Bigg|_{\frac{p_{\text{in}}^2}{2}=1\,\text{keV}} \approx 0.113. \tag{4.28}$$

These ratios $\eta^{(2)}$ are plotted against the internuclear distance R for two incident electron energies. in Fig. 37.

For small internuclear distances, values around $\eta^{(2)} = 0.06$ are obtained. Here, the Lotz formula [22] is applied for $\sigma_{\text{H}}^{(1)}$, while Eq. (4.23) yields $\sigma_{\text{HHe}}^{(2)}$. The ratio saturates for $R \lesssim 12\,\text{a.u.}$, where $\Gamma \approx \Gamma_{\text{aug}}$. Here, the ratio reaches a maximum of about $\sigma_{\text{HHe}}^{(2)}/\sigma_{\text{H}}^{(1)} \approx 0.2$. This value indicates, that the two-center process makes a noteworthy contribution to the electron-impact ionisation of hydrogen. For the energy $p_{\text{in}}^2/2 = 1\,\text{keV}$ of the incident electron, a smaller ratio of $\sigma_{\text{exc}}^{\text{He}} \approx 0.11\,\text{a.u.}$ is obtained. However, these results show, that the importance of the indirect ionisation process is not restricted to the energy-differential resolution of the cross section.

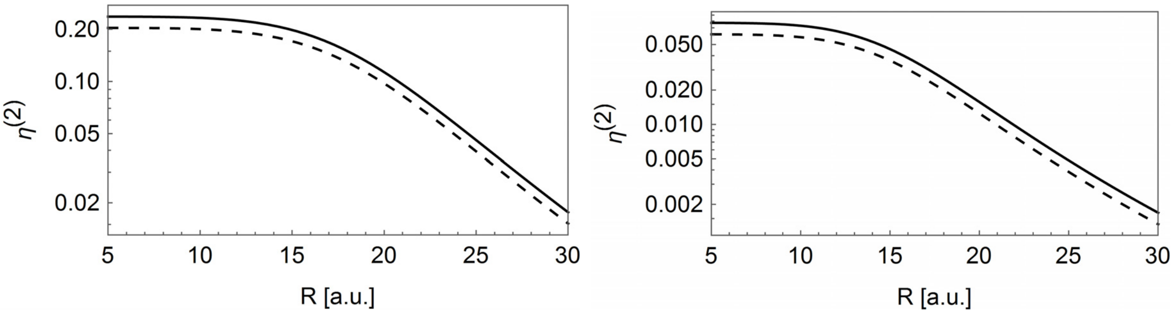

Figure 37: The ratios of total cross sections $\eta^{(2)} = \frac{\sigma^{(2)}}{\sigma^{(1)}}$ are plotted. On the left, the values are computed for HHe using $p_{\text{in}}^2/2 = 250\,\text{eV}$ (solid) and $p_{\text{in}}^2/2 = 1\,\text{keV}$ (dashed). On the right, the values are computed for LiHe employing $p_{\text{in}}^2/2 = 250\,\text{eV}$ (solid) and $p_{\text{in}}^2/2 = 1\,\text{keV}$ (dashed).

Results for LiHe

With the literature values $\Gamma_{\text{rad}} \approx 4.35 \times 10^{-8}\,\text{a.u.}$ [47], $\sigma_{\text{PI}}^{\text{Li}} \approx 0.18\,\text{a.u.}$ [161] and $\sigma_{\text{exc}}^{\text{He}}(1\,\text{keV}) \approx 0.11\,\text{a.u.}$ [162], and $\sigma_{\text{exc}}^{\text{He}}(250\,\text{eV}) = 0.250\,\text{a.u.}$ [47], some of the quantities can be calculated for LiHe as well. Again, the transition in helium to the state $1s2p_0$ is considered and the valence electron in lithium is ionised. Note, however, that no literature values for the energy-differential direct electron-impact ionisation cross section for lithium could be found. For an internuclear distance of $R = 20\,\text{a.u.}$, the two-center Auger decay width of the excited state in helium calculated from $\sigma_{\text{PI}}^{\text{Li}}$ for $\omega = \omega_{\text{B}}$ is approximately a quarter of the radiative width [47]. On resonance, the energy-differential two-center electron-impact cross sections read $\left.\frac{d\sigma_{\text{LiHe}}^{(2)}}{d\varepsilon_k}\right|_{k=k_0} \approx 5.94 \times 10^5\,\text{a.u.}$ for $\frac{p_{\text{in}}^2}{2} = 250\,\text{eV}$ and $\left.\frac{d\sigma_{\text{LiHe}}^{(2)}}{d\varepsilon_k}\right|_{k=k_0} \approx 2.54 \times 10^5\,\text{a.u.}$ for $\frac{p_{\text{in}}^2}{2} = 1\,\text{keV}$. The ratios of the fully integrated cross sections yield:

$$\left.\frac{\sigma_{\text{LiHe}}^{(2)}}{\sigma^{(1)\text{Li}}}\right|_{\frac{p_{\text{in}}^2}{2}=250\text{eV}} \approx 0.012 \tag{4.29}$$

$$\left.\frac{\sigma_{\text{LiHe}}^{(2)}}{\sigma^{(1)\text{Li}}}\right|_{\frac{p_{\text{in}}^2}{2}=1\,\text{keV}} \approx 0.014. \tag{4.30}$$

In Fig. 37 the ratio $\frac{\sigma^{(2)}}{\sigma^{(1)}}$ of the total cross sections is depicted for two incident electron energies. While the contribution of the two-center process in HHe is larger than in LiHe, the ratio of the fully integrated cross sections shows for both systems that the indirect ionisation pathway is worth investigating.

The higher incident electron energy $\frac{p_{\text{in}}^2}{2} = 1\,\text{keV}$ corresponds to an electron velocity of $v_{\text{in}} \approx 8.6\,\text{a.u.}$, fulfilling the condition for perturbation theory ($v_{\text{in}} \gg 1\,\text{a.u.}$), which was discussed in Sec. 4.1. Therefore, $\frac{p_{\text{in}}^2}{2} = 1\,\text{keV}$ rather than $\frac{p_{\text{in}}^2}{2} = 250\,\text{eV}$ will be used in the remainder of the section.

4.3 Numerical results

In order to further investigate the fundamental properties of resonant 2C(e,2e), started in Sec. 4.2, numerical calculations of the energy-differential cross sections are performed. HHe has already been studied as the simplest diatomic system fulfilling the requirements of the two-center process (see Sec. 4.1.2). Although HHe is often investigated as a fragment of collisional processes and potential surfaces have been calculated theoretically for ground and excited states [163, 164], hydrogen and helium do not form a bound ground state [165]. Therefore, the van der Waals molecule ^{7}Li^{4}He is utilised again as the model system to be considered. For helium, the same symmetrised wave functions are used as in Eqs. (3.37) and (3.38) in Sec. 3, including the expansion of the corresponding operator from Eq. (3.40). The interaction with the incident electrons is expanded as

$$W_B^e \to -\frac{Z_B}{|\boldsymbol{\varrho} - \boldsymbol{R}|} + \sum_{\ell=1,2} \frac{1}{|\boldsymbol{\varrho} - \boldsymbol{R} - \boldsymbol{\xi}_\ell|}. \tag{4.31}$$

Again, the expansion results in a factor of 2 for the transition amplitude. In analogy to the previous calculations, also the two-center Auger decay width Γ_{aug} is, in consequence, multiplied by a factor of 2 in order to account for the two electrons on the valence shell. A discussion on the consequences of incorporating both electrons for helium has been carried out in Sec. 3.3. Having chosen the dipole-allowed transition from the ground state to $1s2p_m$, the transition energy $\omega_B = 21.218$ eV is used in order to calculate the effective nuclear charge $Z_B = 1.435$ for both the ground and the excited states. Note, that in principle, the excited state in atom B could be subject to fine structure splitting due to spin-orbit coupling. This effect would lead to an according splitting of the resonance peak, which is typically on the order of 10^{-4} eV in light atoms. Since such a narrow doublet of lines is very difficult to resolve in electron-beam experiments, though, its inclusion was refrained from in the general treatment of resonant 2C(e,2e). Besides, no fine structure arises in the excited $1s2p$ spin-singlet state [47] in helium considered in the current section. For lithium, a hydrogen-like wave function is employed in order for the matrix elements to be analytically solvable. Here, $Z_A = Z_{\text{Li}} = 1.259$ is fitted for lithium to the binding energy $I_A \approx 5.39$ eV of the $2s$-state and remains as in Sec. 3.

For lithium to be ionised, the transition energy of helium $\omega_B > I_A$ has to be sufficiently large, see Sec. 4.1. Excitations to higher lying states (for instance $3p_m$, $4p_m$ etc.) are possible and will be described in a later section (Sec. 4.3.4). However, here, the calculations are restricted to $2p_m$ states in helium. This decision is justified, since the considered transition exhibits the largest dipole transition element from the ground state.

First, separate calculations for the resonant 2C(e,2e) as well as the one-center process are carried out. As before, the linking vector is set along the z-axis, $\mathbf{R} \parallel \mathbf{e}_z$. For reasons of consistency, the value for Γ_{rad} calculated in Eq. (2.25) is employed. Furthermore, the wave functions in Eqs. (3.37) and (3.38) are inserted into all calculations, since the matrix elements in Eq. (2.25) for the decay width are also included in the transition matrix elements of the cross section of 2C(e,2e).

4.3.1 Cross sections

As seen in Sec. 4.2, the energy-differential cross section of the 2C(e,2e) process strongly depends on the energy $k^2/2$ of the ejected electron. For this reason, the energy-differential cross sections for the direct and indirect ionisation channel are calculated for an incident electron energy $\frac{p_{\text{in}}^2}{2} = 1\,\text{keV} \approx 8.57\,\text{a.u.}$ and an internuclear distance of $R = 20\,\text{a.u.}$ around the resonance $k = k_0$ in Fig. 39 and Fig. 40. Before doing this, the fully integrated cross sections for the direct ionisation channel are depicted in Fig. 38 in order to compare them to the values computed from the Lotz formula, see Fig. 4. This is done for hydrogen, for which the used wave function is exact and therefore represents a good possibility of comparison to literature values. Furthermore, values for lithium and helium are given. The electron-impact ionisation of lithium is under investigation in this section. When considering a system which is comprised of lithium and helium, the direct ionisation channel of helium is a competing, but not interfering process. Note again, that in the calculation of the cross section for helium, the value is multiplied by 2 in order to account for its two valence electrons. Here, the helium ground state was used in the form of Eq. (3.37) and the continuum state was described by a Coulomb wave [70]. In the case of helium, an effective nuclear charge $Z = 1.34$ was applied for the residual ion which yields the first ionisation energy of helium.

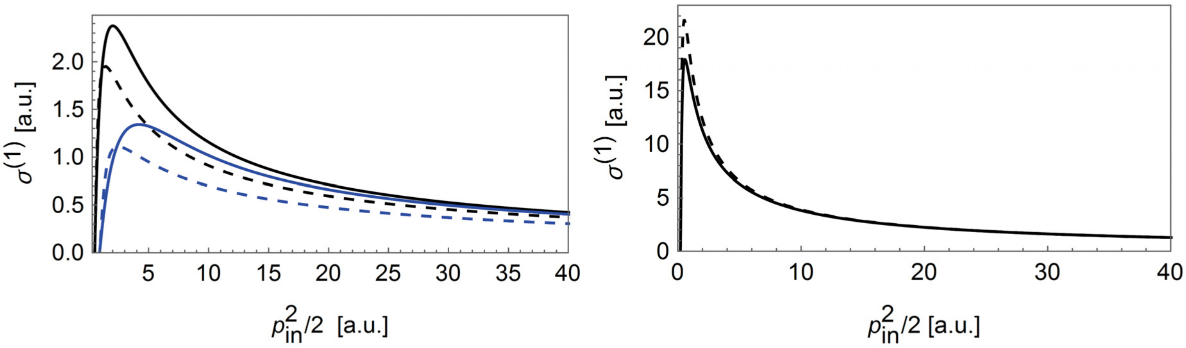

Figure 38: Fully integrated cross sections for the direct electron-impact ionisation for hydrogen (black) and helium (blue) on the left, as well as lithium on the right. For these three elements, the calculations from Lotz (solid) [22] and the perturbative approach (dashed) are compared to each other.

As described in Secs. 2.1.2 and 4.1, the energy of the incident electron has to be large in order to justify the use of an perturbative approach. Therefore, the values in Fig. 38, calculated by applying the perturbative method, converge to the literature values by Lotz for larger energies of the incident electron. For large projectile energies, the calculated values are in good agreement with those given by the Lotz formula.

Now, the energy-differential cross sections for the direct electron-impact ionisation are considered. In order to be comparable to the indirect process, the plot focusses on an interval around the resonant energy $\frac{k_0^2}{2}$ of the two center process. Its value is computed from the energy conservation in Eq. (4.17) and reads $k_0 \approx 1.078\,\text{a.u.}$ for the system of LiHe, when using literature values from [47]. Results are presented for an incident electron energy of $\frac{p_{\text{in}}^2}{2} = 1\,\text{keV}$, as discussed in Sec. 4.2.

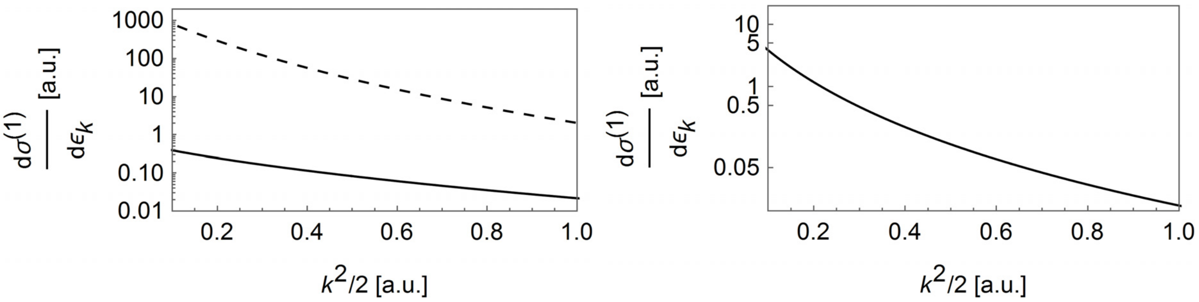

Figure 39: Energy-differential cross sections for the direct electron-impact ionisation for hydrogen (dashed) and helium (solid) on the left, as well as lithium on the right. The energy of the incident electron is set to $\frac{p_{\text{in}}^2}{2} = 1\,\text{keV}$.

As expected, the energy-differential cross sections show a smooth dependence on the energy $\frac{k^2}{2}$ of the emitted electron. As described in Sec. 2.1.2, high energies of the incident electron lead to a small energy transfer. A small value for $q^2/2$ is reflected in low kinetic energies of the emitted electron. Therefore, the descrease of the energy-differential cross section of the direct ionisation process with increasing energy of the emitted electron is a direct consequence. The cross section for lithium will later be compared to the indirect cross section, which is calculated next. The indirect ionisation process of lithium in the presence of helium depends on the internuclear distance, as described in Sec. 4.1.2. Results are plotted for two internuclear distances, $R = 10\,\text{a.u.}$ and $R = 20\,\text{a.u.}$ and, again, the energy of the incident energy is chosen as $\frac{p_{\text{in}}^2}{2} = 1\,\text{keV}$. For these internuclear distances, the two-center Auger decay widths are presented in Table 21.

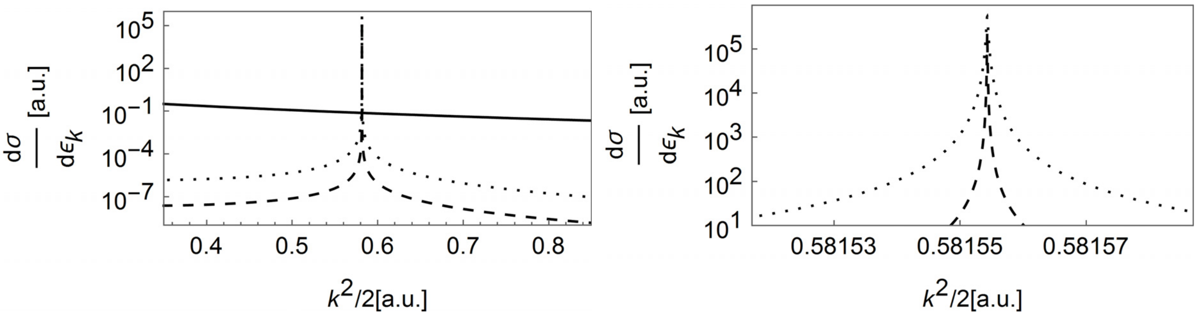

Figure 40: Energy-differential cross sections for the electron-impact ionisation of lithium for an incident electron energy of $\frac{p_{\text{in}}^2}{2} = 1\,\text{keV}$, where $\mathbf{p}_{\text{in}} \parallel \mathbf{e}_z$. The direct process is depicted by the solid line, whereas the values for the indirect process are depicted by the dotted line for $R = 10\,\text{a.u.}$ and the dashed line for $R = 20\,\text{a.u.}$. The orentiation of $\mathbf{R}$ is parallel to the trajectory of the incident electron, which is set along $\mathbf{z}$.

In Fig. 40, the two-center cross section features a peak displaying the resonance for $k = k_0$. This behaviour is in a stark contrast to the direct electron-impact ionisation cross section (see Fig. 39), which shows a smooth dependency on k. For most energies of the ejected electron ε_k, the energy-differential cross section of the direct channel exceeds the indirect ionisation channel. On resonance, however, the two-center process vastly increases and dominates the ionisation process. For comparison, the results obtained from the literature values in Sec. 4.2 and the numerically calculated values are presented in Table 21.

	$\frac{d\sigma^{(2)}}{d\varepsilon_k}\big\|_{R=20\,\text{a.u.}}$	$2\Gamma_{\text{aug}}(20\,\text{a.u.})$	$\frac{d\sigma^{(2)}}{d\varepsilon_k}\big\|_{R=10\,\text{a.u.}}$	$2\Gamma_{\text{aug}}(10\,\text{a.u.})$
I	2.42×10^5	1.32×10^{-8}	5.48×10^5	8.46×10^{-7}
II	2.54×10^5	1.10×10^{-8}	0.86×10^5	7.05×10^{-7}

Table 21: Peak heights of the two-center electron-impact ionisation cross sections and two-center Auger decay widths for the two different methods of calculation. The row marked by I denotes the numerically calculated results whereas the values in the row indicated by II are calculated from the formulas in Sec. 4.2. All entries are given in atomic units.

The two-center Auger decay widths are comparable for the two methods of calculation. For smaller internuclear distances R, the two-center Auger decay represents the main contribution to the total decay width, since it is larger than the radiative width, which is of the order 10^{-8} a.u. . For a small internuclear distance of $R = 10\,\text{a.u.}$, the ratio yields $\frac{2\Gamma_{\text{aug}}}{\Gamma_{\text{rad}}} = 12.79$ for the numerical calculation. When the internuclear distance is increased, the two-center Auger decay width decreases. This leads to a mostly constant total decay width for large R, since the Auger width becomes negligible and Γ_{rad} dominates. For $R = 20\,\text{a.u.}$, the ratio of the decay widths is $\frac{2\Gamma_{\text{aug}}}{\Gamma_{\text{rad}}} = 0.2$, showing the decreasing contribution from the Auger decay.

A good agreement is also achieved for the energy-differential cross section for $R = 20\,\text{a.u.}$. For the smaller interatomic distance $R = 10\,\text{a.u.}$, however, this is not the case. The discrepancy can be seen in Fig. 40, where the energy-differential two-center cross sections are plotted against the internuclear distance. Here, the curves overlap in the region around $R = 20\,\text{a.u.}$ but differ for smaller internuclear distances. The numerical consideration yields the peak heights of the ratios η_k on resonance. The values $\eta_{k_0}(10\,\text{a.u.}) = 5.85 \times 10^6$ and $\eta_{k_0}(20\,\text{a.u.}) = 2.58 \times 10^6$ show a vast dominance of the two-center process for emitted electrons whose energy is close to resonance.

Furthermore, the results of the fully integrated one- and two-center cross sections are included in Table 22.

	$\sigma^{(1)}$	$\sigma^{(2)}\|_{20\,\text{a.u.}}$	$\eta(20\,\text{a.u.})$	$\sigma^{(2)}\|_{10\,\text{a.u.}}$	$\eta(10\,\text{a.u.})$
I	1.381	0.028	0.020	0.3	0.22
II	1.384	0.021	0.015	0.1	0.07

Table 22: Fully integrated values of the electron-impact ionisation cross sections for the two different methods of calculation. The row indicated by I includes the numerically calculated results whereas the row marked by II contains the values calculated from the formulas in Sec. 4.2.

The values calculated from the two different methods match with respect to the order of magnitude. Note, that the ratio $\eta = \frac{\sigma^{(2)}}{\sigma^{(1)}}$ of the fully integrated cross sections has already been calculated in Sec. 4.2. While the two-center pathway tremendously amplifies the ionisation process for ejected electron energies near resonance, the fully integrated cross section shows a ratio, where the indirect process does not seem to be of great importance. The values for the one-center process match excellently. As above, the values for the two methods of calculation yield comparable results for $\sigma^{(2)}$, and therefore the ratio of the fully integrated cross sections η for the larger internuclear distance 20 a.u. are alike. For $R = 10$ a.u. , however, the two calculations give different values, as can be seen in Fig. 40.

To further analyse the influence of the two-center pathway to the electron-impact ionisation, the ratio of the electron-impact ionisation cross sections

$$\eta_k(R, p_{\text{in}}) = \frac{d\sigma^{(2)}}{d\varepsilon_k} \Big/ \frac{d\sigma^{(1)}}{d\varepsilon_k} \tag{4.32}$$

is calculated and plotted in Fig. 41. For a fixed energy of the incident electron $\frac{p_{\text{in}}^2}{2} = 1\,\text{keV}$, its dependencies on the energy of the emitted electron $\frac{k^2}{2}$ as well as on the internuclear distance R are plotted individually. The ratio visualises the dominance of an ionisation process for a particular range of emitted electron energies $\frac{k^2}{2}$.

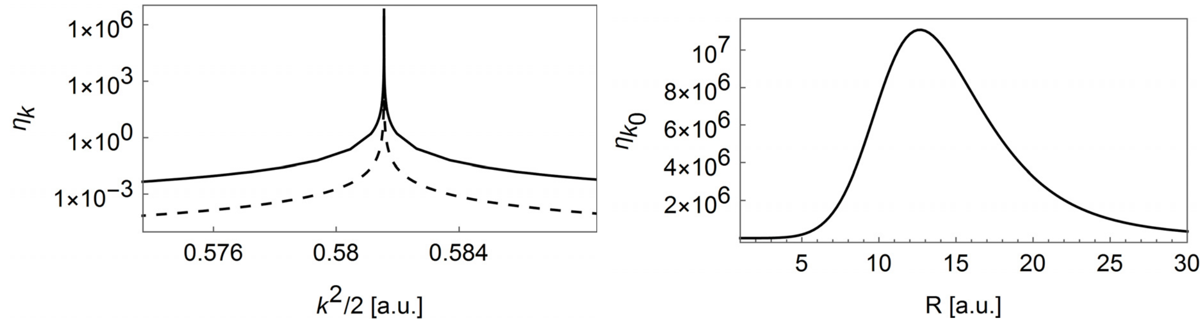

Figure 41: Electron-impact ionisation of lithium for an incident electron energy of $\frac{p_{\text{in}}^2}{2} = 1\,\text{keV}$, where $\mathbf{p}_{\text{in}} \parallel \mathbf{e}_z$. On the left, the ratios of the cross sections are depicted for $R = 10$ a.u. (solid) and $R = 20$ a.u. (dashed). On the right, the dependency of the energy-differential cross section on the internuclear distance is visualised for resonant $k = k_0$.

Fig. 41 depicts the ratio η_k, which is plotted against the energy of the emitted electron and the internuclear distance R. The direct ionisation channel does not depend on the internuclear distance, when ignoring any molecular effects. For small internuclear distances, the ratio increases with R with a maximum at $R \approx 12.75$ a.u.. For larger distances, the dependence on R^{-6} in the two-center Auger decay rate becomes dominant. The same behaviour is explained in more detail in Sec. 3.3.1 and can be seen in Fig. 22. The numerical calculation employing $Z = Z_A$ for the Coulomb wave function yields a cross section of $\sigma_{\text{Li}}^{(1)} \approx 1.381$ a.u. for the one-center pathway, matching the value obtained from the Lotz formula [22].

For energies $k^2/2$ of the emitted electron around resonance, the ratio $\eta_k^{(2)}$ features a peak (see Fig. 40), implying the dominance of the indirect ionisation channel over the direct one. However, this large amplification is restricted to a narrow range of emitted electron energies, which can hardly be resolved experimentally. As already estimated in Sec. 4.2, the fully integrated cross section of the two-center process still contributes to the ionisation of an atom A, since the resonance peak is so pronounced. Therefore, partial cross sections $\sigma_{\text{part}}^{(1,2)}$ with a resolvable energy range around the resonance are considered. The energy-differential cross sections are integrated over an energy interval of 1 eV around the resonance

$$\sigma_{\text{part}}^{(M)} = \int\limits_{\frac{k_0^2}{2}-0.5\,\text{eV}}^{\frac{k_0^2}{2}+0.5\,\text{eV}} d\varepsilon_k \frac{d\sigma^{(M)}}{d\varepsilon_k}. \tag{4.33}$$

The resolution of electron energies in electron-impact experiments ranges from a fraction of an eV [166] to a few eV [167], also depending on the target. The resulting ratio $\eta_{\text{part}}^{(2)} = \frac{\sigma_{\text{part}}^{(2)}}{\sigma_{\text{part}}^{(1)}}$ is plotted against the internuclear distance R in Fig. 42.

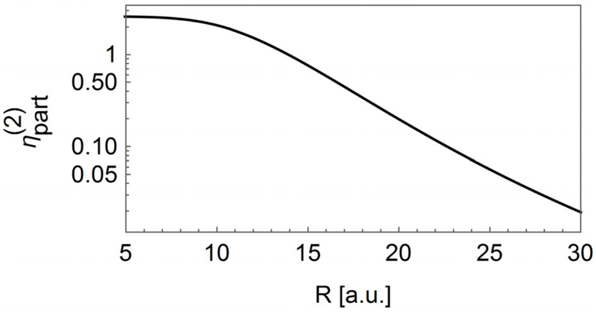

Figure 42: Ratio of the partial cross sections for the electron-impact ionisation of lithium at an incident electron energy of $\frac{p_{\text{in}}^2}{2} = 1\,\text{keV}$, where $\mathbf{p}_{\text{in}} \parallel \mathbf{e}_z$.

Note, that the direct ionisation pathway does not depend on the internuclear distance. Consequently, the value for the partial two-center cross section is divided by a constant, yielding the ratio depicted in Fig. 42. Considering this restricted interval of electron energies, a substantially larger relevance of the two-center process reaching values $\eta_{\text{part}}^{(2)} > 1$, can be observed than seen previously regarding the ratio of the total cross sections in Fig. 37. Consequently, the two-center pathway greatly influences the electron-impact ionisation in a measurable interval of ejection energies.

Within the approach, where the system is considered to consist of two separate atoms, the two-center pathway strongly contributes to the total electron-impact ionisation cross section for emitted electrons with an energy close to resonance. While the amplification is mostly enhanced in a small interval of energies, the ratio of partial cross sections shows that the indirect process is contributing even when integrating around a resolvable electron energy.

4.3.2 Interference of the two processes

Next, the different characteristics of the complete two-center process involving quantum interference are investigated. As explained before, the two pathways of electron-impact ionisation can interfere since they share the same final state. Therefore, the ratio of the energy-differential cross sections

$$\eta_k^{(12)} = \frac{d\sigma^{(12)}/d\varepsilon_k}{d\sigma^{(1)}/d\varepsilon_k} \tag{4.34}$$

is considered. Again, the direct ionisation process of helium competes, but does not interfere with the ionisation processes of lithium. The fully integrated one-center cross section for lithium exceeds the one for helium by more than an order of magnitude [22]. The singly differential cross sections show this behaviour only for small ε_k. Around resonance, one has $d\sigma^{(1)}_{\text{He}}/d\epsilon_k \approx d\sigma^{(1)}_{\text{Li}}/d\varepsilon_k$. This may lead to the conclusion that the background of ejected electrons from impact ionisation of helium as well as the total loss of neutral helium atoms by this process are not very severe. Since atom B and its associated electron are shifted by the internuclear distance $\mathbf{R}$, the transition amplitude for the two-center electron-impact ionisation contains a phase shift $e^{i\mathbf{qR}}$. While this phase shift cancels out for the calculation of the two-center cross sections as well as the ratio η_k, it remains within the mathematical description of the full process $S^{(1+2)} = S^{(1)} + S^{(2)}$.

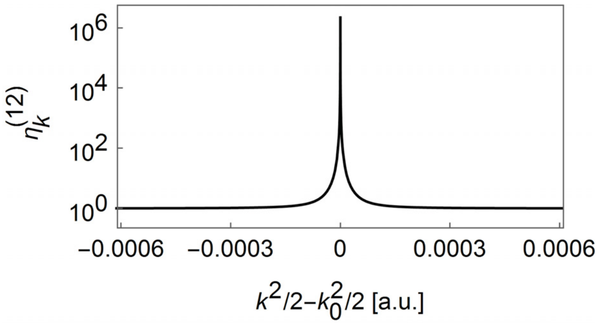

Figure 43: Ratio $\eta_k^{(12)}$ for the electron-impact ionisation of lithium at an incident electron energy of $\frac{p_{\text{in}}^2}{2} = 1\,\text{keV}$, where $\mathbf{p}_{\text{in}} \parallel \mathbf{e}_z$.

In Fig. 43, the ratios $\eta_k^{(12)}$ of cross sections are depicted for a small range of energies $\varepsilon_k = k^2/2$ around the resonance. The ratio between the cross section including the interference of both transition amplitudes $S^{(1)}$ and $S^{(2)}$ and the one-center process takes values close to 1 for ejected electron energies ε_k off resonance. Therefore, the total cross section resembles the smooth curve of the one-center process for most values of k. For a resonant energy of the emitted electron $k^2/2$, however, the ratio experiences the peak, which has already been observed in Fig. 40. The peak representating a tremendous amplification is characterised by a narrow width. As explained before in Sec. 3.3.1, the interference of two pathways creates, in general, a Fano profile, where a peak-shaped minimum leads to an asymmetric curve of the ratio of cross sections. However, in Fig. 43, no Fano profile can be observed. Now, this behaviour is further investigated. When calculating the cross section from the transition amplitude $S^{(12)}$, the expression consists of the individual cross sections $\sigma^{(1)}$ and $\sigma^{(2)}$ as well as a mixed term

$$\sigma^{(12)} = \frac{1}{p_{\text{in}}} \int \frac{d^3p_{\text{f}}}{(2\pi)^3} \int \frac{d^3k}{(2\pi)^3} \frac{1}{\tau} \left(\left|S^{(1)}\right|^2 + \left|S^{(2)}\right|^2 + \underbrace{\left(S^{(1)*}S^{(2)} + S^{(1)}S^{(2)*}\right)}_{\to\mathcal{M}} \right). \tag{4.35}$$

Since $\sigma^{(1)}$ and $\sigma^{(2)}$ have already been considered, the mixed term is now visualised. Therefore, integration is performed in order to obtain a cross section including only the mixed terms. However, a multidifferential cross section is considered, since the ratio of the energy-differential cross sections $\eta_k^{(12)}$ does not give a significant Fano profile, as can be seen in Fig. 43. Consequently, parameters for the angles Ω_k, Ω_{f} as well as the incident electron momentum $\mathbf{p}_{\text{in}}$ have to be fixed, when plotting against the energy of the ejected electron $k^2/2$ with respect ot the resonant energy $k_0^2/2$. This value is going to be called $\mathcal{M}$. Note, that again, the cross section does not depend on the angles φ_{f} and φ_k, which is why these integrations are carried out.

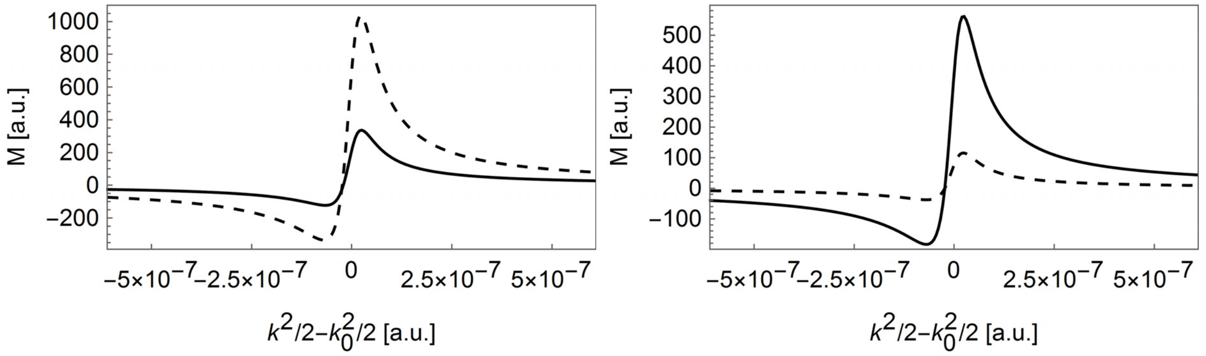

Figure 44: Multidifferential cross section $\mathcal{M}$ of the electron-impact ionisation of lithium at an incident electron energy of $\frac{p_{\mathrm{in}}^2}{2} = 1\,\mathrm{keV}$, where $\mathbf{p}_{\mathrm{in}} \parallel \mathbf{e}_z$. The internuclear distance is $R = 20\,\mathrm{a.u.}$. Left: Fixed angle $\theta_k = \pi/10$ and varied angle $\theta_{\mathrm{f}} = 0.001$ (black, solid) and $\theta_{\mathrm{f}} = 0.01$ (black, dashed). Right: Fixed angle $\theta_{\mathrm{f}} = 0.01$ and varied angle $\theta_k = \pi/20$ (black, solid) and $\theta_k = \pi/100$ (black, dashed).

The asymmetry of the term considered is apparent and shows that interference of the two ionisation pathways occurs. However, the minimum is not as pronounced as in Fig. 24, but reduced to only a small dip. Furthermore, when integrating over the polar angles, the asymmetry becomes unobservable. This can be explained when considering varying combinations of the polar angles. For other polar angles, $\theta_{\mathrm{f}} = \pi/2$ for example, the orientation of the curve is flipped, showing a minimum where the peak appears in the curves of Fig. 44. Therefore, the integration over the polar angles leads to the different shapes of the Fano profile balancing out. Thus, the asymmetry becomes negligible.

4.3.3 Angular distribution of the ejected electron

After investigating the energy-differential two-center electron-impact ionisation cross section, the angular distribution of the ejected electrons is considered. As shortly mentioned in Sec. 2.1.2, the angular distribution of ejected electrons in the direct process of electron-impact ionisation heavily depends on the momentum transfer $\mathbf{q}$, and therefore also on the incident energy $p_{\mathrm{in}}^2/2$. The angular distribution of electrons emitted due to electron impact has been theoretically studied in various systems, for example in the simple system of atomic hydrogen [168] as well as in the intraatomic Auger process in Na [169]. The most sophisticated theories include distortions of the wave functions of both the target and the projectile, Coulombic interactions, exchange effects and post-scattering interactions, and are comparable to experimental data on hydrogen, helium, the noble gases as well as alkali and earth-alkali metals [170]. Commonly, experiments are carried out by fixing the energy and the angle of the scattered projectile and by measuring the probability for the ejected electron to be emitted depending on the angle in a plane, defined by the projectile's initial and final momenta (coplanar plane) [170]. (e,2e)-experiments have been carried out on more complex systems in the perpendicular plane, where the momentum of the incident electron and the outgoing electrons are perpendicular to each other [171].

Here, the focus lies on the differences between the direct and the indirect ionisation process. For this purpose, the doubly differential cross section

$$d^2\sigma^{(2)}/d\theta_k d\varepsilon_k \tag{4.36}$$

is calculated on resonance. Note, that the factor $\sin\theta_k$, which results from the Jacobi determinant, remains in the expression. The polar angle θ_k of the ejected electron is measured with respect to the momentum $\mathbf{p}_{\text{in}} = p_{\text{in}}\mathbf{e}_z$ of the incident electron. Two orientations of the linking vector are considered, $\mathbf{R}_\perp = \frac{R}{\sqrt{2}}(\mathbf{e}_x + \mathbf{e}_y)$ and $\mathbf{R}_\parallel = R\mathbf{e}_z$. For the sake of clarity and comparability to the values calculated in Sec. 4.3, the plot is restricted to $R = 20\,\text{a.u.}$. Again, it has to be noted that in a gas of LiHe dimers, the linking vectors are, in general, randomly oriented. Hence, the experimental detection of the dependence of the ejected electron's angular distribution on the linking vector $\mathbf{R}$ would require a prealignment. First, cross sections for the direct ionisation pathway as well as the indirect channel, including all intermediate states $m = -1, 0, 1$, are presented in Fig. 45.

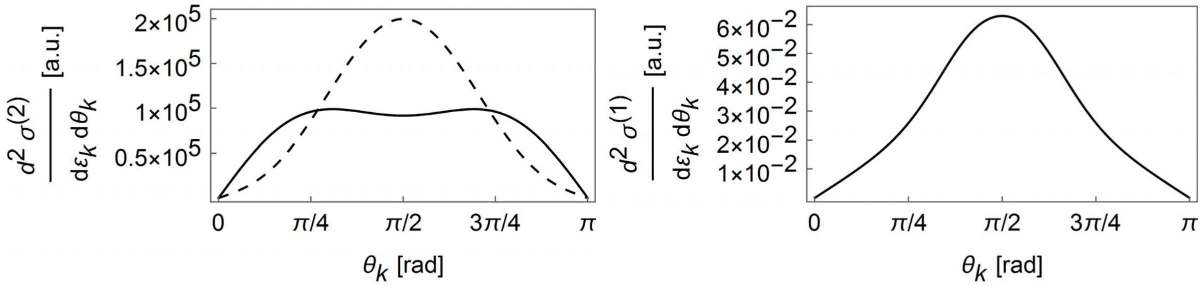

Figure 45: Doubly differential cross sections $d^2\sigma/d\theta_k d\varepsilon_k|_{k=k_0}$ in the system of LiHe for an internuclear distance $R = 20\,\text{a.u.}$, incident energy $p_{\text{in}}^2/2 = 1\,\text{keV}$ and resonant energy $k_0^2/2$ of the emitted electron. Left: Values for two-center electron-impact ionisation of lithium with interatomic orientations $\mathbf{R}_\perp = \frac{R}{\sqrt{2}}(\mathbf{e}_x + \mathbf{e}_y)$ (black dashed) and $\mathbf{R}_\parallel = R\mathbf{e}_z$ (black solid), respectively. Right: Values for the one-center ionisation of lithium. The internuclear distance does not play any role for the direct channel.

In both cases, there is no dependence on the azimuthal angle φ_k. Furthermore, the three curves are all symmetric with respect to the reflection at $\theta_k = \pi/2$. The angular distribution of the direct ionisation process features a maximum for $\theta_k = \frac{\pi}{2}$, as described in Sec. 2.1.2. The orientation of the linking vector $\mathbf{R}$ has no effect, since the helium atom does not partake in the process and molecular effects are ignored. The cross section of the indirect pathway of electron-impact ionisation, however, does strongly depend on the orientation of the linking vector. For $\mathbf{R}_\parallel$, the angular distribution shows two slightly pronounced maxima as well as a shallow minimum at $\theta_k = \pi/2$. Thus, this curve illustrates that the two-center electron-impact ionisation can noticably modify the angular dependency of the ejected electron in contrast to the direct pathway. When varying the orientation to $\mathbf{R}_\perp$, one maximum at $\theta_k = \pi/2$ is obtained. While the general form is similar to the one of the one-center process, the curve differs especially in the slopes on the sides.

In order to further analyse the angular dependencies of the indirect ionisation process, the individual contributions of the intermediate states $m = -1, 0, 1$ are plotted. The results are depicted on the right side of Fig. 46 for the two different orientations of $\mathbf{R}$.

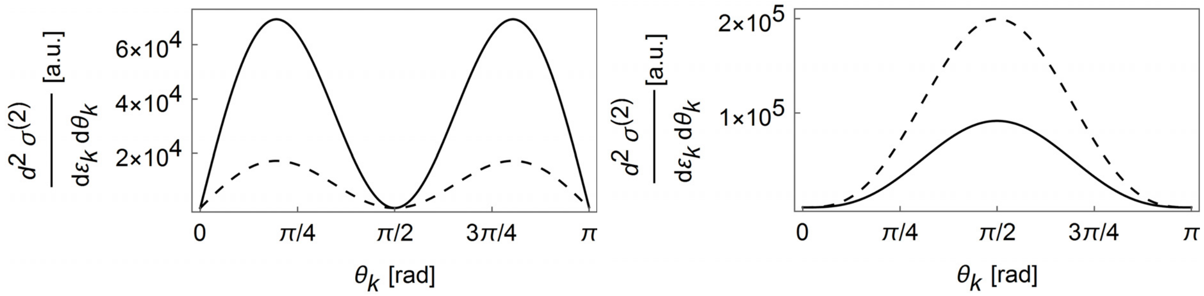

Figure 46: Doubly differential cross sections $d^2\sigma/d\theta_k d\varepsilon_k|_{k=k_0}$ in a LiHe system for an internuclear distance $R = 20\,\text{a.u.}$, incident energy $p_{\text{in}}^2/2 = 1\,\text{keV}$ and energy of the emitted electron $k_0^2/2 \approx 15.8$ eV. The values are depicted for the two-center ionisation of lithium in a LiHe system, with interatomic orientations $\mathbf{R}_\perp = \frac{R}{\sqrt{2}}(\mathbf{e}_x + \mathbf{e}_y)$ (black dashed) and $\mathbf{R}_\parallel = R\mathbf{e}_z$ (black solid), respectively. Left: Cross sections, where only the intermediate state with $m = 0$ is included. Right: Values for the two-center ionisation, considering only the contributions from the excited state $2p_{+1}$ and $2p_{-1}$.

Considering the angular momentum projection $m = 0$ for the $2p$-state in helium, two maxima are obtained as well as a pronounced mimmum at $\theta_k = \pi/2$ for both orientations. When considering $m = +1$, the curves attain one maximum at $\theta_k = \pi/2$. Note, that the curves for $m = -1$ equal those for $m = 1$. This results in a dominance of the terms with $m = \pm 1$ for the interatomic orientation $\mathbf{R}_\perp$. Consequently, the characteristics of the curve with only one maximum resembles the curve on the left side in Fig. 45 for $\mathbf{R}_\perp$ including all excited states. For the parallel orientation $\mathbf{R}_\parallel$, however, all substates yield significant contributions. Therefore, the curve featuring the two pronounced maxima is mixed with the curve with only one maximum. This explains the appearance of the plateau-like curve with the shallow minimum in Fig. 45.
Note, that the individual contributions cannot be 'added up' in order to obtain the full analysis of the curve in Fig. 45. The cross section in Fig. 45 includes the coherent sum over all substates m in the transition amplitude, leading to mixed terms in the cross sections, which were not included in this analysis. However, this individual treatment shows the distinct differences with respect to the direct ionisation channel. The two-center pathway of the electron-impact ionisation clearly modifies the angular distribution of the emitted electrons, since the linking vector $\mathbf{R}$ is included in several places of its mathematical description.

4.3.4 Higher excitations

So far in this section, numerical calculations were restricted to the transition to $1s2p$ in helium. However, excitations to states, requiring a higher transition energy, can occur as well. Therefore, it is crucial to investigate the significance of these higher excitations. For this purpose, the transition to $1s3p$ in helium as atom B is considered. Apart from different matrix elements due to a different wave function of the excited state, the structure of the calculations remains the same and therefore, they will not be repeated here. The transition energy is $\omega_{3p} \approx 0.848\,\text{a.u.}$, which leads to an effective charge of $Z_{\text{He},3p} = 1.228$ in helium. Consequently, the position of the peak is expected to be shifted in comparison to the cross section depicted in Sec. 4.3.1. The altered excitation state also modifies the radiative width to

$$\begin{aligned}
\Gamma^{3p}_{\text{rad}} &= \frac{4\omega^3_{\text{He},3p}}{3c^3}\left|\int\limits_0^{2\pi} d\varphi \int\limits_{-1}^{1} d\cos\vartheta \int\limits_0^{\infty} d\xi \xi^2 \sqrt{\frac{Z^8_{\text{He},3p}}{2\pi^2}}\frac{2}{81}\cos\vartheta \boldsymbol{\xi} e^{-\xi\frac{4}{3}Z_{\text{He},3p}}(6 - Z_{\text{He},3p}\xi)\right|^2 \\
&= \frac{4\omega^3_{\text{He},3p}}{3c^3}\left|\sqrt{\frac{Z^8_{\text{He},3p}}{2\pi^2}}\frac{2}{81}\frac{4\pi}{3}\mathbf{e}_z \int\limits_0^{\infty} d\xi \xi^4 e^{-\xi\frac{4}{3}Z_{\text{He},3p}}(6 - Z_{\text{He},3p}\xi)\right|^2 \\
&= \frac{4\omega^3_{\text{He},3p}}{3c^3}\left|\sqrt{\frac{Z^8_{\text{He},3p}}{2}}\frac{8}{243}\left(\frac{144}{\left(\frac{4}{3}Z_{\text{He},3p}\right)^5} - \frac{120 Z_{\text{He},3p}}{\left(\frac{4}{3}Z_{\text{He},3p}\right)^6}\right)\right|^2 \\
&= 1.87 \times 10^{-8}\,\text{a.u.}. \qquad (4.37)
\end{aligned}$$

While this calculation has been executed employing the excited state $3p_0$, the two other substates with $m = \pm 1$ yield the same value. With respect to the calculated width for the decay from the $1s2p$ state, the radiative width is much smaller, $\Gamma^{3p}_{\text{rad}} \approx 0.3\Gamma^{2p}_{\text{rad}}$. Furthermore, the Auger decay width is changed as well as the two matrix elements including the excited state of helium. For the radiationless deexcitation from $1s3p$, the two-center Auger decay width is smaller than the one for the transition from $1s2p$ for all internuclear distances R. With these changes, the two-center cross section is calculated and compared to the direct ionisation channel, which remains unaltered, since the process does not involve the participation of helium.

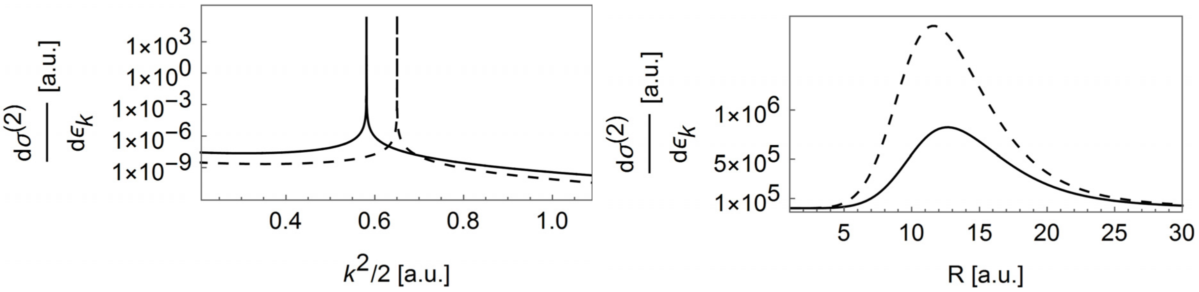

Figure 47: Energy-differential cross sections for the two-center electron-impact ionisation The incident electron energy is $p^2_{\text{in}}/2 = 1\,\text{keV}$. The transition to $1s2p$ in helium is depicted in (black, solid), the transition to $1s3p$ in helium is depicted in (black, dashed). Left side: Dependency of the cross section on the energy of the emitted electron $k^2/2$ for $R = 20\,\text{a.u.}$. Right side: Energy-differential cross section on resonance plotted against the internuclear distance R.

As can be seen in Fig. 47, the resonance peak is shifted to a higher resonant energy of the ejected electron due to the modified transition energy in helium. Furthermore, the peak height of the transition to $1s3p$ surpasses the height of the peak corresponding to the excitation to $1s2p$. However, its width is descreased, leading to a peak that is even more narrow than the one for the transition to $1s2p$. For comparison, the values are listed in Table 23.

	$\frac{d\sigma^{(2)}}{d\varepsilon_k}\big\vert_{R=20\,\text{a.u.}}$	$\Gamma\big\vert_{R=20\,\text{a.u.}}$	$\sigma^{(2)}\big\vert_{R=20\,\text{a.u.}}$	$\frac{d\sigma^{(2)}}{d\varepsilon_k}\big\vert_{R=10\,\text{a.u.}}$	$\Gamma\big\vert_{R=10\,\text{a.u.}}$	$\sigma^{(2)}\big\vert_{R=10\,\text{a.u.}}$
I	2.42×10^5	7.94×10^{-8}	2.82×10^{-2}	5.48×10^5	9.13×10^{-7}	2.96×10^{-1}
II	3.63×10^5	2.08×10^{-8}	4.06×10^{-4}	1.58×10^6	1.56×10^{-7}	1.43×10^{-2}

Table 23: Two-center electron-impact ionisation cross sections and total decay widths for the two different electron-impact excitations $1s2p$ (I) and $1s3p$ (II) for $\mathbf{R} \parallel \mathbf{e}_z$. The total decay width considers the excitation to $m = 0$.

The energy-differential cross sections for the transition to $3p$ surpasses the values for the transition to $2p$ on resonance, see Fig. 47. This is valid for all internuclear distances R, as can be seen on the right side of Fig. 47. However, the fully integrated cross section for the higher excitation cannot reach the values of the $2p$ transition. In Table 23, the difference between the fully integrated cross sections is bigger for larger internuclear distances R. This analysis leads to the conclusion that higher excitations are expected to be insignificant regarding the fully integrated cross sections. Therefore, the sole consideration of the transition to $1s2p$ may not show the full picture of the indirect electron-impact ionisation process in terms of the energy spectrum, but rather amounts to the main contribution to the total yield.

4.4 Summary

In this section, electron-impact ionisation has been studied in a two-center atomic system. Within the process of resonant 2C(e,2e), an atom is ionised due to the presence of a neighbouring atom B. Initially, an autoionising state is created in atom B by electron impact. The deexcitation of this unstable state can lead to a radiationless transfer of energy to atom A via electron-electron interaction. If the transition energy is sufficiently large, atom A can be ionised. This indirect ionisation channel is then compared to the direct ionisation pathway, which represents one of the most fundamental atomic collision processes. The consideration of the two-center process shows considerable effects on the properties of the electron-impact ionisation, which has been well-known for the single center pathway. Particularly, the energy-differential cross section of electron-impact ionisation may be vastly enhanced in a narrow energy range around the resonance ejected electron energy.

Due to the height of the pronounced peak, the two-center channel can provide a fundamental contribution to the cross section of electron-impact ionisation, even to the fully integrated value. The contribution of the indirect ionisation pathway can be stressed even further, when collecting the ejected electron energies within an experimentally resolvable range around the resonance energy. The indirect ionisation process can also lead to the modification of the angular distribution of the ejected electrons. The angular distribution of the two-center process is composed of the contributions of the three substates with $m = -1, 0, 1$. Since these contributions depend on the orientation of the dimer, the different directions lead to varying angular distributions.

Finally, since excitation due to electron impact is not restricted to a particular state, the possibility to excite energetically higher lying states was studied. By means of the $1s3p$ state, it was shown that higher lying excitations can lead to even larger and more pronounced peaks in the energy-differential cross section. However, its fully integrated values cannot attain the values for the transition to the $1s2p$ state since the decreased width of the resonant peak cannot be balanced by the peak height. Therefore, the analysis performed on the excitation to $1s2p$ provides a good insight into the process.

These predictions may be tested experimentally using heteroatomic van der Waals molecules, like LiHe oder HeNe as already described in Sec. 3. Since the experimental investigation automatically includes the motion of the nuclei, it is helpful to incorporate molecular effects into the mathematical description of the two-center electron-impcat ionisation.

5 Influence of the nuclear motion on two-center electron-impact ionisation

In the previous section, two-center electron-impact ionisation was studied assuming fixed nuclei. As in Sec. 3, where the nuclear motion was included in the calculation of two-center photoionisation, the mathematical description of 2C(e,2e) of Sec. 4 is expanded.

The effects of the molecular motion may also influence the characteristics of the electron-impact ionisation in a heteroatomic dimer, which has been described for fixed nuclei in Sec. 3.2. The mathematical description of both the electronic transition and the inclusion of the molecular effects has already been discussed in the sections Sec. 3 and Sec. 4. Therefore, the focus lies on differences between the two ionisation processes with regard to the effects of nuclear motion as well as on the influence of the numerical methods used.

With respect to the process of photoionisation, the description of indirect ionisation via electron-impact is expected to be of larger numerical effort. This is due to the fact that three electronic substates have to be included in the calculation of the transition amplitude. Furthermore, the balance of energy complicates the calculation, since it includes the energy of the incident and scattered electron as well as the emitted electron. Moreover, the expression for the two-center cross section includes the momentum transfer $\mathbf{q}$, which depends on the polar angle of the scattered electron.

However, this complexity also lends itself to further study the process of two-center electron-impact ionisation. As in Sec. 3.4, results will be given for the potential curves calculated in Sec. 3.3.2 as well as for the potential curves from literature. By doing this, the dependencies of the two-center cross-section can be further studied.

5.1 Theoretical description

As explained in Sec. 4, the first step within the two-center electron-impact ionisation process, which is the excitation via electron impact, is not restricted to a selected electronic state. This is in contrast to the dipole selection rules, which apply in the case of photoexcitation. Therefore, the theoretical description of the two-center electron-impact ionisation process requires the inclusion of the excitation to all substates of $1s2p_m$ in helium. As applied in Sec. 4 and investigated in Sec. 4.3.4, however, the consideration is restricted to the excitation of one electron to $n = 2$ in helium. This simplifies the mathematical description while including the transition which is most significant with respect to the fully integrated cross section.

Therefore, the potential surfaces associated with the excited state $1s2p_{\pm1}$ in helium need to be computed in order to include all possible transitions to $1s2p$. Note, that other transitions to states with $n > 2$ are neglected, see Sec. 4.3.4. The three substates $1s2p_m$ are accounted for by the summation of the individual transition amplitudes.

The calculation of the two-center cross section is executed as described in Sec. 3 and Sec. 4. Again, a Morse fit to the potential surfaces yields the parameters for the vibrational wave functions describing the nuclear motion. These are included in the calculation of the decay width, which no longer depends on the internuclear distance R but rather on the vibrational level of the intermediate state ν_a and marginally on ν_f. Furthermore, the overlap of the vibrational wave functions is calculated for every transition. This also applies to the calculation of the direct cross section. As a consequence of the numerous substates, both electronic and vibrational, the cross section includes the summation over m and ν_a in the transition amplitude as well as the summation over ν_f of the integrated expressions. Note, that each electronic substate supports its individual vibrational levels and corresponding energies and wave functions. The amount of bound vibrational levels depends on the potential energy curve which can be different for every electronic substate. Therefore, the notation of the vibrational levels requires an additional index m. In the following, the electronic substate will always be mentioned.

With these considerations, the transition amplitudes read

$$S^{(2)}_\mathrm{mol} = -2\pi i \sum_{m} \sum_{\nu_{\mathrm{a},m}} \delta(E_{\mathbf{p}_\mathrm{f},\mathbf{k},g} + E_\mathrm{f}(\nu_\mathrm{f}) - E_{\mathbf{p}_\mathrm{in},g,g} - E_\mathrm{i}(\nu_\mathrm{i}))\times \frac{\langle \Phi_{\mathbf{k},g}\Psi_{\mathbf{k},g}|V_{AB}(\mathbf{R})|\Phi_{g,e}\Psi_{g,e}\rangle\langle\Phi_{g,e}\Psi_{g,e}|W^e_B|\Phi_{g,g}\Psi_{g,g}\rangle}{\Delta + \frac{i}{2}(\Gamma^B_\mathrm{rad} + \bar{\Gamma}^B_\mathrm{aug}(\nu_\mathrm{a}, m))} \tag{5.1}$$

and

$$S^{(1)}_\mathrm{mol} = -2\pi i \delta(E_{\mathbf{p}_\mathrm{f},\mathbf{k},g} + E_\mathrm{f}(\nu_\mathrm{f}) - E_{\mathbf{p}_\mathrm{in},g,g} - E_\mathrm{i}(\nu_\mathrm{i}))\langle \Phi_{\mathbf{k},g}\Psi_{\mathbf{k},g}|W^e_A|\Phi_{g,g}\Psi_{g,g}\rangle, \tag{5.2}$$

where the detuning $\Delta = \frac{p^2_\mathrm{in}}{2} + E_\mathrm{i}(\nu_\mathrm{i}) - E_{\mathrm{a},m}(\nu_{\mathrm{a},m}) - \frac{p^2_\mathrm{f}}{2}$ now depends on the vibrational energies, as defined in Sec. 3.2.2. Note, that the two-center decay rate $\bar{\Gamma}^B_\mathrm{aug}(\nu_\mathrm{a}, m, \nu_\mathrm{f})$ depends on the vibrational levels of the intermediate and final state.

5.2 Results

The inclusion of molecular features with respect to the one-center and two-center pathways has shown a strong sensitivity to the fit parameters in the context of photoionisation in Sec. 3. Nonetheless, the mostly analytical approach enables the analysis of the underlying processes and is therefore applied to ionisation after electron impact. While the deviations within the calculation of the potential curve for the excited state in helium have been made apparent in Sec. 3.4, results for the associated method described in Sec. 3.3.2 will be presented for comparison. However, the focus lies on the calculations applying the literature values for the intermediate and final state taken from [18] and [128].

Firstly, the potential curves are presented for both the simplified calculations described in Sec. 3.3.2 as well as for the literature values, enabling a comparison between the two. From these, the vibrational wave functions are obtained via the fitting of a Morse potential and are included in the expressions for the cross sections. Since the general form of the vibrational wave functions obtained from the Morse potential has already been described in Sec. 3.3.2, the characteristics of the two-center cross section for electron-impact ionisation can be analysed. Again, emphasis lies on the impact of the different potential energy curves and the consequences for the decay widths, Franck-Condon factors as well as the energies of the resonances. Since the inclusion of the molecular effects requires the summation over all electronic and vibrational intermediate states within the transition amplitude as well as the summation over all final vibrational states in the cross section, the numerical effort with respect to the calculation of the cross sections inflates tremendously.

Therefore, multidifferential cross sections are presented in order to keep the numerical effort manageable. Hereby, the effects of the molecular motion can be analysed not only with respect to the ejected electron but also to the incident electron, which is scattered.

5.2.1 Potential energy surface

Here, the potential curves used in the following calculations are presented. At first, the interaction potentials from the calculations described in Sec. 3.3.2 and proposed in [79] are depicted in Fig. 48. The potential curves for the electronic ground and final state as well as for the intermediate state with $m = 0$ remain unaltered with respect to the values presented in Sec. 3.3.2. However, the interaction between the ground state in lithium and the excited state $1s2p_{\pm 1}$ of helium has to be calculated.

Note, that the potential curve of the initial state, as calculated in Sec. 3.3.2, shows a good agreement with values from literature, see [79]. Therefore, this curve will be included in both calculations without any alterations and is only shown once.

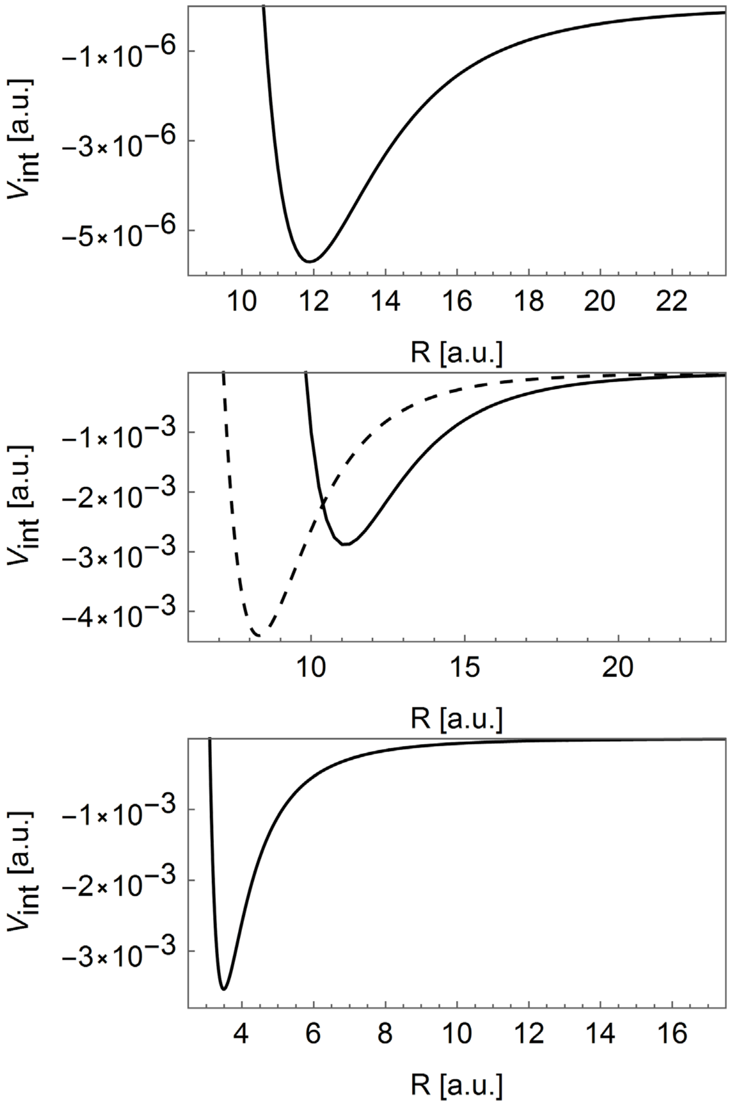

Figure 48: Calculated potential energy curves for the electronic configurations involved in 2C(e,2e) of LiHe. Upper panel: Initial state with both electrons in their ground state. Middle panel: Intermediate states. Plot with $2p_0$ (black, solid) as well as $2p_{\pm 1}$ (black, dashed). Lower panel: Final state with helium being back in its ground state and lithium being ionised.

First note, that the calculations yield the same potential curves for the two substates $m = -1$ and $m = 1$ of the electronic intermediate state. As shown in the middle panel of Fig. 48, the calculation of the potential surface of the $1s2p_{\pm 1}$ leads to a curve, whose minimum is shifted to a smaller internuclear distance R than the minimum calculated for $m = 0$. Furthermore, the depth of the potential is larger than the one for $1s2p_0$. This modification of the potential curves is expected to facilitate the transition between the intermediate and final state with respect to the overlap of the vibrational wave functions, since the two potential minima involved are closer to each other. However, the collisional excitation is expected to be hindered, as the distance between the initial and intermediate potential minima is increased.

The Morse fit yields 11 bound vibrational levels for the configuration $1s2p_{\pm 1}$ in helium, which are included in the transition amplitude of the two-center cross section.

Now, the literature values are considered. Here, the interaction curve for the intermediate state $m = 0$, as well as the potential curve of the final state, already presented in Sec. 3.4, are included. Furthermore, the curves for the substates $m = \pm 1$ are added. As discussed in Sec. 3.4, the potential curves for the intermediate state are taken from [102, 117], whereas the potential curve for the final state stems from [128], since the literature values for all bound vibrational energy levels are provided there.

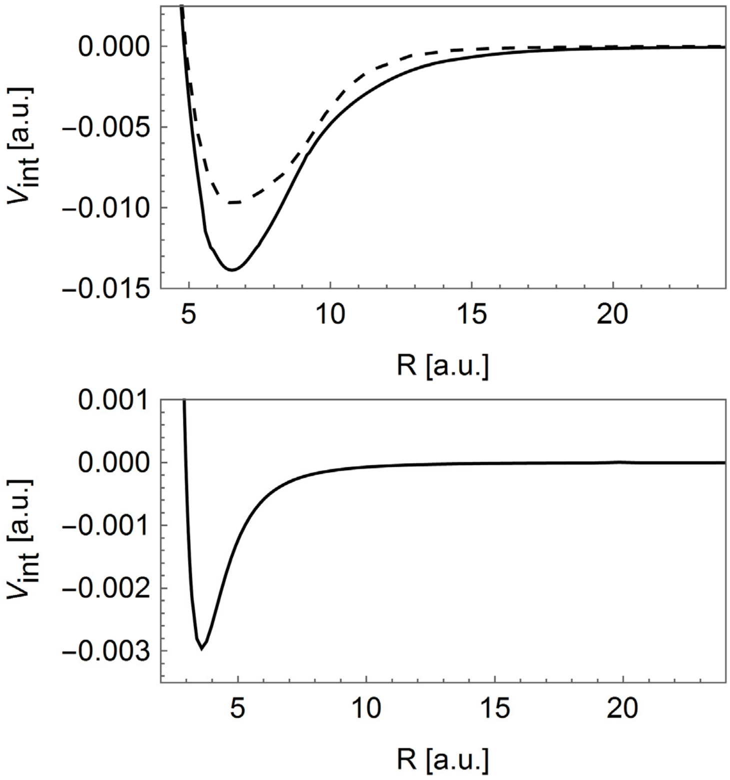

Figure 49: Literature values for the potential energy curves for the electronic configurations involved in 2C(e,2e) of LiHe. Upper panel: Intermediate states: Plot for the excitation to $2p_0$(black, solid) as well as for $2p_{\pm1}$ (black, dashed). Values are taken from [102, 117]. Lower panel: Final state with helium back in its ground state and ionised lithium. Values are from [128].

Firstly, the potential curves for the two substates $m = \pm1$ of the intermediate state equal each other, as do the calculated itneraction potentials in Fig. 48. However, the two potential curves share the position of the minimum, in contrast to the calculations leading to the results in Fig. 48. Furthermore, the minimum is shifted to a significantly smaller internuclear distance R with respect to the values presented in Fig. 48. As already investigated in Sec. 3.4, a reduced equilibrium distance of the intermediate state leads to an enlarged width of the two-center Auger decay, which is crucial for the magnitude of the cross section regarding the two-center electron-impact ionisation. Since the potential minimum for the two substates $m = \pm1$ in Fig. 48 is shifted to smaller internuclear distances, the difference in the results is larger for the substate $m = 0$. The depth of the interaction potential for $2p_0$ is larger than that for $2p_{\pm1}$. This feature is opposite to the characteristics found within the curves in Fig. 48. Furthermore, the curve for $2p_{\pm1}$ exhibits a broader shape near the potential minimum. For the excited state $2p_{\pm1}$ in helium, 27 bound vibrational levels were found in [117], which is 7 more than supported by the interaction potential for $2p_0$. Despite the smaller depth, the broader curve allows for the larger amount of bound vibrational levels.

As explained in Sec. 3.4, the potential curve for the final state in Fig. 49 is similar to the one in the lower panel of Fig. 48, but is favoured, since reference values exist for the vibrational energy shifts, leading to an improvement of the Morse fit.

5.2.2 Decay widths and overlaps

Before calculating the cross sections, decay widths from the intermediate state He($1s2p_{\pm1}$)-Li($1s^2 2s$) are analysed. Furthermore, the Franck-Condon factors including the substates $m = \pm1$

are presented in order to compare the differences between the three excited substates. Note, that all other Franck-Condon factors remain unaltered compared with the values calculated in Sec. 3.3.2 and Sec. 3.4, respectively. For the calculated potential curves, the associated values can be found in Tables 4, 5 and 6. For the improved calculations using the literature values for the potential curves, the Franck-Condon factors are depicted in Tables 15, 17 and 19, where the fitting parameter α is set to 0.58. This Morse parameter is also included in the following calculations for the cross sections.

To begin with, these values are evaluated for the calculated interaction curves depicted in Fig. 48. Again, only those including the new intermediate state $1s2p_{\pm1}$ are illustrated here. Apart from the Morse parameters presented in Table 3, the following parameters were extracted for the intermediate state with $m = \pm1$:

R_{eq}	D	α
8.3	4.4×10^{-3}	0.56

Table 24: Fitted Morse parameters (in a.u.) for the calculated interaction potential curve of the intermediate state $1s2p_{\pm1}$ in helium.

These parameters are inserted into the Morse vibrational wave function in Eq. (3.26). For the description of the two-center ionisation process via the calculated potential curves in Sec. 3.3.2, the total decay widths are given in Table 25 with respect to the deexcitation from $2p_{\pm1}$. Note again, that the values for $m = 0$, depicted in Table 7, are extracted from the cross section data. Here, however, the decay widths are calculated for a fixed vibrational level of the final state, $\nu_{\mathrm{f}} = 5$. Note, that the averaged two-center Auger decay width $\bar{\Gamma}_{\mathrm{aug}}$ is multiplied by 2 in order to account for the two valence electrons in helium.

ν_{a}	Γ	ν_{a}	Γ	ν_{a}	Γ
0	5.30×10^{-7}	4	3.63×10^{-7}	8	1.96×10^{-7}
1	4.88×10^{-7}	5	3.21×10^{-7}	9	1.54×10^{-7}
2	4.46×10^{-7}	6	2.79×10^{-7}	10	1.10×10^{-7}
3	4.05×10^{-7}	7	2.38×10^{-7}		

Table 25: Total decay widths $\Gamma = \Gamma_{\mathrm{rad}} + 2\bar{\Gamma}_{\mathrm{aug}}$ for the deexcitation of the state $1s2p_{\pm1}$ in helium for the calculations illustrated in Sec. 3.3.2. The vibrational level is set to $\nu_{\mathrm{f}} = 5$, since this transition contributes the largest decay widths.

The values in Table 25 are comparable to those in Table 7 for the transition from $1s2p_0$. While the alignment of $\mathbf{R}$ along the z-axis reduces the value of Γ_{aug} from $1s2p_{\pm1}$, the shift of the potential minimum to smaller internuclear distances leads to larger contributions from smaller R in the process of averaging over the vibrational wave function of the intermediate state, resulting in larger values for the two-center Auger decay width.

Furthermore, the overlaps of the vibrational wave functions are considered. The final state remains unaltered, which is why only the Franck-Condon factors FC_{ia} and F_{af} are given here. The overlap for the direct ionisation process is tabulated in Sec. 3.3.2, Table 4.

While for small vibrational levels ν_{a}, the values of FC_{ia} are smaller than those presented in

ν_a	FC_ia	ν_a	FC_ia	ν_a	FC_ia
0	2.49×10^{-2}	4	6.19×10^{-2}	8	1.49×10^{-1}
1	2.65×10^{-2}	5	7.57×10^{-2}	9	1.94×10^{-1}
2	3.90×10^{-2}	6	9.53×10^{-2}	10	2.84×10^{-1}
3	4.74×10^{-2}	7	1.18×10^{-1}		

Table 26: Franck-Condon factors FC_ia for the excitation to the state $1s2p_{\pm 1}$ in helium. The excited state in LiHe dimer is described by the potential curve from Fig. 48. The only bound vibrational level of the initial state is $\nu_\text{i} = 0$.

Table 5 for the substate $m = 0$, the overlaps become similar for higher vibrational levels. This can be explained by the shifted position of the potential minimum for the excited state. As a consequence, small vibrational levels ν_a cannot provide an overlap similar to the one produced by the wave functions associated to two potential minima situated more closely to each other. For larger vibrational excitations, however, the vibrational wave function is spread out more and therefore, larger overlaps with wave functions for largely different equilibrium distances are enabled.

The overlap of the vibrational wave functions involved in the process of radiationless energy transfer and subsequent ionisation depends on both vibrational levels ν_a and ν_f and therefore leads to an overpowering amount of Franck-Condon factors. Hence, only two vibrational levels of the final state $\nu_\text{f} = 0$ an $\nu_\text{f} = 5$ are considered in the following table.

ν_a	FC_af	ν_a	FC_af	ν_a	FC_af
0	4.22×10^{-10}	4	2.03×10^{-9}	8	2.56×10^{-9}
1	-7.27×10^{-10}	5	-2.37×10^{-9}	9	-2.23×10^{-9}
2	1.16×10^{-9}	6	2.59×10^{-9}	10	1.63×10^{-9}
3	-1.61×10^{-9}	7	-2.66×10^{-9}		
ν_a	FC_af	ν_a	FC_af	ν_a	FC_af
0	8.98×10^{-4}	4	4.72×10^{-4}	8	2.79×10^{-4}
1	-5.34×10^{-4}	5	-4.17×10^{-4}	9	-2.25×10^{-4}
2	5.98×10^{-4}	6	3.75×10^{-4}	10	1.56×10^{-4}
3	-4.96×10^{-4}	7	-3.28×10^{-4}		

Table 27: Franck-Condon factors FC_af for the excitation to the state $1s2p_{\pm 1}$ in helium. The excited state in LiHe dimer as well as the potential curve for the final state are given by the values in Fig. 48. The vibrational level of the final state is set to $\nu_\text{f} = 0$ for the upper table and $\nu_\text{f} = 5$ in the lower table.

When comparing these values to the ones for the transition from $1s2p_0$, which are presented in Table 6, the overlaps are, in general, larger than those for the excited state $2p_{\pm 1}$ in helium. For $\nu_\text{f} = 0$, the values in Table 27 are larger by 5 orders of magnitude while the Franck-Condon factors for $\nu_\text{f} = 5$ are only larger by one order of magnitude. This seems reasonable, since, due to the shifted potential minimum of the intermediate state, the two potential minima are closer to each other as is the case for the state $2p_0$. Furthermore, for a large vibrational level of the final state, the corresponding wave function reaches large internuclear distances, enabling a larger overlap with the wave funtion of the intermediate state.

Now, these values are also calculated for the vibrational wave functions corresponding to the improved potential curves, as explained in detail in Sec. 3.4 for the process of photoionisation. Therefore, the decay widths and Franck-Condon factors have already been presented for all transitions including the intermediate state $1s2p_0$ in helium. Hence, the remaining values associated with the intermediate state $1s2p_{\pm1}$ are presented here. For this curve, the Morse parameters are the following:

R_{eq}	D	α
6.6	9.67×10^{-3}	0.3575

Table 28: Morse parameters (in a.u.) fitted to the interaction potential curve of the intermediate state $1s2p_{\pm1}$ from [102, 117].

Note, that the Morse parameter α is chosen, as discussed in Sec. 3.4, such that it takes the biggest value for which the last vibrational level $\nu_{\mathrm{a}} = 26$ still yields a bound wave function. This method was also applied in order to extract the value $\alpha = 0.58$ for the intermediate state $1s2p_0$ in Sec. 3.4. As investigated there, the fit parameter α strongly influences the vibrational wave function and therefore impacts the Franck-Condon factor as well as the Auger decay width. In order to visualise this aspect even further, a small insertion is made showing the vibrational wave function of the intermediate state $1s2p_{\pm1}$ for two different fit parameters α. In Fig. 50 the vibrational wave function is calculated with the parameters D and R_{eq} from Table 28. The two different values of α represent the smallest and the largest value in order to obtain exactly 27 bound vibrational levels.

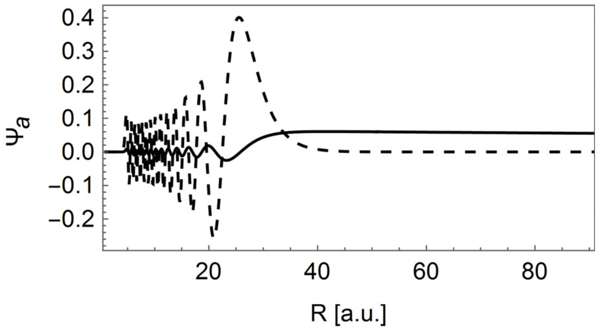

Figure 50: Plot of the vibrational wave functions of the last bound vibrational level $\nu_{\mathrm{f}} = 26$ with parameters D and R_{eq} from Table 28. The solid curve stems from $\alpha = 0.3575$, whereas the dashed curve is calculated with $\alpha = 0.345$.

The two curves show two different behaviours. While the wave function for $\alpha = 0.345$ strongly oscillates with a rather large, increasing amplitude for small R, it decreases rapidly for larger internuclear distances. The fitting parameter $\alpha = 0.3575$, however, yields a wave function which features oscillations with small amplitudes for small internuclear distances. For larger R, the wave function descreases slowly leading to a wave function, which is spread over a large intervall of internuclear distances. This comparison illustrates the sensitivity of the vibrational wave function to the fit parameter. Note, however, that this difference is especially drastic for the last bound vibrational level. As mentioned before, the calculations will continue with the larger value $\alpha = 0.3575$ in order to keep consistency.

Firstly, the total decay widths are given in Table 29 for a fixed value of the final vibrational level $\nu_{\mathrm{f}} = 7$. Again, this vibrational level is chosen since it provides the largest contribution to the decay width.

ν_{a}	Γ	ν_{a}	Γ	ν_{a}	Γ	ν_{a}	Γ
0	1.99×10^{-6}	7	1.76×10^{-6}	14	1.26×10^{-6}	21	5.95×10^{-7}
1	1.98×10^{-6}	8	1.70×10^{-6}	15	1.18×10^{-6}	22	4.91×10^{-7}
2	1.96×10^{-6}	9	1.64×10^{-6}	16	1.08×10^{-6}	23	3.86×10^{-7}
3	1.93×10^{-6}	10	1.57×10^{-6}	17	9.92×10^{-7}	24	2.80×10^{-7}
4	1.89×10^{-6}	11	1.50×10^{-6}	18	8.96×10^{-7}	25	1.74×10^{-7}
5	1.85×10^{-6}	12	1.42×10^{-6}	19	7.98×10^{-7}	26	6.68×10^{-8}
6	1.81×10^{-6}	13	1.35×10^{-6}	20	6.97×10^{-7}		

Table 29: Total decay widths $\Gamma = \Gamma_{\mathrm{rad}} + 2\bar{\Gamma}_{\mathrm{aug}}$ for the deexcitation of the state $1s2p_{\pm 1}$ in helium. The excited state in the LiHe dimer is described by the potential curve from [102, 117], whereas the potential curve for the final state is given by the values in [128]. The vibrational level of the final state is set to $\nu_{\mathrm{f}} = 7$ as in Table 13.

When comparing these widths to the ones in Table 13, the values presented in Table 29 are smaller by less than one order of magnitude. Since the potential curves share their position of the minimum and the shapes of the potential curves are not extremely different, the averaging over the vibrational wave function does not appear to be the main reason for the differences in the decay width. However, the orientation of the vector $\mathbf{R}$, linking the two atoms, strongly influences the value of the two-center decay width. For the alignment of $\mathbf{R}$ along the z-axis, the width resulting from the radiationless energy transfer from $2p_0$ is amplified. In contrast, the decay width for the deexcitation from $2p_{\pm 1}$ is favoured when $\mathbf{R}$ comprises contributions from the x- and y-components. Therefore, the comparison of the total decay width strongly depends on the orientation of internuclear linking vector.

Besides, the Franck-Condon factors are considered for the transitions including the intermediate states. The overlaps of the vibrational wave functions are illustrated in the following tables.

ν_{a}	FC_{ia}	ν_{a}	FC_{ia}	ν_{a}	FC_{ia}	ν_{a}	FC_{ia}
0	2.67×10^{-3}	7	2.97×10^{-2}	14	8.09×10^{-2}	21	1.75×10^{-1}
1	4.74×10^{-3}	8	3.58×10^{-2}	15	8.96×10^{-2}	22	1.99×10^{-1}
2	7.48×10^{-3}	9	4.24×10^{-2}	16	9.87×10^{-2}	23	2.38×10^{-1}
3	1.07×10^{-2}	10	4.93×10^{-2}	17	1.08×10^{-1}	24	2.38×10^{-1}
4	1.46×10^{-2}	11	5.67×10^{-2}	18	1.18×10^{-1}	25	3.19×10^{-1}
5	1.91×10^{-2}	12	6.45×10^{-2}	19	1.29×10^{-1}	26	5.33×10^{-1}
6	2.41×10^{-2}	13	7.25×10^{-2}	20	1.42×10^{-1}		

Table 30: Franck-Condon factors FC_{ia} for the excitation to the state $1s2p_{\pm 1}$ in helium. The excited state in LiHe dimer is described by the potential curve from [102, 117]. The only bound vibrational level of the initial state is $\nu_{\mathrm{i}} = 0$.

ν_{a}	FC_{af}	ν_{a}	FC_{af}	ν_{a}	FC_{af}	ν_{a}	FC_{af}
0	4.22×10^{-6}	7	-8.11×10^{-5}	14	1.76×10^{-4}	21	-1.72×10^{-4}
1	-9.78×10^{-6}	8	9.68×10^{-5}	15	-1.84×10^{-4}	22	1.58×10^{-4}
2	1.74×10^{-5}	9	-1.12×10^{-4}	16	1.89×10^{-4}	23	-1.40×10^{-4}
3	-2.71×10^{-5}	10	1.28×10^{-4}	17	-1.92×10^{-4}	24	2.38×10^{-1}
4	3.86×10^{-5}	11	-1.42×10^{-4}	18	1.92×10^{-4}	25	-8.31×10^{-5}
5	-5.17×10^{-5}	12	1.55×10^{-4}	19	-1.88×10^{-4}	26	6.14×10^{-6}
6	6.60×10^{-5}	13	-1.67×10^{-4}	20	1.82×10^{-4}		

ν_{a}	FC_{af}	ν_{a}	FC_{af}	ν_{a}	FC_{af}	ν_{a}	FC_{af}
0	8.65×10^{-5}	7	1.02×10^{-5}	14	9.10×10^{-5}	21	-4.99×10^{-6}
1	1.04×10^{-5}	8	3.24×10^{-5}	15	-6.05×10^{-6}	22	5.23×10^{-5}
2	-1.57×10^{-4}	9	4.02×10^{-6}	16	8.59×10^{-5}	23	-2.74×10^{-6}
3	1.77×10^{-5}	10	7.05×10^{-5}	17	-6.60×10^{-6}	24	2.38×10^{-1}
4	-1.12×10^{-4}	11	-9.53×10^{-7}	18	7.64×10^{-5}	25	1.87×10^{-6}
5	1.59×10^{-5}	12	8.77×10^{-5}	19	-6.21×10^{-6}	26	4.21×10^{-6}
6	-3.11×10^{-5}	13	-4.27×10^{-6}	20	6.49×10^{-5}		

Table 31: Franck-Condon factors FC_{af} for the excitation to the state $1s2p_{\pm 1}$ in helium. The excited state in LiHe dimer is described by the potential curve from [102, 117] and the potential curve for the final state is given by the values in [128]. The vibrational level of the final state is set to $\nu_{\mathrm{f}} = 0$ for the upper table and $\nu_{\mathrm{f}} = 7$ in the lower table.

The overlaps in Tables 30 and 31 are similar to the values obtained for the excited state $2p_0$ in helium tabulated in Sec. 3.4. Since the Franck-Condon factors remain almost unchanged, whereas the decay widths are reduced, the resulting contributions to the cross section are expected to be amplified in comparison to the ones from the excitation to $2p_0$.

Note, however, that for the calculation of the cross sections, the respective matrix element, included in the description of the radiationless energy transfer, is not only incorporated in the calculation of the two-center Auger decay rate, but also in the numerator of the transition amplitude. Therefore, a reduced two-center Auger decay width also leads to a reduction of the numerator in the transition amplitude.

As described in Sec. 3.4, the modified potential curves strongly increase the decay widths and also influence the Franck-Condon factors with respect to the results stemming from the calculated potential curves. As a consequence, different processes and subprocesses are either favoured or disadvantaged in comparison to the values calculated in the way described in Sec. 3.3.2. With these preliminary results, the cross sections are evaluated next.

5.2.3 Cross sections

Due to the expected multiplet of resonance peaks, a meaningful resolution of the cross sections requires a larger numerical effort compared to the case, where the nuclear distance is fixed, as described in Sec. 4. To ensure the informative value at a reasonable numerical effort, multidifferential cross sections will be shown in the following. In theoretical and experimental studies, processes including electron impact are often described using multidifferential cross sections, resolving dependencies on the angular distribution of both the scattered and the emitted electron as well as their energy distribution. In doing so, an analysis with respect to the various angle dependencies and also to the electron energies is possible.

Here, two multidifferential cross sections for the process of two-center electron-impact ionisation are considered. The cross section can be analysed with respect to the scattered electron, characterised by its momentum $\mathbf{p}_\mathrm{f}$, as well as to the emitted electron with a momentum $\mathbf{k}$. As above, results are shown first for the interaction potential curves calculated as explained in Sec. 3 and depicted in Fig. 39.

Initially, the cross section is considered with respect to the emitted electron. Therefore, the squared transition amplitude from Eq. (5.1) is integrated over the angles concerning the scattered electron $d\Omega_\mathrm{f}$. Furthermore, the integral over the momentum p_f is carried out by applying the Dirac function, which links p_f to k and p_in. Consequently, when fixing the incident electron energy to 1 keV, the differential cross section depends on the momentum and angular distribution of the scattered electron. When integrating over φ_f, the cross section is independent of φ_k. Therefore, values will be given for a fixed polar angle θ_k, with a performed integration over φ_k. Whereas the cross sections is independent of φ_k, it depends heavily on θ_k, as described in Sec. 4.3.3. To begin with, the cross section is calculated for $\theta_k = \pi/2$, where the cross section was found to be maximised, see Sec. 4.3.3. This is also valid within the molecular approach. Note, that due to this method of calculation, the cross sections in this section are not directly comparable to those presented in Sec. 4.

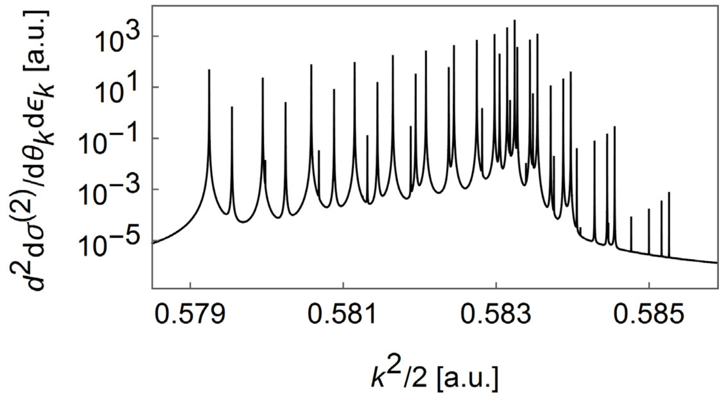

Figure 51: Doubly differential two-center electron-impact ionisation cross section. The polar angle of the emitted electron is set to $\theta_k = \pi/2$ and the energy of the emitted electron varies. The energy of the incident electron is $p_\mathrm{in}^2/2 = 1\,\mathrm{keV}$.

In Fig. 51 the differential cross section is plotted for a fixed polar angle $\theta_k = \pi/2$ and varying momenta k of the ejected electron. As observed in Sec. 3, the single resonance peak is fanned out into a multiplet of peaks. However, the shape of the curve is not as neatly structured as in Sec. 3.3.2. More peaks are visible, of which some are more pronounced than the neighbouring one. On the right side of the distribution, resonance peaks can be seen, whose values cannot keep up with the ones of the left side. As studied in Sec. 4.3.3, the electronic substates yield different angular distributions of the emitted electron, which also depend on the orientation of the linking vector $\mathbf{R}$. For the polar angle $\theta_k = \pi/2$, the substate $m = 0$ does not contribute, as can be seen in the angular distribution in Sec. 4.3.3.

For the electronic substates $m = \pm 1$, 11 bound vibrational levels have been calculated. However, more than 11 resonance peaks are visible in Fig. 51. This is in contrast to the resonance peaks of the 2CPI cross sections depicted in Sec. 3.2.2 and Sec. 3.4, where the amount of resonance peaks equals the amount of bound vibrational levels of the intermediate states included in the calculation. Note, that the vibrational energy levels, and therefore positions of the resonance peaks, are equal for $m = 1$ and $m = -1$, since the potential energy curves are the same.

For a resonance peak to appear, the energy detuning has to vanish in the denominator in Eq. (5.1). The detuning $\Delta = \frac{p_{\mathrm{in}}^2}{2} + E_{\mathrm{i}}(\nu_{\mathrm{i}}) - E_{\mathrm{a},m}(\nu_{\mathrm{a},m}) - \frac{p_{\mathrm{f}}^2}{2}$ contains direct dependencies on ν_{i} and $\nu_{\mathrm{a},m}$ due to the energy shift. However, the only bound vibrational level of the initial state defines the vibrational level $\nu_{\mathrm{i}} = 0$. Furthermore, the momentum of the scattered electron p_{f} can be linked to the momentum of the emitted electron k due to the conservation of energy, which is implied in the Dirac function in Eq. (5.1). Here, also the vibrational level of the final state ν_{f} is included. Consequently, the resonant energies of the emitted electron are not only influenced by the vibrational level of the intermediate state, but also by the one of the final state when plotting the cross section against the energy of the emitted electron. Therefore, more than 11 peaks are produced. 66 peaks would be expected, accounting for 11 levels (0-10) of the intermediate and 6 levels (0-5) of the final state. However, some resonance energies are virtually the same, leading to an overlap of peaks. Furthermore, many vibrational transitions do not contribute to a peak that is large nough to be visible in Fig. 51.

Due to the choice of the polar angle, the calculated cross section does not include conntributions from the substate $m = 0$. Therefore, the cross section is calculated again, while restricting the states to $m = 0$ and $m = \pm 1$, respectively, and choosing suitable polar angles. For the excitation to $m = \pm 1$, the polar angle is again set to $\theta_k = \pi/2$. Therefore, one expects the same plot as shown above. For the excitation to $m = 0$, the investigations in Sec. 4.3.3 show two maxima in the angular distribution. The numerical evaluation leads to one favoured angle of $\theta_k \approx 0.615$. For these two sets of parameters, the two-center cross section is calculated.

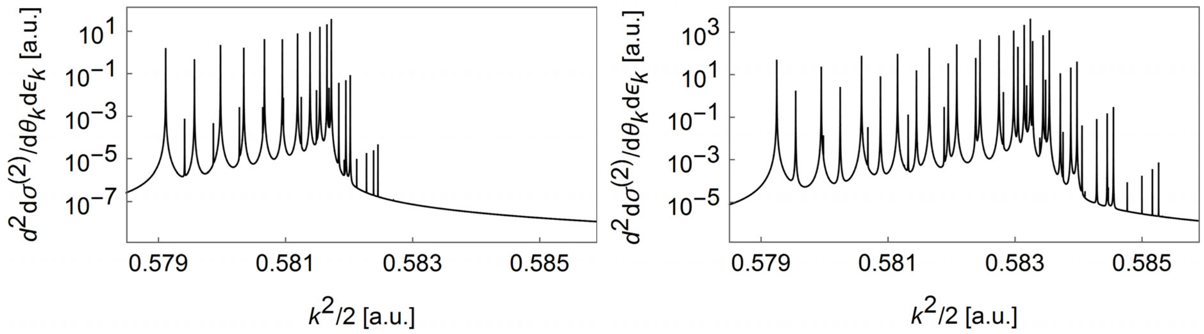

Figure 52: Doubly differential two-center electron-impact ionisation cross sections with restricted electronic substates $m = 0$ on the left side and $m = \pm 1$ on the right side. The polar angle of the emitted electron is set to $\theta_k = \pi/2$ for $m = \pm 1$ and $\theta_k \approx 0.615$ for $m = 0$. The energy of the emitted electron $k^2/2$ varies and the energy of the incident electron is $p_{\mathrm{in}}^2/2 = 1\,\mathrm{keV}$.

The cross section including the excitation to the electronic substate $m = 0$ features a distribution of resonance peaks, which are condensed to the left side of the plot. This means that the resonant energies of the emitted electron is small compared to the values presented in Fig. 51. Furthermore, the peak heights are reduced, with a reduction of the maximum value by two orders of magnitude. Note, however, that for the excitation to $m = \pm 1$, two orientations are included. Moreover, the differences in the Franck-Condon factors and decay widths have been discussed in Sec. 5.2.2.

Although $\theta_k \approx 0.615$ is the optimised polar angle for the transition to $m = 0$, the contribution from $m = \pm 1$ still dominates, as can be seen in Fig. 53.

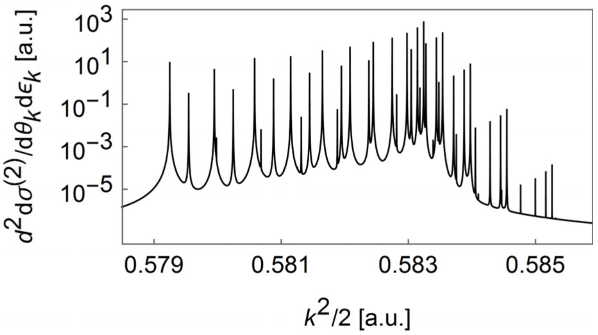

Figure 53: Doubly differential two-center electron-impact ionisation cross section including the transitions to the substates $m = -1$ and $m = 1$. The polar angle of the emitted electron is set to $\theta_k \approx 0.615$. The energy of the emitted electron $k^2/2$ varies and the energy of the incident electron is $p_{\mathrm{in}}^2/2 = 1\,\mathrm{keV}$.

The optimised angles stem from the electron-electron interaction within the transition amplitude in Eq. (5.1). For the transition from $m = 0$, the calculation of the corresponding matrix element yields a dependency on $\mathbf{e}_z$, which results in a factor of $\sin\theta_k \cos^2\theta_k$ in the integral over the squared transition amplitude. For the transition from $m = \pm 1$, however, where the $2p_{\pm 1}$ wave function is employed for helium, the matrix element includes the vector $\mathbf{e}_x \pm i\mathbf{e}_y$. Therefore, the angular dependency in the integral reads $\sin^3\theta_k$, leading to a favoured angle of $\theta_k = \pi/2$.

Next, the cross section is considered with respect to the scattered electron. Therefore, the squared transition amplitude from Eq. (5.1) is integrated over the angles concerning the emitted electron $d\Omega_{\mathrm{k}}$ and the integral over the momentum k is executed by applying the conservation of energy linking the three momenta involved. Again, the relevant polar angle θ_{f} will be fixed, whereas the integration over φ_{f} is performed. Since the momentum transfer $\mathbf{q}$ depends on the polar angle of the scattered electron, the angular distribution with respect to the preference of one or two polar angles is not straightforward. Therefore, two polar angles are chosen for which the cross section is maximised regarding a respective vibrational transition. In general, favoured values of the polar angle are small, particularly in contrast to the favoured angles of the emitted electron. This behaviour is reasonable, since the interaction of the incident electron is assumed to be weak in order to justify the use of perturbation theory. As described in Sec. 2.1.2, a large incident electron energy leads to a small momentum transfer, which goes along with small scattering angles.

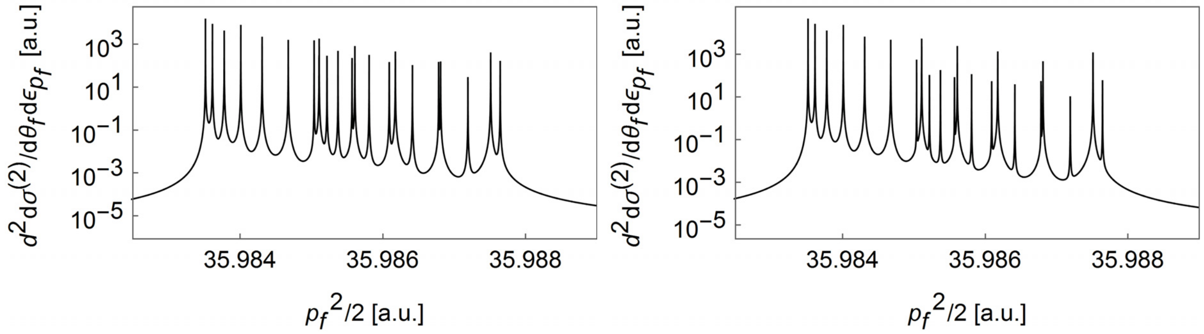

Figure 54: Doubly differential two-center electron-impact ionisation cross sections with two different polar angles of the scattered electron $\theta_\mathrm{f} = 0.00616$ (left) and $\theta_\mathrm{f} \approx 0.0177$ (right). The energy of the scattered electron $p_\mathrm{f}^2/2$ varies and the energy of the incident electron is $p_\mathrm{in}^2/2 = 1\,\mathrm{keV}$.

As can be seen in Fig. 54, the resonance peaks appear for high energies of the scattered electron, describing a small energy transfer. When compared to the cross section depicted in Fig. 52, less resonance peaks are visible. This is due to the fact, that the vanishing of the energy detuning depends directly on the momentum of the scattered electron. Therefore, the resonance peaks do not fan out additionally.

When comparing the two plots in Fig. 54 to each other, the overall shape of the curve is similar. However, some peaks are more or less pronounced. One example is the peak furthest to the right. This is due to the angular dependencies within the transition amplitude. Since only two angles, favouring one transition each, are chosen, other peaks can be disadvantaged.

For the polar angle of $\theta_\mathrm{f} = 0.00616$, the cross section is calculated while restricting the included electronic substates in order to further analyse the two-center cross section.

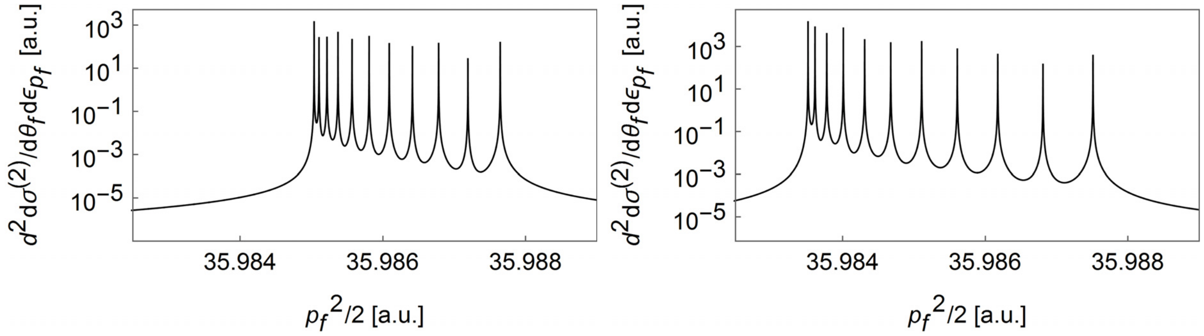

Figure 55: Doubly differential two-center electron-impact ionisation cross sections with the fixed different polar angle of the scattered electron $\theta_\mathrm{f} = 0.00616$ and restricted electronic substates $m = 0$ (left) and $m = \pm 1$ (right). The energy of the scattered electron $p_\mathrm{f}^2/2$ varies and the energy of the incident electron is $p_\mathrm{in}^2/2 = 1\,\mathrm{keV}$.

In Fig. 55, the restriction of the included electronic substates leads to the disintegration of the multitude of resonance peaks. This allows for the contributing states to be identified more easily, leading to the observation, that the peak for the vibrational level

$$\nu_{\mathrm{a}} = 0$$

of the intermediate state is situated at the far right. The peaks are such that the vibrational level increases from right to left. This is because the energy difference between the initial and intermediate state increases the higher the vibrational excitation is.
When comparing these cross sections with respect to those, where the energy of the final electron is displayed, the peak structure is more complicated when considering the emitted electron. Here, however, the angular dependencies are relatively straightforward. The opposite is true when refering to the scattered electron. Consequently, the two methods of approach can resolve different characteristics of the two-center ionisation process.
The two-center cross section is now calculated using the literature values for the potential cuves depicted in Fig. 49. When considering the emitted electron, the same angular dependency applies as already described for the values using the calculated potential curves.
First, the cross section is depicted with respect to the energy of the emitted electron.

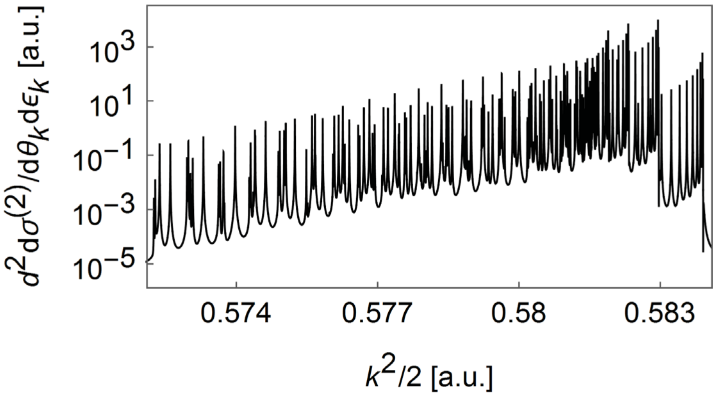

Figure 56: Doubly differential two-center electron-impact ionisation cross section with the fixed different polar angle of the emitted electron $\theta_k = \pi/2$ and a varying energy $k^2/2$ with the energy of the incident electron being $p_{\mathrm{in}}^2/2 = 1\,\mathrm{keV}$.

In contrast to the previous calculation, due to the augmented amount of bound vibrational levels of the intermediate state, the resonance peaks are fanned out even more. As before, the substate $m = 0$ does not contribute to the cross section for $\theta_k = \pi/2$. Recall, that the intermediate state with $m = \pm 1$ supports 27 bound vibrational levels and the final state supports 8 levels. Due to the balance of energy in the denominator, a multitude of energies can fulfill the resonance condition. When comparing the cross sections for the two different potential energy curves in Figs. 51 and 56, the resonance peaks reach similar maximum heights. Next, the contributions from the different substates are considered for appropriate polar angles of the emitted electron in order to better resolve the distribution of resonance peaks.

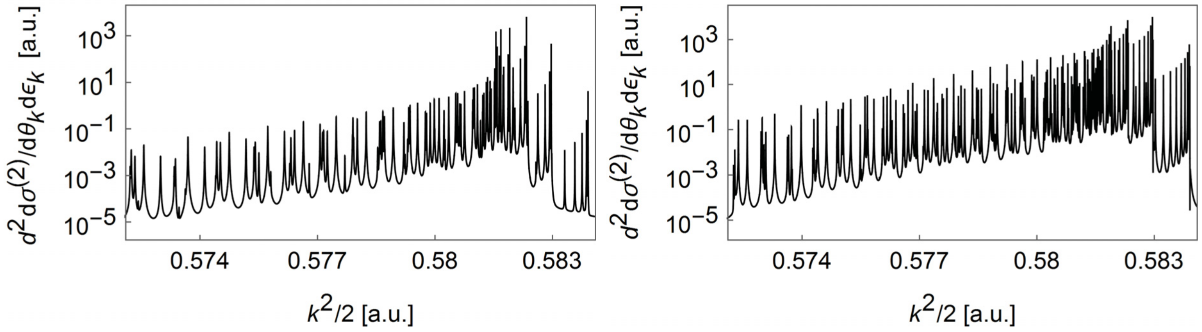

Figure 57: Doubly differential two-center electron-impact ionisation cross sections with restricted electronic substates $m = 0$ on the left side and $m = \pm 1$ on the right side. The polar angle of the emitted electron is set to $\theta_k = \pi/2$ for $m = \pm 1$ and $\theta_k \approx 0.615$ for $m = 0$. The energy of the emitted electron $k^2/2$ varies and the energy of the incident electron is $p_{\text{in}}^2/2 = 1\,\text{keV}$.

With a polar angle of $\theta_k = \pi/2$, the substates $m = \pm 1$ give the full contribution to the cross section of Fig. 56. Excitation to the substate $m = 0$ leads to no contribution for $\theta_k = \pi/2$ but is maximised for $\theta_k = 0.615$. According to the reduced amount of bound intermediate levels (20 in contrast to 27), the diversification of the cross section on the left is less extreme than observed in the curve depicted on the right.

Now, the energy of the scattered electron is considered. Here, a reduction of the resonance peaks is expected, since p_{f} is included explicitly in the energy detuning Δ and therefore, no additional dependency on the vibrational level of the final state is created. First all electronic substates are considered. Since the polar angle θ_{f}, for which the cross section is maximised, varies for every combination of vibrational levels, two different polar angles are incorporated in Fig. 58.

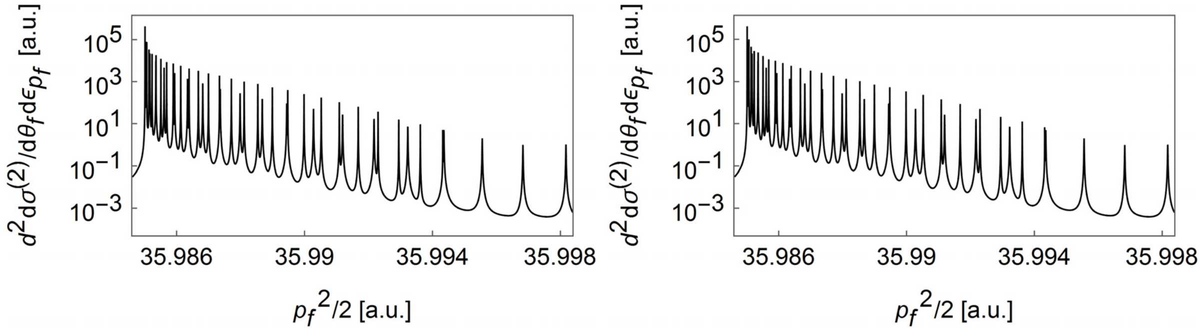

Figure 58: Doubly differential two-center electron-impact ionisation cross sections with two different polar angles of the scattered electron $\theta_{\text{f}} = 0.00607$ (left) and $\theta_{\text{f}} \approx 0.00709$ (right). The energy of the scattered electron $p_{\text{f}}^2/2$ varies and the energy of the incident electron is $p_{\text{in}}^2/2 = 1\,\text{keV}$.

Here, no noteworthy differences can be observed, the two angles yield similar curves. Upon further inspection, only marginal differences can be noted regarding the heights of the individual peaks. Due to the amount of resonance peaks, the optimum angles for each peak do not greatly differ. Therefore, the choice of angle does not have a strong influence on the shape of the curve within the interval of maximised angles for the transitions.

When setting the polar angle to $\theta_\mathrm{f} = 0.00607$, the contributions from the different electronic substates can be resolved. For this purpose, the substate is restricted in the numerical calculation, which is depicted in Fig. 59.

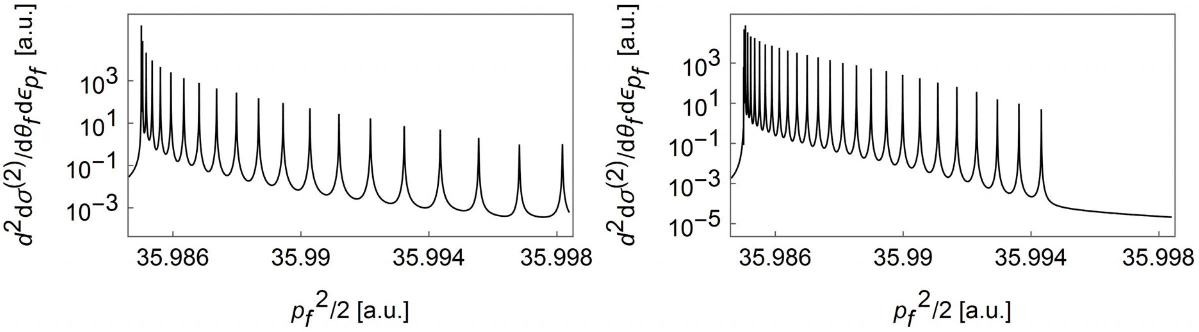

Figure 59: Doubly differential two-center electron-impact ionisation cross sections with the fixed different polar angle of the scattered electron $\theta_\mathrm{f} = 0.00607$ and restricted electronic substates $m = 0$ (left) and $m = \pm 1$ (right). The energy of the scattered electron $p_\mathrm{f}^2/2$ varies and the energy of the incident electron is $p_\mathrm{in}^2/2 = 1\,\mathrm{keV}$.

As can be seen in Fig. 59, the resonance peaks for $m = 0$ are spread over a wider range of energies. The number of peaks on the left is 20 and therefore smaller than the 27 peaks observed for $m = \pm 1$ on the right. On the left, the first peak is especially pronounced since the polar angle is optimised for this transition. For $m = \pm 1$, the peaks are concentrated around smaller energies and consequently are positioned closer to each other.

Note, that the positioning of the resonance peaks, especially in comparison with the distribution in Fig. 52, is heavily influenced by the vibrational wave function and its corresponding vibrational energy shift. The fitting parameter of the Morse potential strongly modifies the spacing of the energy levels and therefore the distance between two adjacent peaks.

Again, the vibrational level of the intermediate state ν_a decreases with increasing energy of the scattered electron $p_\mathrm{f}^2/2$. This is because the transformation to a highly excited vibrational state of the intermediate state requires a larger energy transfer from the incident electron.

When considering the two different sets of potential curves regarding the two-center electron-impact ionisation, the amount of resonance peaks as well as their positions deviate according to the differences between the potential curves and following vibrational wave functions. However, the general characteristics, especially concerning the two ways of visualisation, are shared between the two methods. The differences between the characteristics of the two-center cross section regarding the emitted and scattered electron, respectively, reinforce the observation, that the energy balance for the electron-impact ionisation is more complex than the one for the photoionisation. This is especially true when including molecular effects.

5.3 Summary

In this section, the process of two-center electron-impact ionisation in a heteroatomic dimer has been considered including molecular effects, which were previously discussed in detail in Sec. 3 with regard to two-center photoionisation. As in the sections before, numerical results are calculated for the dimer LiHe. Here, hydrogen-like wave functions as depicted in Sec. 4 are employed for the computation of the electronic transition. The calculations of the potential curves, however, were carried out using the improved wave function for lithium as described in Sec. 3. On the basis of the LiHe dimer, the numerical results for the two-center electron-impact ionisation cross sections are obtained by applying the two sets of interaction potential curves, which were either calculated as in Sec. 3.3.2 or taken from [128] and [102, 117], for the intermediate and final electronic state. The inclusion of the three electronic substates of the transition to $1s2p_m$ in helium gives rise to substantially more energies, for which the resonance condition can be fulfilled. The form of the double-differential cross section was analysed with respect to the emitted, as well as the scattered electron. Here, differences concerning the resonant energies are due to the detuning in the denominator of the transition amplitude, which depends on the energy of the incident and scattered electron as well as on the vibrational energy shift of the intermediate state. Conservation of energy, however, links the energy of the scattered electron to the energy of the emitted one as well as the vibrational level of the final state. Therefore, an additional splitting arises, where the resonant energy depends on ν_{a} and ν_{f}, when evaluating the cross section with regard to the energy of the emitted electron. While the two methods of calculation show similar maximum peak heights and a similar overall structure, the widths of the individual peaks as well as the amount of them are tremendously different. As in Sec. 3.4, the values obtained are highly sensitive to the fitting parameters. Therefore, the analysis of the process is restricted regarding the quantitative predictive power. However, the nuclear motion is observed to create a complex structure of resonance peaks, visualising the interconnection between the different energies and angular dependencies. Therefore, further investigations regarding the two-center electron-impact ionisation in a van der Waals dimer, both theoretically and experimentally, are expected to provide additional insights into the intramolecular dynamics within the process.

6 Summary and Outlook

In this section, the thesis is summarised and directions for further investigations are outllined.

In Sec. 2, the fundamental basics for the description of direct and indirect ionisation pathways in heteroatomic van der Waals dimers were presented. After the discussion of direct excitation and ionisation mechanisms by photon and electron impact, processes between multiple electrons in one or many atoms in vicinity of each other were considered. Such processes, which rely on autoionising states and electron correlations, augment the possible pathways of excitation and ionisation within or between atoms. Among those, the efficient ionisation process of interatomic Coulombic decay (ICD), which relies on dipole-dipole interactions, offers promising possibilities of insights concerning molecular structures and dynamics of electron-electron correlations. The general form of the relevant interaction between the electrons, the decay of the metastable state, as well as the employed wave functions were introduced with the objective of the mostly analytical description of the direct and indirect ionisation processes in a dimer. Furthermore, key elements concerning the description of the nuclear motion in a dimer, for which numerical results were to be calculated, were introduced.

Moreover, characteristics of van der Waals dimers, for which the ionisation processes were considered within this thesis, were illustrated. This investigation led to the choice and description of the model system, LiHe, a heteroatomic van der Waals dimer combining an alkali and a rare gas atom.

In Sec. 3, the process of two-center photoionisation in a system of two atoms, for which tremendous amplifications with respect to the direct process had been predicted theoretically assuming fixed nuclei, was studied in the system of LiHe. The analytical mathematical description employing perturbation theory was expanded in order to include the motion of the nuclei. For this purpose, interaction potentials were calculated yielding vibrational wave functions for each electronic state involved. The inclusion of the nuclear motion resulted in a diversification of the resonance energy, leading to a multiplet of peaks within the two-center photoionisation cross section. Within a first approach, it was found that the cross section of the two-center ionisation pathway splits into a multitude of resonance peaks, which was also observed experimentally for HeNe. Due to the vibrational energy shift, which is included in the energy detuning, the resonance energy depends on the vibrational level of the intermediate electronic state. Regarding the amplification of the total cross section for photoionisation by the indirect pathway it was obtained that the value is not very substantially reduced by the consideration of molecular effects, but rather split between the different peaks. This was especially a result of the decay widths, which remained almost unaltered and provided large cross sections, also in comparison to the system of HeNe. However, the introduction of more precise potential curves increases not only the total decay width, but also the contribution of the direct ionisation cross section. Moreover, the sensitivitiy of the results on the fit process for the vibrational wave functions was analysed. The consideration assuming fixed nuclei overestimates the efficiency of the two-center ionisation process for internuclear distances around the ground state equilibrium. However, distances smaller than the mean distance of the ground state can produce values similar to those obtained by the molecular calculation. Therefore, the approach assuming two separate atoms can roughly predict the relevance regarding the ionisation process.

In Sec. 4, the general idea of a two-center ionisation process described in the section above was transferred to the interaction with an incident electron. Therefore, the perturbative description of the direct and indirect electron-impact ionisation was established and first considered for for fixed nuclei while ignoring any molecular effects. First approximative results showed the resonant behaviour of the indirect pathway. Whereas the indirect ionisation mechanism strongly dominates when considering the energy-differential cross section close to the resonance, the ratio of the fully integrated values shows relevant contributions from both processes. However, the efficiency of the indirect ionisation process can be heightened significantly by considering a resolvable energy interval around the resonance. Furthermore, the indirect ionisation pathway can also modify the angular distribution of the emitted electrons, depending on the orientation of the linking vector $\mathbf{R}$ with respect to the direction of the incident electron. Consequently, transitions to selected substates m can be favoured or hindered, leading to different angular distributions. Additionally, it was shown that while the peak height is increased, the contribution of the fully integrated cross section is reduced for the excitations to higher lying states, making those transitions less relevant.

In Sec. 5, the process of two-center ionisation following electron impact was revisited including the molecular effects. Since the indirect ionisation pathway, in general, does not restrict the electronic substates which are attained, the resolution of the vibrational structure leads to an even more complex distribution of resonant energies. The process allows for an analysis regarding both the scattered electron as well as the emitted electron. Due to the balance of energy, the corresponding energy-differential cross sections reveal different structures. These visualise the interconnection between the energies and angular dependencies of the incident and the emitted electron. Again, the numerical calculations here show the sensitivity to potential curves and resulting vibrational wave functions.

The theoretical predictions motivate the experimental examination for LiHe, for which the experimental detection was provided in recent years, as well as similar dimers such as ArNe and HeNe. This is especially relevant, since the process of two-center ionisation can be used in order to suppress selected ionisation processes and therefore, their specific products. The analytical investigation has also shown the great sensitivity of the indirect process to fitting parameters and the accuracy of potential curves and vibrational wave functions. Given the structural results of the analytical calculations, future elaborate numerical results may be able to further resolve the interior dynamics and dependencies of such interatomic processes. In particular, the inclusion of dissociative states promises deeper insights into ionisation processes within a multiatomic system.

In comparison to photon-induced interatomic ionisation processes, far less research has been conducted regarding processes induced by electron impact. As briefly mentioned, the influence of the impact energy would have to be included when considering small energies of the incident electron. For large energies, however, relativistic effects have to be incorporated.

7 Appendices

7.1 Calculations of matrix elements

In these sections, the calculations of the matrix elements for the considerations in Secs. 3, 4 and 5 are presented.

The dipole-dipole interaction, included in the Auger decay width as well as the radiationless energy transfer, contains the matrix elements

$$\langle \chi_{1s} \left| \boldsymbol{\xi} \right| \chi_{2p_0} \rangle = \sqrt{\frac{Z_{\mathrm{He}}^8}{32\pi^2}} \int\limits_0^{2\pi} d\varphi \int\limits_0^{\infty} d\xi \xi^2 \int\limits_{-1}^{1} d\cos\vartheta \boldsymbol{\xi} \xi \cos\vartheta e^{-\xi \frac{3}{2} Z_{\mathrm{He}}} \tag{7.1}$$

$$= \frac{4\pi}{3} \sqrt{\frac{Z_{\mathrm{He}}^8}{32\pi^2}} \int\limits_0^{\infty} d\xi \xi^4 e^{-\xi \frac{3}{2} Z_{\mathrm{He}}} \mathbf{e}_z$$

$$= \frac{4\pi}{3} \sqrt{\frac{Z_{\mathrm{He}}^8}{32\pi^2}} \mathbf{e}_z \frac{24}{\left(\frac{3}{2} Z_{\mathrm{He}}\right)^5} \tag{7.2}$$

and

$$\left\langle \chi_{1s} \left| \boldsymbol{\xi} \right| \chi_{2p_{\pm 1}} \right\rangle = \sqrt{\frac{Z_{\mathrm{He}}^8}{64\pi^2}} \int\limits_0^{2\pi} d\varphi \int\limits_0^{\infty} d\xi \xi^2 \int\limits_0^{\pi} d\vartheta \sin\vartheta e^{\pm i\varphi} \boldsymbol{\xi} \xi \sin\vartheta e^{-\xi \frac{3}{2} Z_{\mathrm{He}}} \tag{7.3}$$

$$= \frac{4\pi}{3} \sqrt{\frac{Z_{\mathrm{He}}^8}{64\pi^2}} \int\limits_0^{\infty} d\xi \xi^4 e^{-\xi \frac{3}{2} Z_{\mathrm{He}}} (\mathbf{e}_x \pm i\mathbf{e}_y)$$

$$= \frac{4\pi}{3} \sqrt{\frac{Z_{\mathrm{He}}^8}{64\pi^2}} (\mathbf{e}_x \pm i\mathbf{e}_y) \frac{24}{\left(\frac{3}{2} Z_{\mathrm{He}}\right)^5} \tag{7.4}$$

7.1.1 Matrix elements for the photoionisation

The transitions induced by the external field and dipole-dipole interaction are calculated for the system of LiHe. The wave functions employed here read

$$\chi_{1s}(\xi) = \sqrt{\frac{Z_{\mathrm{He}}^3}{\pi}} e^{-Z_{\mathrm{He}}\xi} \tag{7.5}$$

$$\chi_{2p_0}(\boldsymbol{\xi}) = \sqrt{\frac{Z_{\mathrm{He}}^5}{32\pi}} \xi \cos(\vartheta) e^{-Z_{\mathrm{He}}\xi/2} \tag{7.6}$$

$$\varphi_{2s}(r) = \frac{1}{\sqrt{8\pi}} \frac{1}{\Gamma(a+1)} \left(\frac{2}{a}\right)^{a+1/2} r^u \left(1 + \frac{v}{r}\right) e^{-r/a} \tag{7.7}$$

$$\varphi_{\mathbf{k}}(r) = 2Z \sqrt{\frac{\pi}{2}} (\mathbf{e}_k \mathbf{e}_r) \sqrt{\frac{1+\nu^2}{\nu\left(1 - e^{-2\pi\nu}\right)}} r e^{-ikr} F(2 + i\nu, 4, 2ikr), \tag{7.8}$$

where the parameters a, v and u are defined as in Sec. 3.1 and Sec. 3.3. Furthermore, $\nu = Z/k$ is the Sommerfeld parameter, where $\mathbf{k}$ is the momentum of the emitted electron.

The direct ionisation of lithium is described by

$$\left\langle \varphi_{\mathbf{k}} \left| \frac{A_0 \boldsymbol{\varepsilon}}{2c} \mathbf{p} \right| \varphi_{2s} \right\rangle^* \tag{7.9}$$

$$= \underbrace{\frac{1}{\sqrt{8\pi}} \frac{1}{\Gamma(a+1)} \left(\frac{2}{a}\right)^{a+1/2} \frac{A_0 \boldsymbol{\varepsilon}}{2c} (-i) 2Z \sqrt{\frac{\pi}{2}} \sqrt{\frac{1+\nu^2}{\nu\left(1-e^{-2\pi\nu}\right)}}}_{=\mathbf{K}}$$

$$\times \int\limits_0^{2\pi} d\varphi \int\limits_0^{\pi} d\vartheta \sin\vartheta \int\limits_0^{\infty} drr^2 re^{-ikr} F(2+i\nu, 4, 2ikr)(\mathbf{e}_k \mathbf{e}_r) \frac{\partial}{\partial r} \left(r^u \left(1 + \frac{v}{r}\right) e^{-r/a} \right) \tag{7.10}$$

$$= \mathbf{K} \frac{4\pi}{3} \mathbf{e}_k \int\limits_0^{\infty} drr^3 e^{-ikr} F(2+i\nu, 4, 2ikr) r^{u-2} \frac{1}{a} \left(r(au-v) + av(u-1) - r^2 \right) e^{-r/a} \tag{7.11}$$

$$\overset{\lambda=\frac{1}{a}+ik}{\overbrace{=}} \mathbf{K} \frac{4\pi}{3} \mathbf{e}_k \frac{1}{a} \Big(av(u-1)\Gamma(u+1)\lambda^{-(u+1)} F(2+i\nu, u+1, 4, \frac{k}{\lambda}) + (au-v)\Gamma(u+2)\lambda^{-(u+2)}$$

$$\times F(2+i\nu, u+2, 4, \frac{k}{\lambda}) - \Gamma(u+3)\lambda^{-(u+3)} F(2+i\nu, u+3, 4, \frac{k}{\lambda}) \Big), \tag{7.12}$$

taking advantage of (f.2) in [70]. For the dipole-dipole interaction, the necessary matrix element reads

$$\left\langle \varphi_{\mathbf{k}} \left| \mathbf{r} \right| \varphi_{2s} \right\rangle^* \tag{7.13}$$

$$= \frac{1}{\sqrt{8\pi}} \frac{1}{\Gamma(a+1)} \left(\frac{2}{a}\right)^{a+1/2} 2Z \sqrt{\frac{\pi}{2}} \sqrt{\frac{1+\nu^2}{\nu\left(1-e^{-2\pi\nu}\right)}}$$

$$\times \int\limits_0^{2\pi} d\varphi \int\limits_0^{\pi} d\vartheta \sin\vartheta \int\limits_0^{\infty} drr^2 re^{-ikr} F(2+i\nu, 4, 2ikr)(\mathbf{e}_k \mathbf{e}_r) \mathbf{r} \left(r^u \left(1 + \frac{v}{r}\right) e^{-r/a} \right) \tag{7.14}$$

$$= \frac{1}{\sqrt{8\pi}} \frac{1}{\Gamma(a+1)} \left(\frac{2}{a}\right)^{a+1/2} 2Z \sqrt{\frac{\pi}{2}} \sqrt{\frac{1+\nu^2}{\nu\left(1-e^{-2\pi\nu}\right)}} \frac{4\pi}{3} \mathbf{e}_k$$

$$\times \int\limits_0^{\infty} drr^4 e^{-ikr} F(2+i\nu, 4, 2ikr) \left(r^u \left(1 + \frac{v}{r}\right) e^{-r/a} \right) \tag{7.15}$$

$$= \frac{1}{\sqrt{8\pi}} \frac{1}{\Gamma(a+1)} \left(\frac{2}{a}\right)^{a+1/2} 2Z \sqrt{\frac{\pi}{2}} \sqrt{\frac{1+\nu^2}{\nu\left(1-e^{-2\pi\nu}\right)}} \frac{4\pi}{3} \mathbf{e}_k$$

$$\times \left(\Gamma(u+4)\lambda^{-(u+4) F(2+i\nu, u+4, 4, \frac{k}{\lambda})} + v\Gamma(u+3)\lambda^{-(u+3) F(2+i\nu, u+3, 4, \frac{k}{\lambda})} \right), \tag{7.16}$$

where (f.3) from [70] was employed.

7.1.2 Matrix elements for the electron-impact ionisation

As described in Sec. 4.1, the transitions induced by electron impact and dipole-dipole interaction are calculated for the system of LiHe. The wave functions employed here read

$$\chi_{1s}(\xi) = \sqrt{\frac{Z_{\mathrm{He}}^3}{\pi}} e^{-Z_{\mathrm{He}}\xi} \tag{7.17}$$

$$\chi_{2p_0}(\boldsymbol{\xi}) = \sqrt{\frac{Z_{\mathrm{He}}^5}{32\pi}} \xi \cos(\vartheta_\xi) e^{-Z_{\mathrm{He}}\xi/2} \tag{7.18}$$

$$\chi_{2p_{\pm1}}(\boldsymbol{\xi}) = \sqrt{\frac{Z_{\mathrm{He}}^5}{64\pi}} \xi \sin(\vartheta_\xi) e^{-Z_{\mathrm{He}}\xi/2} e^{\pm i\varphi} \tag{7.19}$$

$$\varphi_{2s}(r) = \sqrt{\frac{Z_{\mathrm{Li}}^3}{32\pi}} \left(2 - Z_{\mathrm{Li}} r\right) e^{-Z_{\mathrm{Li}} r/2} \tag{7.20}$$

$$\varphi_{\mathbf{k}}^{(-)}(r) = \frac{1}{\sqrt{V}} e^{\frac{\pi}{2k}} \Gamma(1 + \frac{i}{k}) e^{i\mathbf{kr}} F(-\frac{i}{k}, 1, -1(kr + \mathbf{kr})) \quad . \tag{7.21}$$

The Auger decay width is recalculated for the hydrogen-like wave function of the $2s$ state in lithium.

$$\begin{aligned}
&\langle \varphi_k \left| \mathbf{r} \right| \varphi_{2s} \rangle \\
&= 2Z \sqrt{\frac{\pi}{2}} \sqrt{\frac{1+\nu^2}{\nu\left(1-e^{-2\pi\nu}\right)}} \sqrt{\frac{Z_{\mathrm{Li}}^3}{32\pi}} \int\limits_0^\infty dr r^2 \int\limits_0^\pi \sin\vartheta \\
\times &\int\limits_0^{2\pi} d\varphi \, \mathbf{r}(2 - Z_{\mathrm{Li}} r) e^{-Z_{\mathrm{Li}} r/2} r e^{ikr} F(2 - i\nu, 4, -2ikr)(\mathbf{e}_k \mathbf{e}_r)
\end{aligned} \tag{7.22}$$

$$\begin{aligned}
&= 2Z \sqrt{\frac{Z_{\mathrm{Li}}^3}{64}} \sqrt{\frac{1+\nu^2}{\nu\left(1-e^{-2\pi\nu}\right)}} \frac{4\pi}{3} \mathbf{e}_k \int\limits_0^\infty dr r^4 (2 - Z_{\mathrm{Li}} r) e^{-Z_{\mathrm{Li}} r/2} e^{ikr} F(2 - i\nu, 4, -2ikr) \\
&= 2Z \sqrt{\frac{Z_{\mathrm{Li}}^3}{64}} \sqrt{\frac{1+\nu^2}{\nu\left(1-e^{-2\pi\nu}\right)}} \frac{4\pi}{3} \mathbf{e}_k \Big[2\Gamma(5) \left(\frac{Z_{\mathrm{Li}}}{2} - ik\right)^{-5} F(2 - i\nu, 5, 4, \frac{-2ik}{\frac{Z_{\mathrm{Li}}}{2} - ik}) \\
&- Z_{\mathrm{Li}} \Gamma(6) \left(\frac{Z_{\mathrm{Li}}}{2} - ik\right)^{-6} F(2 - i\nu, 6, 4, \frac{-2ik}{\frac{Z_{\mathrm{Li}}}{2} - ik}) \Big]
\end{aligned} \tag{7.23}$$

The excitation of atom B via electron impact is calculated the following way.

$$\begin{aligned}
&\left\langle \chi_{2p_0}(\boldsymbol{\xi})) \left| -Z_N + e^{i(\mathbf{p}_{\mathrm{in}} - \mathbf{p}_{\mathrm{f}})\boldsymbol{\xi}} \right| \chi_{1s}(\xi) \right\rangle = \left\langle \chi_{2p_0}(\boldsymbol{\xi}) \left| e^{i(\mathbf{p}_{\mathrm{in}} - \mathbf{p}_{\mathrm{f}})\boldsymbol{\xi}} \right| \chi_{1s}(\xi) \right\rangle \\
&= \sqrt{\frac{Z_{\mathrm{He}}^8}{32\pi^2}} \int\limits_0^{2\pi} d\varphi \int\limits_{-1}^{1} d\cos\vartheta \cos\vartheta \int\limits_0^\infty d\xi \xi^3 e^{-\xi \frac{3}{2} Z_{\mathrm{He}}} e^{-i\mathbf{q}\cdot\boldsymbol{\xi}}
\end{aligned} \tag{7.24}$$

$$= \sqrt{\frac{Z_{\mathrm{He}}^8}{32\pi^2}} \int\limits_0^{2\pi} d\varphi \int\limits_{-1}^{1} d\cos\vartheta \cos\vartheta \int\limits_0^\infty d\xi \xi^3 e^{-\xi \frac{3}{2} Z_{\mathrm{He}}} e^{-i\xi(q_\perp \sin\vartheta \cos(\varphi - \varphi_d) + q_z \cos\vartheta))}$$

For the integration over φ, 3.715.18 in [173] is utilised.

$$= \sqrt{\frac{Z_{\mathrm{He}}^8}{32\pi^2}} \int\limits_{-1}^{1} d\cos\vartheta \cos\vartheta \int\limits_0^\infty d\xi \xi^3 e^{-\xi \frac{3}{2} Z_{\mathrm{He}}} e^{-i\xi q_z \cos\vartheta} 2\pi J_0\left(q_\perp \xi \sin\vartheta\right)$$

$$= 4\pi\sqrt{\frac{Z_{\mathrm{He}}^8}{32\pi^2}}\, i\int\limits_0^\infty d\xi\xi^3 e^{-\xi\frac{3}{2}Z_{\mathrm{He}}}\int\limits_0^{q_\perp\xi}\frac{dy\, y}{(q_\perp\xi)^2}\sin\left(\frac{q_z}{q_\perp}\sqrt{(q_\perp\xi)^2-y^2}\right)J_0\left(y\right)$$

$$= 4\pi\sqrt{\frac{Z_{\mathrm{He}}^8}{32\pi^2}}\sqrt{\frac{\pi}{2}}\, i\int\limits_0^\infty d\xi\xi^{5/2}e^{-\xi\overbrace{\frac{3}{2}Z_{\mathrm{He}}}^{=\alpha}}J_{3/2}\left(q\xi\right)q_z q^{-3/2}$$

$J_{3/2}$ and J_0 are Bessel functions [172], and 6.688.2 from [173] enables the integration over y

$$= 4\pi\sqrt{\frac{Z_{\mathrm{He}}^8}{32\pi^2}}\sqrt{\frac{\pi}{2}}\, i\left(\alpha^2+q^2\right)^{-7/4}\Gamma(5)P_{5/2}^{-3/2}\left(\sqrt{1+\frac{q^2}{\alpha^2}}^{-1}\right)q_z q^{-3/2}$$

$$= 4\pi\sqrt{\frac{Z_{\mathrm{He}}^8}{32\pi^2}}\, i\frac{q_z}{\alpha^2 q^3}\left(1+\frac{q^2}{\alpha^2}\right)^{-2}\left(-\frac{2q}{\alpha}\cos\left(2\arctan\left(\frac{q}{\alpha}\right)\right)+\left(1+3\frac{q^2}{\alpha^2}\sin\left(2\arctan\left(\frac{q}{\alpha}\right)\right)\right)\right) \tag{7.25}$$

with $\mathbf{q} = \mathbf{p}_{\mathrm{f}} - \mathbf{p}_{\mathrm{in}}$. The integration over ξ is performed by employing 6.621.1 from [173], where

$$\begin{aligned}
P_{\sigma+1/2}^{-3/2}(x) &= P_{5/2}^{-3/2}\left(\sqrt{1+\frac{q^2}{\alpha^2}}^{1}\right)\\
&= \frac{\sqrt{\frac{2}{\pi}}x^2}{\sigma(\sigma+1)(\sigma+2)}\frac{\left(-\sigma\frac{\sqrt{1-x^2}}{x}\cos(\sigma\arccos x)+x^{-2}\left(1+\sigma(1-x^2)\sin(\sigma\arccos x)\right)\right)}{\left(1-x^2\right)^{-3/4}}\\
&= \frac{\sqrt{\frac{2}{\pi}}}{24}\frac{\left(-\frac{2q}{\alpha}\cos\left(2\arctan\left(\frac{q}{\alpha}\right)\right)+\left(1+3\frac{q^2}{\alpha^2}\sin\left(2\arctan\left(\frac{q}{\alpha}\right)\right)\right)\right)}{\left(1+\frac{q^2}{\alpha^2}\right)^{1/4}\left(\frac{q}{\alpha}\right)^{3/2}}
\end{aligned} \tag{7.26}$$

is the associated Legendre function, [173]. For the excitations with $m = \pm 1$, similar calculation is performed.

$$\left\langle\chi_{2p_{\pm1}}(\boldsymbol{\xi}))\left|-Z_N+e^{i(\mathbf{p}_{\mathrm{in}}-\mathbf{p}_{\mathrm{f}})\boldsymbol{\xi}}\right|\chi_{1s}(\xi)\right\rangle = \left\langle\chi_{2p_{\pm1}}(\boldsymbol{\xi}))\left|e^{i(\mathbf{p}_{\mathrm{in}}-\mathbf{p}_{\mathrm{f}})\boldsymbol{\xi}}\right|\chi_{1s}(\xi)\right\rangle$$

$$= \sqrt{\frac{Z_{\mathrm{He}}^8}{62\pi^2}}\int\limits_0^{2\pi}d\varphi e^{\pm i\varphi}\int\limits_0^{\pi}d\vartheta\sin^2\vartheta\int\limits_0^\infty d\xi\xi^3 e^{-\xi\frac{3}{2}Z_{\mathrm{He}}}e^{-i\mathbf{q}\cdot\mathbf{r}}$$

$$= \sqrt{\frac{Z_{\mathrm{He}}^8}{62\pi^2}}e^{\pm i\varphi_q}(2\pi i)\int\limits_0^{\pi}d\vartheta\sin^2\vartheta\int\limits_0^\infty d\xi\xi^3 e^{-\xi\frac{3}{2}Z_{\mathrm{He}}}e^{-i\xi q_z\cos\vartheta)}J_1\left(-q_\perp\xi\sin\vartheta\right) \tag{7.27}$$

$$= \sqrt{\frac{Z_{\mathrm{He}}^8}{62\pi^2}}e^{\pm i\varphi_q}(-4\pi i)\int\limits_0^\infty d\xi\xi^{5/2}e^{-\xi\overbrace{\frac{3}{2}Z_{\mathrm{He}}}^{=\alpha}}J_{3/2}\left(qr\right)\sqrt{\frac{\pi}{2}}\frac{q_\perp}{q^{3/2}} \tag{7.28}$$

$$= \sqrt{\frac{Z_{\mathrm{He}}^8}{62\pi^2}}e^{\pm i\varphi_q}(-4\pi i)\left(qr\right)\sqrt{\frac{\pi}{2}}\frac{q_\perp}{q^{3/2}}\left(\alpha^2+q^2\right)^{-7/4}\Gamma(5)P_{5/2}^{-3/2}\left(\sqrt{1+\frac{q^2}{\alpha^2}}^{1}\right) \tag{7.29}$$

with $e^{i\varphi_q} = \frac{q_x+iq_y}{q_\perp}$. The direct electron-impact ionisation of lithium, when described as a $2s$

hydrogen-like wave function requires the calculation of the following matrix element. Here, as described in Sec. 2.6, a Coulomb wave accounts for the influence of the remaining ion. The calculation is most comprehensible when first considering the transition from the $1s$ state. Parabolic coordinates $x = \sqrt{\zeta\eta}\cos\varphi$, $y = \sqrt{\zeta\eta}\sin\varphi$, $z = \frac{1}{2}(\zeta - \eta)$ are used [70].

$$\begin{aligned}
&\left\langle \varphi_{\mathbf{k}} \left| -Z_N + e^{(\mathbf{p}_{\text{in}} - \mathbf{p}_{\text{f}})\boldsymbol{\xi}} \right| \varphi_{1s} \right\rangle \\
&= \underbrace{\sqrt{\frac{Z_{1s}^3}{\pi}} \frac{\Gamma(1 - \frac{Z_{1s} i}{k})}{\sqrt{V}} e^{\frac{Z_{\text{Li}}\pi}{2k}}}_{=C(k)} \int_0^{2\pi} d\varphi \int_0^{\infty} d\zeta \\
&\times \int_0^{\infty} d\eta \frac{1}{4}(\zeta + \eta) e^{-\frac{ik}{2}(\zeta - \eta)} e^{-\frac{\lambda}{2}(\zeta + \eta)} F(\frac{Z_{1s} i}{k}, 1, ik\zeta) e^{-iq(\sin\gamma\sqrt{\zeta\eta}\cos\varphi + \cos\gamma\frac{\zeta - \eta}{2})} \qquad (7.30) \\
&= \frac{C(k) 2\pi(-2)}{4} \frac{\partial}{\partial\lambda} \int_0^{\infty} d\zeta \int_0^{\infty} d\eta e^{-\frac{ik}{2}(\zeta - \eta)} e^{-\frac{\lambda}{2}(\zeta + \eta)} F(\frac{Z_{1s} i}{k}, 1, ik\zeta) e^{-iq(\cos\gamma\frac{\zeta - \eta}{2})} J_0\left(-q\sin\gamma\sqrt{\zeta\eta}\right)
\end{aligned}$$

The integration over η is executed by employing 6.614.1 in [173].

$$\begin{aligned}
&= \frac{C(k) 2\pi(-2)}{4} \frac{\partial}{\partial\lambda} \int_0^{\infty} d\zeta \frac{2e^{-\frac{q^2\sin^2\gamma\zeta}{2(\lambda - ik - iq\cos\gamma)}}}{\lambda - ik - iq\cos\gamma} e^{-\frac{\zeta}{2}(ik + \lambda + iq\cos\gamma)} F(\frac{Z_{1s} i}{k}, 1, ik\zeta) \qquad (7.31) \\
&= \frac{C(k) 2\pi(-2)}{4} \frac{\partial}{\partial\lambda} \frac{4}{k^2 + \lambda^2 + q^2 + 2kq\cos\gamma} \\
&\times \left(\frac{k^2 + \lambda^2 + q^2 + 2kq\cos\gamma}{2(\lambda - ik + iq\cos\gamma)}\right)^{\frac{Z_{1s} i}{k}} \left(\frac{\lambda^2 + q^2 - k^2 - 2ik\lambda}{2(\lambda - ik - iq\cos\gamma)}\right)^{-\frac{Z_{1s} i}{k}} \qquad (7.32)
\end{aligned}$$

Here, $\gamma = \vartheta_q$ is the polar angle corresponding to the momentum transfer $\mathbf{q}$ and $\lambda = Z_{1s}$. The last integration is carried out using f.3 of [70] and [173]. This result can be transferred to the ionisation from the $2s$ state. In this case, $\tilde{\lambda} = Z_{2s/2}$.

$$\begin{aligned}
&\left\langle \varphi_{\mathbf{k}} \left| -Z_N + e^{(\mathbf{p}_{\text{in}} - \mathbf{p}_{\text{f}})\boldsymbol{\xi}} \right| \varphi_{2s} \right\rangle \\
&= \underbrace{\sqrt{\frac{Z_{\text{Li}}^3}{32\pi}} \frac{\Gamma(1 - \frac{Z_{\text{Li}} i}{k})}{(2\pi)^{3/2}} e^{\frac{Z_{\text{Li}}\pi}{2k}}}_{=\tilde{C}(k)} \int_0^{2\pi} d\varphi \int_0^{\infty} d\zeta \int_0^{\infty} d\eta \frac{1}{4}(\zeta + \eta) e^{-\frac{ik}{2}(\zeta - \eta)} e^{-\frac{\tilde{\lambda}}{2}(\zeta + \eta)} F(\frac{Z_{\text{Li}} i}{k}, 1, ik\zeta) \\
&\times e^{-iq(\sin\gamma\sqrt{\zeta\eta}\cos\varphi + \cos\gamma\frac{\zeta - \eta}{2})} (\underbrace{2}_{=I} - \underbrace{Z_{\text{Li}}\frac{\zeta + \eta}{2}}_{=II}) \qquad (7.33) \\
&= I_I - I_{II} \qquad (7.34)
\end{aligned}$$

The integral including I equals, apart from prefactors, the calculations above. For the integral including II, however, further work is required.

$$\begin{aligned}
I_{II} &= \tilde{C}(k)\int\limits_0^{2\pi} d\varphi \int\limits_0^{\infty} d\zeta \int\limits_0^{\infty} d\eta \frac{1}{4}(\zeta+\eta)e^{-\frac{ik}{2}(\zeta-\eta)}e^{-\frac{\tilde{\lambda}}{2}(\zeta+\eta)} \\
&\times F(\frac{Z_{\mathrm{Li}}i}{k},1,ik\zeta)e^{-iq(\sin\gamma\sqrt{\zeta\eta}\cos\varphi+\cos\gamma\frac{\zeta-\eta}{2})}Z_{\mathrm{Li}}\frac{\zeta+\eta}{2} \qquad (7.35) \\
&= \frac{Z_{\mathrm{Li}}\tilde{C}(k)}{2}\frac{\partial^2}{\partial\tilde{\lambda}^2}\int\limits_0^{2\pi} d\varphi \int\limits_0^{\infty} d\zeta \int\limits_0^{\infty} d\eta e^{-\frac{ik}{2}(\zeta-\eta)}e^{-\frac{\tilde{\lambda}}{2}(\zeta+\eta)}F(\frac{Z_{\mathrm{Li}}i}{k},1,ik\zeta)e^{-iq(\sin\gamma\sqrt{\zeta\eta}\cos\varphi+\cos\gamma\frac{\zeta-\eta}{2})} \\
&= \frac{Z_{\mathrm{Li}}}{4}\frac{\partial}{\partial\tilde{\lambda}}I_I \qquad (7.36)
\end{aligned}$$

For the excitation to the $3p$ state in helium, the matrix elements read

$$\begin{aligned}
\langle\chi_{1s}|\boldsymbol{\xi}|\chi_{3p_0}\rangle &= \sqrt{\frac{Z^8_{\mathrm{He,3p}}}{2\pi^2}}\frac{2}{81}\int\limits_0^{2\pi} d\varphi\int\limits_{-1}^{1} d\cos\vartheta\cos\vartheta\int\limits_0^{\infty} d\xi\xi^2\boldsymbol{\xi}\xi(6-Z_{\mathrm{He,3p}}\xi)e^{-\frac{4}{3}Z_{\mathrm{He,3p}}\xi} \qquad (7.37) \\
&= \frac{4}{\pi}\sqrt{\frac{Z^8_{\mathrm{He,3p}}}{2\pi^2}}\frac{2}{81}\mathbf{e}_z\int\limits_0^{\infty} d\xi\xi^4(6-Z_{\mathrm{He,3p}}\xi)e^{-\frac{4}{3}Z_{\mathrm{He,3p}}\xi} \\
&= \frac{4}{\pi}\sqrt{\frac{Z^8_{\mathrm{He,3p}}}{2\pi^2}}\frac{2}{81}\mathbf{e}_z\left(\frac{6561}{512Z^5_{\mathrm{He,3p}}}\right), \qquad (7.38)
\end{aligned}$$

$$\begin{aligned}
\langle\chi_{1s}|\boldsymbol{\xi}|\chi_{3p_{\pm1}}\rangle &= \sqrt{\frac{Z^8_{\mathrm{He,3p}}}{\pi^2}}\frac{1}{81}\int\limits_0^{2\pi} d\varphi\int\limits_0^{\pi} d\vartheta\sin\vartheta\sin\vartheta\int\limits_0^{\infty} d\xi\xi^2\boldsymbol{\xi}\xi(6-Z_{\mathrm{He,3p}}\xi)e^{-\frac{4}{3}Z_{\mathrm{He,3p}\xi}} \qquad (7.39) \\
&= \frac{4}{\pi}\sqrt{\frac{Z^8_{\mathrm{He,3p}}}{\pi^2}}\frac{1}{81}(\mathbf{e}_x\pm i\mathbf{e}_y)\int\limits_0^{\infty} d\xi\xi^4(6-Z_{\mathrm{He,3p}}\xi)e^{-\frac{4}{3}Z_{\mathrm{He,3p}\xi}} \\
&= \frac{4}{\pi}\sqrt{\frac{Z^8_{\mathrm{He,3p}}}{\pi^2}}\frac{1}{81}(\mathbf{e}_x\pm i\mathbf{e}_y)left(\frac{6561}{512Z^5_{\mathrm{He,3p}}} \qquad (7.40)
\end{aligned}$$

as well as

$$\begin{aligned}
&\left\langle\chi_{3p_0}(\boldsymbol{\xi})\left|-Z_N+e^{(\mathbf{p}_{\mathrm{in}}-\mathbf{p}_{\mathrm{f}})\boldsymbol{\xi}}\right|\chi_{1s}(\xi)\right\rangle = \left\langle\chi_{3p_0}(\boldsymbol{\xi}))\left|e^{i(\mathbf{p}_{\mathrm{in}}-\mathbf{p}_{\mathrm{f}})\boldsymbol{\xi}}\right|\chi_{1s}(\xi)\right\rangle \\
&= \sqrt{\frac{Z^8_{\mathrm{He},3p}}{2\pi^2}}\frac{2}{81}\int\limits_0^{2\pi} d\varphi\int\limits_{-1}^{1} d\cos\vartheta\cos\vartheta\int\limits_0^{\infty} d\xi\xi^3e^{-\xi\frac{4}{3}Z_{\mathrm{He},3p}}e^{-i\mathbf{q}\cdot\mathbf{r}}(6-Z_{\mathrm{He},3p}\xi) \\
&= \sqrt{\frac{Z^8_{\mathrm{He},3p}}{2\pi^2}}\frac{4\pi}{81}\int\limits_{-1}^{1} d\cos\vartheta\cos\vartheta\int\limits_0^{\infty} d\xi\xi^3e^{-\xi\frac{4}{3}Z_{\mathrm{He}}}e^{-i\xi q_z\cos\vartheta)}J_0\left(q_\perp\xi\sin\vartheta\right)\left(6-Z_{\mathrm{He},3p}\xi\right)
\end{aligned}$$

The substitutions $x=\cos\vartheta$ and $y=q_\perp\xi\sqrt{1-x^2}$ yield

$$
\begin{aligned}
&= \sqrt{\frac{Z_{\mathrm{He},3p}^8}{2\pi^2}} \frac{8\pi i}{81} \int_0^\infty d\xi \xi^3 e^{-\xi \frac{4}{3} Z_{\mathrm{He}}} \int_0^{q_\perp \xi} \frac{dy\, y}{(q_\perp \xi)^2} \sin\left(\frac{q_z}{q_\perp} \sqrt{(q_\perp \xi)^2 - y^2} \right) J_0\left(y\right) \left(6 - Z_{\mathrm{He},3p}\xi\right) \\
&= \sqrt{\frac{Z_{\mathrm{He},3p}^8}{2\pi^2}} \frac{8\pi i}{81} \sqrt{\frac{\pi}{2}} \int_0^\infty d\xi \xi^{5/2} e^{-\xi \overbrace{\frac{4}{3} Z_{\mathrm{He}}}^{=\alpha}} J_{3/2}\left(qr\right) q_z q^{-3/2} (6 - Z_{\mathrm{He},3p}\xi) \\
&= \sqrt{\frac{Z_{\mathrm{He},3p}^8}{2\pi^2}} \frac{8\pi i}{81} \sqrt{\frac{\pi}{2}} q_z q^{-3/2} \left(6 \left(\alpha^2 + q^2\right)^{-7/4} \Gamma(5) P_{5/2}^{-3/2} \left(\sqrt{1 + \frac{q^2}{\alpha^2}}^{-1} \right) \right. \\
&\left. - Z_{\mathrm{He},3p} \left(\alpha^2 + q^2\right)^{-9/4} \Gamma(6) P_{7/2}^{-3/2} \left(\sqrt{1 + \frac{q^2}{\alpha^2}}^{-1} \right) \right)
\end{aligned}
\tag{7.41}
$$

Again, $P_{7/2}$ is the associated Legendre function from [173]

$$
P_{7/2}^{-3/2} \left(\sqrt{1 + \frac{q^2}{\alpha^2}}^{-1} \right) = \sqrt{\frac{2}{\pi}} \frac{1}{60} \frac{\left(-\frac{3q}{\alpha} \cos\left(3 \arctan\left(\frac{q}{\alpha}\right)\right) + \left(1 + 4\frac{q^2}{\alpha^2} \sin\left(3 \arctan\left(\frac{q}{\alpha}\right)\right)\right)\right)}{\left(1 + \frac{q^2}{\alpha^2}\right)^{1/4} \left(\frac{q}{\alpha}\right)^{3/2}}.
\tag{7.42}
$$

Likewise, the transition to the substates with $m = \pm 1$ is calculated.

$$
\begin{aligned}
&\left\langle \chi_{3p_{\pm 1}}(\boldsymbol{\xi})) \left| -Z_N + e^{(\mathbf{p}_{\mathrm{in}} - \mathbf{p}_{\mathrm{f}})\boldsymbol{\xi}} \right| \chi_{1s}(\xi) \right\rangle = \left\langle \chi_{3p_{\pm 1}}(\boldsymbol{\xi})) \left| e^{i(\mathbf{p}_{\mathrm{in}} - \mathbf{p}_{\mathrm{f}})\boldsymbol{\xi}} \right| \chi_{1s}(\xi) \right\rangle \\
&= \sqrt{\frac{Z_{\mathrm{He},3p}^8}{\pi^2}} \frac{1}{81} \int_0^{2\pi} d\varphi \int_0^\pi d\vartheta \sin^2\vartheta \int_0^\infty d\xi \xi^3 e^{-\xi \frac{4}{3} Z_{\mathrm{He}.3p}} e^{-i\mathbf{q}\cdot\mathbf{r}} (6 - Z_{\mathrm{He},3p}\xi) e^{\pm i\varphi} \\
&= \sqrt{\frac{Z_{\mathrm{He},3p}^8}{\pi^2}} \frac{-2\pi i}{81} \int_0^\pi d\vartheta \sin^2\vartheta \int_0^\infty d\xi \xi^3 e^{-\xi \frac{4}{3} Z_{\mathrm{He}}} e^{-i\xi q_z \cos\vartheta)} J_1\left(q_\perp \xi \sin\vartheta\right) \left(6 - Z_{\mathrm{He},3p}\xi\right) e^{\pm i\varphi_q} \\
&= \sqrt{\frac{Z_{\mathrm{He},3p}^8}{\pi^2}} \frac{-4\pi i}{81} \int_0^\infty d\xi \xi^3 e^{-\xi \frac{4}{3} Z_{\mathrm{He}}} \int_0^{q_\perp \xi} \frac{dyy}{(q_\perp \xi)^2} \sin\left(\frac{q_z}{q_\perp} \sqrt{(q_\perp \xi)^2 - y^2} \right) J_1\left(y\right) \left(6 - Z_{\mathrm{He},3p}\xi\right) e^{\pm i\varphi_q} \\
&= \sqrt{\frac{Z_{\mathrm{He},3p}^8}{2\pi^2}} \frac{-4\pi i}{81} \sqrt{\frac{\pi}{2}} \int_0^\infty d\xi \xi^{5/2} e^{-\xi \overbrace{\frac{4}{3} Z_{\mathrm{He}}}^{=\alpha}} J_{3/2}\left(qr\right) q_z q^{-3/2} (6 - Z_{\mathrm{He},3p}\xi) e^{\pm i\varphi_q} \\
&= \sqrt{\frac{Z_{\mathrm{He},3p}^8}{2\pi^2}} \frac{-4\pi i}{81} \sqrt{\frac{\pi}{2}} \left(\sqrt{1 + \frac{q^2}{\alpha^2}}^{-1} \right) q_z q^{-3/2} e^{\pm i\varphi_q} \\
&\times \left(6 \left(\alpha^2 + q^2\right)^{-7/4} \Gamma(5) P_{5/2}^{-3/2} \left(\sqrt{1 + \frac{q^2}{\alpha^2}}^{-1} \right) - Z_{\mathrm{He},3p} \left(\alpha^2 + q^2\right)^{-9/4} \Gamma(6) P_{7/2}^{-3/2} \left(\sqrt{1 + \frac{q^2}{\alpha^2}}^{-1} \right) \right)
\end{aligned}
\tag{7.43}
$$

From this point on, the calculation follows the one leading to Eq. (7.41).

8 List of publications

Here the publications which emerged from this thesis work are listed. Furthermore, a short depiction of my contributions to the associated research is given.

Two-center electron-impact ionization via collisional excitation-autoionization
In this project, the process of two-center ionisation following electron impact is studied. For this purpose, the heteroatomic dimer LiHe is investigated, treating the two constituents as separate atoms with spatially fixed nuclei. My contributions include the analytical modelling of both the direct ionisation process as well as the two-center ionisation mechanism applying perturbation theory. This included the calculation of the various transition matrix elements as well as considerations concerning the energy balance. Furthermore, all numerical calculations were implemented and carried out by me and I also prepared the manuscript.

F. Grüll, A. B. Voitkiv, and C. Müller, Phys. Rev. A **100**, 032702 (2019)

Influence of nuclear motion on resonant two-center photoionization
Within this project, the process of resonant two-center photoionisation, which was first introduced in 2010, was analysed with respect to the inclusion of effects of nuclear motion. I expanded the theoretical description using perturbation theory by effects of the molecular motion for both the direct and indirect ionisation mechanism in the system of LiHe. Therefore, I introduced the interaction potential curve, the fitting of a Morse potential in order to find analytical vibrational wave functions as well as the Franck-Condon factors, which denote the overlap of the vibrational wave functions. Aside from the calculation of the relevant matrix elements using improved wave functions, I performed all numerical calculations concerning the system of LiHe and the reference values for HeNe. Furthermore, the manuscript was prepared by me.

F. Grüll, A. B. Voitkiv, and C. Müller, Phys. Rev. A **102**, 012818 (2020)

Interatomic distance dependence of resonant energy-transfer phenomena
On the basis of the publication above, the results were further concretised in order to establish a general evaluation of the significance of the two-center photoionisation pathway in dimers. I was involved in finding a simplified expression for the ratio of the indirect and direct ionisation mechanism including some molecular effects. Furthermore, I conducted all necessary numerical calculations for LiHe and provided approximative results for the comparison to the dimer of HeNe.

F. Grüll, A. B. Voitkiv, and C. Müller, Phys. Rev. Research **2**, 033303 (2020)

Bibliography

[1] H. Hertz, Annalen der Physik **267**, 8983-1000 (1887)

[2] W. Hallwachs, Annalen der Physik **269**,2 301-312 (1888)

[3] A. Einstein, Annalen der Physik **322**(6) 132-148 (1905)

[4] H. Ehrhardt, M. Schulz, T. Tekaat, and K. Willmann, Phys. Rev. Lett. **22**, 89 (1969)

[5] D. You, H. Fukuzawa, Y. Sakakibara, T. Takanashi, Y. Ito, G. G. Maliyar, K. Motomura, K. Nagaya, T. Nishiyama, K. Asa, Y. Sato, N. Saito, M. Oura, M. Schöffler, G. Kastirke, U. Hergenhahn, V. Stumpf, K. Gokhberg, A. I. Kuleff, L. S. Cederbaum & K. Ueda, Nature Communications **8**, 14277 (2017)

[6] T. Jahnke, U. Hergenhahn, B. Winter, R. Dörner, U. Frühling, P. V. Demekhin, K. Gokhberg, L. S. Cederbaum, A. Ehresmann, A. Knie, and A. Dreuw, Chem. Rev. **120**, 20, 11295–11369 (2020)

[7] L. S. Cederbaum, J. Zobeley, and F. Tarantelli, Phys. Rev. Lett. **79**, 4778 (1997)

[8] S. Marburger, O. Kugeler, U. Hergenhahn, and T. Möller, Phys. Rev. Lett. **90**, 203401 (2003)

[9] T. Jahnke, A. Czasch, M. S. Schöffler, S. Schössler, A. Knapp, M. Käsz, J. Titze, C. Wimmer, K. Kreidi, R. E. Grisenti, A. Staudte, O. Jagutzki, U. Hergenhahn, H. Schmidt-Böcking, and R. Dörner, Phys. Rev. Lett. **93**, 163401 (2004)

[10] Y. Morishita, X.-J. Liu, N. Saito, T. Lischke, M. Kato, G. Prömper, M. Oura, H. Yamaoka, Y. Tamenori, I.H. Suzuki, K. Ueda, Phys. Rev. Lett. **96**, 243402 (2006)

[11] T. Havermeier, T. Jahnke, K. Kreidi, R. Wallauer, S. Voss, M. Schöffler, S. Schössler, L. Foucar, N. Neumann, J. Titze, H. Sann, M. Kühnel, J. Voigtsberger, J. H. Morilla, W. Schöllkopf, H. Schmidt-Böcking, R. E. Grisenti, and R. Dörner, Phys. Rev. Lett. **104**, 133401 (2010)

[12] T. Jahnke, H. Sann, T. Havermeier, K. Kreidi, C. Stuck, M. Meckel, M. Schöffler, N. Neumann, R. Wallauer, S. Voss, A. Czasch, O. Jagutzki, A. Malakzadeh, F. Afaneh, Th. Weber, H. Schmidt-Böcking & R. Dörner, Nature Phys. **6**, 139-142 (2010)

[13] T. Jahnke, J. Phys. B: At. Mol. Opt. Phys. **48**, 082001 (2015)

[14] R. Dörner, J. M. Feagin, C. L. Cocke, H. Bräuning, O. Jagutzki, M. Jung, E. P. Kanter, H. Khemliche, S. Kravis, V. Mergel, M. H. Prior, H. Schmidt-Böcking, L. Spielberger, J. Ullrich, M. Unversagt, and T. Vogt, Phys. Rev. Lett. **77**, 1024 (1996)

[15] K. Rzaznewski, and J. H. Eberly, Phys. Rev. Lett. **47**, 408 (1981)

[16] B. Najjari, A. B. Voitkiv, and C. Müller, Phys. Rev. Lett. **105**, 153002 (2010)

[17] B. Friedrich, Physics **6**, 42 (2013)

[18] F. Trinter, J. B. Williams, M. Weller, M. Waitz, M. Pitzer, J. Voigtsberger, C. Schober, G. Kastirke, C. Müller, C. Goihl, P. Burzynski, F. Wiegandt, R. Wallauer, A. Kalinin, L. Ph. H. Schmidt, M. S. Schöffler, Y.-C. Chiang, K. Gokhberg, T. Jahnke, and R. Dörner, Phys. Rev. Lett. **111**, 233004 (2013)

[19] A. Mhamdi, F. Trinter, C. Rauch, M. Weller, J. Rist, M. Waitz, J. Siebert, D. Metz, C. Janke, G. Kastirke et al., Phys. Rev. A **97**, 053407 (2018)

[20] A. Hans, P. Schmidt, C. Ozga, C. Richter, H. Otto, X. Holzapfel, G. Hartmann, A. Ehresmann, U. Hergenhahn, and A. Knie, J. Phys. Chem. Lett. **10**, 1078-1082 (2019)

[21] F. Schwabl, Quantenmechanik (QMI), 7. Auflage, Springer (2007)

[22] W. Z. Lotz, Zeitschrift für Physik **206**, 205-211 (1967)

[23] H. Ehrhardt, K. Jung, G. Knoth, and P. Schlemmer, Differential cross sections of direct single electron impact ionization, Z. Phys. D **1**,3 (1985)

[24] K. L. Nixon, A. J. Murray, C. Kaiser, J. Phys. B: At. Mol. Opt. Phys. **43**(8), pp.85202 (2010)

[25] J.D. Gorfinkel, and J. Tennyson, J. Phys. B: At. Mol. Opt. Phys.**38** 1607 (2005)

[26] X. Ren, T. Pflüger, J. Ullrich, O. Zatsarinny, K. Bartschat, D.H. Madison, and A. Dorn, Phys. Rev A, **85**, 032702 (2012)

[27] G. H. Wannier, Phys. Rev. **90**, 817–825 (1953)

[28] J. Li, S. B. Zhang, B. J. Ye, J. G. Wang, and R.K. Janev, Physics of Plasmas **23**, 123511 (2016)

[29] J. F. Williams, P. L. Bartlett, and A. T. Stelbovics, Phys. Rev. Lett. **96**, 123201 (2006)

[30] W. Nolting, Grundkurs Theoretische Physik 5/2, 8. Auflage, Springer-Lehrbuch (2013)

[31] B. M. Smirnov, Physics of Atoms and Ions, Springer (2003)

[32] T. Amthor, M. Reetz-Lamour, S. Westermann, J. Denskat, and M. Weidemüller, Phys. Rev. Lett. **98**, 023004 (2007)

[33] W. Demtröder, Experimentalphysik 3 - Atome, Moleküle und Festkörper, Springer-Lehrbuch (2016)

[34] H. Friedrich, Theoretische Atomphysik, Zweite Auflage, Springer-Lehrbuch (1994)

[35] B.H. Bransden, and C.J. Joachain, Physics of atoms and molecules, 2nd edition, Prentice Hall Pearson (2003)

[36] L. Meitner, Zeitschrift für Physik, **11**, 1, pp. 35–54, (1922)

[37] P. Auger, Journal de Physique et le Radium **6**, 6, pp. 205–208, (1925)

[38] F. Holzmeier, T. J. A. Wolf, C. Gienger, I. Wagner, J. Bozek, S. Nandi, C. Nicolas, I. Fischer, M. Gühr, and R. F. Fink, J. Chem Phys. **149** 034308 (2018)

[39] F. M. Penning, Naturwissenschaften **15**, 818 (1927)

[40] S. Falcinelli, F. Pirani, P. Candori1, B. G. Brunetti, J. M. Farrar, and F. Vecchiocattivi, Front. Chem. 7:445 (2019)

[41] A. Ghosh, L. S. Cederbaum, and K. Gokhberg, J. Chem. Phys. **150**, 164309 (2019)

[42] C. Buth, R. Santra, and L. S. Cederbaum, J. Chem. Phys. **119**, 7763 (2003)

[43] J. Zobeley, R. Santra, and L. S. Cederbaum, J. Chem. Phys. **115**, 5076 (2001)

[44] I. Unger, R. Seidel, S.Thürmer, M. N. Pohl, E. F. Aziz, L. S. Cederbaum, E. Muchová, P. Slavíček, B. Winter, & N. V. Kryzhevoi, Nature Chemistry **9**, 708–714 (2017)

[45] G.A. Jones, and D.S. Bradshaw, Front. Phys. 7:100 (2019)

[46] U. Hergenhahn, J. Electron Spectros. Relat. Phenom. **184**, 78–90 (2011)

[47] Atomic spectra database of the National Institute of Standards and Technology (NIST) (https://www.nist.gov/pml/atomic-spectra-database)

[48] S. Scheit, L.S. Cederbaun, and H.-D. Meyer, J. Chem. Phys. **118**, 2092 (2003)

[49] R. Santra, J. Zobeley, L. S. Cederbaum, and N. Moiseyev, Phys. Rev. Lett. **85**, 4490 (2000)

[50] R. Santra, and L. S. Cederbaum, Physics Reports **368** 1, pp. 1–117, (2002)

[51] V. Averbukh, I. B. Müller, and L. S. Cederbaum, Phys. Rev. Lett. **93**, 263002 (2004)

[52] K. Gokhberg, V. Averbukh, L.S. Cederbaum, J. Chem. Phys. **124**, 144315 (2006)

[53] A. C. LaForge, M. Shcherbinin, F. Stienkemeier, R. Richter, R. Moshammer, T. Pfeifer & M. Mudrich, Nature Physics **15**, 247–250 (2019)

[54] N. Moiseyev, J. Chem. Phys. **114**, 7351 (2001)

[55] P. Kolorenč, N. V. Kryzhevoi, N. Sisourat, and L. S. Cederbaum, Phys. Rev. A **82**, 013422 (2010)

[56] F. Trinter, J. B. Williams, M. Weller, M. Waitz, M. Pitzer, J. Voigtsberger, C. Schober, G. Kastirke, C. Müller, C. Goihl, P. Burzynski, F. Wiegandt, T. Bauer, R. Wallauer, H. Sann, A. Kalinin, L. Ph. H. Schmidt, M. Schöffler, N. Sisourat, and T. Jahnke, Phys. Rev. Lett. **111**, 093401 (2013)

[57] J. Rist, T. Miteva, B. Gaire, H. Sann, F. Trinter, M. Keiling, N. Gehrken, A. Moradmand, B. Berry, M. Zohrabi, M. Kunitski, I. Ben-Itzhak, A. Belkacem, T. Weber, A. L. Landers, M. Schöffler, J. B. Williams, P. Kolorenč, K. Gokhberg, T. Jahnke, R. Dörner, Chemical Physics **482**, 185-191 (2017)

[58] A. Hans, C. Küstner-Wetekam, P. Schmidt, C. Ozga, X. Holzapfel, H. Otto, C. Zindel, C. Richter, L. S. Cederbaum, A. Ehresmann, U. Hergenhahn, N. V. Kryzhevoi, and A. Knie, Phys. Rev. Research **2**, 012022(R) (2020)

[59] L. Liu, P. Kolorenč, and K. Gokhberg Phys. Rev. A **101**, 033402 (2020)

[60] W. Pokapanich, N. V. Kryzhevoi, N. Ottosson, S. Svensson, L. S. Cederbaum, G. Öhrwall, and O. Björneholm, J. Am. Chem. Soc. **133**, 13430 (2011)

[61] S. Barth, S. Joshi, S. Marburger, V. Ulrich, A. Lindblad, G. Öhrwall, O. Björneholm, and U. Hergenhahn, J. Chem. Phys. **122**, 241102 (2005)

[62] G. Jabbari, S. Klaiman, Y.-C. Chaing, T. Jahnke, K. Gokhberg, J. Chem. Phys. **140**, 224305 (2014)

[63] K. Gokhberg, A.B. Trofimov, T. Sommerfeld, and L. S. Cederbaum, EPL **72**, 228 (2005)

[64] M. Shcherbinin, A.C. LaForge, V. Sharma, M. Devetta, R. Richter, R. Moshammer, T. Pfeifer, and M. Mudrich, Phys. Rev A **96**, 013407 (2017)

[65] H. Sann, T. Havermeier, H.-K. Kim, F. Sturm, F. Trinter, M. Waitz, S. Zeller, B. Ulrich, M. Meckel, S. Voss, T. Bauer, D. Schneider, H. Schmidt-Böcking, R. Wallauer, M. Schöffler, J.B. Williams, R. Dörner, T. Jahnke, Chem. Phys. **482**, 221-225 (2017)

[66] K. Schnorr, A. Senftleben, G. Schmid, S. Augustin, M. Kurka, A. Rudenko, L. Foucar, A. Broskaa, K. Meyer, D. Anielski, R. Boll, D. Rolles, M. Kübel, M. F. Kling, Y. H. Jiang, S. Mondal, T. Tachibana, K. Ueda, T. Marchenko, M. Simon, G. Brenner, R. Treusch, S. Scheit, V. Averbukh, J. Ullrich, T. Pfeifer, C. D. Schröter, R. Moshammer, Journal of Electron Spectroscopy and Related Phenomena **204**, 245-256 (2015)

[67] P. A. M. Dirac, Proc. Roy. Soc. **A114** (767) (1927)

[68] E. Fermi, Nuclear Physics, University of Chicago Press (1950) formula VIII.2

[69] S. Gozem, A. O. Gunina, T. Ichino, D.L. Osborn, J.F. Stanton, and A. I. Krylov, J. Phys. Chem. Lett. **6**, 22, 4532–4540 (2015)

[70] L. D. Landau, and E. M. Lifshitz, Course of theoretical Physics, Volume 3, Quantum Mechanics, (Pergamon, Oxford, 1965); see Sec.36, Sec.136 and App. e and f

[71] L. D. Landau, and E. M. Lifshitz, Course of theoretical Physics, Volume 4, Part 1, Relativistic Quantum Theory, (Pergamon, Oxford, 1971); see Sec. 56

[72] L.I. Schiff, Quantum Mechanics, McGraw-Hill Education; 3. Rev. Edition (1968)

[73] D. R. Bates, and A. Damgaard, Philosophical Transactions of the Royal Society of London. Series A, Mathematical and Physical Sciences **242** 842 (1949)

[74] D. R. Bates, and I.Esterman, Advances in Atomic and Molecular Physics 5, Academic Press (1969)

[75] N. B. Delone, V. P. Kraĭnov, Multiphoton Processes in Atoms, Second Edition Springer Science & Business Media (2000)

[76] A.S. Eddington, Nature **120**, 117 (1927)

[77] Y. Sugiura, Phil. Mag. Ser. **7**, vol. 4, p. 498-504 (1927)

[78] D. R. Hartree, Proc. Camb. Philos. Soc. **24**, 01, 89 (1927)

[79] S. H. Patil, J. Chem. Phys. **94**, 8089 (1991)

[80] I.V. Hertel, and C.-P. Schulz, Atome, Moleküle und optische Physik 2 Moleküle und Photonen - Spektroskopie und Streuphysik, Springer-Lehrbuch (2010)

[81] C. Mortimer, U. Müller, 13. vollständig überarbeitete Auflage, Thieme (2019)

[82] G. Mie, Annalen der Physik **316**, 657-697 (1903)

[83] A. Lombardi, N. Faginas-Lago, L. Pacifici, and G. Grossi, J. Chem. Phys. **143**, 034307 (2015)

[84] A. van der Avoird, P. E. S. Wormer, F. Mulder, R. M. Berns, Van der Waals Systems pp 1-51, Conference paper, Springer, (2005)

[85] E. Arunan, Resonance **14**, 346–356 (2009)

[86] N. A. Al Taisan, Spectroscopic Detection of the Lithium Helium (LiHe) van der Waals Molecule, Master thesis,University of Nevada, Reno, (2013) (weinsteinlab.org/wp-content/uploads/2019/12/NadaAlTaisan2013.pdf)

[87] F. London, Zeitschrift für Physik **63**, Issue 3-4 Pages 245-279 (1930)

[88] F. London, Trans. Faraday Soc. **33**, 8b–26 (1937)

[89] K. T. Tang and J. P. Toennies, Angew. Chem. Int. Ed. **49**, 9574 (2009)

[90] M. Fowler, Van der Waals Forces between Atoms, http://galileo.phys.virginia.edu/classes/752.mf1i.spring03/vanderWaals.pdf (2007)

[91] N. Brahms, T. V. Tscherbul, P. Zhang, J. Klos, R. C. Forrey, Y. Shan Au, H. R. Sadeghpour, A. Dalgarno, J. M. Doyle, and T. G. Walker, Phys. Chem. Chem. Phys. **13**, 19125–19141 (2011)

[92] N. Balakrishnan, J. Chem. Phys. **121**, 5563–5566 (2004)

[93] B.L. Blaney, and G.E. Ewing, Ann. Rev. Phys. Chem. **27**, 553-584 (1976)

[94] M. V. Johnston, Trends in Analytical Chemistry **3**, 2, Pages 58-61(1984)

[95] U. Kleinekathöfer, K.T. Tang, J.P. Toennies, C.L. Yiu, Chem. Phys. Lett. **249**, 3–4, 257-263 (1996)

[96] J.C. Slater, Phys. Rev. **32**, 339, (1928)

[97] J. B. Anderson, C. A. Traynor, and B. M. Boghosian, J. Chem. Phys. **99**,345 (1993)

[98] M. Przybytek, W. Cencek, B. Jeziorski, and K.Szalewicz Phys. Rev. Lett. **119**, 123401 (2017)

[99] F. Luo, C. McBane, G. Kim, C.F. Giese, and W.R. Gentry, J. Chem. Phys.**98**, 3564 (1993)

[100] W. Schöllkopf, and J. P. Toennies, Science **266**, 1345(1966)

[101] J. Voigtsberger, H.-K. Kim, H. Sann, M. Waitz, F. Trinter, R. A. Costa-Frage, F. Sturm, A. Kalinin, A. Vredenborg, J. Wu, A. Czasch, O. Jagutzki, L. Ph. Schmidt, T. Jahnke, and R. Dörner, J. Phys.: Conf. Ser. **388** 032031 (2012)

[102] A. Landau, A. Ben-Asher, K. Gokhberg, L. S. Cederbaum, and N. Moiseyev, J. Chem. Phys. **152**, 184303 (2020)
Additional data concerning the potential curves was kindly provided by the authors.

[103] N. Sisourat, H. Sann, N. V. Kryzhevoi, P. Kolorenc,T. Havermeier, F. Sturm, T. Jahnke, H.-K. Kim, R. Dörner and L. S. Cederbaum, Phys. Rev. Lett. **105**,173401 (2010)

[104] T.G. Wright, B.R. Gray, L.A. Viehland and R. Johnsen, J. Chem. Phys. **129**, 184307 (2008)

[105] Y. Zhao, and D.G. Truhlar, J. Phys. Chem. A **110**, 5121-5129 (2006)

[106] T. Miteva, S. Klaiman, E.V. Gromov, and K. Gokhberg, J. Chem. Phys. **140**, 204320 (2014)

[107] M. Jungen and V. Staemmler, J. Phys. B: At. Mol. Opt. Phys. 21 463 (1988)

[108] U. Kleinekathöfer, M. Lewerenz, and M. Mladenović, Phys. Rev. Lett. **83**, 4717 (1999)

[109] H. P. Latscha, M. Mutz, Chemie-Basiswissen IV: Chemie der Elemente, 1. Aufl., XIII, 284 S., 83 Abb., Geb. ISBN: 978-3-642-16914-4, Springer (2011)

[110] P. Dehmer and L. Wharton, J. Chem. Phys. **57**, 4821 (1972)

[111] W. Behmenburg, A. Makonnen, A. Kaiser, F. Rebentrost, V. Staemmler, M. Jungen, G. Peach, A. Devdariani, S. Tserkovnyi, A. Zagrebin, J. Phys. B At. Mol. Opt. Phys. **29**, 3891-3910 (1996)

[112] S. K. Kerkines, A. Mavridis, J. Phys. Chem. A **104**, 408-412, (2000)

[113] D. Dell'Angelo, G. Guillon, A. Viel, J Chem Phys. **136** 114308 (2012)

[114] A. Hernando, R. Mayol, M. Pi, M. Barranco, I. S. K. Kerkines, A. Mavridis, International Journal of Quantum Chemistry **111**, 400-405 (2011)

[115] Naima Tariq, Nada Al Taisan, Vijay Singh, and Jonathan D. Weinstein Phys. Rev. Lett. **110**, 153201 (2013)

[116] W. Schöllkopf, and J. P. Toennies, Science **266**, 5189 (1994)

[117] A. Ben-Asher, A. Landau, L.S. Cederbaum, and N. Moiseyev, J. Phys. Chem. Lett. **11**,6600-6605 (2020)

[118] V. Singh, K.S. Hardman, N. Tariw, M.-J. Lu, A. Ellis, M. J. Morrsion, and J.D. Weinstein, Phys. Rev. Lett. **108**, 203201 (2012)

[119] C. Makrides, D. S. Barker, J. A. Fedchak, J. Scherschligt, S. Eckel, and E. Tiesinga, Phys. Rev. A **101**, 012702 (2020)

[120] M. Hoener, L. Fang, O. Kornilov, O. Gessner, S. T. Pratt, M. Gühr, E. P. Kanter, C. Blaga, C. Bostedt, J. D. Bozek, P. H. Bucksbaum, C. Buth, M. Chen, R. Coffee, J. Cryan, L. DiMauro, M. Glownia, E. Hosler, E. Kukk, S. R. Leone, B. McFarland, M. Messerschmidt, B. Murphy, V. Petrovic, D. Rolles, and N. Berrah, Phys. Rev. Lett. **104**, 253002 (2010)

[121] A. Mhamdi, J. Rist, R. Dörner, T. Jahnke, and P.V. Demekhi, Phys. Rev. A **101**, 023404 (2020)

[122] A.B. Voitkiv, C. Müller, S.F. Zhang, and X. Ma, New J. Phys, **21**, 103010 (2019)

[123] A. B. Voitkiv and B. Najjari, Phys. Rev. A **82**, 052708 (2010)

[124] F. Grüll, A. B. Voitkiv, and C. Müller, Phys. Rev. A **102**, 012818 (2020)

[125] F. Grüll, A. B. Voitkiv, and C. Müller, Phys. Rev. Research **2**, 033303 (2020)

[126] J. A. C. Gallas, Phys. Rev. A **21**, 6 (1980)

[127] K. T. Tang, J. P. Toennies, J. Chem Phys. **80**, 3726 (1984)

[128] P. Soldán, E. P. F. Lee, J. Lozeille, J. N.Murrell, T. G.Wright, Chemical Physics Letters **343**,3-4, 429-436 (2001)

[129] H. Helm, Experimentalphysik V Atom-, Molekül- & Optische Physik, WS 08/09, Albert-Ludwigs-Universität Freiburg, (2009)

[130] H. Koc, Journal of Chemistry 3147981 (2018)

[131] V.P. Gupta, Principles and Applications of Quantum Chemistry, Academic Press Inc (2015)

[132] J. G. Duque, H. Chen, A. K. Swan, A. P. Shreve, Svetlana Kilina, S. Tretiak, X. Tu, M. Zheng, and S.K. Doorn, ACS Nano, 5, 6, 5233-5241 (2011)

[133] J. Yuan, and C. D. Lin, J. Phys. B **31**, L637 (1998)

[134] C. Z. Bisgaard, O. J. Clarkin, G. Wu, A. M. D. Lee, O.Gener, C. C. Hayden and A. Stolow, Science **323**, 14641468(2009)

[135] J.-Y- Zhang, L.-Y. Tang, T.Y. Shi, Z.C. Yan, U. Schwingenschlögl, Phys. Rev. A **86**, 064701 (2012)

[136] N. Sisourat, N. V.Kryzhevoi, P. Kolorenc, S. Scheit, and L. S. Cederbaum, Phys. Rev. A **82**, 053401 (2010)

[137] L. Ben Ltaief, M. Shcherbinin, S. Mandal, S. R. Krishnan, A. C. LaForge, R. Richter, S. Turchini, N. Zema, T. Pfeifer, E. Fasshauer, N. Sisourat, and M. Mudrich, J. Phys. Chem. Lett. **10**, 21, 6904-6909 (2019)

[138] F. Grüll, A. B. Voitkiv, and C. Müller, Phys. Rev. A **100**, 032702 (2019)

[139] A. Eckey, A. B. Voitkiv, and C. Müller, J. Phys. B **53**, 055001 (2020)

[140] A. Eckey, A. Jacob, A. B. Voitkiv, and C. Müller, Phys. Rev. A **98**, 012710 (2018)

[141] N. Sisourat, T. Miteva, J. D. Gorfinkiel, K. Gokhberg, and L. S. Cederbaum, Phys. Rev. A **98**, 020701(R) (2018)

[142] T. D. Märk and G. H. Dunn (eds.), *Electron Impact Ionization* (Springer, Wien, 1985)

[143] A. Müller, Adv. At. Mol. Opt. Phys. **55**, 293 (2008)

[144] K. J. LaGattuta and Y. Hahn, Phys. Rev. A **24**, 2273(R) (1981)

[145] B. Peart and K. T. Dolder, J. Phys. B **1**, 872 (1968)

[146] A. Müller, K. Tinschert, G. Hofmann, E. Salzborn, and G. H. Dunn, Phys. Rev. Lett. **61**, 70 (1988)

[147] S. Yan, P. Zhang, X. Ma, S. Xu, B. Li, X. L. Zhu, W. T. Feng, S. F. Zhang, D. M. Zhao, R. T. Zhang, D. L. Guo, and H. P. Liu, Phys. Rev. A **88**, 042712 (2013)

[148] S. Yan, P. Zhang, X. Ma, S. Xu, S. X. Tian, B. Li, X. L. Zhu, W. T. Feng, and D. M. Zhao, Phys. Rev. A **89**, 062707 (2014)

[149] S. Yan, P. Zhang, V. Stumpf, K. Gokhberg, X. C. Zhang, S. Xu, B. Li, L. L. Shen, X. L. Zhu, W. T. Feng, S. F. Zhang, D. M. Zhao, and X. Ma, Phys. Rev. A **97**, 010701(R) (2018)

[150] C. Müller, A. B. Voitkiv, J. R. Crespo Lopez-Urrutia, and Z. Harman, Phys. Rev. Lett. **104**, 233202 (2010)

[151] K. Gokhberg and L. S. Cederbaum, Phys. Rev. A **82**, 052707 (2010)

[152] K. Gokhberg and L. S. Cederbaum, J. Phys. B **42**, 231001(FTC) (2009)

[153] F. M. Pont, A. Bande, and L. S. Cederbaum, Phys. Rev. B **88**, 241304(R) (2013)

[154] F. M. Pont, A. Bande, and L. S. Cederbaum, J. Phys.: Cond. Matter **28**, 075301 (2016)

[155] T. Pflüger, X. Ren and A. Dorn, Phys. Rev. A **91**, 052701 (2015)

[156] X. Ren, E. J. Al Maalouf, A. Dorn and S. Denifl, Nature Commun. **7**, 11093 (2016)

[157] I. Bray, D. V. Fursa, A. S. Kadyrov, A. Müller, A. Borovik, Jr., and S. Schippers, Phys. Rev. A **100**, 012707 (2019)

[158] I. Bray, H. Hayat, D. V. Fursa, and A. S. Kadyrov, Phys, Rev. A **101**, 022703 (2020)

[159] J.A.R. Samson, Adv. Atom. Molec. Phys. **2**, 177 (1966)

[160] T.W. Shyn, Phys. Rev. A **45**, 5 (1992)

[161] A. K. Bhatia, A. Temkin, and A. Silver, Phys. Rev. A **12**, 2044 (1975)

[162] P.S. Ganas, Journal of Applied Physics **52**, 19 (1981)

[163] J. Loreau, J. Liévin, P. Palmeri, P. Quinet, and N. Vaeck, Journal of Physics B **43** (2010)

[164] L. Bomble, A. Chenel, C. Meier and M. Desouter-Lecomte, J. Chem. Phys. **134** 204112 (2011)

[165] J. M. H. Lo, M. Klobukowski, D. Bielińska-Waż, E. W. S. Schreiner and G. H. F. Diercksen, Journal of Physics B, **39**, 11 (2006)

[166] B. Wang,L. Wei, Y. Zhang, W. Yu, Y. Zou,L. Chen, and B. Wei, J. Phys. B: At. Mol. Opt. Phys.**53** 155205(2020)

[167] K.K. Irikura, J. Phys. Chem. A **121**, 40, 7751–7760 (2017)

[168] J. Berakdar, Phys. Rev. A, **56**, 1 (1997)

[169] V. V. Balashov, A. N. Grum-Grzhimailo and N. M. Kabachnik, J. Phys. B: At. Mol. Opt. Phys. **30**, 1269-1291 (1997)

[170] O. Al-Hagan, C. Kaiser, D. Madison, A. Murray, Nature Physics **5**, 59–63 (2009)

[171] K.L. Nixon, A.J. Murray, H. Chaluvdi, S. Amami, D.H Madison and C. Ning, J. Chem. Phys. **136**, 094302 (2012)

[172] M. Abramovitz, I.A. Stegun, Handbook of Mathematical Functions, Formulas, Graphs and Mathematical Tables, Dover Publications, 0009-Revised Edition (1965)

[173] I.S. Gradshteyn, I.M. Ryzhik, Table of Integrals, Series, and Products, Seventh Edition, Academic Press (2007)

Acknowledgements

I would like to thank Prof. Dr. Dr. Carsten Müller and Dr. habil. Alexander B. Voitkiv for their advice and support during my study. I also would like to thank Prof. Dr. Reinhold Egger for reviewing my thesis. Furthermore, I am grateful for the discussions with my fellow members of the institute Alina Golub, Alexandra Eckey, Andreas Jacob and Lars Reichwein. I also greatly appreciate Götz Lehmann's mentorship, even though the cake supply has been a bit one-sided. I also want to thank Elvira Gröters, Ute Birkenkamp-Pickshaus and Eugen Braun for their support in the institute. Finally, I deeply appreciate the companionship of Laura and Bastian Hagmeister, Matthias Gau, and Jacqueline Fedyk throughout my journey.

Eigenständigkeitserklärung

Ich versichere an Eides Statt, dass die Dissertation von mir selbständig und ohne unzulässige fremde Hilfe unter Beachtung der „Grundsätze zur Sicherung guter wissenschaftlicher Praxis an der Heinrich-Heine-Universität Düsseldorf“ erstellt worden ist.
Ich habe keine anderen als die im Literaturverzeichnis angegebenen Quellen genutzt; wörtliche oder sinngemäße Inhalte anderer Werke oder Quellen sind als solche kenntlich gemacht.
Weiterhin erkläre ich, dass die vorliegende Arbeit zuvor weder von mir, noch- soweit mir bekannt- von anderen Personen an dieser oder an einer anderen Hochschule eingereicht wurde und ich bisher weder erfolglose noch erfolgreiche Promotionsversuche unternommen habe. Darüber hinaus ist mir bekannt, dass jedweder Betrugsversuch zum Nichtbestehen oder zur Aberkennung der Prüfungsleistung führen kann.

Düsseldorf, den